



HAL
open science

Implantable microelectrodes on soft substrate with nanostructured active surface for stimulation and recording of brain activities

Valentina Castagnola

► To cite this version:

Valentina Castagnola. Implantable microelectrodes on soft substrate with nanostructured active surface for stimulation and recording of brain activities. Micro and nanotechnologies/Microelectronics. Université Toulouse III Paul Sabatier, 2014. English. NNT: . tel-01137352

HAL Id: tel-01137352

<https://hal.science/tel-01137352>

Submitted on 31 Mar 2015

HAL is a multi-disciplinary open access archive for the deposit and dissemination of scientific research documents, whether they are published or not. The documents may come from teaching and research institutions in France or abroad, or from public or private research centers.

L'archive ouverte pluridisciplinaire **HAL**, est destinée au dépôt et à la diffusion de documents scientifiques de niveau recherche, publiés ou non, émanant des établissements d'enseignement et de recherche français ou étrangers, des laboratoires publics ou privés.



THÈSE

En vue de l'obtention du

DOCTORAT DE L'UNIVERSITÉ DE TOULOUSE

Délivré par : *l'Université Toulouse 3 Paul Sabatier (UT3 Paul Sabatier)*

Présentée et soutenue le 18/12/2014 par :

VALENTINA CASTAGNOLA

**Implantable Microelectrodes on Soft Substrate with
Nanostructured Active Surface for Stimulation and
Recording of Brain Activities**

JURY

M. FRÉDÉRIC MORANCHO
M. BLAISE YVERT
MME YAEL HANEIN
M. PASCAL MAILLEY
M. CHRISTIAN BERGAUD
MME EMELINE DESCAMPS

Professeur d'Université
Directeur de recherche
Professeur d'Université
Directeur de recherche
Directeur de recherche
Chargée de Recherche

Président de jury
Rapporteur
Rapporteur
Examineur
Directeur de thèse
Directeur de thèse

École doctorale et spécialité :

GEET : Micro et Nanosystèmes

Unité de Recherche :

Laboratoire d'Analyse et d'Architecture des Systèmes (UPR 8001)

Directeur(s) de Thèse :

M. Christian BERGAUD et Mme Emeline DESCAMPS

Rapporteurs :

M. Blaise YVERT et Mme Yael HANEIN

a Luca...

"Nihil est in intellectu quod non fuerit in sensu, excipe: nisi intellectus ipse"
Gottfried Wilhelm von Leibniz, *Monadology*

"To light a candle is to cast a shadow"
Ursula K. Le Guin, *A Wizard of Earthsea*

"Siamo ancora dove il buon pan si cuoce..."
Anonimo montanaro

Abstract

Implantable microelectrodes on soft substrate with nanostructured active surface for stimulation and recording of brain activities

Implantable neural prosthetics devices offer, nowadays, a promising opportunity for the restoration of lost functions in patients affected by brain or spinal cord injury, by **providing the brain with a non-muscular channel able to link machines to the nervous system. The long-term reliability of these devices constituted by implantable electrodes has emerged as a crucial factor in view of the application in the "brain-machine interface" domain.** However, current electrodes for recording or stimulation still fail within months or even weeks.

This lack of long-term reliability, mainly related to the chronic **foreign body reaction**, is induced, at the beginning, by **insertion trauma**, and then exacerbated as a result of mechanical **mismatch between the electrode and the tissue during brain motion**. All these inflammatory factors lead, over the time, to the encapsulation of the electrode by an insulating layer of reactive cells thus impacting the quality of the interface between the implanted device and the brain tissue. To overcome this phenomenon, both **the biocompatibility of materials and processes, and the mechanical properties of the electrodes have to be considered.**

During this PhD, we have addressed both issues by developing a simple process to fabricate soft implantable devices fully made of parylene. The resulting flexible electrodes are fully biocompatible and more compliant with the brain tissue thus limiting the inflammatory reaction during brain motions.

Once the fabrication process has been completed, our study has been focused on the device performances and stability. The use of high density micrometer electrodes with a diameter ranging from 10 to 50 μm , on one hand, provides more localized recordings and allows converting a series of electrophysiological signals into, for instance, a movement command. On the other hand, as the electrode dimensions decrease, the impedance increases affecting the quality of signal recordings. Here, an organic conductive polymer, the poly(3,4-ethylenedioxythiophene), PEDOT, has been used to improve the recording characteristics of small electrodes. PEDOT was deposited on electrode surfaces by electrochemical deposition with a high reproducibility. Homogeneous coatings with a high electrical conductivity were obtained using various electrochemical routes. Thanks to the increase of the surface to volume ratio provided by the PEDOT coating, a **significant lowering of the electrode impedance (up to 3 orders of magnitude) has been obtained** over a wide range of frequencies. Thermal accelerated ageing tests were also performed without any significant impact on the electrical properties demonstrating the stability of the PEDOT coatings over several months.

The resulting devices, made of parylene with a PEDOT coating on the active surface of electrodes, have been tested *in vitro* and *in vivo* in mice brain. An improved signal to noise ratio during neural recording has been measured in comparison to results obtained with commercially available electrodes.

In conclusion, the technology described here, combining long-term stability and low impedance, make these implantable electrodes suitable candidates for the development of chronic neural interfaces.

Résumé

Microélectrodes implantables souples à surface nanostructurée pour la stimulation et l'enregistrement de l'activité cérébrale

Les prothèses neuronales implantables offrent de nos jours une réelle opportunité pour restaurer des fonctions perdues par des patients atteints de lésions cérébrales ou de la moelle épinière, en associant un canal non-musculaire au cerveau ce qui permet la connexion de machines au système nerveux. **La fiabilité sur le long terme de ces dispositifs, se présentant sous la forme d'électrodes implantables, est un facteur crucial pour envisager des applications dans le domaine des interfaces cerveau-machine.** Cependant, les électrodes actuelles pour l'enregistrement et la stimulation se détériorent en quelques mois voire quelques semaines.

Ce défaut de fiabilité sur le long terme, principalement lié à une **réaction chronique contre un corps étranger**, est induit au départ par le traumatisme consécutif à l'insertion du dispositif et s'aggrave ensuite, durant les mouvements du cerveau, à cause des **propriétés mécaniques inadaptées de l'électrode par rapport à celles du tissu**. Au cours du temps, l'ensemble de ces facteurs inflammatoires conduit à l'encapsulation de l'électrode par une couche isolante de cellules réactives détériorant ainsi la qualité de l'interface entre le dispositif implanté et le tissu cérébral.

Pour s'affranchir de ce phénomène, **la biocompatibilité des matériaux et des procédés, ainsi que les propriétés mécaniques de l'électrode doivent être pris en considération.** Durant cette thèse, nous avons abordé la question en développant un procédé de fabrication simple pour réaliser des dispositifs implantables souples en parylène. Les électrodes flexibles ainsi obtenues sont totalement biocompatibles et leur compliance est adaptée à celle du tissu cérébral ce qui limite fortement la réaction inflammatoire occasionnée par les mouvements du cerveau.

Après avoir optimisé le procédé de fabrication, nous avons focalisé notre étude sur les performances du dispositif et sa stabilité. L'utilisation d'une grande densité d'électrodes micrométriques, avec un diamètre de 10 à 50 μm , permet de localiser les zones d'enregistrement en rendant possible, par exemple, la conversion d'un ensemble de signaux électrophysiologiques en une commande de mouvement. En contrepartie, la réduction de la taille des électrodes conduit à une augmentation de l'impédance ce qui dégrade la qualité d'enregistrement des signaux. Ici, un polymère conducteur organique, le poly(3,4-ethylenedioxythiophène), PEDOT, a été utilisé pour améliorer les caractéristiques électriques d'enregistrement d'électrodes de petites dimensions. Le PEDOT a été déposé sur la surface des électrodes par électrochimie avec une grande reproductibilité. Des dépôts homogènes avec des conductivités électriques très élevées ont été obtenus en utilisant différents procédés électrochimiques. Grâce à l'augmentation du rapport surface/volume induit par la présence de la couche de PEDOT, **une diminution significative de l'impédance de l'électrode (jusqu'à 3 ordres de grandeur) a été obtenue** sur une large plage de fréquences. De tests de vieillissement thermique accéléré ont également été effectués sans influence notable sur les propriétés électriques démontrant ainsi la stabilité de la couche de PEDOT durant plusieurs mois.

Les dispositifs ainsi obtenus, fabriqués en parylène avec un dépôt de PEDOT sur la surface active des électrodes, ont été testés *in vitro* et *in vivo* sur des cerveaux de souris. **Un meilleur rapport signal sur bruit a été mesuré durant des enregistrements** neuronaux en comparaison avec des résultats obtenus avec des électrodes commerciales.

En conclusion, la technologie décrite ici, associant stabilité sur le long terme et faible impédance, a permis d'obtenir des **électrodes implantables parfaitement adaptées pour le développement d'interfaces neuronales chroniques.**

Thank you, Merci, Grazie...

"Se si escludono istanti prodigiosi e singoli che il destino ci può donare, l'amare il proprio lavoro (che purtroppo è privilegio di pochi) costituisce la migliore approssimazione concreta alla felicità sulla terra: ma questa è una verità che non molti conoscono."

Primo Levi, *La chiave a stella*

I wished to thank **Prof. Yael Hanain**, **Dr. Blase Yvert**, **Dr. Pascal Mailley** and **Prof. Frédéric Morancho** for having accepted our invitation to participate to my PhD Jury defense, and for the time devoted to the review of the present manuscript.

I would like to express my sincere thanks to my supervisors **Christian Bergaud** and **Emeline Descamps** for giving me the opportunity to work on such interesting project and for helping and supporting me at any difficulty though the 3 years of my PhD study.

Christian, merci pour nos discussions, pour ta disponibilité, pour tous les bons conseils et pour avoir toujours encouragé mon besoin de parler sur l'art, la littérature, le cinéma et la musique (jazz).

Emeline, c'était un honneur être ta première thésarde et un plaisir de tout partager autour de ce projet avec toi: satisfactions, dépressions, enthousiasme, problèmes et découvertes. Ensemble on a tout commencé, et j'espère que ce projet pourra se poursuivre dans le meilleur des modes, avec plein de réussite. Je te souhaite tout le meilleur pour la suite de ton travail et de ta vie!

I want to thank my trainees, **Chloé Bayon** and **Aziliz Lecomte**, for the great work accomplished. My gratitude also goes to the entire **NanoBioSystems group**.

I would also like to express my thanks to all the collaborators of this project: **Philippe Marque**, **Christophe Jouffrais**, **Marc Macé**, **Lionel Nowak**, **Lionel Dahan**, **Jessica Remaud**, **Eric Leclerc** and **Jean-Luc Duval**.

Un grand merci à Lionel Dahan pour m'avoir aidé à compléter mes recherches et pour être "a creative night owl".

Thank you to the **LAAS-CNRS** for hosting me and allowing me to use its extraordinary equipment, to the **IPBS** (**Serge Mazerès** and **Audrey Montigny**) for the cell lines, to the **ENSIACET** (**Francis Maury**, **Francois Senocq**, **Diane Samelor** and **Daniel Sadowski**) for allowing me to use the parylene equipment and for the friendly welcome.

I would also like to thank the **CIRIMAT** (**Emmanuel Flahaut**) for hosting me one

week and for the work on carbon nanotubes.

Emmanuel, j'ai immédiatement admiré ta façon d'être: compétent, enthousiaste et gentil. J'ai beaucoup appris en regardant comment tu travail et j'espère pouvoir travailler à nouveau avec toi à l'avenir.

To all the technical stuff, **TEAM** and **I2C**, many thanks!

*En particulier je tiens à remercier **Charline Blatché** pour ta disponibilité, ta rigueur et l'enthousiasme que tu mets dans ton travail ainsi que **Sandrine Assié-Souleille**, **Samuel Charlot**, **Adrian Laborde**, **Ludovic Salvagnac**, **Benjamin Reig**, **David Bourrier** et **Aurélie Lecestre** avec lesquels j'ai travaillé en étroite collaboration. Merci pour votre aide et votre disponibilité. Merci à **Xavier Dollat** pour toutes les cellules électrochimiques (et pas seulement), pour la vitesse d'exécution et pour être un blues brother!*

Thanks to the small **electrochemical community** of the LAAS, it was a pleasure to discuss and share knowledge with you all.

Thanks to **Pierre Temple Boyer**, **Jérôme Launay**, **Isabelle Seguy**, **Laurent Bouscayrol**, **Véronique Conedera**, **Frédéric Ruaul de Beaulieu**.

Finally, I really want to thank some extraordinary people I had the chance to meet during these 3 years who have always been kind and open to every kind of discussion and have demonstrated to be real friends:

***Said Houmadi**, merci pour avoir été le meilleur compagnon de bureau que j'aurais pu avoir, et pour toute l'aide, en particulier avec l'AFM.*

***George Deligeorgis** (techno-dad) and **Georgina Kaklamani** (bio-mama) thank you for making me benefit from you skills and for being so "greek" (una faccia una razza)!*

***Fadhila Sekli** merci pour avoir partagé avec moi les joies et les peines de l'électrode- $\text{Alp\hat{o}t}$ de PEDOT, pour ta gentillesse, ta curiosité et parce qu'ensemble nous ne voudrions jamais arrêter de travailler!*

Without the help of all of you nothing of this would have been possible.

I cannot forget my friends, which are the salt and pepper of my life...they have made these years, in Toulouse, unforgettable. Thanks to **Amelia**, **Nuria**, **Tugce**, **Yin & Lin**, **Katie**, **Malley**, **Viola** and **the great Pierre!**

Thank you "Australian" family: **Didi**, **Patty** and **Aliki**, but also thanks to **Carlos**, **Laurence**, **Hélène**, **Richard**, **Florian** and all the others! Thanks to **Youssef**, **François**, **Sab** and **Didier**. You are all special guys!

I switch in Italian for a special thanks to my LAAS "little Italy" and for my family which could, at least, understand few lines on the entire manuscript:

***Sandro**, **Francé** e **Simo** siete stati una fantastica squadra di pause caffè, cene, risate, supporto fisico e morale. Vi ringrazio per tutti i bei momenti che abbiamo condiviso e per avermi fatto sentire "uno" di voi! **Fuccio**, **Sebastiano** e **Fabio**, vecchia guardia, grazie per il vostro spirito giovane, la vostra voglia di divertirvi e di stare insieme! Avete reso lavorare al LAAS decisamente piacevole (e molto italiano)!*

Grazie **Cesco** e **Marta**, che ci supportate sempre, condividete con noi la passione per la scienza, la gioie e le difficoltà di questo percorso, è bello essere un quartetto così affiatato!

Alla **mia famiglia** va un ringraziamento speciale, per essere sempre presente, anche da lontano, per darmi tanto supporto anche non capendo bene cosa sto facendo e magari soffrendo della mia lontananza. Spero che siate orgogliosi e felici!

A **Luca**, l'ultimo ringraziamento... a te è dedicato questo lavoro, perché è con te e grazie a te che sono arrivata fin qui, e per tutte le cose (scientifiche e non) che abbiamo fatto e che vogliamo ancora fare insieme!

I hope to have not forgotten anyone, in any case thank you for these years so full and meaningful both from scientific and human point of view!

Table of Contents

| | |
|--|-----------|
| List of Acronyms | VI |
| List of Figures | VI |
| List of Tables | X |
| Glossary | XI |
| Preface | 1 |
| Chapter 1 General Introduction | 3 |
| 1.1 Neurons and neural circuits | 3 |
| 1.1.1 The discovery of the neurons | 3 |
| 1.1.2 The neural circuits | 5 |
| 1.1.3 The generation of electrical potentials | 6 |
| 1.2 Measurement of electrical neural signals | 8 |
| 1.3 Recording signals from implanted electrodes | 11 |
| 1.3.1 Intra and extra cellular recordings | 12 |
| 1.3.2 Implantable electrodes: history and state-of-the-art | 13 |
| 1.4 The electrode-tissue interface | 17 |
| 1.4.1 Conductive polymers for biointerfaces | 18 |
| 1.5 The body reaction to implanted devices | 19 |
| 1.5.1 Definition of biocompatibility | 19 |
| 1.5.2 The foreign body reaction | 20 |
| 1.5.2.1 The acute phase response | 21 |
| 1.5.2.2 The chronic phase response | 22 |
| 1.6 Stiff vs flexible electrodes: the mechanical mismatch | 23 |
| 1.6.1 The choice of a soft substrate | 25 |
| 1.6.2 The lack of stiffness in flexible probes | 25 |
| 1.6.2.1 Stiffening strategies: state-of-the-art | 26 |
| 1.7 Neural probe applications | 29 |
| 1.7.1 Treatment of neural diseases: deep brain stimulation | 29 |
| 1.7.2 Brain-computer interfaces | 30 |
| 1.7.2.1 Signal recording for BCIs | 31 |
| 1.7.2.1.1 Brief history of BCI: | 32 |
| 1.7.2.2 Restoration of sensory impairments | 34 |
| 1.7.2.3 Restoration of motor impairments in humans | 35 |
| 1.8 Scope of the Thesis | 38 |
| Bibliography | 39 |

How can we limit the foreign body reaction due to implantation? 57

| | | |
|------------------|---|-----------|
| Chapter 2 | Implantable microelectrodes on soft substrate | 59 |
| 2.1 | Introduction | 59 |
| 2.2 | Soft technology for microelectrode fabrication: choice of the materials . . . | 59 |
| 2.3 | Polyimide-based prototype electrodes | 60 |
| 2.3.1 | Polyimide formation | 60 |
| 2.3.2 | Polyimide-based electrode design | 60 |
| 2.3.3 | Connection for the prototype polyimide device | 60 |
| 2.3.4 | Originality in the process on polyimide | 61 |
| 2.3.5 | Technological process | 62 |
| 2.4 | Parylene-based electrodes | 65 |
| 2.4.1 | The poly(chloro-p-xylylene) or Parylene-C | 65 |
| 2.4.2 | Parylene deposition | 66 |
| 2.4.3 | Parylene-based electrode design | 67 |
| 2.4.4 | Connection for the implantable parylene device | 68 |
| 2.4.5 | Technological process | 68 |
| 2.4.5.1 | Parylene etching: issues and optimization | 71 |
| 2.5 | Temporary stiffening of flexible electrodes using silk coating | 73 |
| 2.6 | <i>In vitro</i> cytotoxicity of the devices | 74 |
| 2.6.1 | Test on cell culture: the cell line | 74 |
| 2.6.2 | Substrate sterilization | 74 |
| 2.6.2.1 | Cell viability | 75 |
| 2.6.3 | Cell morphology assessment | 76 |
| 2.7 | <i>In vitro</i> biocompatibility | 77 |
| 2.7.1 | Organotypic culture | 77 |
| 2.7.2 | Organotypic culture on Parylene-C | 78 |
| 2.7.3 | Organotypic culture on PEDOT:PSS | 80 |
| 2.8 | Conclusion | 82 |
| | Bibliography | 83 |

How can we enhance the signal-to-noise ratio of implantable microelectrodes? 91

| | | |
|------------------|--|-----------|
| Chapter 3 | Nanostructuring of microelectrode active sites | 93 |
| 3.1 | Introduction | 93 |
| 3.1.1 | Conductive polymers for biointerfaces | 93 |
| 3.1.2 | Synthesis of conductive polymers | 95 |
| 3.1.2.1 | Electrochemical polymerization | 95 |
| 3.2 | Electrochemical polymerization of PEDOT | 97 |
| 3.2.1 | State-of-the-art | 97 |
| 3.3 | Electrochemical polymerization of PEDOT through different electrochemical routes | 98 |
| 3.3.1 | Microelectrode cleaning procedure | 102 |
| 3.3.2 | Electrochemical estimation of the active electrode area | 102 |
| 3.4 | Morphological characterization of PEDOT:PSS deposition | 103 |
| 3.4.1 | Effect of the metal surface | 103 |
| 3.4.2 | Effect of the electropolymerization route | 105 |

| | | |
|---|---|------------|
| 3.4.3 | Effect of the deposition time and oxidation potential in PS mode . . . | 105 |
| 3.4.4 | Effect of the surface area | 106 |
| 3.4.5 | Parameters impacting the deposition on the ultramicroelectrode . . . | 106 |
| 3.5 | Electrical characterization of PEDOT:PSS deposition | 108 |
| 3.5.1 | PEDOT conductivity: principles | 108 |
| 3.5.2 | Impedance lowering on PEDOT-modified microelectrodes | 109 |
| 3.5.3 | Local conductivity on PEDOT-modified microelectrodes | 113 |
| 3.5.4 | Coating thickness | 113 |
| 3.5.4.1 | Conductive-AFM measures and calculation of local conductivity | 113 |
| 3.5.5 | Temperature dependence of the conductivity at the microscale . . . | 116 |
| 3.5.6 | Accelerated ageing test | 118 |
| 3.5.6.1 | Accelerated thermal ageing at a macroscale | 118 |
| 3.5.6.2 | Accelerated thermal ageing at a microscale | 120 |
| 3.6 | Conclusion | 121 |
| Bibliography | | 122 |
| Chapter 4 Preliminary results on brain signal recording | | 129 |
| 4.1 | Introduction | 129 |
| 4.1.1 | Consideration about noise during brain recording | 129 |
| 4.2 | <i>In vitro</i> recording in brain slice | 131 |
| 4.2.1 | Experimental set-up | 131 |
| 4.2.2 | Pristine and PEDOT-modified commercial unitary electrodes: noise comparison | 133 |
| 4.2.3 | PEDOT-modified commercial electrodes: signal recording | 135 |
| 4.3 | <i>In vivo</i> recording in mice brain | 135 |
| 4.3.1 | Implantation in the hippocampus | 135 |
| 4.3.2 | Experimental set-up | 136 |
| 4.3.3 | Signal recording | 139 |
| 4.4 | Conclusion | 139 |
| Bibliography | | 139 |
| Chapter 5 General conclusion and perspectives | | 143 |
| 5.1 | Main outcomes emerged from this work | 143 |
| 5.2 | Short-term perspectives | 145 |
| 5.3 | Future research guidelines for this project | 145 |
| Bibliography | | 147 |
| Appendix | | 151 |
| A. Microfabrication Techniques | | 153 |
| B. Electrochemical processes | | 159 |
| C. Conductive Atomic Force Microscopy | | 166 |
| D. Materials and Equipments | | 172 |
| <hr/> <i>Implantable Microelectrodes on Soft Substrate with Nanostructured...</i> | | III |

| | |
|--------------------------------------|------------|
| E. Ethical issues related to the BCI | 176 |
| Valorization | 181 |

List of Acronyms

| | |
|--------------------|--|
| ACSF | Artificial CerebroSpinal Fluid |
| AFM | Atomic Force Microscopy |
| ALS | Amyotrophic Lateral Sclerosis |
| AP | Action Potentials |
| BCI | Brain Computer Interface |
| C-AFM | Conductive-Atomic Force Microscopy |
| CNS | Cental Nervous System |
| CNTs | Carbon Nanotubes |
| CPE | Constant Phase Element |
| CPs | Conductive Polymers |
| DBS | Deep Brain Stimulation |
| DMEM | Dulbecco's Modified Eagle's Medium |
| ECM | Extracellular Matrix |
| ECoG | ElectroCorticography |
| EEG | ElectroEncephalography |
| FDA | Food and Drug Administration |
| FPs | Field Potentials |
| GFAP | Glial Fibrillary Acidic Protein |
| ISO | International Organization for Standardization |
| JMHW | Japanese Ministry of Health and Welfare |
| LFP | Local Field Potentials |
| LiClO ₄ | Lithium Perchlorate |
| LIS | Locked-in Syndrome |
| LSV | Linear Sweep Voltammetry |
| MEA | Microelectrodes Array |
| MEMS | MicroElectroMechanical Systems |

| | |
|-------|---|
| MRI | Magnetic Resonance Imaging |
| NGF | Nerve Growth Factor |
| OLED | Organic Light-Emitting Diode |
| PBS | Phosphate Buffer Saline |
| PCB | Printed Circuit Board |
| PDMS | PolyDiMethylSiloxane |
| PECVD | Plasma-Enhanced Chemical Vapor Deposition |
| PEDOT | Poly(3,4-EthyleneDiOxyThiophene) |
| PEG | PolyEthylene Glycol |
| PGMEA | Propylene Glycol Methyl Ether Acetate |
| PSD | Power Spectral Density |
| PSS | Polystyrene Sulfonate |
| PVD | Physical Vapour Deposition |
| PXC | Parylene-C |
| RIE | Reactive Ion Etching |
| SCE | Saturated Calomel Electrode |
| SEM | Scanning Electron Microscopy |
| UME | UltraMicroElectrode |

List of Figures

| | | |
|------|--|----|
| 1.1 | Visualization of individual neurons through Golgi's stain. | 4 |
| 1.2 | Mouse brain neurons stained with brainbow technique. | 4 |
| 1.3 | Structure of a neuron. | 5 |
| 1.4 | Various steps during the trigger of an action potential and related trans- membrane Na^+/K^+ ion channels behaviour during the steps. | 7 |
| 1.5 | Mechanism of action potentials propagation along the axon. | 8 |
| 1.6 | Placement of implanted and non-implanted recording devices over, onto or inside the brain and related recorded signals. | 9 |
| 1.7 | EEG and an ECoG measurement set-up. | 10 |
| 1.8 | Examples of signals that can be recorded from the brain by invasive and non-invasive techniques. | 11 |
| 1.9 | Patch clamp technique illustration. | 12 |
| 1.10 | Utah microelectrode array | 13 |
| 1.11 | Microelectrode wires and microwire tetrode. | 14 |
| 1.12 | Michigan electrodes and Utah array. | 15 |
| 1.13 | Flexible implantable electrodes. | 16 |
| 1.14 | Hydrogel-coated microelectrode array. | 17 |
| 1.15 | The electrode-electrolyte interface. | 17 |
| 1.16 | Conductive polymers in biological applications. | 18 |
| 1.17 | Summary of wound healing response in the brain versus non-neural tissue. . | 20 |
| 1.18 | Acute and chronic response to an implanted electrode. | 21 |
| 1.19 | Glial scar formation over time imaged by GFAP staining. | 22 |
| 1.20 | Schematic of insertion and inflammatory reaction with stiff and compliant electrode. | 24 |
| 1.21 | Tethered and un-tethered implantation techniques. | 24 |
| 1.22 | Retinal prosthesis. | 25 |
| 1.23 | Parylene-based open-architecture and parylene-based sharp-tipped micro- probes. | 27 |
| 1.24 | Flexible polymer probe with a silicon stiffener. | 27 |
| 1.25 | Parylene-based neural probe with a PEG-filled microchannel. | 28 |
| 1.26 | Silk coated probe with tip shown. Silk solution was mixed with blue dye prior to coating for better visualization[138]. | 28 |
| 1.27 | Schematic representation of a BCI system. | 30 |
| 1.28 | Different classes of BCIs. | 33 |
| 1.29 | Cortical control of a prosthetic arm for self-feeding in monkey. | 33 |
| 1.30 | The cochlear implant. | 34 |
| 1.31 | The artificial retina. | 35 |
| 1.32 | Cathy Hutchinson controlling a robotic arm with BrainGate system. | 36 |
| 2.1 | Formation of a polyimide. | 60 |
| 2.2 | Design for the prototype polyimide-based electrodes. | 61 |

| | | |
|------|---|-----|
| 2.3 | Connection for the polyimide prototype electrode. | 61 |
| 2.4 | Peeled off polyimide-based electrodes used for preliminary tests. | 63 |
| 2.5 | Schematic illustration of the main steps for the fabrication of polyimide-based electrodes. | 65 |
| 2.6 | Chemical structure of parylene-C. | 65 |
| 2.7 | Synthesis procedure for parylene-C film. | 67 |
| 2.8 | Design for parylene-based devices. | 68 |
| 2.9 | Electrical connection for the parylene electrode. | 68 |
| 2.10 | Relation between the starting mass of PXC precursor and the thickness of the obtained film. | 69 |
| 2.11 | Contact angle of water on PXC before and after the UV ozone treatment. | 69 |
| 2.12 | Schematic illustration of the main steps for the fabrication of the parylene-based microelectrodes. | 70 |
| 2.13 | Release of PXC-based devices in water and final appearance of the electrode. | 71 |
| 2.14 | Etching residues for a 10 μm opening with three different photoresist masks. | 72 |
| 2.15 | Etching parylene residues on the sidewalls before stripping the resist. | 72 |
| 2.16 | Cutting of electrode edges by plasma etching. | 72 |
| 2.17 | Optical microscope image of silk deposition on the backside of the probe. | 73 |
| 2.18 | Insertion test in Agarose gel before and after the silk deposition. | 73 |
| 2.19 | Optical microscope image of SH-SY5Y cells. | 74 |
| 2.20 | Seeding method for the cultivation of SH-SY5Y on top of the device. | 75 |
| 2.21 | Calcein-AM fluorescent images showing SH-SY5Y cultivated on top of the device for 24 h, 48 h and 168 h. | 75 |
| 2.22 | SEM images on a SH-SY5Y cell line cultured on top of the device for 48h and 168h. | 76 |
| 2.23 | Schematic representation of the organotypic culture method set-up. | 77 |
| 2.24 | Biocompatibility assessment of parylene-C through organotypic tests. | 79 |
| 2.25 | SEM pictures showing the brain explant and the liver explant grown on parylene-C. | 80 |
| 2.26 | Electrochemical cell for the PEDOT/PSS deposition on Thermanox®. | 80 |
| 2.27 | Biocompatibility assessment of PEDOT through organotypic tests. | 81 |
| 2.28 | SEM pictures showing the brain explant on PEDOT:PSS. | 82 |
| | | |
| 3.1 | Examples of conductive polymers chemical structures. | 93 |
| 3.2 | Schematic representation of the reversible variation of volume associated with the electrochemical-switching conducting polymers. | 94 |
| 3.3 | The three electropolymerization routes. | 96 |
| 3.4 | Mechanism for heterocycle polymerization via electrochemical synthesis. | 96 |
| 3.5 | Chemical structure of PEDOT. | 97 |
| 3.6 | Electrochemical PEDOT deposition through galvanostatic and potentiostatic conditions. | 97 |
| 3.7 | Representation of the three routes of polymerization with the corresponding current (or potential) curves. | 99 |
| 3.8 | Cyclic voltammetry for polymerization for a 50 μm -diameter electrode. | 100 |
| 3.9 | Schematic illustration of the first steps of the electrochemical polymerization process. | 101 |
| 3.10 | Formation of PEDOT nuclei, overlapping and full covering of the surface during the polymerization progress. | 102 |
| 3.11 | Au electrode voltammogram before and after electrode area cleaning. | 103 |
| 3.12 | Electrochemical estimation of the active electrode area. | 104 |

| | | |
|------|---|-----|
| 3.13 | Optical Microscope and SEM images of the PEDOT:PSS films formed on very smooth and scratched gold surface. | 104 |
| 3.14 | SEM and AFM images of the PEDOT:PSS films formed under various conditions. | 105 |
| 3.15 | Optical Microscope, SEM and tapping mode AFM images of the PEDOT:PSS films formed under potentiostatic conditions. | 106 |
| 3.16 | SEM images of a PEDOT:PSS layers on a 10 μm and 50 μm -diameter electrode (right). | 107 |
| 3.17 | SEM images of different morphologies of PEDOT:PSS layers related to different electrochemical deposition parameters. | 107 |
| 3.18 | Energy level diagram of conductive polymers. | 108 |
| 3.19 | Neutral and oxidized state for PEDOT. | 109 |
| 3.20 | Mean impedance of gold electrode with related error bar for different electrodes diameters. | 110 |
| 3.21 | Electrochemical mean impedance spectroscopy and charge capacity for the pristine gold electrode and for the PEDOT-modified electrode. | 111 |
| 3.22 | Electrochemical impedance spectroscopy for a 100 μm -diameter electrode polymerized through different electropolymerization routes. | 111 |
| 3.23 | Impedance lowering and related morphology for different deposition conditions. | 112 |
| 3.24 | Nyquist diagram for a PEDOT-modified 10 μm diameter electrode and related fitting curve using the equivalent circuit. | 112 |
| 3.25 | Optical microscope image of the gold electrode passivated with a photoresist and the electrode PEDOT covered after the dissolution of the photoresist. | 113 |
| 3.26 | Contact mode AFM topography of PEDOT:PSS layer and current corresponding images with C-AFM. | 114 |
| 3.27 | C-AFM I-V curve for the samples electropolymerized by three different ways. | 115 |
| 3.28 | Contact mode AFM topography of PEDOT layer and current corresponding images with C-AFM under an applied potential of 50 mV at different temperatures. | 117 |
| 3.29 | Variation of conductivity with temperature for PEDOT:PSS layers. | 118 |
| 3.30 | Impedance curve before and after PEDOT:PSS polymerization and after thermal accelerated ageing. | 119 |
| 3.31 | Impedance curve before and after PEDOT:PSS deposition, suddenly after the ageing process, and 1 day after the ageing process. | 119 |
| 3.32 | Contact mode AFM topography of PEDOT:PSS layer and current corresponding images with C-AFM after 1 month of ageing at 70°C. | 120 |
| 4.1 | Picture of the experimental set-up for recording signals in brain slices. | 132 |
| 4.2 | PEDOT:PSS deposited on an FHC PtIr unitary electrode. | 132 |
| 4.3 | Comparison of electric hum recorded in a mouse brain slice maintained <i>in vitro</i> , using identical commercial microelectrodes: pristine and nanostructured | 133 |
| 4.4 | Action potentials recorded in area CA3 of the mouse hippocampus maintained <i>in vitro</i> | 134 |
| 4.5 | Structure of human and rodent brain and the hippocampus cross section. | 135 |
| 4.6 | Cross section of the hippocampus and the placement of the stimulation and recording electrodes. | 136 |
| 4.7 | Picture of the positioning of the mouse head into the stereotaxic headholder, skin incision and electrodes positioning. | 137 |

| | | |
|-----|---|-----|
| 4.8 | Images of the recording, stimulation and reference electrodes employed during the <i>in vivo</i> measurements | 137 |
| 4.9 | Signal recording and magnification of LFPs at different stimulation intensities. | 138 |
| 5.1 | SEM image of CNTs-PEDOT:PSS embedded electrochemical deposited on a gold electrode. | 145 |
| 5.2 | Schematic representation of the OLED integrated electrode and first test of blue (470 nm) OLED encapsulation into parylene-C. | 146 |
| 3 | Scheme of the spin coating. | 153 |
| 4 | Scheme of the main processes in the photolithography. | 155 |
| 5 | Scheme of the lift off process. | 155 |
| 6 | The three different photoresist profiles. | 156 |
| 7 | Scheme of the PVD machine. | 156 |
| 8 | Picture and scheme of the plasma etching machine used in our process. | 158 |
| 9 | Scheme of a classical three-electrode cell. | 159 |
| 10 | Schematic image of the mass transport and charge transfer at the electrode/solution interface. | 160 |
| 11 | Diffusion flux and diffusion profile for plane conventional electrode and disk microelectrode. | 162 |
| 12 | Schematic image of the interface electrode/solution and associated Randles circuit. | 163 |
| 13 | Nyquist-type diagram. | 164 |
| 14 | Interaction between the tip and the surface in the AFM. | 166 |
| 15 | Schematic drawing of a conductive AFM. | 167 |
| 16 | The used AFM equipment. | 168 |
| 17 | Cantilever dimensions. | 169 |

List of Tables

| | | |
|-----|---|-----|
| 1.1 | Stiffening strategies in the literature. | 26 |
| 2.1 | Fabrication procedure steps for the polyimide-based electrodes. | 64 |
| 2.2 | Fabrication procedure steps for parylene-based electrodes. | 70 |
| 3.1 | PEDOT electropolymerization parameters for the three routes. | 99 |
| 3.2 | Electropolymerization parameters for the three routes. | 112 |
| 3.3 | Mean thickness value and standard deviation for three different electropolymerization routes. | 113 |
| 3.4 | Conductivity related to the applied voltage for a PEDOT:PSS layer deposited under PD conditions. | 116 |
| 3.5 | Conductivity values for the three polymerization routes. | 116 |
| 3.6 | Conductivity values (related to different potentials applied within the ohmic zone) before and after the accelerated thermal ageing for two different coatings with different surface morphologies. | 120 |

Glossary

astrocytes also known collectively as astroglia, are characteristic star-shaped glial cells in the brain and spinal cord that perform many functions, including a role in the repair and scarring process of the brain and spinal cord following traumatic injuries. 22

basal ganglia (or basal nuclei) are a group of nuclei of varied origin in the brains of vertebrates that act as a cohesive functional unit. They are associated with a variety of functions including: control of voluntary motor movements, procedural learning, routine behaviours, eye movements, cognition and emotion. 29

cerebral cortex is the brain outer layer of neural tissue in humans and other mammals, typically 2-3 mm thick. 3

cochlea is the auditory portion of the inner ear. It is a spiral-shaped cavity in the bony labyrinth and it is divided into three fluid-filled parts. Two are canals for the transmission of pressure and, in the third, is the sensitive organ of Corti, which detects pressure impulses and responds with electrical impulses which travel along the auditory nerve to the brain. 34

Gliosis is a nonspecific reactive change of glial cells in response to damage to the central nervous system (CNS). In most cases, gliosis involves the proliferation of several different types of glial cells, including astrocytes and microglia, and, in its most extreme form, the proliferation associated with gliosis leads to the formation of a glial scar. 22

microglia are specialized macrophages of the central nervous system (CNS) that are distinguished from other glial cells, such as astrocytes and oligodendrocytes, by their origin, morphology, gene expression pattern and functions. they act as the first and main form of active immune defense in the central nervous system (CNS). 21

necrosis is a form of cell injury that results in the premature death of cells in living tissue by autolysis. 79

phagocytose major mechanism of the immune system, discovered in 1882 by Élie Metchnikoff, it is the process by which a cell, often a phagocyte or a protist, engulfs a solid particle or a pathogenic microorganism in order to trap and eventually digest it. 22

purkinje cell are a class of neurons located in the cerebellum that take the name from the czech anatomist Jan Evangelista Purkyně who first discovered them in 1837. These cells are some of the largest neurons in the human brain with an intricately elaborate dendritic arbor, characterized by a large number of dendritic spines and plays a fundamental role in controlling motor movement. 3

pyramidal cells are a type of neuron found in areas of the brain including the cerebral cortex, the hippocampus, and the amygdala first discovered and studied by Santiago Ramón y Cajal. 3

reversible charge injection limit is the amount of charge that can move from the electrode to the surroundings without causing a chemical reaction that is irreversible. 17

scala tympani is a channel in the cochlea, the part of the ear where sounds are converted into electrical signals and sent to the brain. 34

thalamus is a midline symmetrical structure of two halves, within the vertebrate brain, situated between the cerebral cortex and the midbrain. Some of its functions are the relaying of sensory and motor signals to the cerebral cortex, and the regulation of consciousness, sleep, and alertness. 29

Preface

The PhD project presented in this manuscript lies in the context of the Brain-Computer interfaces (BCIs). BCIs are systems that allow a user to control a machine (e.g., a computer, an automated wheelchair, or an artificial limb) solely with brain activity rather than the peripheral nervous system. They usually combine neurophysiological measurement technology with machine learning software, in order to automatically detect patterns of brain activity that relate to a specific mental task. Implementation of a BCI requires brain activity to be measured and the quality of the implanted device (neuroprosthesis) play a crucial role in the long-term performances of the BCI system.

Research on neuroprosthetics has really taken off in the USA. With few institutes involved (CEA-LETI and Institut de la Vision), France is really behind.

In 2010, a *Consortium* was constituted in Toulouse based on the collaboration with Philippe Marque, professor and head of the physical medicine and rehabilitation department at the Rangueil Hospital of Toulouse (Centre Hospitalier Universitaire de Toulouse, CHU), Christian Bergaud (Laboratoire d'Analyse et d'Architecture des Systèmes, LAAS-CNRS), Christophe Jouffrais (Institut de Recherche en Informatique de Toulouse, IRIT) and Lionel G. Nowak (Centre de Recherche Cerveau et Cognition, CerCo). The idea behind the *Consortium* was to cover, with different expertises, all the aspects related to a BCI system, from the conception and realization of a neural probe to the clinical application.

A starting funding has been obtained in 2010 with the program PIR CNRS NEURO-IC. The project has started concretely in 2011, under the name of NANOSTIM, with this PhD grant from the Université Paul Sabatier (UPS) of Toulouse, in conjunction, the same year, with Emeline Descamps's recruitment at CNRS.

During this year, the *Consortium* has expanded, fostering mutual enrichment for neurophysiological expertise and the biocompatibility issues, thanks to the collaboration with Lionel Dahan (Centre de Recherches sur la Cognition Animale, CRCA), Eric Leclerc and Jean-Luc Duval (Laboratoire de Biomécanique et de Génie Biomédical (UTC) de l'Université de Technologie de Compiègne). All these partners, most of them located in the same city have contributed to form a very effective cross-disciplinary *Consortium* which has represented a key point in this project.

The main difficulties highlighted in this work, are related to the fact that this new project has lead us to open a new research field within our laboratory.

Nevertheless, the potential outcomes for severely disabled people of this challenging project, have been the driving force in these years, especially during the hard times that every researcher has to experience.

The present manuscript

The first Chapter, **General Introduction**, will present an overview of all the aspects related to this project, starting from the understanding of the nervous system and the generation of neural electrical signals. In order to measure these signals, which is the scope of the present work, the concept of neural interface will be introduced, giving an overview about the different kinds of neural signals and a brief state-of-the-art of the implantable devices from the first insulated wire to microelectrode arrays. Then the discussion will focus on the biocompatibility aspects and the problem of the acute and chronic body reaction against the implanted probe, pointing out the importance of the materials choice for the neuroprosthesis fabrication. A brief part will be devoted to the ethical problems related to this subject (deepened in Appendix E). After this contextualization, the thesis project will be introduced and motivated, summarizing the state of the art, the main problems to face and the proposed strategies and solutions.

Once given the basis to contextualize this work, the manuscript will be split into two main streams:

1) the biocompatibility: how to limit the body reaction after implantation?

The second Chapter, **Implantable microelectrodes on biocompatible soft substrate**, will focus on the microfabrication procedures employed to develop neural probes on flexible polymeric substrate, with a particular attention to the materials that will represent both the innovation and the difficulty of this project within our laboratory. At the end of the Chapter, the biocompatibility of the device will be assessed through cytotoxicity and biocompatibility tests performed on cell and organotypic cultures.

2) the stability of the electrical performances: how to enhance the signal-to-noise ratio during the recording?

In the third Chapter, **Nanostructuring of microelectrode active sites**, the improvement of the electrical properties of microelectrode active areas through an electrochemical deposition of a conductive polymer (nanostructuring) will be shown. Different parameters of deposition have been used and a fully characterization of the resulting films, in terms of morphological and electrical properties, will be reported. In the fourth Chapter, **Brain signals recordings**, the validation of the nanostructuring procedure both from *in vitro* and *in vivo* tests will be described. The results of signal recording in mouse brain will be presented and discussed.

In the final Chapter, **Conclusion and perspectives**, the main results achieved along the course of this thesis will be summarized and new directions of our research for the short and long term will be introduced.

General Introduction

1.1 Neurons and neural circuits

The brain is the organ that serves as the center of the nervous system and neurons are its core components. The functions of the brain depend on the ability of neurons to transmit electrochemical signals to other cells, and to respond appropriately to electrochemical signals received from them. The electrical properties of neurons are controlled by a wide variety of biochemical and metabolic processes, most notably the interactions between neurotransmitters and receptors that take place at synapses[1].

Neurophysiology, from greek neuron, "nerve"; physis, "nature, origin"; and -logia, works on the understanding basic brain functions and the analysis of the causes of their dysfunctions. To this purpose, the study of the functioning of the nervous system starts by acquiring knowledge about its building blocks (neurons) and the mechanism behind the signal transmission between them.

1.1.1 The discovery of the neurons

In this section a brief history of the discovery of the neurons will be reported, mostly based on the fundamental book written by Dale Purves *et al.*, "**Neuroscience**"[2].

In the early nineteenth century, even if the cell was recognized as the fundamental unit of all living organisms, biologist were confused by the structure and organizational behaviour of the nerve cells and very little was known about the microanatomy and the functioning of the nervous system. Individual nerve cells, indeed, with an extraordinarily complex shapes and extensive branches packed together, were very difficult to resolve from one another with microscopes and cell staining techniques available at that time.

Therefore, an on-going debate among researchers about the organization of the nervous system, took place. Some biologists, called reticularist, "*concluded that each nerve cell was connected to its neighbours by protoplasmic links, forming a continuous nerve cell network, or reticulum*"[2].

The Italian pathologist **Camillo Golgi** discovered a method of staining nervous tissue that could stain a limited number of cells at random, in their entirety. This enabled him to view the paths of nerve cells in the brain for the first time (Fig.1.1.a). However, Golgi himself was led to a conviction that nervous system was composed of a single network, not of separate cells (Fig.1.1.b).

Santiago Ramón y Cajal made a masterful use of the staining technique invented by Camillo Golgi, also modifying it, allowed him to be the first to report with precision the fine anatomy of the nervous system (Fig.1.1)[3].

The reticular theory of the nervous system, eventually fell from favour and was replaced

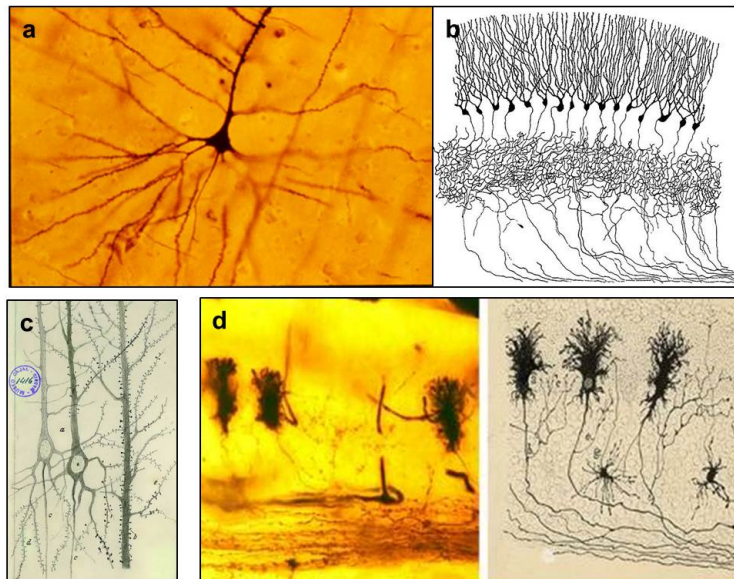


Figure 1.1: a) Visualization of an individual neuron through Golgi's stain. b) Schematic drawing of a part of the hippocampal formation, proposed by Camillo Golgi in support of the reticular theory. c) Original drawing by Cajal showing pyramidal cells of rabbit cerebral cortex. d) Embryonic purkinje cell from newborn dog stained with Golgi method (correlation between the histological slides and the drawing by Cajal). Cajal's original preparations are housed at the Cajal Museum (Cajal Institute, CSIC, Madrid, Spain). Adapted from [4, 5, 6].

by what came to be known as the "**neuron doctrine**", in which the work of Cajal played a central role. Cajal demonstrated that the nervous system was made up of individual cells connected to each other by small contact zones. Both Cajal and Golgi received the 1906 Nobel Award in Medicine and Physiology.

Also during this decade Sir Charles Sherrington (who first coined the term *synapses*), described the junction between nerve and muscle, demonstrating the transfer of electrical signals at synaptic junctions between nerve cells, in 1897. This provided strong support of the neuron doctrine, however, "*it was not until the advent of electron microscopy in the 1950s that any lingering doubts about the discreteness of neurons were resolved*"[2].

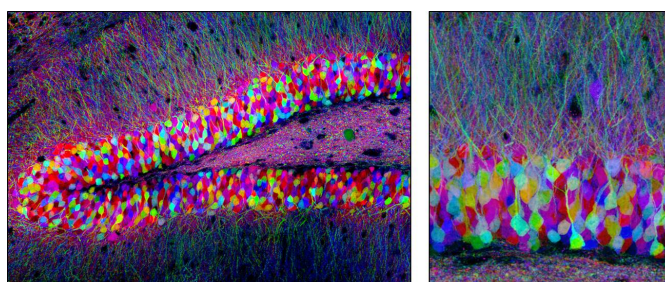


Figure 1.2: Mouse brain neurons stained with brainbow technique (adapted from [7, 8]).

In 2007 an impressive method of staining called "*rainbow*" was implemented by Jeff W. Lichtman and Joshua R. Sanes, both professors of Molecular & Cellular Biology in the Department of Neurobiology at Harvard Medical School[9], shown in Fig.1.2. This powerful tool is a genetic method which make use of transgenic mice that express a number

of different fluorescent proteins in individual neurons. In this way it is possible to label each individual nerve cell with a different color to identify and track axons and dendrites over long distances. The so-generated images, not only allow to construct specific maps of neural circuits but they are also considered a work of art.

From all these histological studies it has been stated that the cells of the nervous system can be divided into two broad categories: *"nerve cells, or neurons, and supporting cells called neuroglia (or simply glia). Nerve cells are specialized for electrical signaling over long distances. Glial cells, in contrast to nerve cells, are not capable of significant electrical signaling; nevertheless, glia have several essential functions in the developing and adult brain. They are also essential contributors to repair of the damaged nervous system-in some cases promoting regrowth of damaged neurons, and in others preventing such regeneration"*[2].

1.1.2 The neural circuits

A typical neuron is constituted by a cell body (soma), dendrites, and an axon (Fig.1.3). The term *"neurite"* is used to describe either a dendrite or an axon, particularly in its undifferentiated stage. **Dendrites** are thin structures that arise from the cell body, often extending for hundreds of micrometers and branching multiple times, giving rise to a complex *"dendritic tree"*. An **axon** is a special cellular extension that arises from the cell body at a site called the *axon hillock* (where membrane potentials propagated from synaptic inputs are summated before being transmitted to the axon) and travels for a distance, as far as 1 meter in humans or even more in other species. The cell body of a neuron frequently gives rise to multiple dendrites, but never to more than one axon, although the axon may branch hundreds of times before it terminates.

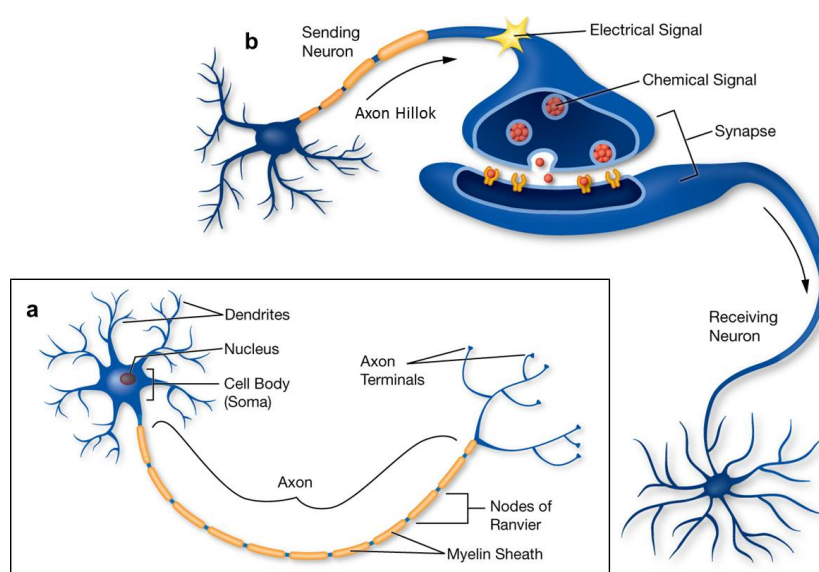


Figure 1.3: a) Structure of neuron with axon, dendrites and synapses. b) Structure of a synaptic connection (from [10]).

"Neurons never function in isolation; they are organized into ensembles called **neural circuits** that process specific kinds of information and provide the foundation of sensation, perception, and behaviour"[2]. Neurons communicate with each other by sending chemicals, called neurotransmitters, across a tiny space, (the **synaptic connections**), between the axons and dendrites of adjacent neurons.

Neural circuits are basically constituted by three functional classes of neurons: **afferent neurons** (which carry information from the periphery toward the brain or spinal cord), **efferent neurons** (which carry information away from the brain or spinal cord) and inter-neurons (which possess short axons and only participate in local aspects). Afferent neurons can be also considered **sensory neurons**, since they carry information from the sense organs (such as the eyes and ears) to the brain while efferent neurons can be called **motor neurons**, since they control voluntary muscle activity such as speaking and carry messages from nerve cells in the brain to the muscles.

1.1.3 The generation of electrical potentials

In their ground-breaking work, **Hodgkin and Huxley** mathematically described the initiation and propagation of the electrical signals in neurons[11, 12, 13].

Neurons employ several different types of electrical signals to encode and transfer information. First of all, they have a means of generating a constant voltage across their membranes when at rest. This voltage, called the **resting membrane potential**, depends on the type of neuron being examined, but it is always a fraction of a volt (typically -40 to -90 mV). **The electrical signals produced by neurons are caused by responses to stimuli, which then change the resting membrane potential.**

Receptor potentials are due to the activation of sensory neurons by external stimuli while another type of electrical signal is associated with communication between neurons at synaptic contacts. Activation of these synapses generates synaptic potentials, which allow transmission of information from one neuron to another. Although neurons and axons are both capable of passively conducting electricity, the electrical properties of neurons compare poorly to an ordinary electric wire. To compensate for this deficiency, neurons have evolved a "*booster system*" that allows them to conduct electrical signals over great distances despite their intrinsically poor electrical characteristics. The electrical signals produced by this booster system are called **action potentials (which are also referred to as "spikes" or "impulses")**.

To understand the principle of an action potential we need first to understand the functioning of the ionic channel on the cell wall (a lipid bilayer membrane which separates the intracellular fluid from the extracellular space). Enzymes (proteins) located in the neuronal membrane behave like pumps which move ions in and out from the cell. As the result of a different concentration of ions inside and outside of the cell, an electrical potential difference is created across the membrane. In the **resting state**, if the potential of extracellular space is used as the reference, the membrane potential is about -70

mV (Fig.1.4). The neuron with the resting potential difference is said to be polarized.

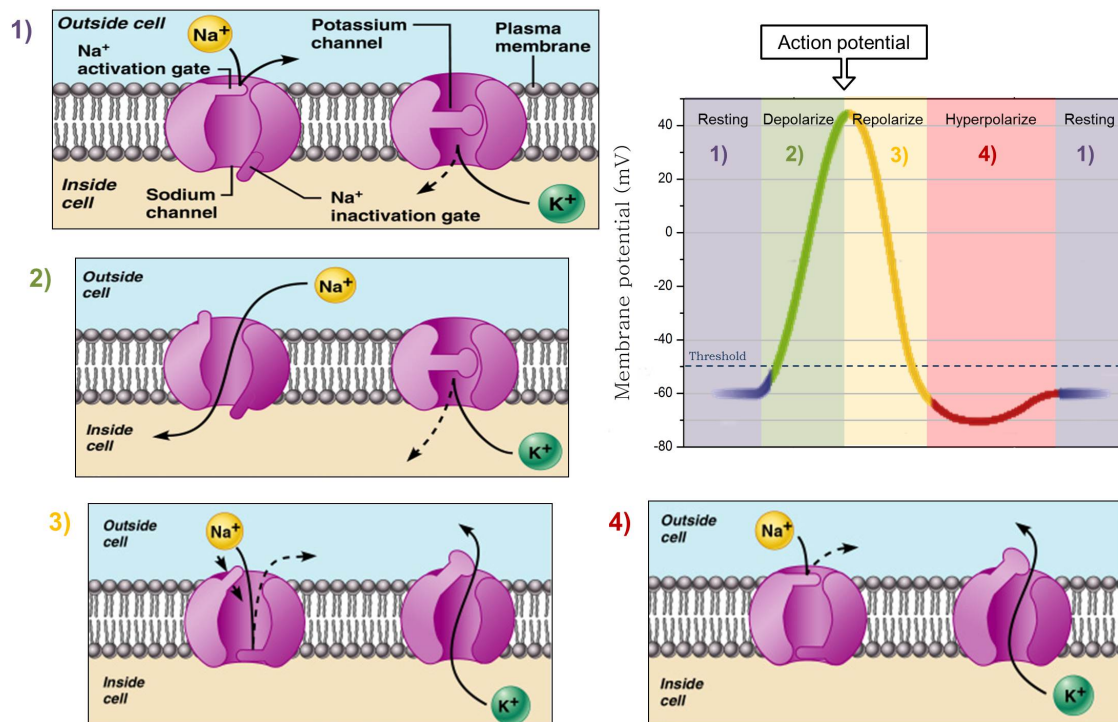


Figure 1.4: Various steps during the trigger of an action potential and related transmembrane Na^+/K^+ ion channels behaviour during the steps. Transmembrane proteins form two types of nongated ion channels, the K^+ channels and the Na^+ channels, through the membrane. Due to the ion concentration gradients, the nongated K^+ channels leak potassium ions out from the neuron, and the nongated Na^+ channels leak sodium ions into the neuron. As there are more K^+ channels than Na^+ channels, there are more out going K^+ ions than in coming Na^+ ions. The concentration of Na^+ is higher in the extracellular fluid and the concentration of K^+ is higher in the intracellular fluid. 1) When a passive current flows across the membrane following a synaptic or receptor potential, the depolarized membrane potential triggers the voltage-gated Na^+ channels to open. The inward Na^+ ionic currents enhance the depolarization which triggers more Na^+ channels to open to let in more ionic currents. This is a positive feedback loop called the Hodgkin-Huxley cycle. If the initial depolarization caused by a passive current is not strong enough to reach a **threshold (about -48 mV)**, it will diminish without triggering any significant response from the neuron. 2) If the depolarized membrane potential passes the threshold (about -48 mV) (Fig.1.4.2), the Na^+ channel currents dominate the process and the membrane potential is highly depolarized to form a positive peak. 3) With a short delay after the opening of the voltage-gated Na^+ channels, membrane depolarization triggers the voltage-gated K^+ channels to open and the outward K^+ currents lead to a strong repolarization. 4) After a phase of hyperpolarization the membrane potential returns to its resting level. Adapted from [14, 15].

When a passive current flows across the membrane, it induces a depolarization. If the depolarized membrane potential passes the threshold (about -48 mV) (Fig.1.4.2), the membrane potential is highly depolarized to form a positive peak (a spike), the action potential, whose amplitude is independent of the initial depolarization. Note that the intensity of the neural signal transmitted in a neuron is not coded by the magnitude of the membrane potential (as all action potentials are of the same intensity), but by the number of action potentials generated per unit time, called the **firing rate**. This phenomenon is

followed by a strong **repolarization** (Fig.1.4.3). The membrane potential drops quickly from the positive peak to a negative level, even lower than the resting potential. This phase is called **hyperpolarization** (Fig.1.4.4), the second phase of the action potential. After a **few milliseconds** the membrane potential returns to its resting level. During the time following the repolarization phase of the action potential, the voltage-gated Na^+ channels are inactivated and unable to be opened, regardless of how much the membrane is depolarized. This is the absolute **refractory period**, which is followed by a short relative refractory period during which action potential can be generated but only with larger-than-normal depolarization. This limited rate of action potential generation determines the **neurons frequency resolution**.

One way to elicit an action potential is to pass an electrical current across the membrane of the neuron.

As we said before, passive current across the membrane caused by a synaptic or receptor stimulation does not travel far because the depolarization declines with distance, due to the leakage through the transmembrane ion channels. However, if this initial depolarization is strong enough to pass the threshold, an action potential will be triggered (usually initiated at the interface between the cell body and axon), which travel down the axon to depolarize new pieces of membrane to continue the process. The sequentially triggered action potentials relay the neuronal signal from the synapse or the receptor along the axon to its terminators, where the signal is passed on to other neurons (Fig.1.5).

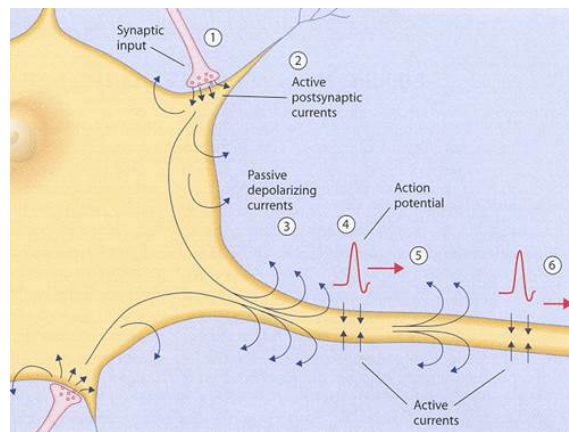


Figure 1.5: Mechanism of action potentials propagation along the axon.

1.2 Measurement of electrical neural signals

A detailed picture of the events underlying the relationship between the functional connectivity map of neuronal circuits and their physiological functions can be obtained by **electrophysiological recording**. Nowadays the available methodologies for recording neural activity include both **invasive (implanted)** and **non-invasive (non-implanted) approaches**.

The first category can be divided in turn into **intracellular and extracellular recordings** to which belong sharp or patch electrodes placed inside the cell or substrate integrated microelectrodes arrays (MEAs) placed near the cell of interest, respectively. These methods will be treated in the next Section (1.3).

However, it is important to point out the fact that the term "invasive", even though commonly used for these devices, possesses an inherent negative undertone. Nonetheless, many are of the opinion that even the so-called non-invasive procedures, can induce a so strong awkwardness, due to the process for fixing the electrode on the scalp or the long learning/calibration time, to be considered as much invasive as a surgery.

These invasive and non-invasive techniques allow to record different kinds of neural signals, depending of the placement of the recording electrodes (Fig.1.6).

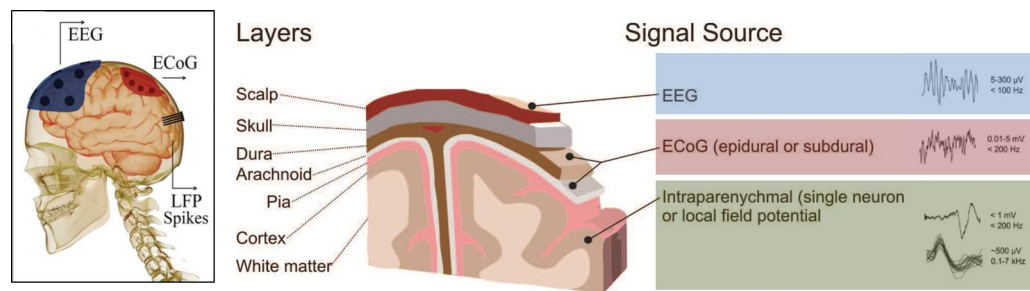


Figure 1.6: Placement of implanted and non-implanted recording devices at different depths, over, onto or inside the brain and the related recorded signals (adapted from [16, 17]).

As regards the non-invasive approach, it has been known, since the pioneering work of Hans Berger[18] more than 80 years ago, that the brain **electrical activity can be recorded** through electrodes on the surface of the scalp[19].

Some of the most common non-invasive recording methods are:

- **Functional magnetic resonance imaging (fMRI)** works by detecting the changes in blood oxygenation and flow that occur in response to neural activity. When a brain area is more active it consumes more oxygen and, to meet this increased demand, blood flow increases to the active area. fMRI can be used to produce activation maps showing which parts of the brain are involved in a certain process.
- **Electroencephalography (EEG)** is the recording of brain electrical activity over a short period of time, usually 20-40 minutes, through multiple electrodes placed along the scalp (Fig.1.7). The resulting traces are known as an electroencephalogram and represent an electrical signal from a large number of neurons. The EEG is capable of detecting changes in electrical activity in the brain on a millisecond-level. It is one of the few techniques available that has such high temporal resolution.
- Other non-invasive techniques to monitor the brain activity are Computed Tomography (CT), Positron Emission Tomography (PET), Magnetoencephalography (MEG) and Near Infrared Spectroscopy (NIRS). In the same category optical imaging technologies of extrinsic fluorescent indicators or genetically encoded molecular probes

can be also mentioned.

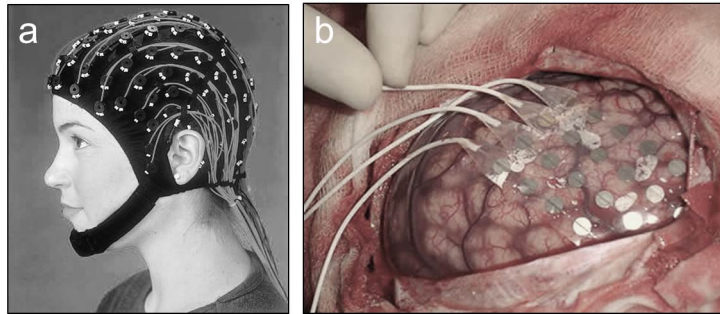


Figure 1.7: Appearance of a) EEG and b) ECoG measurement set-up.

Another recording technique, which lies between invasive and non-invasive, has to be mentioned.

- **Electrocorticography (ECoG)**, or intracranial EEG (iEEG), was first adopted in 1950s by the neurosurgeons Wilder Penfield and Herbert Jasper, at the Montreal Neurological Institute for the study of epilepsy[20]. This approach make use of electrodes placed directly on the exposed surface of the brain to record electrical activity from the cerebral cortex. Even though the brain tissue is not penetrated, a craniotomy (a surgical incision into the skull, see Fig.1.7) is required to place the electrode grid. For this reason ECoG can be considered as an invasive procedure. ECoG signals are composed of **synchronized postsynaptic potentials (local field potentials, LFPs)**, recorded directly from the exposed surface of the cortex.

Non-invasive approaches are designed to record activity from very large scale neural populations, and are not suitable for single neuron resolution. Electrodes on the surface of the scalp, indeed, are at some distance from brain tissue, separated from it by the skull, subcutaneous tissue, and scalp. As a result, the signal is considerably degraded, and only the synchronized activity of large numbers of neural elements can be detected, limiting the resolution with which brain activity can be monitored. Moreover, scalp electrodes pick up activity from sources other than the brain, including environmental noise (such as 50Hz or 60Hz activity from power lines) and biological noise (such as activity from the heart, skeletal muscles, and eyes)[21]. Nevertheless, non-invasive technique such as EEG, are nowadays widely used in many application field (as it will be described in section 1.7.2).

Some of the most common kinds of signals that are possible to detect by a non-invasive measurement are shown in Fig.1.8:

- **Slow cortical potentials (SCPs)** are slow voltage changes generated in cortex that occur over 0.5-10 s among the lowest frequency features of the scalp recorded EEG. Negative SCPs are typically associated with movement and other functions involving cortical activation, while positive SCPs are usually associated with reduced cortical activation[22, 23].

- The **sensorimotor-rhythm** is an 8-12 Hz oscillation detected over sensorimotor cortex during both actual and imagined movements and it is produced by the synchronized and rhythmic synaptic activation[24, 19]. This activity, is called mu-rhythm when focused over somatosensory or motor cortex and visual alpha rhythm when focused over visual cortex[25].
- The **P300 (P3) wave** is a positive peak at about 300 ms evoked by infrequent or particularly significant auditory, visual, or somatosensory stimuli, when interspersed with frequent or routine stimuli[26, 27].

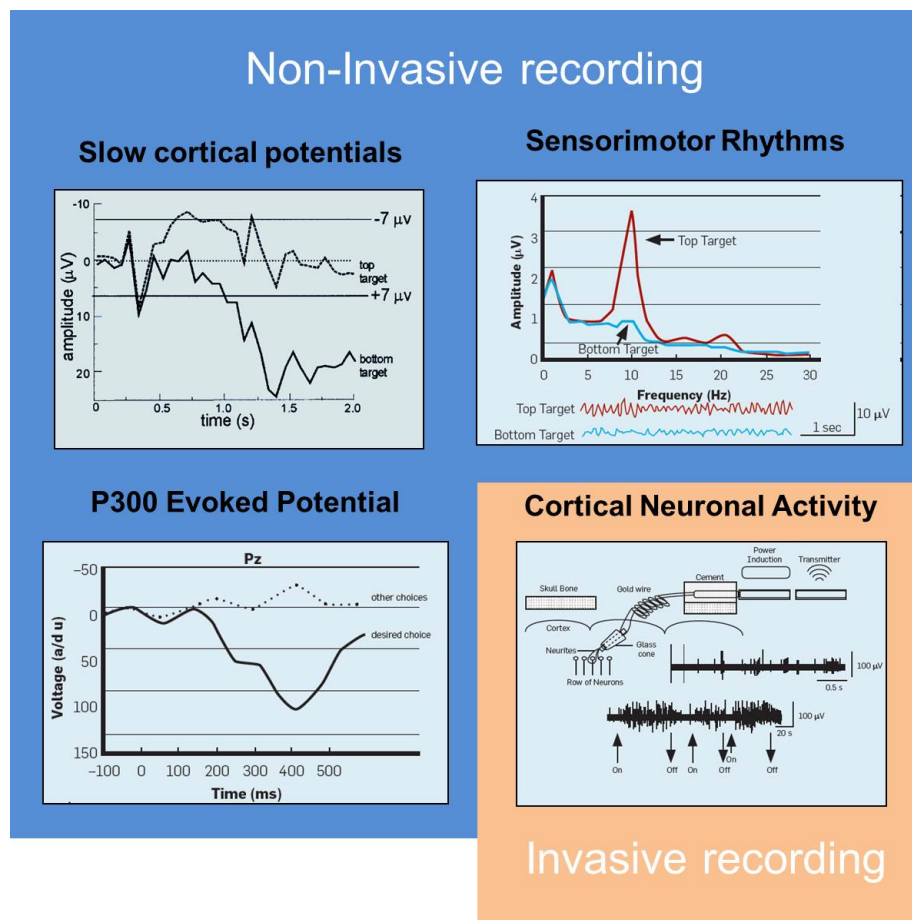


Figure 1.8: Some examples of signals that can be recorded from the brain by invasive and non-invasive techniques (adapted from [28]).

1.3 Recording signals from implanted electrodes

As mentioned before, through invasive techniques it is possible to detect single action potential. **Extracellular field potential recordings (ambiguously referred to as local field potentials (LFPs) or field potentials (FPs))** reflect the spike activity of individual neurons or the superposition of fast action potentials (APs), synaptic potentials

and slow glial potentials in both time and space[29].

Theoretical models predict that action potentials cannot be observed above noise farther than approximately $130\ \mu\text{m}$ from a recording site and that the neuron cell body contributes to the majority of the recorded signal. However, direct measurements have shown that the maximum distance is much less, somewhere between 50 and $100\ \mu\text{m}$. Thus, the distance required to maintain a recording between an electrode site and a neuron cell body is of the order of cell dimensions[30]. The intracellular potential of cells can be in tens of millivolts but the electrical signals recorded from neurons in the brain range in tens of microvolts when we talk about single spike activity or local field potentials as intracortical signals. Single spike activity occurs in the kHz range, while slow field potentials range from zero to hundreds of Hz.

1.3.1 Intra and extra cellular recordings

Intracellular recordings are used to study the physiology of single cells, giving information about transmembrane signals such as post synaptic potentials or other small potential changes.

The classical microelectrode for this application is a glass micropipette filled with an electrolyte and a contact wire that interfaces the pipette to the recording instrumentation; the method involves the micropipette penetration to the cell membrane, thus creating an electrical connection with low resistance. This simple technology has been used in electrophysiology since the 1920s. The power of intracellular recording systems is that they exhibit very good electrical coupling with the cell and provide accurate readout of the entire dynamic range of voltages generated by cells without distorting the readout over time.

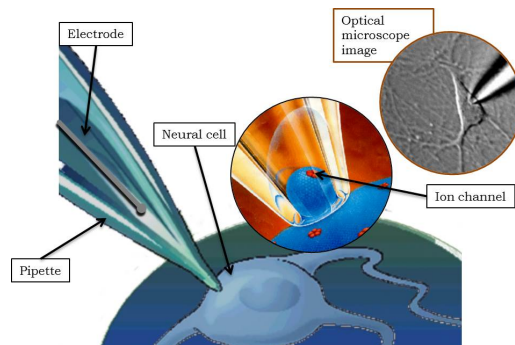


Figure 1.9: Patch clamp technique illustration.

The renowned **patch-clamp method** (Fig.1.9), developed by Neher and Sakmann in the late 70s and early 80s, allowed for the first time to **record currents of single ion channels**[31]. Thereafter, intracellular recording with glass pipette electrodes has remained the most widely used method for studying the electrophysiological properties of biological membranes. In this method, however, there are several drawbacks: not only is it invasive, but the contact between the electrode and cell is notably hard to maintain for more than several hours[32] and the electrolyte in the pipette tip will diffuse into the tissue after a certain time. In addition, it is difficult to integrate these glass electrodes with microelectronics for recording from freely behaving animals.

Extracellular recordings, on the contrary, circumvent the main obstacles of intracellular recordings, as they do not need to penetrate the cell membrane and allow recording from individual cells or complete networks[33, 34]. Such methods, however, tend to suffer from a rather low signal-to-noise ratio, preventing them from measuring subthreshold events on account of their imprecise positioning relative to the cell, and the poor electrical communication at the electrode/cell interfacial contact[35].

Extracellular MEAs used for *in vitro* recordings and polytrodes (high-density silicon-based electrode arrays for multiunit recording) employed *in vivo* (Fig.1.10), largely attenuate and temporally filter the electrical signals. Nonetheless, they enable simultaneous recording and stimulation of large populations of excitable cells for days (*in vitro*) or months (*in vivo*), without inflicting mechanical damage to the neuron plasma membrane.

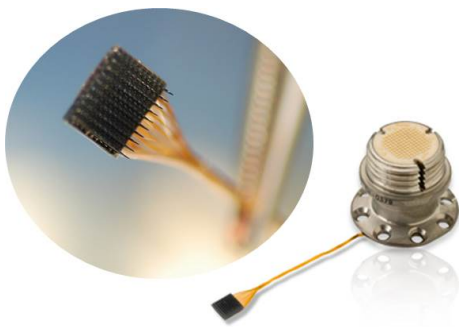


Figure 1.10: Utah microelectrode array

Even though a great deal of information can be gained by using polytrodes, the information harboured in spike-pattern fingerprints is limited. **A key challenge would be the ability to perform specific excitation or recording from a single neuron, or even a single neurite.** Nanotechnology allows, nowadays, the fabrication of electrodes and devices small enough to enable selective stimulation and recording of a targeted population of neurons, down to single cells. Nanomaterials-based devices have the potential to interact with biological systems on the molecular scale[36]. In particular, various configurations of nanowire-based devices have been applied to form an electrical interface with cells and tissues. Ideally, the recording device should be made as small as possible, so as to increase the spatial resolution and minimize the invasive aspect of the procedure. In practice, **electrodes suffer from a definite limit to miniaturization and implantation process.**

Intra and extra cellular recordings are, therefore, two complementary techniques[37, 38]; for example, neurons that do not fire action potentials during a recording session are not visible to extracellular electrodes, that are practically "blind" to the subthreshold events. In some brain areas, 90% of the neurons are not spiking or are firing occasionally at very low rates. Intracellular recordings of synaptic potentials from such neurons would disclose a great deal of information as to the role of this "silent majority" in information processing and the importance of individual neurons to the circuit behaviour.

1.3.2 Implantable electrodes: history and state-of-the-art

Insulated microwires and tetrode: The first generation of implantable microelectrodes simply consisted of known electrically conductive materials, insulated except for the tip, that were stiff enough to be inserted through the pia or the dura mater without

buckling, so they could be used to access deep brain structures (Fig.1.11.a). These insulated microwires, developed in the 1950s, allowed neurophysiologists to study the activity of individual neurons in awake, behaving animals and they could be fabricated easily with available technology[39]. This breakthrough technique is still extensively in use today for both acute and chronic extracellular recording, without having fundamentally changed in the last decades.

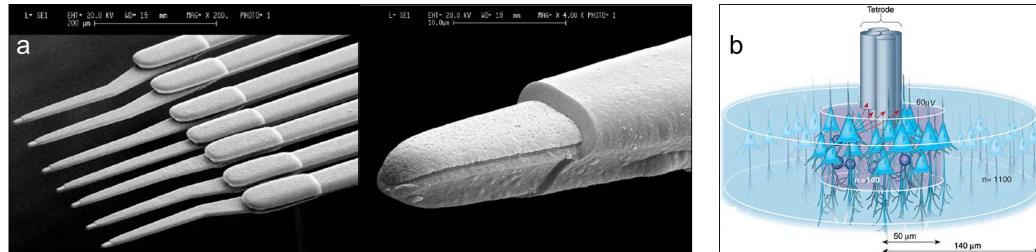


Figure 1.11: a) SEM Micrographs of microelectrodes wires with an insulation layer consisting of Parylene-C and microelectrode tip regions (from [40]). b) The microwire tetrode (from [41]).

Another commonly used implantable device was the microwire tetrode (Fig.1.11.b), which allowed estimating the position of individual recorded neurons by triangulation. Neurons within a radius of $50 \mu\text{m}$ (c.a. 100 in the human cortex) can be separated using clustering methods[41]. Nevertheless, due to their high impedance and small site sizes, in order to be effective, these electrodes must be rigorously positioned near their target neurons using precision micromanipulation. Recordings can only be held for several minutes to several hours before repositioning is required. Moreover, they are limited in their geometries and reproducibility, cause considerable insertion damage, and tend to splay out in tissue, making exact site placements uncertain. All these drawbacks reduce the attractiveness of this technique for long-term chronic implant.

Microelectrode arrays: Since each neuron contributes to many neural ensembles and neural information is spread across population of neurons[42], it was quickly clear that arrays of electrodes, would be needed to really understand the signal processing performed in complex neural networks[43]. Multi-neuronal recording permits simultaneous recording at the level of neuronal populations as well as the single-neuron level, thus more information can be extracted from the brain[41, 44]. In the 1960s, the growing development of photolithographic techniques and silicon etching technology provided a new tool set for fabricating recording electrodes, permitting the microfabrication of structures with high precision in which the spatial resolution between the electrode sites is defined and remains fixed. The needed technology was developed over the next two decades as part of the more general development of integrated sensors and microelectromechanical systems (MEMS)[43].

One of the first silicon-based multielectrode arrays was made by Wise, Starr and Angell[45, 46]. These structures have then evolved in what we know nowadays as **Michigan array** (Fig.1.12.a). In this array several microelectrode sites are patterned on each shank of the structure, providing higher density of sensors while reducing the displaced tissue

when compared to a microwire bundle implant[47].

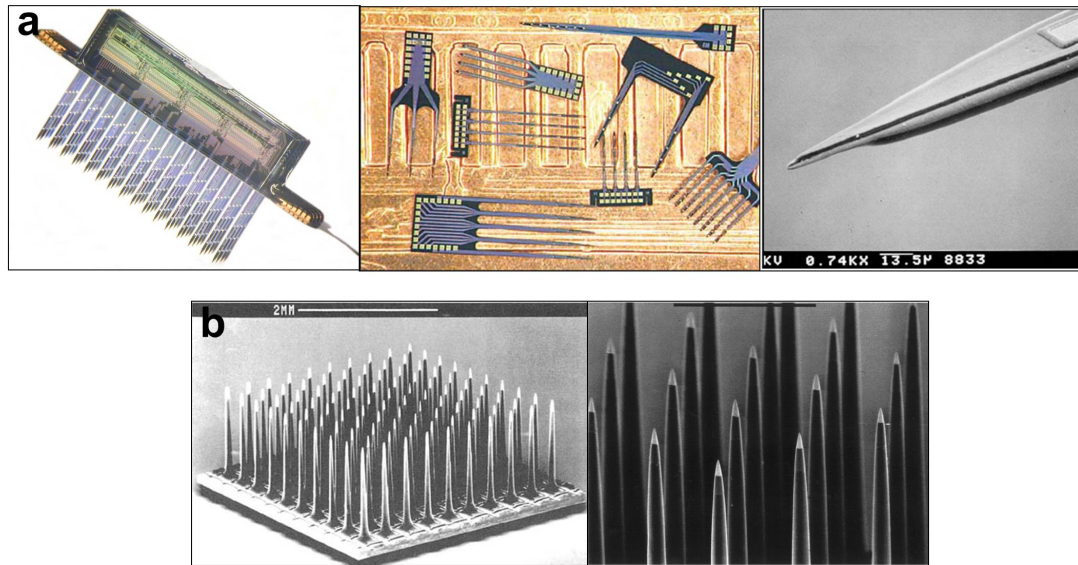


Figure 1.12: a) the Michigan electrodes: 64-site probes assembled in 3D structures, a variety of silicon probes on the back of a U.S. penny and SEM image of the recording site (from [43]). b) The Utah array and the insulation coated electrodes with exposed platinum tips (from [48]).

Another well-known example is represented by the **Utah array** (Fig.1.12.b). This three-dimensional electrode array consists in 100 conductive sharpened silicon needles, each of them electrically isolated from its neighbours in which the tip is coated with platinum and the shanks are insulated with polyimide. Electrical contact is made from the back side of the structure using insulated gold wire[49, 50]. Researchers now routinely employ multiple single microelectrodes aligned into arrays to provide ever-increasing numbers of electrode sites in one device. Some of these devices have positionable electrodes, while others have modified single electrodes (with larger site sizes and/or reduced impedances) which are capable of recording neural activity without precise positioning. These devices can remain functional upon implant for few months, but the same individual neurons cannot be "tracked" longer than about six weeks. Like the first generation of devices, **these intracortical interfaces can remain into the brain for extended time periods, but recording quality and electrode yield typically diminish with time.** The surface area substrate/encapsulation material is much larger compared to the areas of the active electrode sites; therefore, these materials have an important role in long-term stability and functioning of neural implants and they need to be biocompatible, biostable and to exhibit good dielectric properties.

A first example of intracortical device for long-term recording can be found in the **neurotrophic electrode**, introduced by Philip Kennedy in 1992[51, 52]. This electrode combines a standard wire recording technique with neural regeneration since it consists of insulated gold wires fixed inside a hollow glass cone which is coated with Matrigel and nerve growth factor. These so-called neurotrophic factors encourage the

expansion of neurites through the glass cone tip.

The neurotrophic electrode has been used in the BCI applications, in particular concerning silent speech methodologies for normal and disabled individuals, demonstrating the capability of providing useful neural recordings for over 4 years[53, 54].

Implantable electrodes on soft substrate: There has been, therefore, a growing interest toward developing polymer-based implant materials (Fig.1.13) that could be flexible enough to mimic living tissue and reduce the mechanical damage without evoking any adverse tissue reaction. In the last 20 years, polymer-based implants using, for example, polyimide[55, 56, 57, 58], SU8[59, 60], BCB (benzocyclobutene)[58] and parylene[61, 62, 63, 64, 65, 66, 67] as both the structural and insulation material have been micromachined for both acute and chronic recordings[68]. The fabrication of these devices typically involves metal sites sandwiched by thin film of polymer using standard planar photolithographic techniques.

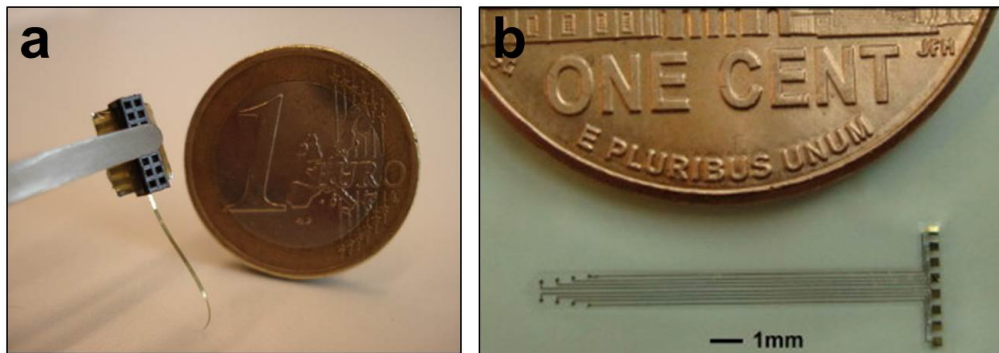


Figure 1.13: Two examples of flexible implantable electrodes fabricated on a) polyimide (from [55]) and b) parylene (from [62]).

Bioactive coatings for implantable electrodes: In the last decade, a new generation of implantable neural interfaces has been developed. These latter intracortical electrodes incorporate "bioactive" components. The electrode designs use standard electrically conductive materials in combination with biologically active species in an effort to improve the performance and function of the neural interface. Initial attempts were centered on the use of microfluidic technology to pump drug-carrying solutions through microfluidic channels built into micromachined implantable probes both in silicon-based devices[69, 70, 71] and in flexible polymer-based devices[64, 72, 73]. Nevertheless, these microfluidic approaches are practical challenges concerning channel patency, biofouling during insertion and chronic attachment to a pump and have led to the development of alternative drug delivery strategies.

The incorporation of bioactive species could be achieved by the use of hydrogels[57, 74] or biodegradable polymer embedding the whole electrode. In 2011, Han *et al.* reported a coating for multielectrode arrays with poly(ethylene glycol)-poly(ϵ -caprolactone) (PEGPCL)

hydrogel with a neurotrophin, nerve growth factor (NGF) eluted in the PEGPCL hydrogel layer into an electrospun fiber mat (EFM) as shown in Fig.1.14. This kind of composite coatings has the potential to improve neural prosthesis biocompatibility by delivering NGF at biologically significant concentrations in a controlled and sustained manner to stimulate neural survival and differentiation[75].

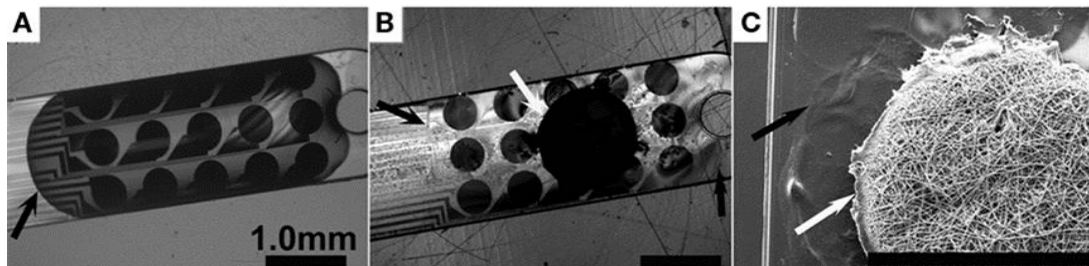


Figure 1.14: A) Optical micrographs of the tip of a microelectrode array coated with PEGPCL hydrogel and B) coated with PEGPCL hydrogel-EFM composite. C) SEM micrograph of the tip of an MEA coated with PEGPCL hydrogel-PCL EFM composite (from [75]).

Collagen (gelatine) and chitosan, for example, have shown haemostatic and antibacterial properties[76, 77] which can favour tissue healing post-insertion. In the recent work of Lewitus *et al.*[78] a coating with tyrosine-derived terpolymer, while enhancing the mechanical properties of the probe is also able to locally deliver dexamethasone (anti-inflammatory agent). Kato *et al.*[79] reported the incorporation of nerve growth factor (NGF) microspheres coated with poly(lactic-co-glycolic acid) (PLGA) in a polyethylene glycol (PEG) matrix. Moreover, PEG has shown potential in treating spinal cord and traumatic brain injuries by inducing cellular recovery due to its hydrophilicity[80, 81].

1.4 The electrode-tissue interface

When the metal is put into contact with the ionic extracellular medium, an equilibrium is established at the electrode-electrolyte interface. The charged metal surface attracts a layer of oriented water molecules, which define the **inner Helmholtz plane**, plus another layer of hydrated ions, which define the **outer Helmholtz plane**. This double layer is followed by a diffuse space charge layer in the bulk solution (Fig.1.15).

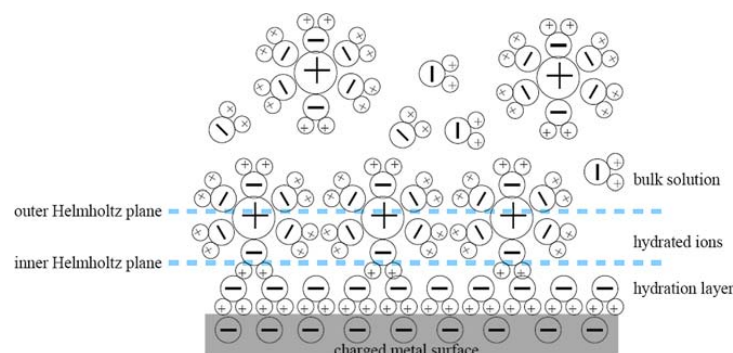


Figure 1.15: The electrode-electrolyte interface[47].

For recording electrodes, **the metal-tissue interface has a linear current-voltage relationship, and the capacitive mechanism of charge transfer dominates**: ionic currents in the extracellular medium cause an electric current in the metal electrode with no charge carriers passing through the phase boundary. No electrochemical reactions should occur in this low voltage and current regime. For stimulation, the higher current amplitudes may result in Faradaic current flows, in which electrons pass through the phase boundary. Irreversible reactions can occur and change the chemical composition of the electrode-electrolyte interface. For noble metals such as platinum or iridium, the metal oxides created during the Faradaic reactions are bound to the metal surface, and the reactions are reversed upon application of a current in the opposite direction. The reversible charge injection limit depends on the electrode material, shape, size, the chemical composition of the electrolyte, and the stimulation waveform[47]. The current to excite single cells using patch clamp techniques are in the range of picoamperes. Nerve and muscle stimulation require the delivery of hundreds of microamperes and milliampere of current respectively. **Electrodes must be optimized to have a high reversible charge injection limits in order to minimize irreversible electrochemical reaction products at the electrode surface**[82].

1.4.1 Conductive polymers for biointerfaces

Used as stable electron- and ion-conducting biomaterials, as we will see in Chapter 3, conductive polymers (CPs) can be employed in various biomedical applications. **They can be used at the interface with biomolecules, cells or living tissues, to detect biological activities by monitoring their electrical properties** (Fig.1.16).

Until now, CPs have been used as a sensing materials for several types of electrochemical biosensors by monitoring the resistance, impedance, charge transport, or surface potential[83, 84].

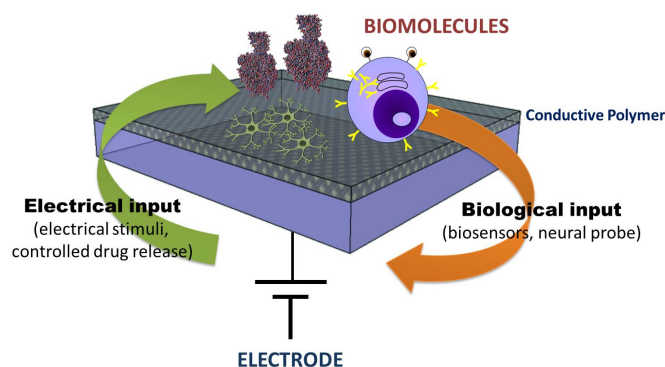


Figure 1.16: Conductive polymers in biological applications.

Particularly interesting in the context of this project, organic semiconductors are now being used in bioelectronics to realize efficient communication between artificial devices and neural networks. CPs are widely used as interfaces with nerve cells for recording

their activities[85, 86] and electrical stimuli can be applied directly to the cells through CPs. Moreover, as reported in section 1.3.2, CPs can act as a matrix to embed bioactive components, in order to enhance the biocompatibility of the device-tissue interface.

1.5 The body reaction to implanted devices

The clinical use of implantable microelectrodes is limited due to their inability to record neural signals for extended periods[87, 88]. Their inability to chronically interface with the neurons in the brain is an immediate obstacle to their use in clinical applications, such as treatment of full or partial paralysis, which requires these implants to maintain a stable performance for the lifetime of the recipient.

One of the main reasons at the origin of this failure is the inflammatory response directed against the implanted foreign body. In particular two aspects arise as critical factors to assure long lasting performances of the implanted device:

- the **biocompatibility of the materials**: the progress made in recent years in the areas of biotechnology and, in particular, of implantable devices, resulted in an increased attention on this aspect since it remains the critical issue in limiting device longevity and functionality[89, 90]. An intimate and prolonged contact between the implanted device and the biological tissues implicates a severe testing schedule before human use and efficacy assessment.
- the **mechanical properties** of the device: often the failure in the ability to record neuronal action potentials is due to a number of mechanical failures of the device itself (oxidation, corrosion, degradation of the passivation layer, etc.). Moreover it has been demonstrated that the mechanical mismatch between current neural devices and neural tissue has a clear contribution in the neuroinflammatory response[91, 88].

In the following sections, we will introduce the main events that follow the implantation of a device in the body, pointing out the advantages related to the use of a soft polymeric substrate compared with the classical silicon rigid substrate in terms of attenuation of the inflammatory response.

1.5.1 Definition of biocompatibility

A first definition of the term "**biocompatibility**" could be *not having harmful effects, nor observing a tissue response comparable to control materials* but the term remains in this way poorly defined. In 1987 Williams[92] provided an interesting definition that referred to *the ability of a material to perform with an appropriate host response in a specific application*. This definition seems to be more appropriate since **no material can perform with an appropriate response in all situations and each particular case has to be considered**. The selection and evaluation of materials and devices intended for use in humans require a structured program of assessment to establish biocompatibility

and safety. Current regulations, whether in accordance with the U.S. **Food and Drug Administration (FDA)**, the **International Organization for Standardization (ISO)**, or the **Japanese Ministry of Health and Welfare (JMHW)**, require that manufacturers conduct adequate safety testing of their finished devices through pre-clinical and clinical phases as part of the regulatory clearance process. In vitro cell culture tests are often used to screen the biocompatibility of implantable devices. In particular in vitro testing is covered by ISO 10993-5 and includes positive and negative control materials, extraction conditions, choice of the cell line and the cell media, etc.

1.5.2 The foreign body reaction

The greatest challenge to obtain consistent or stable intracortical recordings is **the biological response that the brain produces against implanted electrodes**. Therefore, in order to design neural probes that minimize the tissue response of the central nervous system (CNS) it is necessary to understand the biological mechanism involved.

However, the immunological status in the CNS is very peculiar because the cascade of inflammatory events and immune reactions that occur in the brain as a result of a device implantation are still very poorly known compared to other organs or tissues[30, 93].

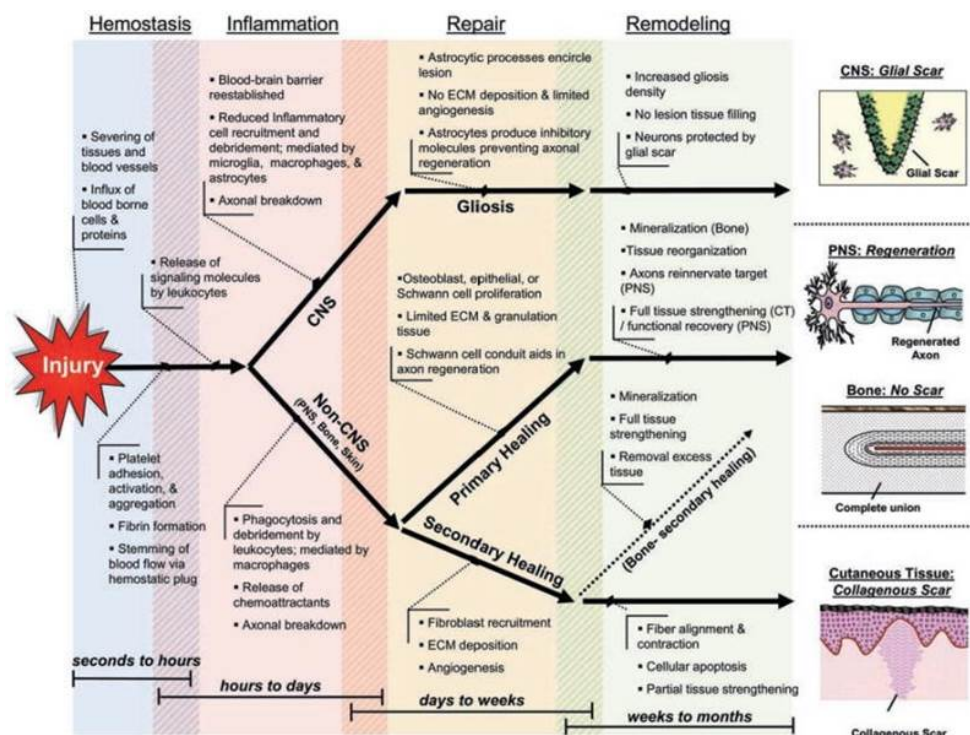


Figure 1.17: Summary of wound healing response in the brain versus non-neural tissue (from [94]).

As can be seen in Fig.1.17, following the implantation of a biomaterial, an **inflammatory process** is initiated consisting of a complex series of reactions tending to prevent the ongoing tissue damage, isolate and destroy the foreign material and activate the repair

processes.

In the long-term, the chronic presence of a microelectrode array *in vivo* influence and modify the composition of tissue around the implant at the molecular and cellular level, in a process that stabilize over a period of several weeks after implantation (Fig.1.17)[95].

The early events constitute the **acute phase response**, which can destroy the implanted system or lead to a **chronic inflammation phase**: this represents the so-called **foreign body reaction**. The degree of this reaction depends on the properties of the device, such as shape, size, surface chemistry and roughness, morphology and porosity, sterility issues, contact duration and degradation.

1.5.2.1 The acute phase response

When a tissue is injured by the mechanical trauma of insertion, neural tissue, capillaries and blood vessels are severed, ripped or sliced, initiating the wound healing response through a series of complex events called acute inflammatory response (Fig1.18.b).

In this acute phase, the tissue around the implant may swell and push the neighbouring neurons away from the electrode surface, blood vessel dilate and excess of blood flows into the injury site to start the coagulation process in order to close the wound[96, 97]. Salts, proteins, and water diffuse through the endothelial junctions of the capillary walls, probably as attempt to dilute the insulting agent, reducing the concentration of harmful molecules, resulting in edema[89]. The acute phase is a process of relatively short duration, up to a few days. During the first week post-implantation, **activated microglia** approach the site of the injury, coming from a blood vessel. These inflammatory cells release numerous neurotoxic factors: after about 6-8 days of implantation, microglia have degraded most cellular debris and damaged matrix by phagocytosis[89, 98].

The physiological changes occurring near an implanted electrode during acute response can appear as a spike in the impedance values during *in vivo* impedance spectroscopy measurements. To obtain reliable signals, indeed, the distance from microelectrode to neuron should be within 50-100 μm . Initially, few neurons can be found within 100 μm of the electrode, but the neuron density is almost normal outside this zone. The area around the implant is therefore defined as a "kill zone"[99, 100]. Since

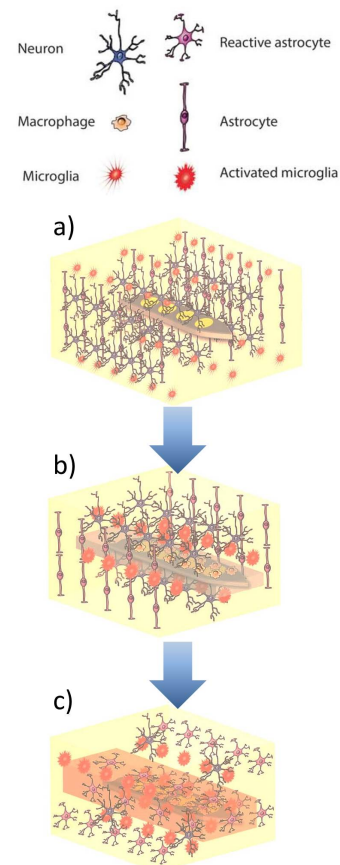


Figure 1.18: a) Schematic of insertion of a neural electrode inside the brain; b) schematic of acute response to an implanted electrode; c) schematic of chronic response to an implanted electrode (adapted from [16]).

the acute response normally causes neuronal death, it takes roughly 4 to 6 months for healthy-appearing neurons to grow closer to the electrode. Among the viable neurons that have survived the acute reaction, remaining electrically active in proximity of the chronically implanted electrode is an important factor determining the strength of the neuronal signals to be recorded by implants. Once acute inflammation declines, chronic response will initiate[16].

1.5.2.2 The chronic phase response

Persistent inflammatory stimuli, such as the continual presence of a foreign object, lead to chronic inflammation (Fig.1.18.c). This phase is characterized by the presence of both **reactive astrocytes** and **activated microglia**.

After the initial wound healing is complete, activated microglia remain at the surface of the implanted microelectrode. This colonization intends to lead to the degradation of the foreign material through the release of lytic enzymes and reactive oxygen agents. Microglia, indeed, attempt to phagocytose the foreign objects and complete the elimination process.

Starting from the second week after implantation, reactive astrocytes and activated microglia tends form a dense sheath around the implant called **glial scar**. Gliosis lead to astrocyte proliferation which creates glial scars, a protection against further injury or infection[30, 101]. **Gliosis (Fig.1.19) is the most common observation of the CNS response to chronically implanted neural electrodes.**

Microglia regulate the production of a thin layer of extracellular matrix (ECM) proteins: collagen, elastin, structural glycoproteins and proteoglycans that can aid in organizing the glial scar. ECM acts not only as a physical scaffold but also as a crucial modulator of biologic processes, including differentiation, development regeneration, tumor progression and repair.

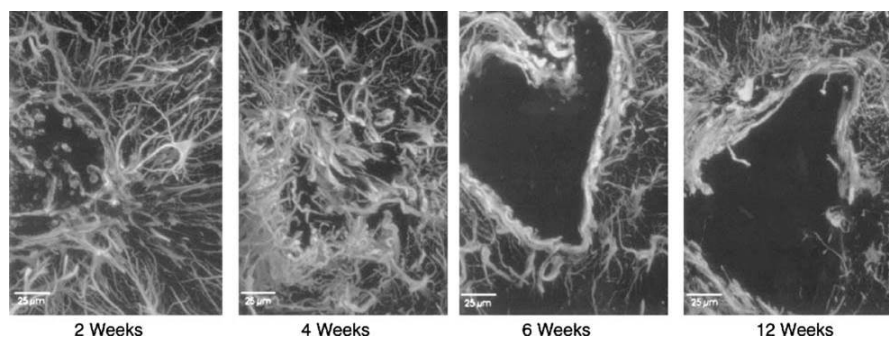


Figure 1.19: Glial scar formation over time imaged by GFAP staining. At the 2- and 4-week time points, the astrocytic processes refill the void left by removal of the probe for tissue processing. Glial scar formation is completed by 6 weeks, when the sheath extends 50-100 μm around the insertion site (from [30]).

Studies have shown that glial scars isolate neural electrodes from the surrounding tissue, in a process similar to the fibrotic encapsulation, in which non-degradable implants are encapsulated in soft tissues. **Gliosis pushes away the surrounding tissues, inhibiting**

the neurite extension around the sheath and extending the distance between the electrode and its nearest target neurons, thus dramatically degrading the amplitude of the recording signals from neurons and increasing the impedance of the tissue-electrode interface[16].

Chronic inflammation stabilize at around 6 weeks post-implantation and it is less uniform histologically compared to acute inflammation[89].

Several studies have addressed different methods of improving the performance of the chronic neuron implant interface by modifying these implants using novel biomaterial designs. Some approaches use surface-immobilized cues to improve the attachment and growth of neurons, including electrochemical deposition of conducting polymers[102, 103] and neuron-promoting biomolecules on the electrodes[104], covalent immobilization of bioactive peptides on dextran-coated[105] and amino silane-modified[106] silicon substrates, covalent[107] or electrostatic layer-by-layer deposition of laminin[108], microcontact printing of poly-L-lysine[109], electrospinning of silk-like polymer containing the laminin fragment IKVAV[110, 111] and incorporation of nerve growth factor and dexamethasone for controlled release to promote neuronal ingrowth or reduce glial inflammation[112, 113].

1.6 Stiff vs flexible electrodes: the mechanical mismatch

As we already mentioned, the biocompatibility of materials is not the only parameter that influences the body reaction. The acute inflammatory response occurs mainly **due to a difference between the mechanical properties of the implanted electrode (e.g., elastic modulus of ca. 150-170 GPa for silicon) and the neighbouring tissues (e.g., elastic modulus of ca. 3-100 kPa for brain tissue)**. Silicon has been extensively employed in neuroprosthetics, due to its well known electrical properties[114], but the rigidity of silicon-based probes represents a considerable problem for *in vivo* implantations[100, 115]. Brain pulsation can be attributed to changes in intracranial pressure due to breathing and the cardiac pulse and we define as micromotions the relative movement between the implant and the brain tissue. The mismatch between the mechanical properties of the stiff probe and the much softer surrounding tissues may result in tissue damage that may lead to tolerability issues (Fig.1.20).

The role of mechanical mismatch has not been fully elucidated through *in vivo* studies to explain the interplay of chemical and mechanical factors that contribute to glial scarring surrounding intracortical implants. A certain number of studies indicates that indwelling electrodes exert forces on local populations of cells[117, 118, 119]. Over time, the implanted electrode is anchored to the tissue via the extracellular matrix (ECM) and neural inflammatory cells (including microglia and astrocytes), resulting in cellular attachments to the electrode modifying the forces exerted on the brain tissue[118]. Micromotion associated with electrode movement within the tissue and the mechanical properties of the electrode dynamically change the level of exerted forces on the cortical tissue during scar maturation.

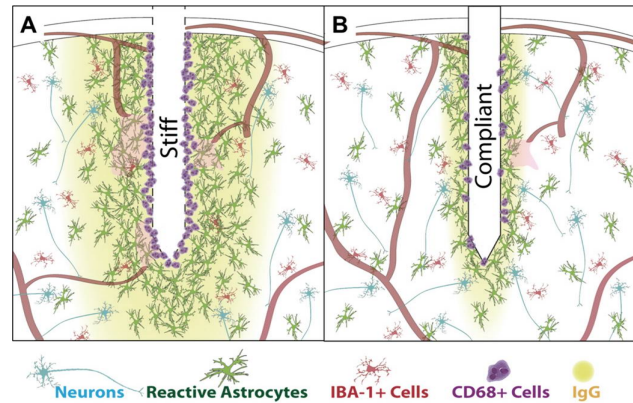


Figure 1.20: a) Schematic of insertion and inflammatory reaction with a A) stiff and B) compliant electrode (from[116]).

This phenomenon can also be exacerbated as a result of **mechanical tethering** of the electrodes to the skull[99, 120, 67]. Current implants, indeed, are anchored to the skull at one end, and remain floating in the brain tissue at the end where the recording sites are located (Fig.1.21): micromotions or rather microforces, between the implanted probe and the tissue, cause small injuries that constantly maintain an inflammatory process[30, 121, 98]. Consequent motion artefacts may significantly distort the recorded signal and complicate data analysis.

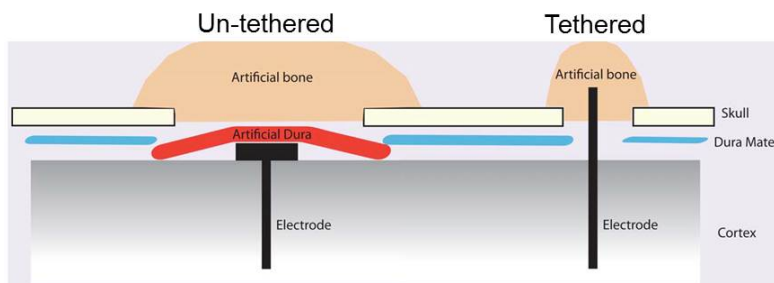


Figure 1.21: Tethered and un-tethered implantation techniques: the un-tethered set-up is ensured by adding artificial dura on top of the implant, separating the implant from the skull. In contrast, tethered implant is glued to the sealant materials (from [122]).

Even if it has been stated that untethered implants reduce the extent of the glial scar, in a recent work, Lind *et al.*[122, 123] observed that untethered probes also left substantial scars around the implant. This could be explained with the presence of substantial inertial and gravitational forces between tissues and probes because of their great **difference in density**. Electrodes are often made from metals such as stainless steel (density = 8 g/cm^3), tungsten (density = 19.25 g/cm^3), or even platinum (density = 21.45 g/cm^3) and iridium (density = 22.6 g/cm^3), the density of which is much greater than the density of the brain tissue (density = 0.99 g/cm^3). These differences in density will inevitably lead to inertial forces that arise every time the implanted entity changes direction or velocity.

1.6.1 The choice of a soft substrate

A neural probe may need to be designed such that it can conform to motion of the brain while electrical functionality is maintained during deformation. One way to mitigate this problem is to select substrate materials according to a more suitable combination of their electrical and mechanical properties[124, 125]. To this purpose, several **flexible and biocompatible polymers**, are being increasingly used as substrate and/or encapsulation materials[126, 127, 128, 129] and they may even be biochemically functionalized to deliver bioactive substances. The flexibility of the resulting devices provides a lot of advantages:

- **a more conformal coverage** of the living tissue surface and a certain degree of strain relief against the micro-motion forces.
- **an improved signal-to-noise ratio (SNR)** since a more uniform electrical contact is established at the electrode-tissue interface.[62].
- **a reduced insertion damage** proved by histology tests and a reduced inflammatory response as compared to stiffer silicon probes[55].

Nevertheless, microelectrode arrays (MEA) fabricated on soft substrates are mostly employed for retinal stimulation (Fig.1.22), since they can easily conform with the eye shape[130, 63], or for electrocorticography (ECoG) measures, in which the probe is placed on the brain surface[131].

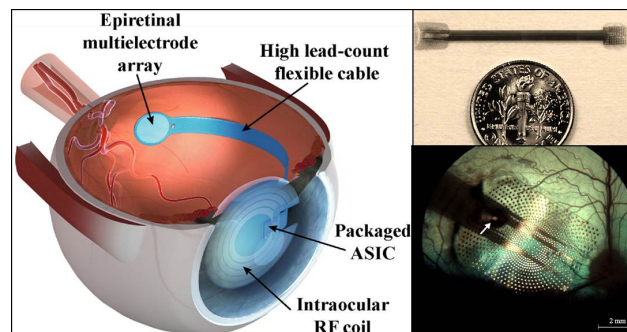


Figure 1.22: Placement and components of envisioned intraocular retinal prosthesis and parylene MEAs tacked to the right retina[63].

The use of flexible polymers as a substrate for penetrating electrodes presents some additional difficulties, mainly related to the lack of stiffness of the probe during the insertion into the brain tissue.

1.6.2 The lack of stiffness in flexible probes

Traditionally, stiff electrodes for cortical implants are inserted into the brain cortex through the dura and pia, or the dura is removed and the electrodes lowered through the pia alone but the low buckling force of soft polymer-based electrodes precludes the use of this implant technique.

Going at the same place with the development of flexible probes, several insertion techniques or stiffening strategies have been proposed in the last 10 years in order to address this issue.

Rousche *et al.*, in 2001, have developed and tested an alternate technique to allow the safe implantation of polyimide-base flexible devices in rat brains[57]. A pial incisions for each shaft of the electrode was created, by the use of a scalpel or a stiff 100 μm -diameter tungsten wire. The incisions were created to match the shaft spacing pattern. Even though the incisions is tried to be made with as little associated tissue damage as possible, this technique entails a high tax of invasivity and trauma.

Therefore, different stiffening strategies started to be found in the literature since 2004. The strategies revolve on three main ideas which are summarized in Table 1.1:

| | | | | | |
|------------|---|-------------------------------|---------|--------------------------|-----------------|
| I | Permanent integrated stiff layer | silicon stiffener[58] | | parylene structure[132] | |
| II | Removable external stiffener | PEG glued stiffener[133, 134] | | SAM glued stiffener[135] | |
| III | Temporary biodegradable polymers stiffener | glucose[136, 56, 137] | PEG[64] | Silk[138] | others[78, 139] |

Table 1.1: Stiffening strategies in the literature.

1.6.2.1 Stiffening strategies: state-of-the-art

I. Permanent integrated stiff layer: a simple solution resides in the integration of a stiff backbone on the flexible probe, as in the work of Singh *et al.* who realized a polyimide-based electrode using a 5-10 μm thick silicon backbone[58].

A more elegant kind of permanent stiffener has been proposed by Egert and Najafi in 2011: a parylene-based neural probe with engineered mechanical stiffness, low cross-sectional area and sharp tip (Fig.1.23.a)[132]. Thanks to the use of a thick photoresist with patterned trenches, they could shape the probe shank, and refilling these trenches with Parylene using conformal vapor deposition. Therefore they could increase the moment of inertia without altering the cross-section of the probe.

Seymour *et al.* implemented a probe design with a conventional, thick shank that supported a 5-mm-thick lateral platform (Fig.1.23.b)[129]. The thicker shank provided the structural strength to penetrate the rat pia matter and advance straight into the cortex. They also underlined the relationship between probe size and shape and the reactive tissue responses in a chronic animal implantation.

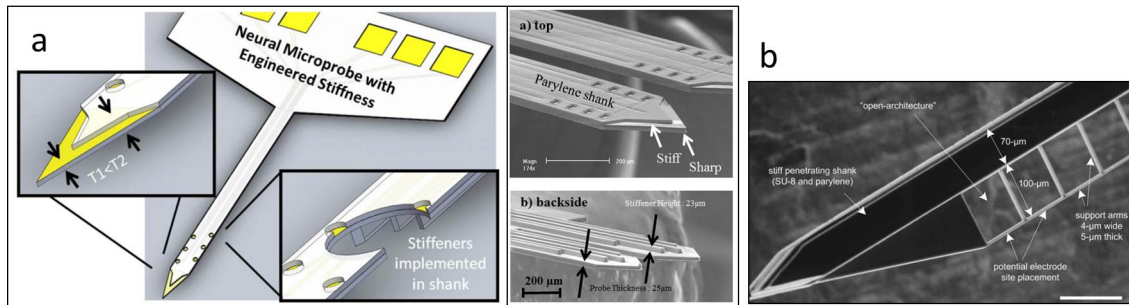


Figure 1.23: a) parylene-based sharp-tipped microprobes, with shanks of 2 mm-long, 20 μm -thick and 380 μm -wide[132]. b) parylene-based open-architecture with a thick shank and an integrated thin lateral platform [129].

Finally, thermoforming of parylene have been used by Kuo *et al.* to create the three dimensional sheath structures from flat surface micromachined microchannels using solid microwires as molds[140]. A procedure for implantation of the neural probe was developed and successfully demonstrated *in vitro* into an agarose brain tissue model.

However, a permanent approach cannot be considered relevant, since it could reduce the intended flexibility of the probe.

II. Removable external stiffener: the use of retractable insertion shuttle to temporarily change the stiffness of the probe own the advantage to recover the original flexibility of the probe after insertion.

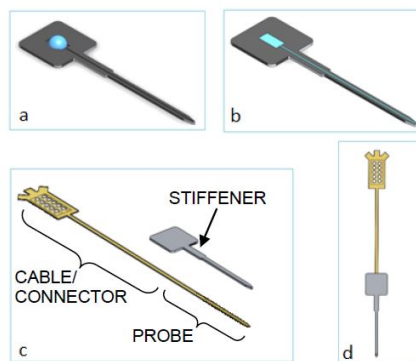


Figure 1.24: Process to assemble a flexible polymer probe to a silicon stiffener with polyethylene glycol[134].

Recently, Felix *et al.*[134] proposed the use of a temporary mechanical stiffener, fixed to the device with biodegradable adhesive polyethylene glycol (PEG) and removable after insertion. PEG, that has a melting point around 60° C, is solid at room temperature but dissolves itself when in contact with physiological liquid; it is well-known for its biocompatibility and already largely diffused in drug delivery strategies. The silicon stiffener included a handling tab and a channel that can be filled with PEG, as shown in Fig.1.24.

In 2009, Kozai *et al.*[135] developed silicon insertion shuttles to provide temporary stiffness to polyimide-based probes. These shuttles were coated with a carboxyl terminal self-assembled monolayer (SAM), highly hydrophilic so that water molecules from physiological liquids would be attracted to the SAM coating. In this way, after insertion, the polymer probe separates from the shuttle.

Nevertheless, the drawback of this this approach is related to the risk associated with the retraction of the stiffener.

III. Temporary biodegradable polymers stiffener: this approach involves stiffening coatings able to degrade themselves into physiological liquids after insertion. These kinds of coatings also allow to integrate biomolecules or bioactive agents into the polymer matrix as we mentioned in Section 1.3.2.

Singh *et al.* developed BCB (benzocyclobutene) based electrode and made use of a glucose coating to perform the insertion. The glucose was deposited by deep coating and surrounded by a layer of mineral oil to postpone biodegradation[136].

Another strategy, developed by Takeuchi *et al.*, involved a microfluidic channel filled with PEG (Fig.1.25)[64]. The small cross section provided by the microchannel allowed to increase the PEG dissolution time up to 200 seconds.

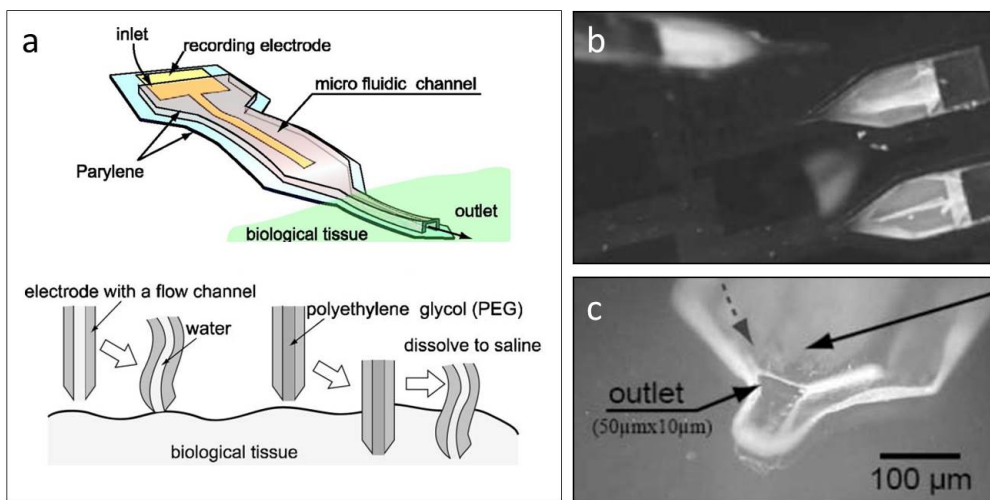


Figure 1.25: a) Takeuchi *et al.*[64] parylene-based neural probe with microchannel; b) filling of the channel with PEG to increase the stiffness; c) the limited PEG exposed area to the physiologic liquid through the outlet should reduce the dissolution time.

Silk-I protein polymer can be processed to become bioresorbable, thus being a suitable candidate for a flexible electrode stiff coating. Silk is indeed one of the strongest natural fibres, and possess good indications on its biocompatibility[141]. Moreover, the silk coating can be biodegraded between 30 minutes and 25 hours depending on the time during which the silk fibres have been annealed, thus leading to a great modularity for the probe implantation.

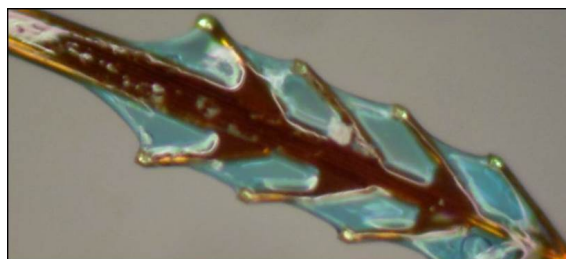


Figure 1.26: Silk coated probe with tip shown. Silk solution was mixed with blue dye prior to coating for better visualization[138].

A recent study by Wu *et al.* showed that silk can be used to embed a fish-bone-shaped polyimide neural probe, providing temporary mechanical strength during insertion[138].

1.7 Neural probe applications

Neural interfaces connect neurons, the electrically active cells of the nervous system, and electronic circuitry. They are used, therefore, in basic neuroscience, to study physiological processes at the cellular level, to understand basic brain functions, and to analyze causes of their dysfunctions.

The possibility of interfacing the nervous system with electronic devices has long fascinated scientist, engineers and physicians. In general, the ability to expand the bandwidth of the communication between brain and machine would provide many interesting possibilities ranging from faster human-computer interfaces and direct remote control to the restoration of functions in the nervous system.

Several examples of implantable neural interfaces already commercially available for the treatment of certain diseases (Alzheimer, Parkinson, Epilepsy) through deep brain stimulation and to restore sensory or motor impairments.

Amyotrophic lateral sclerosis (ALS), locked-in syndrome (LIS) brainstem stroke, brain or spinal cord injury, cerebral palsy, muscular dystrophies, multiple sclerosis, and numerous other diseases that impair the neural pathways that control muscles or impair the muscles themselves, affect millions of lives worldwide. At the present time, few (if any) therapeutic options are available for restoring motor or sensory function lost. Different approaches have been used in order to bypass the reparation through, for example, increasing the capabilities of remaining pathways: people largely paralyzed by massive brainstem lesions can, for example, use eye movements to answer questions, give simple commands, or even operate a word processing program.

An alternative option, however, is to **provide the brain with a non-muscular communication channel for conveying messages and commands to the external world, as in the case of Brain-Computer Interface systems.**

1.7.1 Treatment of neural diseases: deep brain stimulation

Deep brain stimulation (DBS) uses chronically implanted electrodes to treat a wide range of neurological conditions, especially movement disorders, by delivering high frequency electrical stimulation to targeted regions of the brain. In contrast, pharmacological agents have a far more limited spatial resolution and temporal specificity. In particular, DBS has shown a great effectiveness in treating movement disorders[142, 143]. It has been understood, for some time, that modulation of deep brain nuclei within the basal ganglia and thalamus can have a therapeutic effect in patients with movement disorders. Because of its reversibility and adjustability, DBS has largely come to replace traditional ablation procedures. The clinical effects of DBS vary, depending both on the target being stimulated and on the parameters of stimulation. Both aspects are currently the subject of substantial research and discovery. The most common targets for DBS treatment include the subthalamic nucleus for the treatment of advanced Parkinson's disease, the ventral intermediate nucleus of the thalamus for the treatment of medically

refractory essential tremor, and the globus pallidus interna for the treatment of both cervical and generalized dystonias and Parkinson's disease[142].

Particularly remarkable in this field, the work of Prof. Benabid's group[144, 145, 146] that showed in 1991 the usefulness of high-frequency stimulation of the ventral intermediate nucleus as the first neurosurgical procedure in disabling tremor in patients with Parkinson's disease. Benabid was honoured in 2014 by the Lasker-DeBakely Clinical Medical Research Award for his work on the development of deep brain stimulators.

In 2002 DBS (Activa® Parkinson's Control System) was approved by the FDA as medical therapy for essential tremor in Parkinson's disease[147], and current research is investigating its efficacy in treating **epilepsy, depression, and obsessive-compulsive disorder**[148, 149, 150].

1.7.2 Brain-computer interfaces

A Brain-computer interface (BCI) is a system that allows its user to control a prosthesis without using nerves and muscles. The principle behind a BCI functioning can be schematized as in Fig.1.27.

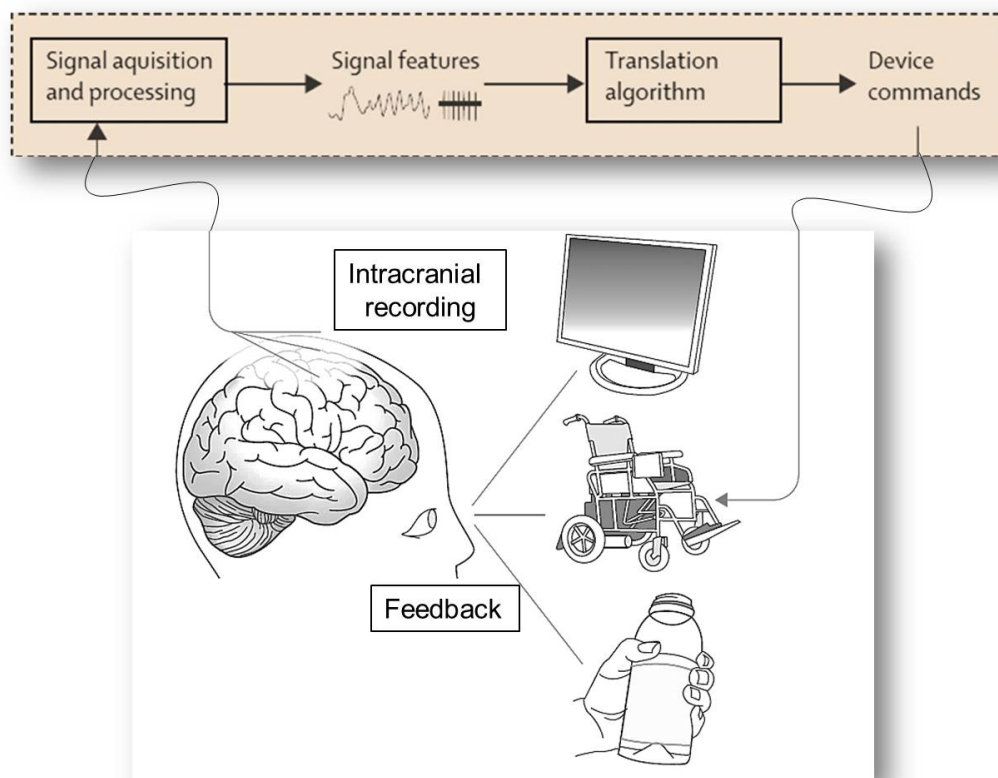


Figure 1.27: Schematic representation of a BCI system (adapted from [151]).

In general, **intracranial recordings** are used to sample the extracellular activity of a population of neurons in different cortical areas. In this "**signal acquisition**" phase, the input is acquired by the recording electrodes, amplified and digitized. **The combined**

activity of these neuronal populations is processed, in real time, by a series of simple mathematical models designed to extract motor-control parameters from the raw brain signals. The outputs of these models are used to control, for instance, the movements of a robot arm, a wheelchair or a moving cursor on a video screen. To complete a closed-loop control BCI, information describing the performance of the robot arm is relayed back to the patient using artificially generated **visual and proprioceptive/tactile feedback signals** that inform the patient about the performance of the device controlled by brain-derived signals. BCIs can be divided in two main classes:

- **dependent BCIs**: they need at least a partially intact peripheral system. For example, they could be used for flashing letters on a screen that the user can select by looking directly at it, exploiting the direction of eye gaze. It is essentially an alternative method for detecting messages carried in the brain normal output pathways.
- **independent BCIs**: they does not need activity in the brain normal output pathways because the message is not carried by peripheral nerve and muscles. To come back to the same example, flashing letters would be chosen by the user in this case not by gazing but by "thinking" them. The thinking, if properly trained, produces certain electrical patterns that trigger action of the BCI.

While dependent BCIs are easier to make, very severely handicapped people might only profit from independent ones.

1.7.2.1 Signal recording for BCIs

Another important distinction in BCIs can be done on the basis of the technologies employed for the electrophysiological recording:

- **invasive (implanted) BCIs** are performed through surgery by implanting the essential sensors intracranially. These devices deliver the finest signals, but put users under the major risk in terms of its potential for brain damage.
- **non-invasive (non-implanted) BCIs** do not require electrodes to be implanted by surgery then it holds the great advantage of not exposing the patient to the risk of brain surgery.

Non-implanted BCI: All of the non-implanted recording technologies described before, such as, EEG, ECoG, MRI, etc. provide some representation of the brain activity. The choice of a specific method is often determined by a balance between factors such as health risks, user comfort, signal quality, portability, and cost.

For example, in 2006, Japan's Honda Motor Corp. and ATR Computational Neuroscience Laboratories positioned participants within an **MRI scanner** asking to move their hand or fingers in a certain way. The scanner detected the subject's brain signals sending

them to a computer, which processed the information and then used software to issue commands that operated a robotic hand[152].

EEG-based BCIs are likely to offer some practical solution for patients for example in the case of cursor and wheelchair control or computer operation. Several classes of EEG-based systems, which differ according to the cortical areas recorded, the features of EEG signals extracted (visual evoked potentials, VEPs), P300 evoked potential, etc.), and the sensory modality providing feedback to subjects have been developed[153, 154, 155]. Nevertheless, even if it holds a certain clinical utility[156], EEG-based BCIs show well-known deficiency and they could not be significantly enhanced in the near future as reported in the literature[157].

EEG-based BCIs provide communication channel of limited capacity and motor recovery using these systems has been limited. Generally, EEG-based BCIs try to decipher the subject's voluntary intentions and decisions through measurements of the combined electrical activity of massive neuronal populations. As such, both the spatial and temporal resolutions of EEGs become limited owing to the overlapping electrical activity generated by different cortical areas. Furthermore, during the passive conductance of these signals through brain tissue, bone and skin, resolution is also lost owing to the low-pass filtering of the EEG signals.

Moreover, as a replacement for the brain normal output channel, a BCI also depends on feedback and on adaptation of the brain activity based on that feedback. As explained, the BCI operation is based on the interaction between the user's brain which produces the measured signals and the BCI itself which translates these signals into specific commands. To this end, a successful BCI operation requires that the user develops new skills, consisting in proper control of specific electrophysiological signals. Training to operate EEG-based BCIs can take many days and visual feedback is the essential part of this training.

Implanted BCI: To improve the resolution of brain potentials monitored by BCIs, recording method such as **ECoG**, using subdural electrodes, have been implemented, showing a better accuracy[159, 160] but it is with the use of penetrating microelectrodes that the performances of BCIs can be notably enhanced[161].

In Fig.1.28, different classes of BCI are schematized, starting from the main distinction between implanted and non-implanted and underlying advantages and drawbacks related to each one.

1.7.2.1.1 Brief history of BCI: The early origin of the term "Brain-Computer Interface" can be traced back to the 1970, when Jacques Vidal used the term to describe any computer-based system that produces detailed information on brain function. In the course of his work, he developed a system that actually satisfied the current definition of dependent BCI: visual evoked potentials recorded from the scalp over visual cortex were used to determine the direction of eye gaze, in order to determine the direction in which

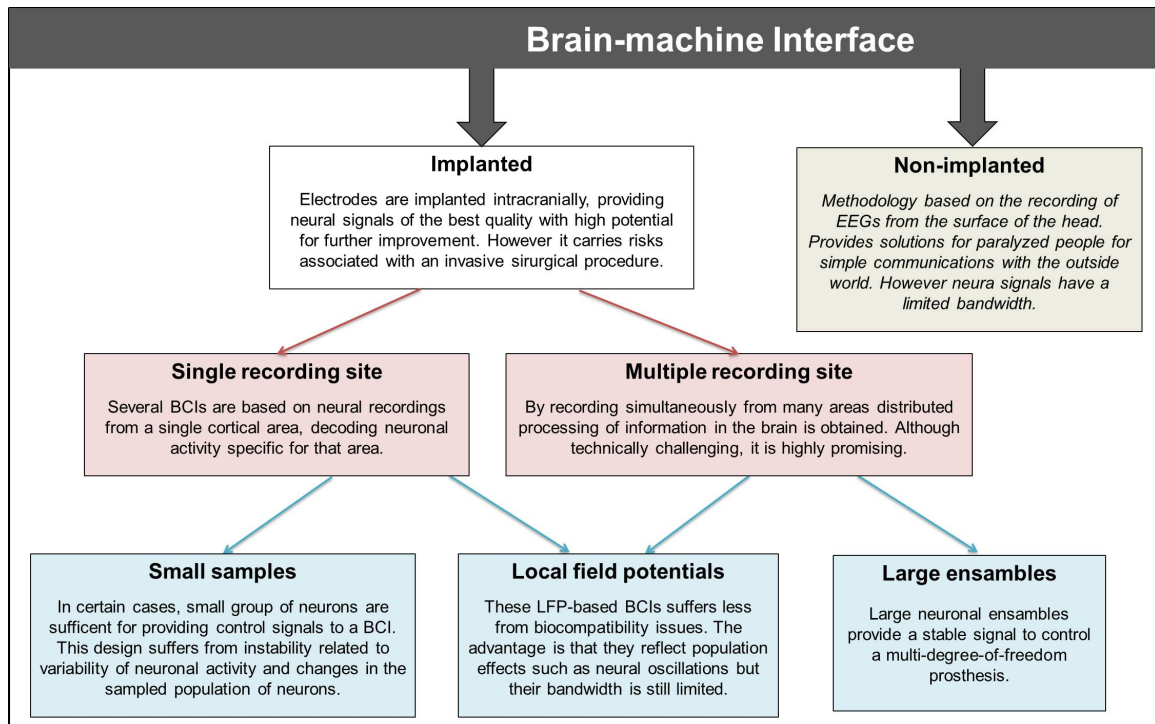


Figure 1.28: Scheme summarizing advantages and drawbacks of different classes of BCIs (adapted from [158]).

the user wished to move a cursor[162].

The approach proposed in 1980 by the neurophysiologist Edward Schmidt[163], assumes that voluntary motor commands can be extracted in real time from the collective electrical activity of populations of cortical or subcortical neurons spared by the underlying illness, and then used to enact motor functions either by directly stimulating the patient's musculature or by controlling the movements of artificial actuators, such as robot arms[164].

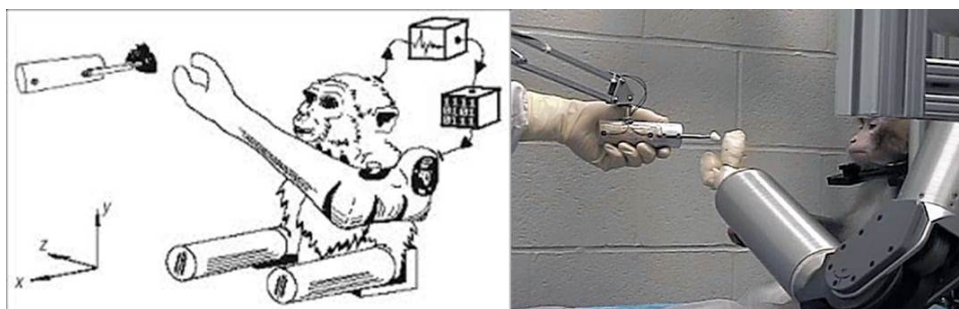


Figure 1.29: The implantation performed by Andrew Schwartz *et al.* in 2008[165]. The monkey had its arms restrained by inserting them in horizontal tubes and a prosthetic arm positioned next to its shoulder. Spiking activity was processed and used to control the three-dimensional arm velocity and the gripper aperture velocity in real time. Food targets were presented at arbitrary positions.

Born as a highly multidisciplinary field, basic research in BCIs has quickly progressed since the first experiment demonstration of independent BCI in 1999, in which a cortical electrode array could directly control a robotic manipulator[166]. In 2003, Miguel Nicolelis

and his colleagues at Duke University implanted electrode arrays into a monkey's brain that were able to detect the monkey's motor intent and thus able to control reaching and grasping movements performed by a robotic arm[167]. In 2008 the same experiment was performed by Schwartz *et al.* and the results are shown in Fig.1.29[165].

1.7.2.2 Restoration of sensory impairments

Cochlear implants: The restoration of sensory impairments represents a very promising field of applications of BCIs[168]. Work to develop implantable prosthetic devices for the deaf and the blind began in the 1960s using arrays of metal electrodes implanted in the cochlea[169, 170], auditory nerve[171, 172], and visual cortex[173, 174]. Auditory prostheses work by converting features of acoustic signals, such as speech, into patterns of electrical stimuli that are then delivered through an array of chronically implanted electrodes to auditory nerve fibers lying on the basilar membrane of the cochlea[164].

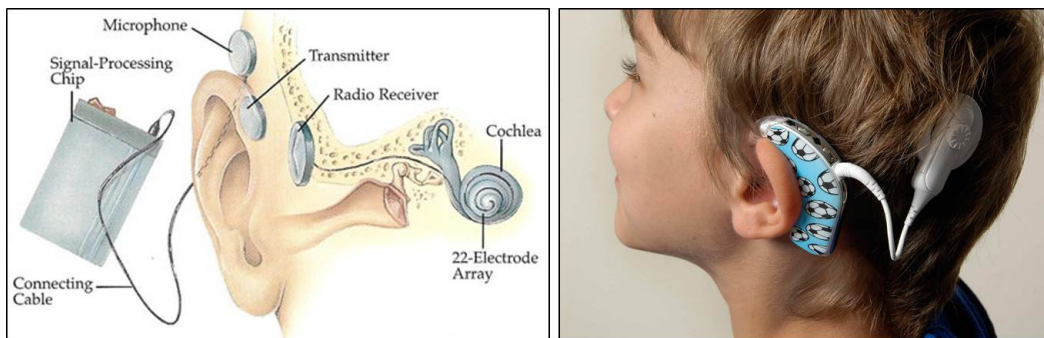


Figure 1.30: A schematic (left) and real (right) cochlear implant.

The cochlear implant (Fig.1.30) was the first success story in BCIs. It includes a speech processor, which takes input from a microphone and maps the sounds into electrical charge levels and stimulations sites, for loudness and pitch, respectively. The receiver-stimulator decodes this data, delivering current waveforms to the microelectrodes. As the basilar membrane contains a representation of sound frequencies, known as a tonotopic map, auditory prostheses deliver high-frequency information to the basal region of the cochlea, and low-frequency signals to the apical region, to mimic normal auditory processing[164]. The electrode array has platinum contacts and is inserted into the scala tympani of the cochlea, stimulating the auditory nerve through the bone.

By 2010, according to the FDA, more than 219,000 patients worldwide, ranging in age from 12 months to 80 years, had received cochlear implants. Although results vary from case to case, even slight improvements in auditory performance have helped people to communicate better and to become more aware of their surrounding environment.

Artificial retina: Another remarkable work in restoring sensory impairments is the one done by Dr. Dobbelle's group[175, 176, 177]. The **Artificial Retina Project** was a multi-institutional collaborative effort to develop and implant a device containing an array

of microelectrodes behind the retina of people blinded by retinal disease. The ultimate goal was to design a device to help restore limited vision that enables reading, unaided mobility, and facial recognition.

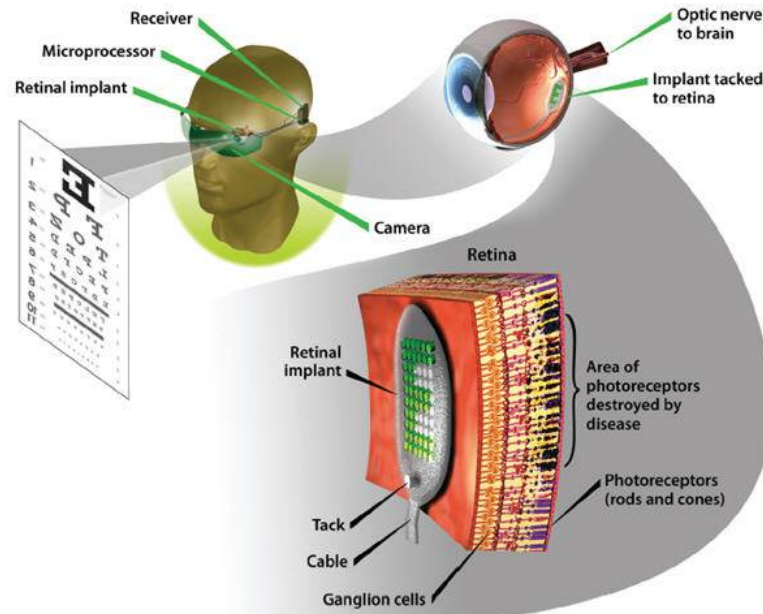


Figure 1.31: Schematic illustration of the artificial retina functioning.

The device, shown in Fig.1.31, is intended to bypass the damaged eye structure of those with retinitis pigmentosa and macular degeneration. These diseases destroy the light-sensing cells (photoreceptors, or rods and cones) in the retina, a multilayered membrane located at the back of the eye. Normal vision begins when light enters and moves through the eye to strike specialized photoreceptor (light-receiving) cells in the retina called rods and cones. These cells convert light signals to electric impulses that are sent to the optic nerve and the brain. Retinal diseases like age-related macular degeneration and retinitis pigmentosa destroy vision by annihilating these cells. With the artificial retina device, a miniature camera mounted in eyeglasses captures images and wirelessly sends the information to a microprocessor (worn on a belt) that converts the data to an electronic signal and transmits it to a receiver on the eye. The receiver sends the signals through a tiny, thin cable to the microelectrode array, stimulating it to emit pulses. The artificial retina device thus bypasses defunct photoreceptor cells and transmits electrical signals directly to the retina's remaining viable cells. The pulses travel to the optic nerve and, ultimately, to the brain, which perceives patterns of light and dark spots corresponding to the electrodes stimulated. Patients learn to interpret these visual patterns.

1.7.2.3 Restoration of motor impairments in humans

Paralysis, one of the most common and debilitating outcomes of severe damage to the central nervous system, continues to cast a long shadow of hopelessness on millions of lives worldwide. Spinal cord injuries (SCI) occur at a rate of 12,000 cases per year in the US,

currently affect up to 400,000 Americans[178].

At the present time, few (if any) therapeutic options are available for restoring voluntary motor control of the limbs in patients suffering from extensive traumatic or degenerative lesions of the motor system. The growing interest in the field of BCIs stems from the considerable potential of this technology for restoration of motor behaviours in severely handicapped patients, particularly those suffering from devastating conditions such as amyotrophic lateral sclerosis (ALS), locked-in syndrome (LIS), spinal cord injury, stroke and cerebral palsy. Moreover, BCI might also hold promise for amputees.

Recent experimental demonstrations in rodents[179, 166], primates[180, 181, 44, 165] and patients[182, 183, 156, 184] contributed to stimulate the interest around this use of neuroprosthetic devices.

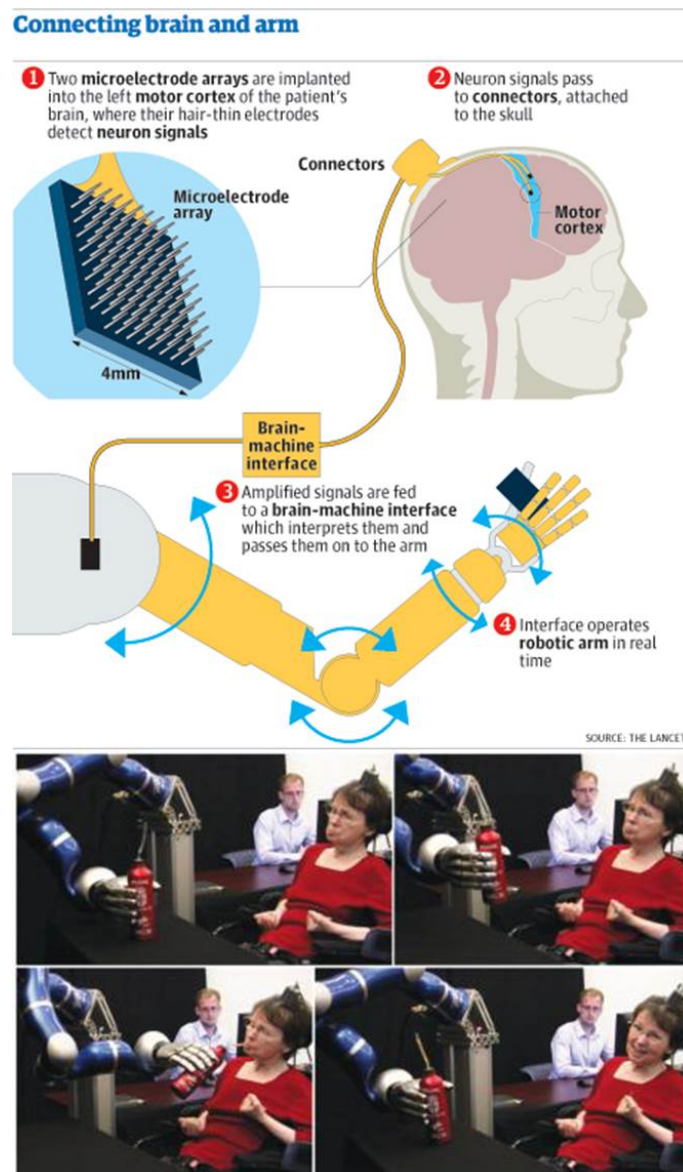


Figure 1.32: Cathy Hutchinson controlling a robotic arm with BrainGate system.

2003 was the year of the birth of **BrainGate™** Neural Interface System (developed

by Cyberkinetics), an American company co-founded by **John P. Donoghue** of Brown University and **Nicholas Hatsopoulos** of the University of Chicago, with the aim to "improve of the quality of life for all disabled humans".

Matthew Nagle was the first person who agreed to participate in a clinical trial involving the BrainGate Neural Interface System. He was a C3 tetraplegic, paralyzed from the neck down after being stabbed. The device (a 96-electrode Utah Array) was implanted on June 22, 2004 by neurosurgeon Gerhard Friehs. A link connected it to the outside of his skull, where it could be connected to a computer, made him able to control a computer cursor, using it then to press buttons, checking e-mail, etc.[185]. Following FDA regulations and the study protocol, the implanted device was removed after one year. After this experience M. Nagle declared: *"I can't put it into words. It's just I use my brain. I just thought it. I said, "Cursor go up to the top right." And it did, and now I can control it all over the screen. It will give me a sense of independence"*.

With the same system, in 2012, **Cathy Hutchinson**, that has been unable to move her own arms or legs for 15 years, could steer a robotic arm towards a bottle, pick it up, and drink her morning coffee. After realizing she could control the robot arm, she said she was *"ecstatic"* (Fig.1.32). Cathy Hutchinson cannot speak so she can type her thoughts through a device that takes its cues from her eye movements. She was optimistic about what the research might one day bring: *"I would love to have robotic leg support"* she said. Hutchinson's experiences, along with those of another quadriplegic patient, were described in a groundbreaking paper published in Nature[186].

The team of Prof. **Andrew Schwartz** at the systems neurophysiology lab "Motorlab", University of Pittsburgh also accomplished, in February 2012, an impressive clinical trial. The 52-year-old patient, **Jan Scheuermann**, lost the use of her limbs more than 10 years before due to a degenerative disease that damaged her spinal cord. The disruption to her nervous system was the equivalent to having a broken neck. Doctors recruited the woman to test a robotic arm that is controlled by computer program that translates the natural brain activity used to move our limbs into commands that has allowed her to move a high-performance prosthetic arm to perform a number of skilled arm and hand movements similar to those used in tasks of daily living. Jan was able to move the robotic arm back, forward, right, left, and up and down only two days into her training. Within weeks she could reach out, and change the position of the hand to pick up objects on a table, including cones, blocks and small balls, and put them down at another location[187].

In the future, BCIs will have the potential to impact not only individual users but also society as a whole. The research and development of future BCIs applications inevitably raise ethical and societal issues (see Appendix E), and a public debate on rights and restrictions must be encouraged. As the neurotechnologies continue to advance, it will be increasingly important to assess the neuroethical ramification of their deployment in society.

1.8 Scope of the Thesis

As it has been mentioned along this introduction chapter, there are several disorders which can disrupt the neuromuscular channels through which the brain communicates with its external environment. They affect nearly two million people in the United States alone, and far more around the world[28]. In this framework, to address and try to solve the problems related to these impairments, the implantation of neural interfaces has rapidly become an invaluable clinical and diagnostic tool[188]. Neural electrodes have been successfully used and demonstrated clinical relevance in the case of deep brain stimulation and cochlear implants. Nevertheless, despite the optimism raised by a number of new accomplishments in this field there are still many issues that preclude the translation of experimental BCI into clinical applications.

The implantation of neural interfaces for long period of time, as in the case of neurobotics BCI, sets the background to this PhD project. To this end, some critical issues remain to be addressed. In particular, **the efficiency, the biocompatibility and the stability of the implanted electrodes are far from being optimized.** In many cases, penetrating recording electrodes can fail within weeks or months because the recording capability usually deteriorates over time[189].

It is easy to understand that if the implanted device needs to be replaced in part or in whole, the patient's safety comes into play. Surgical procedures are inherently dangerous, and it is therefore in the interest of both the neuroprosthesis producers and the patients to have a technology that will withstand natural deterioration and physical trauma. As a consequence, this lack of long-term reliability must be improved to make these technologies viable for widespread use[30].

In this context, we identified two main weak points in the current available neural prosthesis that have been treated along this *General Introduction* Chapter: the chronic body reaction against the implanted probe and the electrical intrinsic features of the probe recording site at the interface with the living tissue. The strategies proposed to address them will constitute the two main parts in which is divided this manuscript:

1) How can we limit the foreign body reaction due to the implantation?

The degradation of signal quality in chronically implanted microelectrodes is attributed to both biotic factors (the hypothesis that the glial scar encapsulates the electrodes[190], functionally insulating the recording surfaces), and to abiotic factors (insulation delamination, corrosion and strain due to micromotions[191, 192]).

2) How can we enhance the signal-to-noise ratio on implantable microelectrodes?

As explained before, the miniaturization of the electrode size is a critical requirement for single neuron recording and for electrical stimulation restricted to small populations of

neuronal elements. In fact, a single square millimeter of brain tissue contains approximately one million neurons. To match this number and density, future BCIs must feature smaller and denser electrode arrays in order to precisely monitor and control neural circuit activity. Furthermore, smaller electrodes may also enable the recording of electrical signals issued from single neurons[193]. Unfortunately, a significant reduction in electrode size greatly increases electrode impedance, limiting the recording sensitivity and the maximum stimulating current deliverable through the electrode-tissue interface. Chronic implantable microelectrodes should exhibit low impedance for recording or safe charge injection for stimulation to ensure a good quality of bidirectional communication with the neural tissue. Therefore, a reduction in electrode size should not be done at the expense of electrode function and the interface where the physical contact between the brain and the neuro-prosthesis occurs.

These two factors are closely linked in a vicious circle: for example, if the electrical performances of the active electrode are poor, the accumulation of charges at the interfaces can lead to a body reaction, in addition to the one promoted by the insertion injury. *Vice versa*, even though the electrodes possess high quality electrical performances, if the acute body reaction leads to the encapsulation the device in a glial scar, the recording quality is drastically affected. Everything contributes to decrease the stability of the implanted probe.

In this work, both factors have been considered at the same time: a highly flexible neural probe fully biocompatible in which the active electrode area is electrochemically modified with a conductive polymer is presented for intracortical implantation. The aim of this research, by coupling the flexibility of the probe substrate and the enhancement of microelectrode electrical properties, was to improve the biocompatibility, the stability at the electrode-tissue interface and, therefore the long term reliability of the implantable devices. In this way, **we intended to propose an effective answer to the major critical requirements for long-term implantation.**

Bibliography

- [1] Eric R Kandel, James H Schwartz, Thomas M Jessell, et al. *Principles of neural science*. McGraw-Hill New York, 4th edition, 2000.
- [2] Dale Purves, George J Augustine, David Fitzpatrick, William C Hall, Anthony-Samuel Lamantia, James O McNamara, and S Mark Williams. *Neuroscience*. Sinauer Associates Inc, 4th edition, 2004.
- [3] Prasanna V Venkataramani. Santiago Ramón y Cajal: Father of Neurosciences. *Resonance*, 15(11):968–976, 2010.
- [4] Camillo Golgi. The neuron doctrine - theory and facts. *Nobel Lecture*, 1906.
- [5] Pablo Garcia-Lopez, Virginia Garcia-Marin, and Miguel Freire. The histological slides and drawings of Cajal. *Frontiers in Neuroanatomy*, 4(9):1–16, 2010.
- [6] Ennio Pannese. The golgi stain: invention, diffusion and impact on neurosciences. *Journal of the history of the neurosciences*, 8(2):132–140, 1999.
- [7] CellPress supported by Zeiss. Cell picture show, @online:<http://www.cell.com/pictureshow/brainbow>.
- [8] Jonah Lehrer. Neuroscience: Making connections. *Nature*, 457(7229):524–527, 2009.
- [9] Jean Livet, Tamily A Weissman, Hyuno Kang, Ryan W Draft, Ju Lu, Robyn A Bennis, Joshua R Sanes, and Jeff W Lichtman. Transgenic strategies for combinatorial expression of fluorescent proteins in the nervous system. *Nature*, 450(7166):56–62, 2007.
- [10] University of Utah. Neurons transport messages in the brain, @online:<http://learn.genetics.utah.edu/content/addiction/neurons>.
- [11] Alan L Hodgkin. Evidence for electrical transmission in nerve Part I. *The Journal of physiology*, 90(2):183–210, 1937.
- [12] Alan L Hodgkin and Andrew F Huxley. Resting and action potentials in single nerve fibres. *The Journal of physiology*, 104(2):176–195, 1945.
- [13] Alan L Hodgkin and Andrew F Huxley. A quantitative description of membrane current and its application to conduction and excitation in nerve. *The Journal of physiology*, 117(4):500, 1952.
- [14] Harvey Lodish, Arnold Berk, S Lawrence Zipursky, Paul Matsudaira, David Baltimore, James Darnell, et al. *Molecular Cell Biology - 21.2 The Action Potential and Conduction of Electric Impulses*. WH Freeman, 4th edition, 2000.
- [15] Diego Lucas. Neural networks, @online:<http://slideplayer.us/user/253510>.

- [16] Pouria Fattahi, Guang Yang, Gloria Kim, and Mohammad R Abidian. A review of organic and inorganic biomaterials for neural interfaces. *Advanced Materials*, 26(12):1846–1885, 2014.
- [17] Eric C Leuthardt, Gerwin Schalk, Jarod Roland, Adam Rouse, and Daniel W Moran. Evolution of brain-computer interfaces: going beyond classic motor physiology. *Neurosurgical focus*, 27(1):E4, 2009.
- [18] Walton T Roth, Adolf Pfefferbaum, Thomas B Horvath, Philip A Berger, and Bert S Kopell. P3 reduction in auditory evoked potentials of schizophrenics. *Electroencephalography and Clinical Neurophysiology*, 49(5):497–505, 1980.
- [19] Ernst Niedermeyer and Fernando Lopes da Silva. *Electroencephalography: Basic principles, clinical applications, and related fields - 9. The Normal EEG of the Waking Adult*. Lippincott Williams & Wilkins, 5th edition, 2005.
- [20] Herbert H Jasper. Electrical signs of epileptic discharge. *Electroencephalography and clinical neurophysiology*, 1(1):11–18, 1949.
- [21] Dennis J McFarland and Jonathan R Wolpaw. Brain-computer interfaces for communication and control. *Communications of the ACM*, 54(5):60–66, 2011.
- [22] Niels Birbaumer. *Brain and behavior past, present, and future - Slow cortical potentials: their origin, meaning, and clinical use*. Purdue University Press, 1th edition.
- [23] Brigitte Rockstroh. *Slow cortical potentials and behaviour*. Urban & Schwarzenberg, 1989.
- [24] James W Kozelka and Timothy A Pedley. Beta and mu rhythms. *Journal of Clinical Neurophysiology*, 7(2):191–208, 1990.
- [25] Robin I Goldman, John M Stern, Jerome Engel Jr, and Mark S Cohen. Simultaneous EEG and fMRI of the alpha rhythm. *Neuroreport*, 13(18):2487, 2002.
- [26] W G Walter, R Cooper, V J Aldridge, W C McCallum, and A L Winter. Contingent negative variation: an electric sign of sensorimotor association and expectancy in the human brain. *Nature*, 203(4943):380–384, 1964.
- [27] Emanuel Donchin and DBD Smith. The contingent negative variation and the late positive wave of the average evoked potential. *Electroencephalography and clinical Neurophysiology*, 29(2):201–203, 1970.
- [28] Jonathan R Wolpaw, Niels Birbaumer, Dennis J McFarland, Gert Pfurtscheller, and Theresa M Vaughan. Brain-computer interfaces for communication and control. *Clinical neurophysiology*, 113(6):767–791, 2002.
- [29] Micha E Spira and Aviad Hai. Multi-electrode array technologies for neuroscience and cardiology. *Nature Nanotechnology*, 8:83–94, 2001.
- [30] Vadim S Polikov, Patrick A Tresco, and William M Reichert. Response of brain tissue to chronically implanted neural electrodes. *Journal of Neuroscience Methods*, 148(1):1–18, 2005.
- [31] Erwin Neher and Bert Sakmann. Single channel currents recorded from membrane of denervated frog muscle fibers. *Nature*, 260(7):799–802, 1976.

-
- [32] Bert Sakmann and Erwin Neher. *Single-channel recording*. Springer New York, 2009.
- [33] Nianzhen Li, Anna Tourovskaia, and Albert Folch. Biology on a chip: microfabrication for studying the behavior of cultured cells. *Critical Reviews in Biomedical Engineering*, 31(5&6), 2003.
- [34] Corina Wirth and Hans-R Lüscher. Spatiotemporal evolution of excitation and inhibition in the rat barrel cortex investigated with multielectrode arrays. *Journal of neurophysiology*, 91(4):1635–1647, 2004.
- [35] Otto J Prohaska, Fethi Olcaytug, P Pfundner, and Heinz Dragaun. Thin-film multiple electrode probes: Possibilities and limitations. *IEEE Transactions on Biomedical Engineering*, (2):223–229, 1986.
- [36] Moria Kwiat, Daniel Stein, and Fernando Patolsky. Nanotechnology meets electrophysiology. *Current opinion in biotechnology*, 24(4):654–663, 2013.
- [37] Aviad Hai, Joseph Shappir, and Micha E Spira. Long-term, multisite, parallel, in-cell recording and stimulation by an array of extracellular microelectrodes. *Journal of neurophysiology*, 104(1):559–568, 2010.
- [38] Kenneth D Harris, Darrell A Henze, Jozsef Csicsvari, Hajime Hirase, and György Buzsáki. Accuracy of tetrode spike separation as determined by simultaneous intracellular and extracellular measurements. *Journal of neurophysiology*, 84(1):401–414, 2000.
- [39] Felix Strumwasser. Long-term recording from single neurons in brain of unrestrained mammals. *Science*, 127:469–470, 1958.
- [40] Chenyang Xu, William Lemon, and Chang Liu. Design and fabrication of a high-density metal microelectrode array for neural recording. *Sensors and Actuators A: Physical*, 96(1):78–85, 2002.
- [41] György Buzsáki. Large-scale recording of neuronal ensembles. *Nature neuroscience*, 7(5):446–451, 2004.
- [42] John K Chapin. Using multi-neuron population recordings for neural prosthetics. *Nature neuroscience*, 7(5):452–455, 2004.
- [43] K D Wise, D J Anderson, J F Hetke, D R Kipke, and K Najafi. Wireless Implantable Microsystems: High-Density Electronic Interfaces to the Nervous System. *Proceedings of the IEEE*, 92(1):76–97, 2004.
- [44] Miguel AL Nicolelis, Dragan Dimitrov, Jose M Carmena, Roy Crist, Gary Lehew, Jerald D Kralik, and Steven P Wise. Chronic, multisite, multielectrode recordings in macaque monkeys. *Proceedings of the National Academy of Sciences*, 100(19):11041–11046, 2003.
- [45] Kensall D Wise and JB Angell. A low-capacitance multielectrode probe for use in extracellular neurophysiology. *IEEE Transactions on Biomedical Engineering*, (3):212–219, 1975.
- [46] Kensall D Wise, James B Angell, and Arnold Starr. An integrated-circuit approach to extracellular microelectrodes. *IEEE Transactions on Biomedical Engineering*, (3):238–247, 1970.

- [47] Karen C Cheung. Implantable microscale neural interfaces. *Biomedical Microdevices*, 9(6):923–938, 2007.
- [48] Richard A Normann, Edwin M Maynard, Patrick J Rousche, and David J Warren. A neural interface for a cortical vision prosthesis. *Vision research*, 39(15):2577–2587, 1999.
- [49] Patrick K Campbell, Kelly E Jones, Robert J Huber, Kenneth W Horch, and Richard A Normann. A silicon-based, three-dimensional neural interface: manufacturing processes for an intracortical electrode array. *IEEE Transactions on Biomedical Engineering*, 38(8):758–768, 1991.
- [50] Almut Branner, Richard B Stein, Eduardo Fernandez, Yoichiro Aoyagi, and Richard A Normann. Long-term stimulation and recording with a penetrating microelectrode array in cat sciatic nerve. *IEEE Transactions on Biomedical Engineering*, 51(1):146–157, 2004.
- [51] Philip R Kennedy, Suzanne S Mirra, and Roy AE Bakay. The cone electrode: ultrastructural studies following long-term recording in rat and monkey cortex. *Neuroscience letters*, 142(1):89–94, 1992.
- [52] Philip R Kennedy and Roy AE Bakay. Activity of single action potentials in monkey motor cortex during long-term task learning. *Brain research*, 760(1):251–254, 1997.
- [53] Philip R Kennedy, Roy AE Bakay, Melody M Moore, Kim Adams, and John Goldwithe. Direct control of a computer from the human central nervous system. *Rehabilitation Engineering, IEEE Transactions on*, 8(2):198–202, 2000.
- [54] Jonathan S Brumberg, Alfonso Nieto-Castanon, Philip R Kennedy, and Frank H Guenther. Brain–computer interfaces for speech communication. *Speech communication*, 52(4):367–379, 2010.
- [55] André Mercanzini, Karen Cheung, Derek L Buhl, Marc Boers, Anne Maillard, Philippe Colin, Jean-Charles Bensadoun, Arnaud Bertsch, and Philippe Renaud. Demonstration of cortical recording using novel flexible polymer neural probes. *Sensors and Actuators A: Physical*, 143(1):90–96, 2008.
- [56] Zhuolin Xiang, Shih-Cheng Yen, Ning Xue, Tao Sun, Wei Mong Tsang, Songsong Zhang, Lun-De Liao, Nitish V Thakor, and Chengkuo Lee. Ultra-thin flexible polyimide neural probe embedded in a dissolvable maltose-coated microneedle. *Journal of Micromechanics and Microengineering*, 24(6):065015, 2014.
- [57] Patrick J Rousche, David S Pellinen, David P Pivin Jr, Justin C Williams, Rio J Vetter, et al. Flexible polyimide-based intracortical electrode arrays with bioactive capability. *IEEE Transactions on Biomedical Engineering*, 48(3):361–371, 2001.
- [58] Keekeun Lee, Amarjit Singh, Jiping He, Stephen Massia, Bruce Kim, and Gregory Raupp. Polyimide based neural implants with stiffness improvement. *Sensors and Actuators B: Chemical*, 102(1):67–72, 2004.
- [59] Ane Altuna, Liset Menendez de la Prida, Elisa Bellistri, Gemma Gabriel, Anton Guimerá, Javier Berganzo, Rosa Villa, and Luis J Fernández. SU-8 based microprobes with integrated planar electrodes for enhanced neural depth recording. *Biosensors and Bioelectronics*, 37(1):1–5, 2012.

-
- [60] Ane Altuna, Elisa Bellistri, Elena Cid, Paloma Aivar, Beatriz Gal, Javier Berganzo, Gemma Gabriel, Anton Guimerà, Rosa Villa, Luis J Fernández, et al. SU-8 based microprobes for simultaneous neural depth recording and drug delivery in the brain. *Lab on a Chip*, 13(7):1422–1430, 2013.
- [61] John P Seymour, Nick B Langhals, David J Anderson, and Daryl R Kipke. Novel multi-sided, microelectrode arrays for implantable neural applications. *Biomedical Microdevices*, 13(3):441–451, 2011.
- [62] Cinzia Metallo, Robert D White, and Barry A Trimmer. Flexible parylene-based microelectrode arrays for high resolution emg recordings in freely moving small animals. *Journal of Neuroscience Methods*, 195(2):176–184, 2011.
- [63] Damien C Rodger, Andy J Fong, Wen Li, Hossein Ameri, Ashish K Ahuja, Christian Gutierrez, Igor Lavrov, Hui Zhong, Parvathy R Menon, Ellis Meng, et al. Flexible parylene-based multielectrode array technology for high-density neural stimulation and recording. *Sensors and Actuators B: chemical*, 132(2):449–460, 2008.
- [64] Shoji Takeuchi, Dominique Ziegler, Yumi Yoshida, Kunihiko Mabuchi, and Takafumi Suzuki. Parylene flexible neural probes integrated with microfluidic channels. *Lab on a Chip*, 5(5):519–523, 2005.
- [65] B J Kim, J T W Kuo, S A Hara, C D Lee, L Yu, C A Gutierrez, T Q Hoang, V Pikov, and E Meng. 3D Parylene sheath neural probe for chronic recordings. *Journal of Neural Engineering*, 10(4):045002, 2013.
- [66] Dion Khodagholy, Thomas Doublet, Moshe Gurfinkel, Pascale Quilichini, Esmá Ismailova, Pierre Leleux, Thierry Herve, Sébastien Sanaur, Christophe Bernard, and George G Malliaras. Highly conformable conducting polymer electrodes for in vivo recordings. *Advanced Materials*, 23(36):H268–H272, 2011.
- [67] Salah Sommakia, Heui C Lee, Janak Gaire, and Kevin J Otto. Materials approaches for modulating neural tissue responses to implanted microelectrodes through mechanical and biochemical means. *Current Opinion in Solid State and Materials Science*, 2014.
- [68] Thomas Stieglitz, Martin Schuettler, J-Uwe Meyer, et al. Micromachined, polyimide-based devices for flexible neural interfaces. *Biomedical Microdevices*, 2(4):283–294, 2000.
- [69] Jingkuang Chen, Kensall D Wise, Jamille F Hetke, and SC Bledsoe. A multichannel neural probe for selective chemical delivery at the cellular level. *IEEE Transactions on Biomedical Engineering*, 44(8):760–769, 1997.
- [70] Demetrios P Papageorgiou, Susan E Shore, Sanford C Bledsoe, and Kensall D Wise. A shuttered neural probe with on-chip flowmeters for chronic in vivo drug delivery. *Microelectromechanical Systems, Journal of*, 15(4):1025–1033, 2006.
- [71] ST Retterer, KL Smith, CS Bjornsson, JN Turner, MS Isaacson, and W Shain. Constant pressure fluid infusion into rat neocortex from implantable microfluidic devices. *Journal of Neural Engineering*, 5(4):385, 2008.
- [72] Stefan Metz, Arnaud Bertsch, Daniel Bertrand, and Ph Renaud. Flexible polyimide probes with microelectrodes and embedded microfluidic channels for simultaneous

- drug delivery and multi-channel monitoring of bioelectric activity. *Biosensors and bioelectronics*, 19(10):1309–1318, 2004.
- [73] Dominik Ziegler, Takafumi Suzuki, and Shoji Takeuchi. Fabrication of flexible neural probes with built-in microfluidic channels by thermal bonding of parylene. *Microelectromechanical Systems, Journal of*, 15(6):1477–1482, 2006.
- [74] John L Skousen, Michael J Bridge, and Patrick A Tresco. A strategy to passively reduce neuroinflammation surrounding devices implanted chronically in brain tissue by manipulating device surface permeability. *Biomaterials*, 2014.
- [75] Ning Han, Shreyas S Rao, Jed Johnson, Kunal S Parikh, Patrick A Bradley, John J Lannutti, and Jessica O Winter. Hydrogel–electrospun fiber mat composite coatings for neural prostheses. *Frontiers in Neuroengineering*, 4(2):1–8, 2011.
- [76] Gustav Lind, Cecilia Eriksson Linsmeier, Jonas Thelin, and Jens Schouenborg. Gelatine-embedded electrodes - a novel biocompatible vehicle allowing implantation of highly flexible microelectrodes. *Journal of Neural Engineering*, 7(4):046005, 2010.
- [77] Frederik Ceysens, Kris van Kuyck, Greetje Vande Velde, Marleen Welkenhuysen, Linda Stappers, Bart Nuttin, and Robert Puers. Resorbable scaffold based chronic neural electrode arrays. *Biomedical Microdevices*, 15(3):481–493, 2013.
- [78] Dan Lewitus, Karen L Smith, William Shain, and Joachim Kohn. Ultrafast resorbing polymers for use as carriers for cortical neural probes. *Acta Biomaterialia*, 7(6):2483–2491, 2011.
- [79] Y Kato, M Nishino, I Saito, T Suzuki, and K Mabuchi. Flexible intracortical neural probe with biodegradable polymer for delivering bioactive components. In *Microtechnologies in Medicine and Biology, 2006 International Conference on*, pages 143–146, 2006.
- [80] Richard B Borgens, Riyi Shi, and Debra Bohnert. Behavioral recovery from spinal cord injury following delayed application of polyethylene glycol. *Journal of experimental biology*, 205(1):1–12, 2002.
- [81] Jian Luo, Richard Borgens, and Riyi Shi. Polyethylene glycol immediately repairs neuronal membranes and inhibits free radical production after acute spinal cord injury. *Journal of neurochemistry*, 83(2):471–480, 2002.
- [82] Matthias Heim, Blaise Yvert, and Alexander Kuhn. Nanostructuring strategies to enhance microelectrode array (MEA) performance for neuronal recording and stimulation. *Journal of Physiology-Paris*, 106(3):137–145, 2012.
- [83] Shruti Nambiar and John T W Yeow. Conductive polymer-based sensors for biomedical applications. *Biosensors and Bioelectronics*, 26(5):1825–1832, 2011.
- [84] Murat Ates. A review study of (bio) sensor systems based on conducting polymers. *Materials Science and Engineering: C*, 33(4):1853–1859, 2013.
- [85] Mohammad R Abidian, Kip A Ludwig, Timothy C Marzullo, David C Martin, and Daryl R Kipke. Interfacing conducting polymer nanotubes with the central nervous system: Chronic neural recording using poly (3, 4-ethylenedioxythiophene) nanotubes. *Advanced Materials*, 21(37):3764–3770, 2009.

-
- [86] Maria Asplund, Tobias Nyberg, and Olle Inganäs. Electroactive polymers for neural interfaces. *Polymer Chemistry*, 1(9):1374–1391, 2010.
- [87] Matthew P Ward, Pooja Rajdev, Casey Ellison, and Pedro P Irazoqui. Toward a comparison of microelectrodes for acute and chronic recordings. *Brain research*, 1282:183–200, 2009.
- [88] Abhishek Prasad, Qing-Shan Xue, Viswanath Sankar, Toshikazu Nishida, Gerry Shaw, Wolfgang J Streit, and Justin C Sanchez. Comprehensive characterization and failure modes of tungsten microwire arrays in chronic neural implants. *Journal of Neural Engineering*, 9(5):056015, 2012.
- [89] Yoshinori Onuki, Upkar Bhardwaj, Fotios Papadimitrakopoulos, and Diane J Burgess. A review of the biocompatibility of implantable devices: current challenges to overcome foreign body response. *Journal of diabetes science and technology*, 2(6):1003–1015, 2008.
- [90] Cristina Marin and Eduardo Fernández. Biocompatibility of intracortical microelectrodes: current status and future prospects. *Frontiers in Neuroengineering*, 3(8):1–6, 2010.
- [91] James C Barrese, Naveen Rao, Kaivon Paroo, Corey Triebwasser, Carlos Vargas-Irwin, Lachlan Franquemont, and John P Donoghue. Failure mode analysis of silicon-based intracortical microelectrode arrays in non-human primates. *Journal of Neural Engineering*, 10(6):066014, 2013.
- [92] David Franklyn Williams. *The Williams dictionary of biomaterials*. Liverpool University Press, 1999.
- [93] E Fournier, C Passirani, CN Montero-Menei, and JP Benoit. Biocompatibility of implantable synthetic polymeric drug carriers: focus on brain biocompatibility. *Biomaterials*, 24(19):3311–3331, 2003.
- [94] William M Reichert. *Indwelling neural implants: strategies for contending with the in vivo environment*. CRC Press, 2010.
- [95] Arati Sridharan, Subramaniam D Rajan, and Jit Muthuswamy. Long-term changes in the material properties of brain tissue at the implant–tissue interface. *Journal of Neural Engineering*, 10(6):066001, 2013.
- [96] James M Anderson. Biological responses to materials. *Annual Review of Materials Research*, 31(1):81–110, 2001.
- [97] Buddy D Ratner and Stephanie J Bryant. Biomaterials: where we have been and where we are going. *Annual Reviews Biomedical Engineering*, 6:41–75, 2004.
- [98] George C McConnell, Howard D Rees, Allan I Levey, Claire-Anne Gutekunst, Robert E Gross, and Ravi V Bellamkonda. Implanted neural electrodes cause chronic, local inflammation that is correlated with local neurodegeneration. *Journal of Neural Engineering*, 6(5):056003, 2009.
- [99] R Biran, D C Martin, and P A Tresco. Neuronal cell loss accompanies the brain tissue response to chronically implanted silicon microelectrode arrays. *Experimental neurology*, 195(1):115–126, 2005.

- [100] D J Edell, V V Toi, V M McNeil, and L D Clark. Factors influencing the biocompatibility of insertable silicon microshafts in cerebral cortex. *IEEE Transactions on Biomedical Engineering*, 39(6):635–643, 1992.
- [101] JN Turner, W Shain, DH Szarowski, M Andersen, S Martins, M Isaacson, and H Craighead. Cerebral astrocyte response to micromachined silicon implants. *Experimental neurology*, 156(1):33–49, 1999.
- [102] Xinyan Cui and David C Martin. Electrochemical deposition and characterization of poly (3, 4-ethylenedioxythiophene) on neural microelectrode arrays. *Sensors and Actuators B: Chemical*, 89(1):92–102, 2003.
- [103] Mohammad R Abidian, Joseph M Corey, Daryl R Kipke, and David C Martin. Conducting-polymer nanotubes improve electrical properties, mechanical adhesion, neural attachment, and neurite outgrowth of neural electrodes. *Small*, 6(3):421–429, 2010.
- [104] Xinyan Cui, Valerie A Lee, Yehoash Raphael, James A Wiler, Jamille F Hetke, David J Anderson, and David C Martin. Surface modification of neural recording electrodes with conducting polymer/biomolecule blends. *Journal of Biomedical Materials Research*, 56(2):261–272, 2001.
- [105] S P Massia, M M Holecko, and G R Ehteshami. In vitro assessment of bioactive coatings for neural implant applications. *Journal of Biomedical Materials Research Part A*, 68(1):177–186, 2004.
- [106] D Hal Davis, C S Giannoulis, R W Johnson, and T A Desai. Immobilization of RGD to <111> silicon surfaces for enhanced cell adhesion and proliferation. *Biomaterials*, 23(19):4019–4027, 2002.
- [107] E Azemi, W R Stauffer, Mark S G, Carl F L, and X T Cui. Surface immobilization of neural adhesion molecule L1 for improving the biocompatibility of chronic neural probes: *In vitro* characterization. *Acta Biomaterialia*, 4(5):1208–1217, 2008.
- [108] W He and R V Bellamkonda. Nanoscale neuro-integrative coatings for neural implants. *Biomaterials*, 26(16):2983–2990, 2005.
- [109] C D James, R Davis, M Meyer, A Turner, S Turner, G Withers, L Kam, G Banker, H Craighead, M Isaacson, J Turner, and W Shain. Aligned microcontact printing of micrometer-scale poly-L-lysine structures for controlled growth of cultured neurons on planar microelectrode arrays. *IEEE Transactions on Biomedical Engineering*, 47(1):17–21, 2000.
- [110] V M Tysseling-Mattiace, V Sahni, K L Niece, D Birch, C Czeisler, M G Fehlings, S I Stupp, and J A Kessler. Self-assembling nanofibers inhibit glial scar formation and promote axon elongation after spinal cord injury. *The Journal of Neuroscience*, 28(14):3814–3823, 2008.
- [111] Y Wu, Q Zheng, J Du, Y Song, B Wu, and X Guo. Self-assembled IKVAV peptide nanofibers promote adherence of PC12 cells. *Journal of Huazhong University of Science and Technology*, 26:594–596, 2006.
- [112] R Wadhwa, C F Lagenaur, and X T Cui. Electrochemically controlled release of dexamethasone from conducting polymer polypyrrole coated electrode. *Journal of Controlled Release*, 110(3):531–541, 2006.

-
- [113] D-H Kim and D C Martin. Sustained release of dexamethasone from hydrophilic matrices using plga nanoparticles for neural drug delivery. *Biomaterials*, 27(15):3031–3037, 2006.
- [114] Kensall D Wise. Silicon microsystems for neuroscience and neural prostheses. *IEEE Engineering in Medicine and Biology Magazine*, 24(5):22–29, 2005.
- [115] C S Bjornsson, S J Oh, Y A Al-Kofahi, Y J Lim, K L Smith, J N Turner, S De, B Roysam, W Shain, and S J Kim. Effects of insertion conditions on tissue strain and vascular damage during neuroprosthetic device insertion. *Journal of Neural Engineering*, 3(3):196, 2006.
- [116] Jessica K Nguyen, Daniel J Park, John L Skousen, Allison E Hess-Dunning, Dustin J Tyler, Stuart J Rowan, Christoph Weder, and Jeffrey R Capadona. Mechanically-compliant intracortical implants reduce the neuroinflammatory response. *Journal of Neural Engineering*, 11(5):056014, 2014.
- [117] H Lee, R V Bellamkonda, W Sun, and M E Levenston. Biomechanical analysis of silicon microelectrode-induced strain in the brain. *Journal of Neural Engineering*, 2(4):81, 2005.
- [118] George C McConnell, Thomas M Schneider, D Jason Owens, and Ravi V Bellamkonda. Extraction force and cortical tissue reaction of silicon microelectrode arrays implanted in the rat brain. *IEEE Transactions on Biomedical Engineering*, 54(6):1097–1107, 2007.
- [119] Jeyakumar Subbaroyan, David C Martin, and Daryl R Kipke. A finite-element model of the mechanical effects of implantable microelectrodes in the cerebral cortex. *Journal of Neural Engineering*, 2(4):103, 2005.
- [120] Young-Tae Kim, Robert W Hitchcock, Michael J Bridge, and Patrick A Tresco. Chronic response of adult rat brain tissue to implants anchored to the skull. *Biomaterials*, 25(12):2229–2237, 2004.
- [121] Michael Polanco, Hargsoon Yoon, Keejoo Lee, and Sebastian Bawab. Predicting brain tissue deformation around an implantable electrode due to dynamic micromotion. In *SPIE Proceedings - Nanosensors, Biosensors, and Info-Tech Sensors and Systems*, volume 8344, pages II–I8. International Society for Optics and Photonics, 2012.
- [122] Jonas Thelin, Henrik Jörntell, Elia Psouni, Martin Garwicz, Jens Schouenborg, Nils Danielsen, and Cecilia Eriksson Linsmeier. Implant size and fixation mode strongly influence tissue reactions in the CNS. *PloS one*, 6(1):e16267, 2011.
- [123] Gustav Lind, Cecilia Eriksson Linsmeier, and Jens Schouenborg. The density difference between tissue and neural probes is a key factor for glial scarring. *Scientific reports*, 3(2942):1–7, 2013.
- [124] Viswanath Sankar, Justin C Sanchez, Edward McCumiskey, Nagid Brown, Curtis R Taylor, Gregory J Ehlert, Henry A Sodano, and Toshikazu Nishida. A highly compliant serpentine shaped polyimide interconnect for front-end strain relief in chronic neural implants. *Frontiers in Neurology*, 4, 2013.
- [125] Dario Farina, Ken Yoshida, Thomas Stieglitz, and Klaus Peter Koch. Multichannel thin-film electrode for intramuscular electromyographic recordings. *Journal of Applied Physiology*, 104(3):821–827, 2008.

- [126] Thomas Stieglitz. Flexible biomedical microdevices with double-sided electrode arrangements for neural applications. *Sensors and Actuators A: Physical*, 90(3):203–211, 2001.
- [127] Thomas Stieglitz, M Schuetter, and Klaus Peter Koch. Implantable biomedical microsystems for neural prostheses. *IEEE Engineering in Medicine and Biology Magazine*, 24(5):58–65, 2005.
- [128] Jui-Mei Hsu, Loren Rieth, Richard A Normann, Prashant Tathireddy, and Florian Solzbacher. Encapsulation of an integrated neural interface device with Parylene-C. *IEEE Transactions on Biomedical Engineering*, 56(1):23–29, 2009.
- [129] John P Seymour and Daryl R Kipke. Neural probe design for reduced tissue encapsulation in CNS. *Biomaterials*, 28(25):3594–3607, 2007.
- [130] J-M Seo, S J Kim, H Chung, E T Kim, H G Yu, and Y S Yu. Biocompatibility of polyimide microelectrode array for retinal stimulation. *Materials Science and Engineering: C*, 24(1):185–189, 2004.
- [131] Dion Khodagholy, Thomas Doublet, Pascale Quilichini, Moshe Gurfinkel, Pierre Leleux, Antoine Ghestem, Esmá Ismailova, Thierry Hervé, Sébastien Sanaur, Christophe Bernard, and George G Malliaras. In vivo recordings of brain activity using organic transistors. *Nature communications*, 4(1575):1–7, 2013.
- [132] Daniel Egert, Rebecca L Peterson, and Khalil Najafi. Parylene microprobes with engineered stiffness and shape for improved insertion. In *TRANSDUCERS 2011 - 16th International Conference on Solid-State Sensors, Actuators and Microsystems*, pages 198–201, 2011.
- [133] John P Seymour and Daryl R Kipke. Fabrication of polymer neural probes with sub-cellular features for reduced tissue encapsulation. In *Engineering in Medicine and Biology Society (EMBS), 28th Annual International Conference of the IEEE*, pages 4606–4609, 2006.
- [134] Sarah Felix, Kedar Shah, Diana George, Vanessa Tolosa, Angela Tooker, Heeral Sheth, Terri Delima, and Satinderpall Pannu. Removable silicon insertion stiffeners for neural probes using polyethylene glycol as a biodissolvable adhesive. In *Engineering in Medicine and Biology Society (EMBC), 34th Annual International Conference of the IEEE*, pages 871–874, 2012.
- [135] Takashi D Yoshida Kozai and Daryl R Kipke. Insertion shuttle with carboxyl terminated self-assembled monolayer coatings for implanting flexible polymer neural probes in the brain. *Journal of Neuroscience Methods*, 184(2):199–205, 2009.
- [136] Amarjit Singh, Haixin Zhu, and Jiping He. Improving mechanical stiffness of coated benzocyclobutene (BCB) based neural implant. In *Engineering in Medicine and Biology Society (EMBS), 26th Annual International Conference of the IEEE*, volume 2, pages 4298–4301, 2004.
- [137] Myounggun Jeon, Jeiwon Cho, Yun Kyung Kim, Dahee Jung, Eui-Sung Yoon, Sehyun Shin, and Il-Joo Cho. Partially flexible MEMS neural probe composed of polyimide and sucrose gel for reducing brain damage during and after implantation. *Journal of Micromechanics and Microengineering*, 24(2):025010, 2014.

-
- [138] Fan Wu, Maesoon Im, and Euisik Yoon. A flexible fish-bone-shaped neural probe strengthened by biodegradable silk coating for enhanced biocompatibility. In *TRANSDUCERS 2011 - 16th International Conference on Solid-State Sensors, Actuators and Microsystems*, pages 966–969, 2011.
- [139] Frederik Ceysens, Kris van Kuyck, Bart Nuttin, and Robert Puers. Neural implants containing a resorbable chitosan matrix. *Procedia Engineering*, 47:688–689, 2012.
- [140] Jonathan TW Kuo, Brian J Kim, Seth A Hara, Curtis D Lee, Christian A Gutierrez, Tuan Q Hoang, and Ellis Meng. Novel flexible parylene neural probe with 3d sheath structure for enhancing tissue integration. *Lab on a Chip*, 13(4):554–561, 2013.
- [141] Jean-Luc Duval, Tony Dinis, Guillaume Vidal, Pascale Vigneron, David L Kaplan, and Christophe Egles. Organotypic culture to assess cell adhesion, growth and alignment of different organs on silk fibroin. *Journal of Tissue Engineering and Regenerative Medicine*, 2014.
- [142] Hong Yu and Joseph S Neimat. The treatment of movement disorders by deep brain stimulation. *Neurotherapeutics*, 5(1):26–36, 2008.
- [143] PA Starr, JL Vitek, and RA Bakay. Deep brain stimulation for movement disorders. *Neurosurgery Clinics of North America*, 9(2):381–402, 1998.
- [144] Alim-Louis Benabid, P Pollak, D Hoffmann, C Gervason, M Hommel, JE Perret, J De Rougemont, and DM Gao. Long-term suppression of tremor by chronic stimulation of the ventral intermediate thalamic nucleus. *The Lancet*, 337(8738):403–406, 1991.
- [145] Patricia Limousin, Paul Krack, Pierre Pollak, AbdelHamid Benazzouz, Claire Ardouin, Dominique Hoffmann, and Alim-Louis Benabid. Electrical stimulation of the subthalamic nucleus in advanced parkinson’s disease. *New England Journal of Medicine*, 339(16):1105–1111, 1998.
- [146] Alim-Louis Benabid, Adnan Koudsié, Abdelhamid Benazzouz, Laurent Vercueil, Valérie Fraix, Stéphan Chabardes, Jean François LeBas, and Pierre Pollak. Deep brain stimulation of the corpus luyisi (subthalamic nucleus) and other targets in parkinson’s disease. extension to new indications such as dystonia and epilepsy. *Journal of neurology*, 248(3):37–47, 2001.
- [147] US Department of Health and Human Services. FDA approves implanted brain stimulator to control tremors. *Press Release P97-24 (August 4, 1997)*, 2006.
- [148] Alim-Louis Benabid, Lorella Minotti, Adnan Koudsié, Anne de Saint Martin, and Edouard Hirsch. Antiepileptic effect of high-frequency stimulation of the subthalamic nucleus (corpus luyisi) in a case of medically intractable epilepsy caused by focal dysplasia: a 30-month follow-up: technical case report. *Neurosurgery*, 50(6):1385–1392, 2002.
- [149] Stéphan Chabardes, Philippe Kahane, Lorella Minotti, Adnan Koudsie, Edouard Hirsch, and Alim-Louis Benabid. Deep brain stimulation in epilepsy with particular reference to the subthalamic nucleus. *Epileptic disorders: international epilepsy journal with videotape*, 4:S83–93, 2002.

- [150] Helen S Mayberg, Andres M Lozano, Valerie Voon, Heather E McNeely, David Seminowicz, Clement Hamani, Jason M Schwalb, and Sidney H Kennedy. Deep brain stimulation for treatment-resistant depression. *Neuron*, 45(5):651–660, 2005.
- [151] Janis J Daly and Jonathan R Wolpaw. Brain–computer interfaces in neurological rehabilitation. *The Lancet Neurology*, 7(11):1032–1043, 2008.
- [152] Sixto Ortiz Jr. Brain-computer interfaces: where human and machine meet. *Computer*, 40(1):17–21, 2007.
- [153] Andrea Kübler, Boris Kotchoubey, Thilo Hinterberger, Nimr Ghanayim, Juri Perelmouter, Margarete Schauer, Christoph Fritsch, Edward Taub, and Niels Birbaumer. The thought translation device: a neurophysiological approach to communication in total motor paralysis. *Experimental Brain Research*, 124(2):223–232, 1999.
- [154] Thilo Hinterberger, Andrea Kübler, Jochen Kaiser, Nicola Neumann, and Niels Birbaumer. A brain–computer interface (bci) for the locked-in: comparison of different eeg classifications for the thought translation device. *Clinical Neurophysiology*, 114(3):416–425, 2003.
- [155] Emanuel Donchin, Kevin M Spencer, and Ranjith Wijesinghe. The mental prosthesis: assessing the speed of a p300-based brain-computer interface. *IEEE Transactions on Rehabilitation Engineering*, 8(2):174–179, 2000.
- [156] Niels Birbaumer, Nimr Ghanayim, Thilo Hinterberger, Iver Iversen, Boris Kotchoubey, Andrea Kübler, Juri Perelmouter, Edward Taub, and Herta Flor. A spelling device for the paralysed. *Nature*, 398(6725):297–298, 1999.
- [157] Niels Birbaumer. Brain–computer-interface research: coming of age. *Clinical Neurophysiology*, 117(3):479–483, 2006.
- [158] Mikhail A Lebedev and Miguel AL Nicolelis. Brain–machine interfaces: past, present and future. *TRENDS in Neurosciences*, 29(9):536–546, 2006.
- [159] Eric C Leuthardt, Gerwin Schalk, Jonathan R Wolpaw, Jeffrey G Ojemann, and Daniel W Moran. A brain–computer interface using electrocorticographic signals in humans. *Journal of Neural Engineering*, 1(2):63, 2004.
- [160] Eric C Leuthardt, Charles Gaona, Mohit Sharma, Nicholas Szrama, Jarod Roland, Zac Freudenberg, Jamie Solis, Jonathan Breshears, and Gerwin Schalk. Using the electrocorticographic speech network to control a brain–computer interface in humans. *Journal of Neural Engineering*, 8(3):036004, 2011.
- [161] Gopal Santhanam, Stephen I Ryu, M Yu Byron, Afsheen Afshar, and Krishna V Shenoy. A high-performance brain–computer interface. *nature*, 442(7099):195–198, 2006.
- [162] Jean-Jacques Vidal. Toward direct brain-computer communication. *Annual review of Biophysics and Bioengineering*, 2(1):157–180, 1973.
- [163] Edward M Schmidt. Single neuron recording from motor cortex as a possible source of signals for control of external devices. *Annals of Biomedical Engineering*, 8(4-6):339–349, 1980.
- [164] Miguel AL Nicolelis. Actions from thoughts. *Nature*, 409(6818):403–407, 2001.

-
- [165] Meel Velliste, Sagi Perel, M Chance Spalding, Andrew S Whitford, and Andrew B Schwartz. Cortical control of a prosthetic arm for self-feeding. *Nature*, 453(7198):1098–1101, 2008.
- [166] John K Chapin, Karen A Moxon, Ronald S Markowitz, and Miguel AL Nicolelis. Real-time control of a robot arm using simultaneously recorded neurons in the motor cortex. *Nature neuroscience*, 2(7):664–670, 1999.
- [167] Jose M Carmena, Mikhail A Lebedev, Roy E Crist, Joseph E O’Doherty, David M Santucci, Dragan F Dimitrov, Parag G Patil, Craig S Henriquez, and Miguel AL Nicolelis. Learning to control a brain–machine interface for reaching and grasping by primates. *PLoS biology*, 1(2):e42, 2003.
- [168] John K Chapin and Karen A Moxon. *Neural prostheses for restoration of sensory and motor function*. CRC Press, 2000.
- [169] Robert A Schindler, Michael M Merzenich, and Mark W White. Multielectrode intracochlear implants: nerve survival and stimulation patterns. *Archives of Otolaryngology*, 103(12):691–699, 1977.
- [170] Gerald E Loeb. Cochlear prosthetics. *Annual review of neuroscience*, 13(1):357–371, 1990.
- [171] F Blair Simmons. Electrical stimulation of the auditory nerve in man. *Archives of Otolaryngology*, 84(1):2–4, 1966.
- [172] Robert V Shannon. Multichannel electrical stimulation of the auditory nerve in man. I. Basic psychophysics. *Hearing Research*, 11(2):157–189, 1983.
- [173] Giles S Brindley and WS Lewin. The sensations produced by electrical stimulation of the visual cortex. *The Journal of physiology*, 196(2):479–493, 1968.
- [174] EM Schmidt, MJ Bak, FT Hambrecht, CV Kufta, DK O’rourke, and P Vallabhanath. Feasibility of a visual prosthesis for the blind based on intracortical micro stimulation of the visual cortex. *Brain*, 119(2):507–522, 1996.
- [175] William H Dobbelle, MG Mladejovsky, and JP Girvin. Artificial vision for the blind: Electrical stimulation of visual cortex offers hope for a functional prosthesis. *Science*, 183(4123):440–444, 1974.
- [176] William H Dobbelle, Donald O Quest, Joao L Antunes, Theodore S Roberts, and John P Girvin. Artificial vision for the blind by electrical stimulation of the visual cortex. *Neurosurgery*, 5(4):521–527, 1979.
- [177] Wm H Dobbelle. Artificial vision for the blind by connecting a television camera to the visual cortex. *ASAIO journal*, 46(1):3–9, 2000.
- [178] National Spinal Cord Injury Statistical Center et al. Spinal cord injury. facts and figures at a glance. *Journal of spinal cord medicine*, 28(4):379–380, 2005.
- [179] Sanjiv K Talwar, Shaohua Xu, Emerson S Hawley, Shennan A Weiss, Karen A Moxon, and John K Chapin. Behavioural neuroscience: Rat navigation guided by remote control. *Nature*, 417(6884):37–38, 2002.

- [180] Johan Wessberg, Christopher R Stambaugh, Jerald D Kralik, Pamela D Beck, Mark Laubach, John K Chapin, Jung Kim, S James Biggs, Mandayam A Srinivasan, and Miguel AL Nicolelis. Real-time prediction of hand trajectory by ensembles of cortical neurons in primates. *Nature*, 408(6810):361–365, 2000.
- [181] Dawn M Taylor, Stephen I Helms Tillery, and Andrew B Schwartz. Direct cortical control of 3D neuroprosthetic devices. *Science*, 296(5574):1829–1832, 2002.
- [182] Jonathan R Wolpaw, Dennis J McFarland, Gregory W Neat, and Catherine A Forneris. An eeg-based brain-computer interface for cursor control. *Electroencephalography and clinical neurophysiology*, 78(3):252–259, 1991.
- [183] P R Kennedy and R AE Bakay. Restoration of neural output from a paralyzed patient by a direct brain connection. *Neuroreport*, 9(8):1707–1711, 1998.
- [184] Michael W Keith, P Hunter Peckham, Geoffrey B Thrope, Kathy C Stroh, Brian Smith, James R Buckett, Kevin L Kilgore, and James W Jatich. Implantable functional neuromuscular stimulation in the tetraplegic hand. *The Journal of hand surgery*, 14(3):524–530, 1989.
- [185] Leigh R Hochberg, Mijail D Serruya, Gerhard M Friebs, Jon A Mukand, Maryam Saleh, Abraham H Caplan, Almut Branner, David Chen, Richard D Penn, and John P Donoghue. Neuronal ensemble control of prosthetic devices by a human with tetraplegia. *Nature*, 442(7099):164–171, 2006.
- [186] Leigh R Hochberg, Daniel Bacher, Beata Jarosiewicz, Nicolas Y Masse, John D Simeral, Joern Vogel, Sami Haddadin, Jie Liu, Sydney S Cash, Patrick van der Smagt, et al. Reach and grasp by people with tetraplegia using a neurally controlled robotic arm. *Nature*, 485(7398):372–375, 2012.
- [187] Jennifer L Collinger, Brian Wodlinger, John E Downey, Wei Wang, Elizabeth C Tyler-Kabara, Douglas J Weber, Angus JC McMorland, Meel Velliste, Michael L Boninger, and Andrew B Schwartz. High-performance neuroprosthetic control by an individual with tetraplegia. *The Lancet*, 381(9866):557–564, 2013.
- [188] Daryl R Kipke, William Shain, György Buzsáki, E Fetzi, Jaimie M Henderson, Jamille F Hetke, and Gerwin Schalk. Advanced neurotechnologies for chronic neural interfaces: new horizons and clinical opportunities. *The Journal of Neuroscience*, 28(46):11830–11838, 2008.
- [189] Ronald W Griffith and Donald R Humphrey. Long-term gliosis around chronically implanted platinum electrodes in the *Rhesus macaque* motor cortex. *Neuroscience letters*, 406(1):81–86, 2006.
- [190] Nicholas A Kotov, Jessica O Winter, Isaac P Clements, Edward Jan, Brian P Timko, Stéphane Campidelli, Smita Pathak, Andrea Mazzatenta, Charles M Lieber, Maurizio Prato, et al. Nanomaterials for neural interfaces. *Advanced Materials*, 21(40):3970–4004, 2009.
- [191] Wolfgang J Streit, Qing-Shan Xue, Abhishek Prasad, Viswanath Sankar, Eric Knott, Aubrey Dyer, John R Reynolds, Toshikazu Nishida, Gerald P Shaw, and Justin C Sanchez. Electrode failure: tissue, electrical, and material responses. *IEEE Pulse*, 3(1):30–33, 2012.

- [192] Roy Biran, Dave C Martin, and Patrick A Tresco. The brain tissue response to implanted silicon microelectrode arrays is increased when the device is tethered to the skull. *Journal of Biomedical Materials Research Part A*, 82(1):169–178, 2007.
- [193] Jacob T Robinson, Marsela Jorgolli, and Hongkun Park. Nanowire electrodes for high-density stimulation and measurement of neural circuits. *Frontiers in Neural Circuits*, 7(38):1–5, 2013.

How can we limit the foreign body reaction due to implantation?

Implantable microelectrodes on soft substrate

2

2.1 Introduction

In this chapter, the fabrication processes of the devices, produced along the course of this thesis, will be presented. All the fabrications have been carried out exploiting a flexible technology on biocompatible polymers. The use of a flexible substrate is, beyond doubt, one of the strong point of our strategy for the long-term implantation purpose. Moreover, this choice represents an originality within our laboratory (mostly known for Si-based micro and nano technologies) and it implied some additional difficulties such as the stability of the polymers during the various technological steps and the etching procedure. As explained in the previous chapter, another difficulty was linked to the *in vivo* insertion of the flexible probe. The adopted stiffening strategy to overcome this problem will be also illustrated along this chapter. Despite the high biocompatibility of the chosen materials, the effective non-cytotoxicity of the fabricated devices after the fabrication steps has been proven, through *in vitro* cell culture viability test and organotypic culture. The results concerning the biocompatibility of the devices will be presented at the end of the chapter.

2.2 Soft technology for microelectrode fabrication: choice of the materials

Recently many different polymer materials have been studied as flexible materials for implantable neural interfaces[1, 2, 3, 4, 5] but our study was focused on two of them:

- **Polyimide** represents one of the most promising materials due to its excellent mechanical properties, biocompatibility[6], flexibility[7] and stability in wet microfabrication processes[8]. On one hand, polyimide can be easily purchase and deposited through the typical clean room facilities. On the other hand, despite the good biocompatibility, polyimide is not suitable for "medical applications involving permanent implantation in the human body" as we can find in the technical data-sheet. For this reason polyimide has been used during the first period of the thesis in order to produce electrode prototypes. These prototypes have been employed for the study of the electrical properties of the electrode active sites, which constitute a huge part of this work and will be treated in depth in Chapter 3.
- For the implantable devices we moved on a **Parylene-C** substrate for the fabrication process. The chronic implantability as an ISO 10993, United States Pharmacopeia (USP) Class VI material (highest biocompatibility class for plastics in the United States), the high flexibility and the mechanical strength of parylene make this material the final candidate for use in a microfabricated implantable device. The deposition

of this polymer implies the use of an appropriate machine that has been available in a second time of the PhD.

2.3 Polyimide-based prototype electrodes

2.3.1 Polyimide formation

A polyimide consists in a diamine (Oxydiphenylene Diamine, ODA) and a dianhydride (Pyromellitic Dianhydride, PMDA)[9] in a solvent. Their reaction promotes the formation of a polyamic acid. To obtain a polyimide, the polyamic acid must be then cyclized by chemical or thermal route. This synthesis procedure is schematized in Fig.2.1.

The so resulting polyimide is thermostable and its molecular weight depends on the molecular weight of the polyamic acid.

It has been chosen to work with the commercial polyimide resin PI-2525, PI-2771 and PI-2611: these resins consist in a polyamic acid with a crosslinking agent in a solvent.

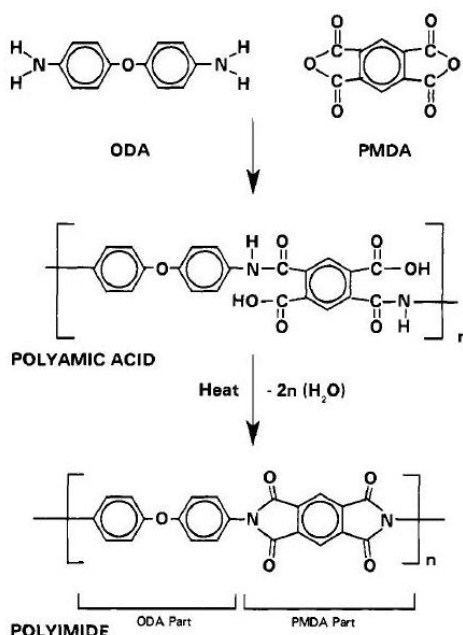


Figure 2.1: Formation of a polyimide.

2.3.2 Polyimide-based electrode design

The design for the prototype electrode is not suitable to be implanted but it is intended to be used for studies about the electrochemical modification of the electrode active sites. As shown in Fig.2.2, each device features 6 round-shaped electrodes of different size areas, in order to test the size effect on the parameters during the electrochemical modification. This will be described in Chapter 3. The sample has a rectangular shape and its dimensions are in the centimeter scale (1 x 6 cm); in this way each single device has been cut and handled easily.

2.3.3 Connection for the prototype polyimide device

The devices produced during this thesis were designed as proof of concept and they are not suitable, for the moment, for a large scale production. Therefore the packaging has been conceived as simple as possible to allow the use of the electrodes in an electrochemical

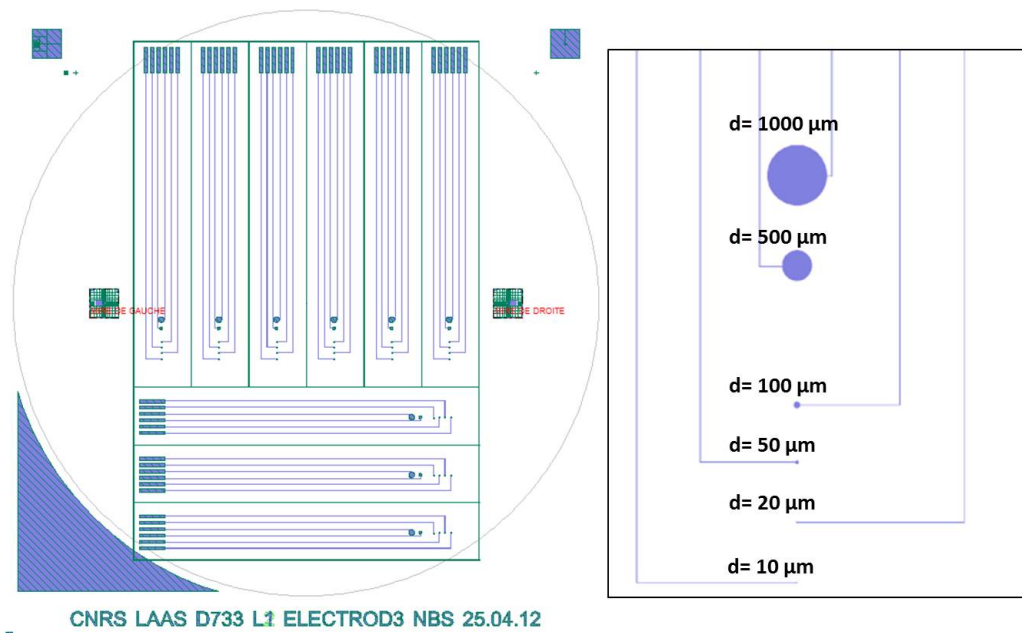


Figure 2.2: Mask design for the prototype polyimide-based electrodes and electrode sizes.

set-up. To that end, the electrodes have been connected by directly plugging them into a commercially available ZIF-connector, after a simple packaging on the flexible structure.

The main problems were related to the low thickness and the high flexibility of the structures, that made difficult their insertion into the connectors. Another issue was related to the thickness of the metal layer (200 nm of Au) since it could be subject to delamination due to frequent insertions and disconnections. Here, the polyimide layer has been glued on a thicker commercial Kapton® sheet in order to increase the thickness, the robustness and better fit into the connector dimensions. As shown in Fig.2.3, a commercially available "micro SD" connector, assembled on a PCB sheet designed *ad hoc* in our laboratory has been used and the devices were directly plugged on it, allowing the connection with any external equipment such as the potentiostat cables for the electrochemical measures, that will be shown in Chapter 3.

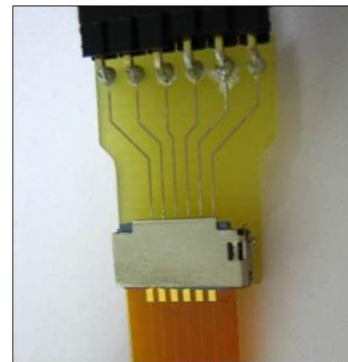


Figure 2.3: Connection for the polyimide prototype electrode.

2.3.4 Originality in the process on polyimide

In most cases, the polyimide devices remain on the host substrate[7] after the fabrication process because the application purpose is rather the encapsulation than the flexibility of the device. In many other cases, structures realized on flexible polymer can be obtained by lamination of a commercial polymer film like Kapton® (usually sold in rolls) on a

host support covered with a double-sided adhesive or a pseudo-adhesive polymer (like PDMS). The drawbacks in the use of these commercial rolls reside also in the surface state: often the surface exhibits a lot of scratches and thickness inhomogeneity. Another common technique is the spin coating of polyimide resin on a thin sacrificial layer such as a metal[10] or a material that can be chemically etched or a non-permanent glue that can be dissolved by heat or UV light. All these procedures allow, in general, to produce very simple monolayer devices using unitary procedures for metallization and passivation with a low resolution alignment. The choice of the sacrificial layer is, indeed, a critical point: during the technological fabrication steps chemical and mechanical stress can be induced on the starting sacrificial layer, leading also to the degradation of the polymer. This results in high mechanical stress between the layers and, as a consequence, in non-planar or cracked, multilayer devices.

To address this issue, polyimide structures without the use of sacrificial layer were employed[11]; in our fabrication process the polyimide layer has been spin coated directly on the silicon host substrate to obtain the best alignment resolution during photolithography that determines the quality of all the technological steps. At the end of the process, the polyimide structures are mechanically peeled off from the silicon substrate, keeping their original planar shape.

2.3.5 Technological process

The process consists of 3 main steps. The basic principles of all the used techniques are described in Appendix A.

I. Polyimide deposition

A standard silicon wafer has been chosen as a substrate and a silicon oxide (SiO_2) layer has been deposited by plasma-enhanced chemical vapor deposition (PECVD) on the wafer surface.

Polyimide layer has been obtained by **spin coating**. It is well known that the adhesion of polyimide on silicon substrate is a critical issue[12, 13], especially in the case of silicon oxide because of its degree of hydration[14]. Indeed, water is adsorbed on the silicon oxide surface (that is non-hygroscopic) and the links between silicon and polyimide are weak Van der Waals hydrogen bonds-type. Therefore, using a silicon oxide substrate, the polyimide layer can be easily released from the host substrate at the end of the fabrication process. Nevertheless a strong adhesion of the polyimide layer on the host substrate is requested during the technological steps, including the use of chemicals and high temperatures, in order to avoid any plastic deformation.

A good adhesion between the resin and the silicon substrate is obtained after the deposition of several layers thanks to the excess of resin that falls on the edges. The polyimide PI2525 (HD Microsystems GmbH, Germany) has been spin coated in two times: the first deposition is done using a low rate of spin coating in order to spread a thick layer

of resin over the wafer. A second faster spin coating allows to homogenize the deposited resin on the wafer surface and to avoid the formation of air bubbles. To evaporate the solvent, a first **soft bake** is then performed. This deposition results in a thickness of about $13\ \mu\text{m}$. To obtain a thicker polyimide layer more suitable to be handled, this deposition procedure was repeated three or four times in order to obtain a device of about $40\ \mu\text{m}$ -thick (each layer is soft baked after the resin induction).

After spin coating, the resin is cured with adapted temperature ramp and plateaus, in order to relax the stress of silicon and polyimide. After curing, the thickness of the polyimide layers decreases slightly.

II. Microelectrode patterning

Gold circular electrodes were patterned on the polyimide surface by photolithography. First, a negative photoresist (AZ-nLOF 2035, MicroChemicals) was spin coated on the wafer then, thanks to a **metallization** followed by a **lift-off process**, the metallic pattern is obtained. A $200\ \text{nm}$ -thick gold (Au) layer was evaporated on the substrate and a thin titanium (Ti) layer ($50\ \text{nm}$) was used to improve adhesion between polyimide and gold.

III. Passivation and contact opening

A passivation layer is deposited on the wafer and patterned in two possible ways:

- **a chemical way:** the use of a photosensitive polyimide (PI2771 HD Microsystems), allows opening the contacts by exposing the resin to UV light and development, following the parameters in Table 2.1. The thickness of the obtained layer is about $6\ \mu\text{m}$ but it is halved after curing, with a minimum resolution of $10\ \mu\text{m}$.
- **a physical way:** a polyimide layer (PI2611 HD Microsystems) is deposited on the wafer as described above. The obtained thickness after curing is, even in this case, about $3\ \mu\text{m}$. A negative resist (AZ-nLOF 2035, MicroChemicals) is then spin coated and patterned on the polyimide passivation layer. The resist is used as a mask during reactive ion etching (RIE) for opening the contacts. In this way, the obtained minimum resolution can be lowered down to $6.5\ \mu\text{m}$.

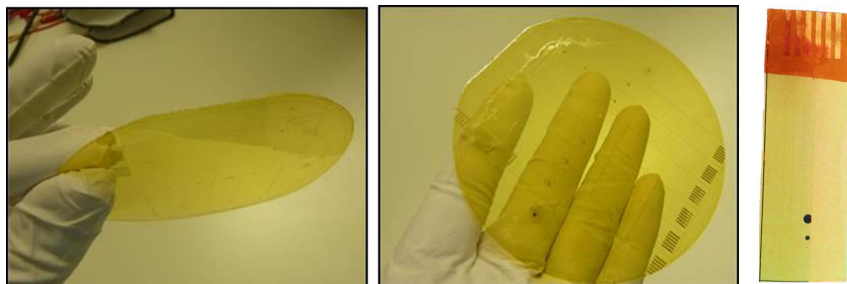


Figure 2.4: Peeled off polyimide-based electrodes used for preliminary tests.

| | | | |
|--------------------------------|-----------------------------------|---|-----------|
| a | Substrate | 4" p-type Si wafer (100), thickness = 525 μm | |
| b | SiO₂ depositon | thickness = 500 nm, PECVD | |
| c | PI2525 deposition | Slow induction: 500 rpm, 30 s | x 3 times |
| | | Fast induction: 2500 rpm, 30 s | |
| Soft bake: 100°C, 120 s | | | |
| | | Curing: 200° C for 30 min → 300° C for 30 min (under inert N ₂ atmosphere) | |
| d | Microelectrodes patterning | AZ-nLOF 2035 induction (5 μm) 1350 rpm, 5000 rpm/s, 30 s soft bake: 110° C for 90 s exposure for 6 s at 405 nm, 25 mW/cm ² development in MFCD26 for 2 min post exposure bake: 110° C for 90 s | |
| e | Metallisation and Lift-off | Ti/Au (50 nm/200 nm) evaporation (PVD) | |
| f | Passivation | A) photosensible PI2771 deposition: 5000 rpm, 60 s soft bake: 100°C, 60 s | |
| | | B) PI2611 deposition: 5000 rpm, 60 s soft bake: 100°C, 60 s curing: 300°C, 30 min | |
| g | Contact opening | A) photosensible PI2771 patterning: exposure at 365 nm development in cyclopentanone bath rinsing in PGMEA and isopropanol | |
| | | B) PI2611 dry etching: AZ-nLOF 2035 induction RIE: O ₂ (80%) = 30 sccm, CF ₄ (20%) = 5 sccm P _r = 5 mT P _{ICP} = 500 W P _{bias} = 40 W | |
| h | Peel-off | | |

Table 2.1: Chronological steps followed for the fabrication procedure of polyimide-based electrodes (rpm = rounds per minute).

At the end, the polyimide-based electrodes can be easily peeled off from the wafer and cut with scissors into separate single devices as shown in Fig.2.4.

The details of the whole process are given in Table 2.1, with the corresponding steps described in Fig.2.5. As shown in Section 2.4.4, the polyimide layer is then glued on commercial Kapton® at the connection level to fit into the electrical connector.

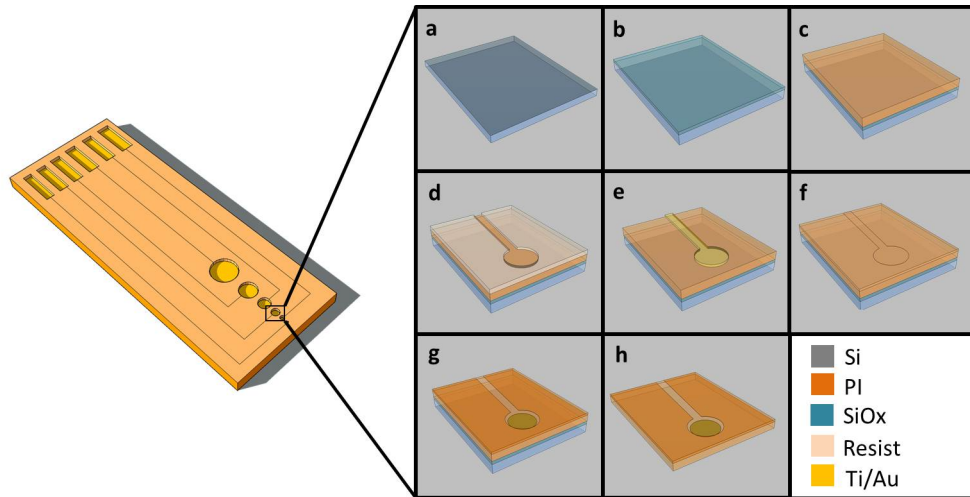


Figure 2.5: Schematic illustration of the main steps for the fabrication of polyimide-based electrodes.

2.4 Parylene-based electrodes

2.4.1 The poly(chloro-p-xylylene) or Parylene-C

Parylene-C (PXC) belongs to the family of poly(para-xylylene), with one chlorine group per repeat unit. The chemical structure of PXC is shown in Fig.2.6.

PXC has desirable material properties for use in a micro-fabricated implantable device. In the case of neuroprostheses the advantages of using parylene-C as the structural material, when compared with technologies based on the use of other materials such as PDMS, polyimide and silicon, include[15]:

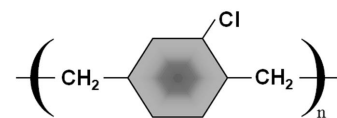


Figure 2.6: Chemical structure of parylene-C.

- pinhole-free conformal coating due partly to its unique room-temperature chemical vapor deposition process;
- **low water permeability**;
- **chronic implantability** as an ISO 10993, United States Pharmacopeia (USP) Class VI material (highest biocompatibility class for plastics in the United States);
- **high flexibility and mechanical strength** (Young's modulus ~ 4 GPa).

The biocompatibility of parylene-C results from being chemically inert and synthesized using a solvent free polymerization process[16]. Critically important to microfabrication, one can generate conformal, pinhole-free barrier films that can be subsequently dry-etched using an oxygen plasma[17]. For these reasons, parylene-C has been used in neurotechnology, especially as a coating material. It has been successfully used for coating microwires[18] and micro-machined silicon arrays[19]. Researchers have also microfabricated planar devices with a parylene-C substrate in a microfluidic device with recording capabilities[20], retinal stimulation array[21, 22], and a flexible nerve cuff[23].

2.4.2 Parylene deposition

The deposition of thin polymeric films of parylene, onto a surface using a gaseous precursor was first observed by Szwarc in 1947 when he found the polymer as one of the products formed in the vacuum thermal decomposition (pyrolysis) of para-xylene. Later, Gorham implemented a much more efficient route to the deposition of parylene films through the vacuum pyrolysis of di-para-xylylene[16]. He demonstrated that, at temperatures above 550° C and at pressures less than 1 Torr, the dimer is quantitatively cleaved into two monomer units (para-xylylene), which are adsorbed onto a surface at room temperature and spontaneously polymerized, yielding high-molecular-weight, linear parylene thin films (see Figure 2.7).

The chemical vapour deposition of parylene consists of several steps: (a) sublimation of dimer in a sublimation furnace; (b) cracking the dimer into monomer in the pyrolysis furnace; (c) transport of the monomer into the deposition chamber; (d) diffusion of monomer from the region above the substrate through any boundary layer that might exist; (e) adsorption of monomer onto the substrate; (f) surface migration and possibly bulk diffusion of monomer; (g) chemical reaction (propagation or initiation). Also note that desorption of monomer can occur any time after adsorption[24].

The thermally activated CVD machine used during this work was designed by the Swiss company COMELEC. This commercial equipment is dedicated to the deposition of thin film of parylene and is composed of four parts, as can be seen in Fig.2.7:

1. a **sublimation chamber** wherein the dimer is positioned in a steel crucible; the chamber is thermostated to allow the sublimation of the precursor.
2. a **pyrolysis chamber** thermostated, as well, in which radical reactive monomers are formed by thermal activation.
3. a room temperature **deposition chamber** where a system of rotation of the sample holder allows to standardize the flow.
4. a **vacuum pumping system** and a **liquid nitrogen trap**.

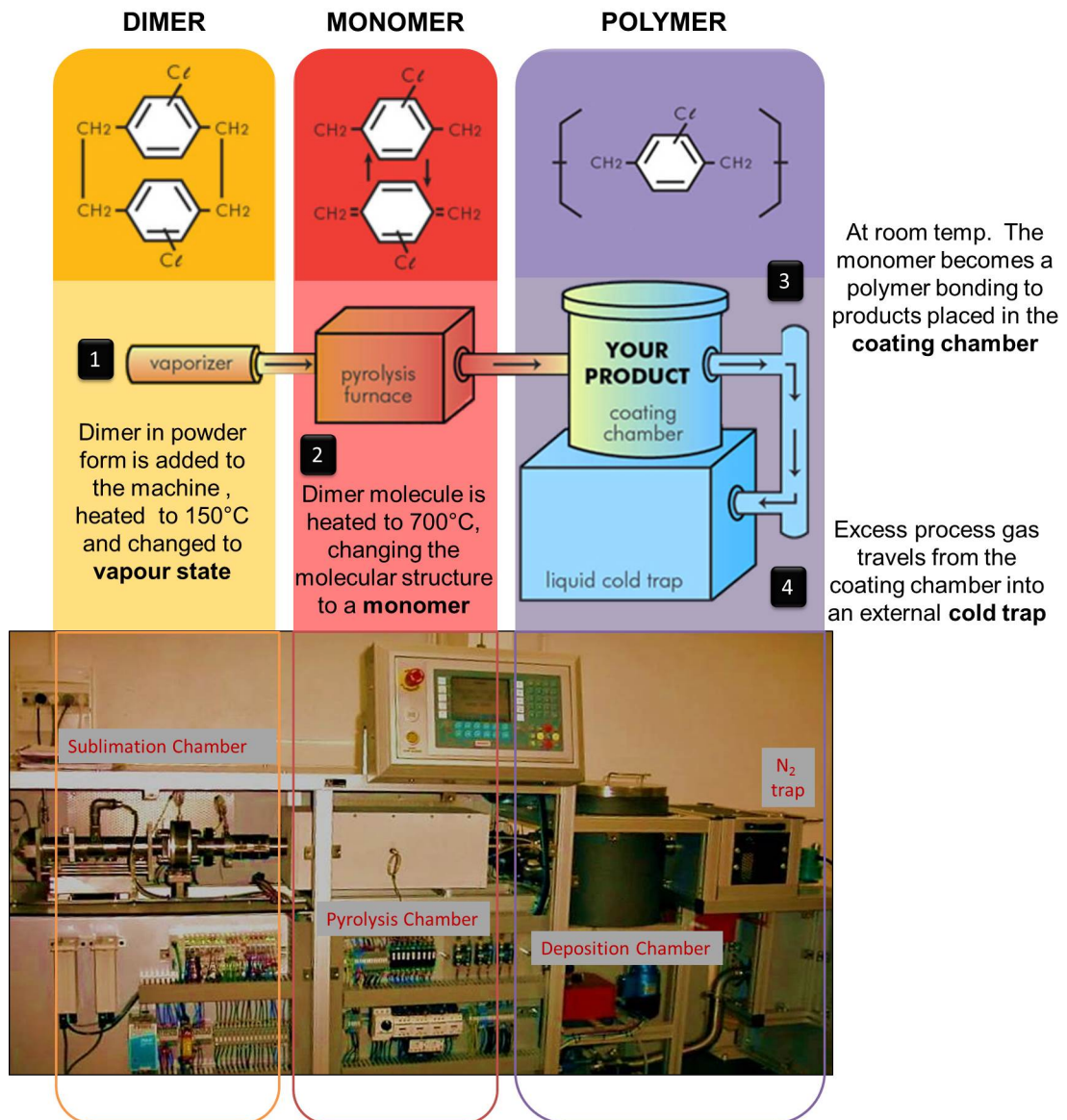


Figure 2.7: Synthesis procedure for parylene-C film (above) and commercial COMELEC machine for the CVD deposition of parylene and its main parts (below).

2.4.3 Parylene-based electrode design

As shown in Fig.2.8, the parylene probe for *in vivo* implantation features 3 or 4 pairs of microelectrodes, placed at different depths resulting in a so-called "hexatrode" or "octatrode".

This electrode arrangement is used to compare the two microelectrodes placed at the same depth (thus recording from the same population of neurons) by leaving one pristine and modifying the second one with a conductive polymer, as we will see in Chapter 3, in order to clearly show the effect of nanostructuring of the microelectrode surface. Basically two different designs of the entire device have been considered: the first one (Fig.2.8.a) is a generic structure, where the second one is optimized (Fig.2.8.b) for the experimental

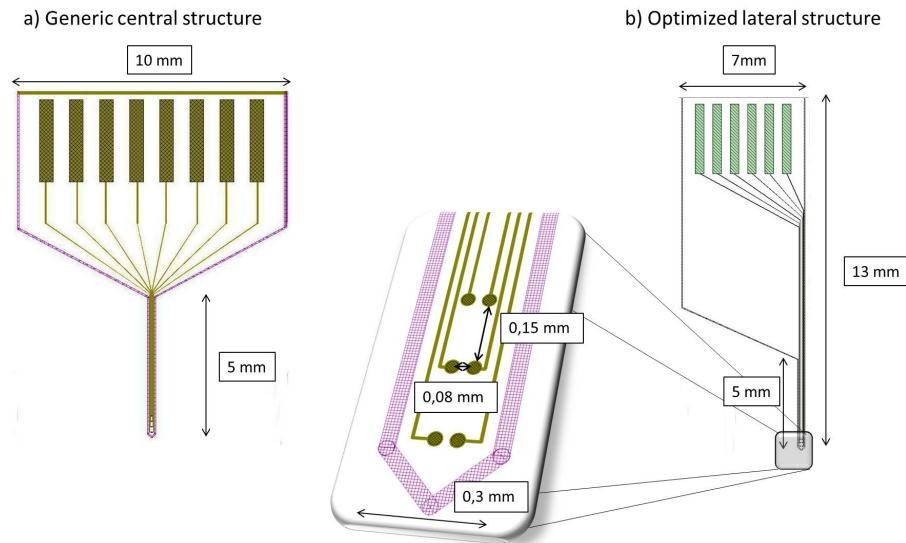


Figure 2.8: The two main configurations of parylene-based devices: a) central octatrode and b) lateral hexatrode (optimized for the *in vivo* recording set-up).

set-up of the electrophysiological measures as will be described in Chapter 4.

2.4.4 Connection for the implantable parylene device

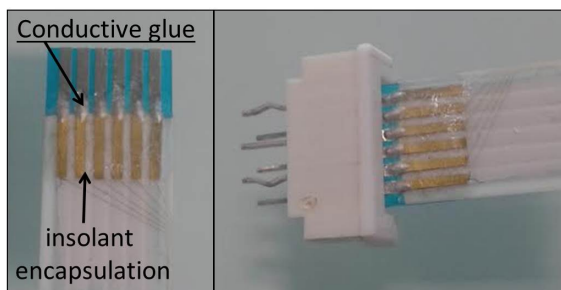


Figure 2.9: Electrical connection for the parylene electrode.

In Fig.2.9, the solution adopted for the implanted device is shown.

The larger part of the device is glued on FFC cable jumper (RadioSpares) with a biological compatible glue (353ND from EPO-TEK®); thanks to a conductive glue (silver conductive epoxy, H20E EPO-TEK®) the electric pads are connected to the FFC cable and then protected with the biological compatible glue. The robustness of the flexible cable allows us to

plug it many times, without damaging the connection. The commercially available cable perfectly fits into the adapted ZIF-type connector (RadioSpares).

This solution was adopted in order to perform *in vivo* experiments over a long period of time and, moreover, to provide a convenient system for the set-up generally used by the electrophysiologists to carry out the *in vivo* studies (Chapter 4).

2.4.5 Technological process

The implantable microelectrode fabrication process is schematized in Fig.2.12.

Again, the whole process can be divided in four main steps.

I. Parylene-C deposition

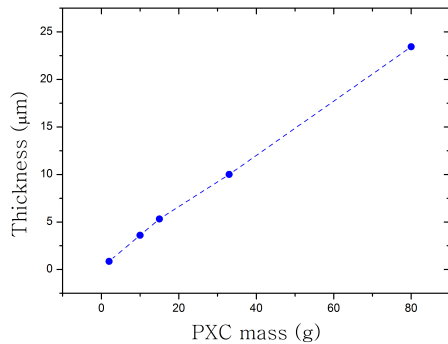


Figure 2.10: Relation between the starting mass of PXC precursor and the thickness of the obtained film.

A standard silicon wafer was used as a substrate for the whole process. Parylene-C (Fig.2.12.a) was deposited through thermally activated CVD at the pyrolysis temperature of 700° C. The thickness of the deposition was measured each time using a standard Profilometer (KLA Tencor) and it was found to be proportional to the mass of precursor dimer charged in the sublimation chamber (see Fig.2.10). A 23 μm -thick PXC film was obtained starting from 80 g of precursor.

The so deposited 23 μm -thick PXC film has a measured roughness of about 30 nm, and the surface presents hydrophobic features that can be easily turned into hydrophilic ones by 15 min of UV ozone exposure (Fig.2.11).

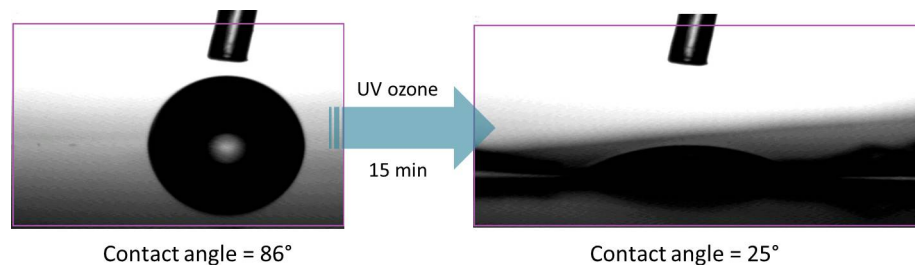


Figure 2.11: Contact angle of water on PXC before and after the UV ozone treatment.

II. Microelectrodes patterning

Similarly to the process carried out on polyimide, Au circular electrodes were patterned on the PXC surface thanks to a metallization followed by a lift-off process (Fig.2.12.a-c).

III. Passivation and contact opening

After the Au electrode patterning, a thin layer of PXC (about 1 μm obtained from 1.6 g of precursor) is deposited on top of the wafer as a passivation layer (Fig.2.12.d).

The electrode surfaces and the contacts were opened by dry etching of the PXC using a photoresist mask (AZ-ECI 3027, MicroChemicals) with a thickness of about 2 μm (Fig.2.12.e).

The etching rate of PXC with these parameters was found to be 350 nm/min, whereas the etching rate of AZ-ECI photoresist is about 450 nm/min (Fig.2.12.f).

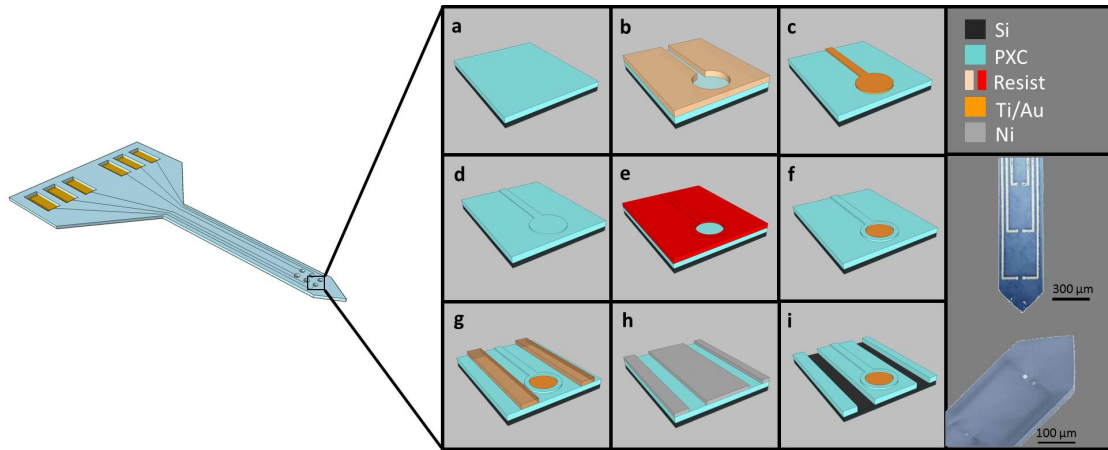


Figure 2.12: Schematic illustration of the main steps for the fabrication of the parylene-based microelectrodes.

| | | | |
|---|--------------------------------|---|--|
| a | Substrate | 4" p-type Si wafer (100), thickness = $525\mu\text{m}$ | |
| b | Parylene-C deposition | CVD at 700°C , 80 g of precursor | |
| c | Microelectrodes patterning | AZ-nLOF 2035 induction (see Table 2.1) | |
| d | Metallisation and Lift-off | Ti/Au (50 nm/200 nm) evaporation (PVD) | |
| e | Passivation | CVD at 700°C , 1,6 g of precursor | |
| f | Contact opening | AZ-ECI 3027 induction ($2,6\ \mu\text{m}$): 1) 5000 rpm, 30 s soft bake: 90° , 30s 2) 1000 rpm, 30 s soft bake: 90° , 75 s post exp. bake: 110° , 75 s exposure for 10 s at 405 nm, $25\ \text{mW}/\text{cm}^2$ development in MFCD26 for 30 s | RIE (4 min): $T = 10^\circ\text{C}$ $\text{O}_2 = 20\ \text{sccm}$ $P_r = 20\ \text{mT}$ $P_{ICP} = 500\ \text{W}$ $P_{bias} = 10\ \text{W}$ |
| g | Cutting patterning | AZ-nLOF 2035 induction (see Table 2.1) | |
| h | Metallisation and Lift-off | Ni (100 nm) evaporation (PVD) | |
| i | Etching for cutting structures | RIE (90 min) | Ni chemical etching $\rightarrow \text{HCl}$ (20%) and H_2O_2 (10%) in H_2O |

Table 2.2: Chronological steps followed for the fabrication procedure of parylene-based electrodes.

IV. Cutting structures

The wafer surface was previously patterned with AZ-nLOF 2035 photoresist (Fig.2.12.g), then a layer of 100 nm of Nickel (Ni) was deposited by electron beam physical vapour deposition on top of it and a second lift-off procedure was performed in order to use the Ni layer as a hard mask for the second etching process (Fig.2.12.h).

The plasma oxygen etching was performed as described above during a time duration (6 cycles of 15 min) long enough to allow the cutting of the 24 μm -thick layer of PXC. During the physical etching it is important to perform short cycles in order to avoid overheating of the sample and prevent Nickel cracking. The Ni layer was then chemically etched (Fig.2.12.i). Finally the PXC on the edge of the Si wafer was scratched with tweezers and the electrode structures were easily peeled off from the Si surface, or released in a water bath (Fig.2.13), keeping their planar shape.

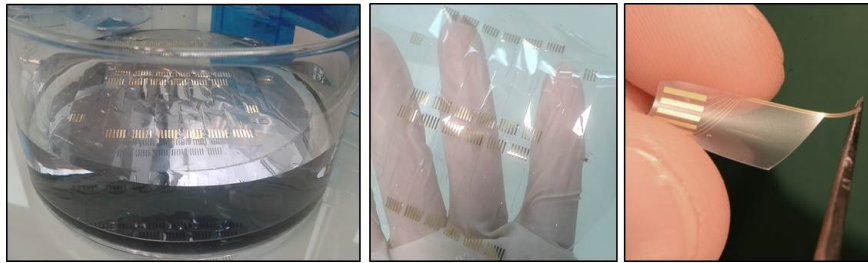


Figure 2.13: Release of PXC-based devices in water and final appearance of the electrode.

The details of the whole process are given in Table 2.2, with the corresponding steps described in Fig.2.12.

2.4.5.1 Parylene etching: issues and optimization

During the fabrication process, the etching procedure for the microelectrode opening was particularly optimized. It has been shown in the literature that some contaminations can be observed after stripping Parylene-C with the oxygen plasma[25], as can be seen in Fig.2.14.d. The possible reason for the contamination is suspected to be the reaction products of the active chlorine group present per repeat unit with the polymer and oxygen under plasma condition[26]. On the contrary, as shown by Wen et al.[25], the etching results of Parylene-N coated samples turn out to be contamination free.

Most of the used photoresists provided a good definition of the sidewalls but they left many etching residues (see Fig.2.14.a and 2.14.b) that have been difficult to remove afterwards. The selectivity and the parylene etching rate have been found pretty low for all the used photoresists.

As can be seen in Fig.2.15, the residues originate from the parylene etched sidewalls and they are redeposited on the resist sidewalls. After the stripping of the resist all these spaghetti-like residues collapse down into the electrode surface, modifying the size of the electrode active area. As a consequence, the amount of residues is directly linked to the

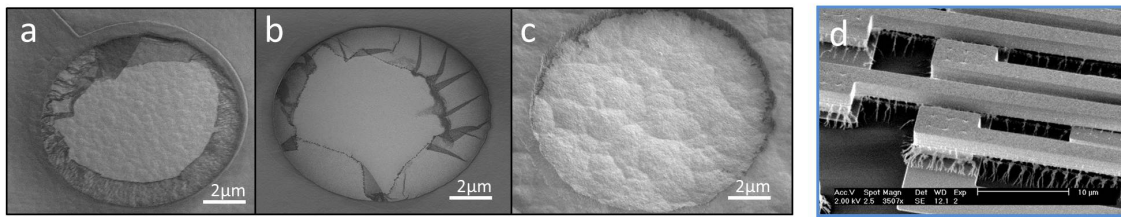


Figure 2.14: Etching residues for a 10 μm opening, using three different photoresist masks: a) AZ-4562, b) AZ-40XT and c) AZ-ECI3027; d) similar kind of residues found in the literature[25].

thickness of the remaining photoresist before stripping.

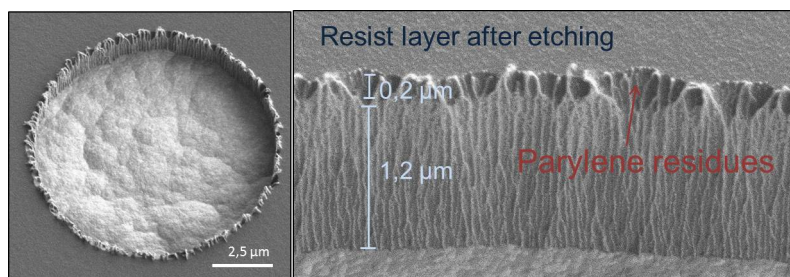


Figure 2.15: Etching parylene residues on the sidewalls before stripping the resist.

The AZ-ECI 3027 photoresist has the ability to be deposited as a thin film. This prevents any redeposition of residues within the electrode active area (see Fig.2.14.c) since the remaining resist layer after etching is only a few hundreds of nanometers (Fig.2.15) to be compared to several micrometers with thick photoresists. This allows avoiding further cleaning procedure in acidic mixture after plasma etching.

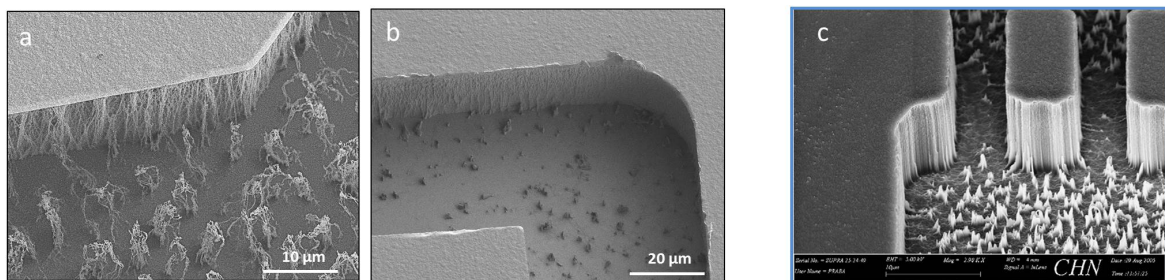


Figure 2.16: Cutting of electrode edges by plasma etching (a) before and (b) after chemical etching of the Nickel mask; (c) example of similar residues in the literature[27].

On the contrary, when considering deep etching for edge cutting, the residues are found directly on the bottom side but they are flattened and partially removed after dissolution of the Nickel mask, as can be seen from Fig.2.16. The bottom stop layer is represented by Si. Even if the bottom is not perfectly clean the etching performed in this way allows us to release the electrodes at the end of the process.

2.5 Temporary stiffening of flexible electrodes using silk coating

In the context of another thesis project started in 2013 with Aziliz Lecomte, different biodegradable polymers have been tested in order to obtain the required stiffness for the electrode to be inserted into the cortex.

Here, the strategy that has shown the best results in terms of stiffness, degradation time and ease of deposition, and that has been used for the *in vivo* implantation experiment is presented.

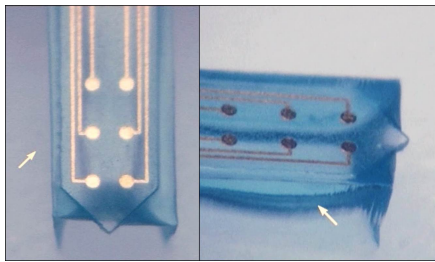


Figure 2.17: Optical microscope image of silk deposition on the backside of the probe.

Silk has demonstrated to be the most suitable polymer for stiffening, thanks to its mechanical properties, its low viscosity in liquid state that allows an easy deposition by syringe, and a degradation rate that is slow enough to allow the implantation procedure to be performed over one hour. Polymers as PEG, that are hydro-soluble, dissolve in a few seconds once immersed in a physiologic liquid, and gelatine from collagen, that becomes stiff in a dehydrated state, is rehydrated in a few seconds in physiologic liquid, losing its mechanical properties. On the opposite,

silk fibroin, that is a natural protein produced by the domestic silkworm *Bombyx mori*, is degradable over a longer time period. As a protein, silk fibroin is susceptible to biological degradation by proteolytic enzymes such as chymotrypsin, actinase, and carboxylase[28, 29, 30].

The extraction procedure of silk fibroin from *Bombyx mori* cocoons presented by Kaplan and co-workers[31] was adopted to obtain liquid silk fibroin. In this liquid state, silk fibroin was deposited on the back side of the electrodes (Fig.2.17) using a syringe and a PDMS mold. The hydrophilicity of the surface, obtained as seen in section 2.4.5 allowed a strong adhesion between silk and parylene. The deposited silk was then water annealed for 6h.

To assure the penetration of the probe during the *in vivo* implantation a "phantom brain" was fabricated to mimic the mechanical behaviour of the brain tissue. Typical values for the elastic modulus of the brain tissue range from 1 to 100 kPa depending on the test method, condition and region of brain (i.e. gray or white matter)[32, 33, 34]. A classical method to obtain these value is the use of an Agarose hydrogel 0.6% w/v. In Fig.2.18, we can see the insertion test in Agarose gel before and after the silk deposition. The electrode covered with silk in the backside could easily penetrate the gel.

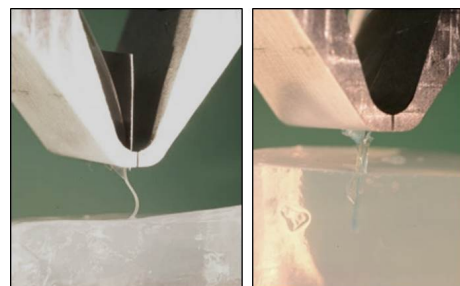


Figure 2.18: Insertion test in Agarose gel before (left) and after (right) the silk deposition.

2.6 *In vitro* cytotoxicity of the devices

The next chapter will be focused on the modification of the microelectrode active area with the conductive polymer poly(3,4-ethylenedioxythiophene) (PEDOT) together with polystyrene sulfonate (PSS). Therefore, the final device, will be composed by four materials (PXC, PEDOT:PSS, gold and silk) which have been especially chosen for their properties of biocompatibility with living matter in order to design a device suitable for long-term implantation. In particular, PXC has a certified biocompatibility of CLASS VI, and the cytotoxicity of PEDOT:PSS[35, 36], and gold[37, 38] have been investigated in the literature. For example, Asplund et al. indicate a non-cytotoxic of PEDOT:heparin surfaces and show no marked difference in immunological response in cortical tissue compared to pure platinum controls[35]. Through cell viability assay, we set the preliminary objective to establish the non-cytotoxicity of the produced devices, after the clean room process, and further investigations on biocompatibility are scheduled in the near future. For that purpose, we first carried out *in vitro* experiments to ensure that no harmful chemical product remains on the wafer after the fabrication process and the electropolymerization PEDOT:PSS on the active area.

2.6.1 Test on cell culture: the cell line

The cell lines often found in the literature to validate the non-cytotoxicity for neuroprosthetics are: PC12 (a cell line derived from a pheochromocytoma of the rat adrenal medulla), SH-SY5Y and L929 (mouse fibroblast).

SH-SY5Y neuroblastoma cell line, shown in a optical microscope image in Fig.2.19, originally derives from a metastatic bone tumor biopsy; cells are a subline of the parental line SK-N-SH that were subcloned three times; first to SH-SY, then to SH-SY5, and finally to SH-SY5Y. SH-SY5Y were deposited to the ATCC® in 1970 by June L. Biedler[39, 40]. SH-SY5Y cells are often used as *in vitro* models of neuronal function and differentiation. The important characteristic of SH-SY5Y cells that should be taken into consideration was that they adhere without the need for a protein adhesion promoter. In this way we could better verify the cell adhesion and proliferation on our substrate.

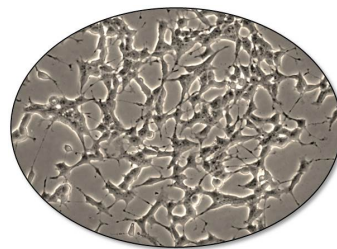


Figure 2.19: Optical microscope image of SH-SY5Y cells.

2.6.2 Substrate sterilization

Since the oxidative degradation of parylene-C can happen above 120°C in air[41], the sterilization in autoclave is not appropriate for our devices. The adopted sterilization method consists in leaving the samples in a mixture of ethanol and deionized water (EtOH 70%) overnight. Other methods, such as the Ethylene Oxide (EtO) sterilization process[42],

can be also considered.

2.6.2.1 Cell viability

SH-SY5Y cells were cultured in Dulbecco's Modified Eagle's Medium (DMEM) with 10% fetal bovine serum, 1% L-glutamine and 1% penicillin-streptomycin added. Cells were seeded in a Petri dish containing the PXC microelectrode with half of the active areas PEDOT-modified, as in the scheme in Fig.2.20. A 100 μ l drop of culture medium containing about 10 000 cells was deposited on the electrode surface and, after 4h (the time required for cell adherence), 2 ml of culture medium was added, giving a cell concentration of 5 000 cells/ml (see Fig.2.20). In this way, the cells were concentrated over the region of interest.

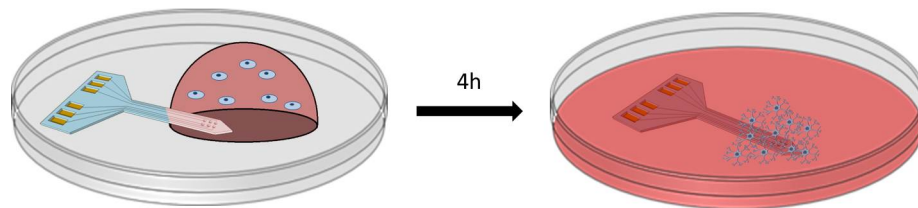


Figure 2.20: Seeding method for the cultivation of SH-SY5Y on top of the device.

A viability assay was performed after 24 h, 72 h and 168 h using the LIVE/DEAD® Viability/Cytotoxicity Assay Kit.

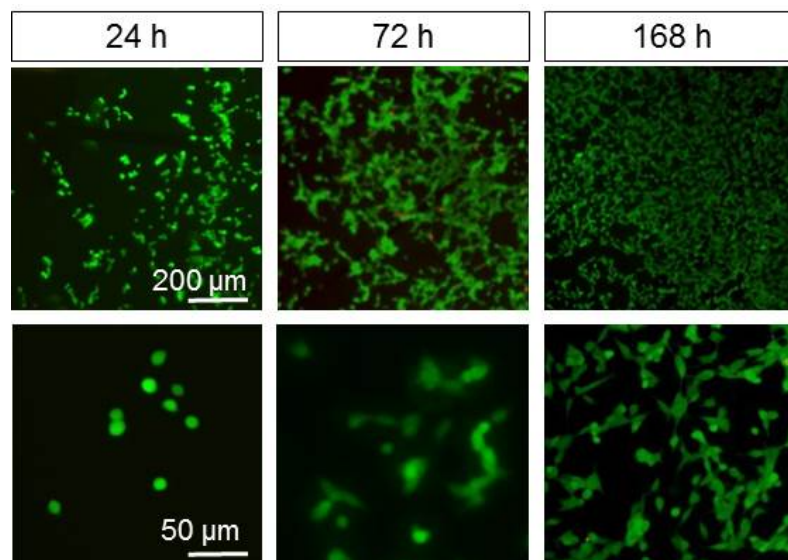


Figure 2.21: Calcein-AM fluorescent images showing SH-SY5Y cultivated on top of the device for 24 h, 48 h and 168 h.

The kit provides a two-color fluorescence cell viability assay that is based on the simultaneous determination of live and dead cells with two probes that measure recognized parameters of cell viability: intracellular esterase activity and plasma membrane integrity. The polyanionic dye calcein is well retained within live cells, producing an intense uniform

green fluorescence. Ethidium homodimer-1 (EthD-1) enters cells with damaged membranes and undergoes a 40-fold enhancement of fluorescence upon binding to nucleic acids, thereby producing a bright red fluorescence in dead cells. EthD-1 is excluded by the intact plasma membrane of live cells.

Fluorescence photos of SH-SY5Y cells cultured on PEDOT-modified PXC based micro-electrodes are shown in Fig.2.21. Cells spread homogeneously and proliferate quickly, demonstrating a good viability on our substrate.

2.6.3 Cell morphology assessment

The morphology of the cells on the electrode substrate was assessed through scanning electron microscopy (SEM).

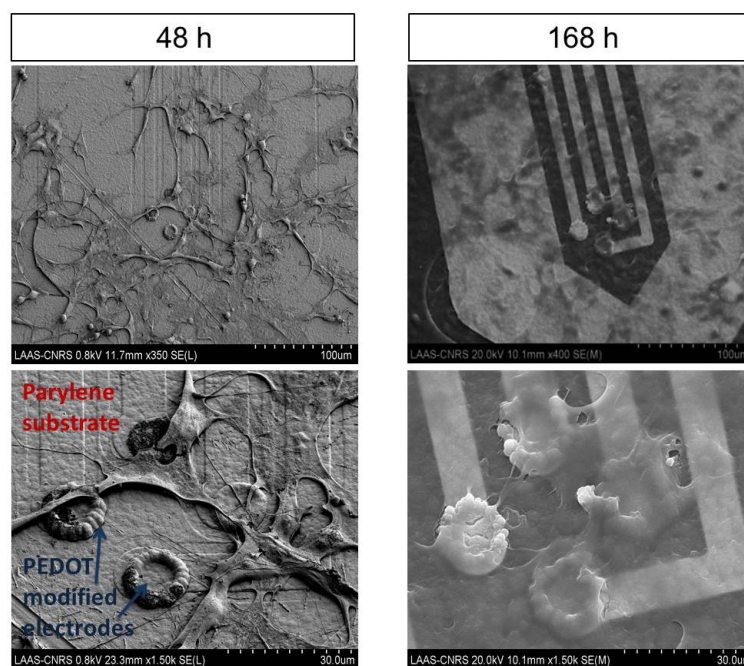


Figure 2.22: SEM images on a SH-SY5Y cell line cultured on top of the device for 48h and 168h. Cells exhibit body cracks, probably as a result of the dehydration process that followed the fixation treatment.

SH-SY5Y cells were seeded in a Petri dish as described above and cultured for 48h and 168h, then the fixation procedure was performed. Before proceeding to the SEM observation, the samples were sputtered with 10 nm of Au in order to avoid charging effect. Individual cells can be recognized in Fig.2.22.a. The cells display extensive processes and appear to be well attached on the surface of our electrodes. Importantly, they do not show a particular preference for different materials and, as can be observed, they spread homogeneously both on PXC substrate and on PEDOT-modified electrode surface. The attachment of cells on our electrode substrate shown in SEM images means that it is possible to get direct, long-term functional contact with the target tissue that is required to the implanted device to operate properly.

2.7 *In vitro* biocompatibility

2.7.1 Organotypic culture

The organotypic culture technique, promoted by Wolff and Haffen[43], is a pre-clinical step which allows the rapid assessment of the behaviour of different organs in contact with biomaterials in order to study their biocompatibility[44, 45, 46, 47, 48]. This method allows rapid estimates of primary cell layer parameters such as adhesion, growth, proliferation and morphology, therefore helping to select biomaterials as a function of their capacities in enhancing these features. The organotypic culture method presents some advantages compared to classical cell culture because it is a low cost technique and it better reproduces the living complexity. Moreover it provides an advantage in making it possible to evaluate a lot of different organs at the same time whereas the cell culture technique needs specific and expensive strains.

To better understand the results, it is important to remind that we are dealing with comparative test. The tissue cell culture plastic Thermanox® is used as negative reference since it is a biocompatible substrate which promotes cell growth.

Two main parameters are used to distinguish cell behaviour cultivated on materials:

- **cell growth** (mm^2) which is the surface of the migration area from the initial explant after culture on the material: the cell layer areas of the different organs is correlated with the ability of the cells to migrate on the biomaterial.
- **cell adhesion** (arbitrary units) which is assessed as the kinetics of cell detachment over time: after cell dissociation and counting, the cell adhesion parameter was estimated using an arbitrary index inversely proportional to the cell detachment kinetics (ratio of cells detached by enzymatic treatment as a function of time, V). This method of calculation ($1/V \cdot 1000$) results in a number n , where $0 < n < 1$, which increase with the increase of the adhesion.

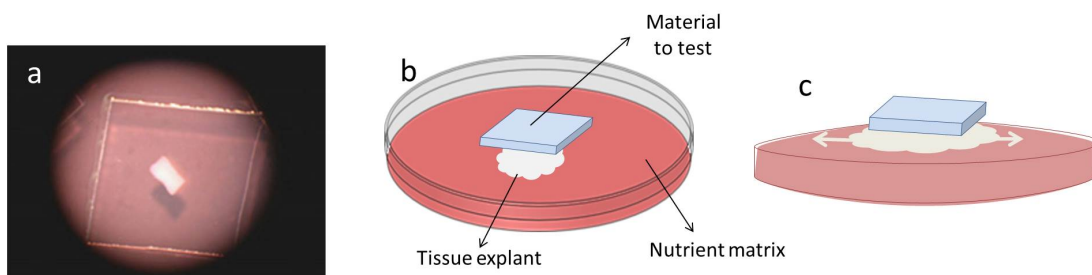


Figure 2.23: a) picture showing the Thermanox® material in contact with the tissue explant; b) schematic representation of the organotypic culture method set-up; c) schematic representation of cell migration outward the tissue onto the surface of the tested material.

Generally, a material is declared cytotoxic when a very low cell migration surface (in the order of 0.2 mm^2) is associated to a necrotic appearance of the cell shape. The importance

of verifying the cell morphology through scanning electron microscopy (SEM) observation arises from the cases of certain materials (as PVC or PMMA) which, even if they do prevent a good cell migration, are not considered as cytotoxic, due to the healthy aspect of the cells cultivated on them. In these cases, other tests have to be performed to state the cytotoxicity[49].

Regarding cell adhesion, this parameter does not state the biocompatibility of a material but is related to the physico-chemical surface properties, in particular roughness and wettability[50]. The wettability is a measure of the hydrophobicity of a material: a hydrophobic surface induces protein adsorption and thus cell adhesion, while a hydrophilic surface often prevents any adsorption and consequently cell adhesion[46, 51, 52, 53]. Regarding the roughness, it has been demonstrated that the rougher is the material, the greater will be the protein adsorption and therefore the cell adhesion[54, 55].

Here, studies have been conducted at the Laboratoire de BioMécanique et BioIngénierie (BMBI) at the Université de Technologie de Compiègne, in close collaboration with Eric Leclerc and Jean-Luc Duval.

The aim of the present work was to **go further in the evaluation of the biocompatibility of the used materials, testing parylene and PEDOT:PSS as growth substrates for various embryonic organs to compare cell morphology, adhesion and growth**. These materials were compared for cell response with Thermanox® and silk fibroin. The latter, used in this thesis as a material for enhancing the mechanical properties of our probe (see Section 2.5) has already been tested, with the same organotypic technique, in a recent publication of Duval and co-workers[56].

2.7.2 Organotypic culture on Parylene-C

Fig.2.24 depicts the migration and adhesion behaviour of the explanted organs (brain and liver) on the parylene substrate compared to other substrates such as Thermanox® and silk fibroin.

It is important to underline that **the migration** on the same material can change depending on the organ used[56]. We verify this behaviour also in the case of Parylene. The migratory behaviour of brain cells on parylene-C, even if lower than the reference Thermanox® is comparable to the database of embryonic chicken cells of the Laboratory. The liver explant presents a drastically lower migration but still good in terms of biocompatibility. The values of cell migration on parylene-C can be considered medium when compared to other organs on Thermanox® where these values can reach 100 mm²[56].

The cell **adhesion** on parylene-C is particularly low; this behaviour is quite surprising because the adhesion is generally inversely proportional to the cell migration and also because of the hydrophobic feature of the parylene-C surface that should induce protein adsorption. The noticeable error bars in migration histograms are due to the low adhesion that leads to the escape of cells during the analysis of biological parameters. Nevertheless, statistical analysis of Tukey-Kramer (see Annex D) shows very significant results ($P <$

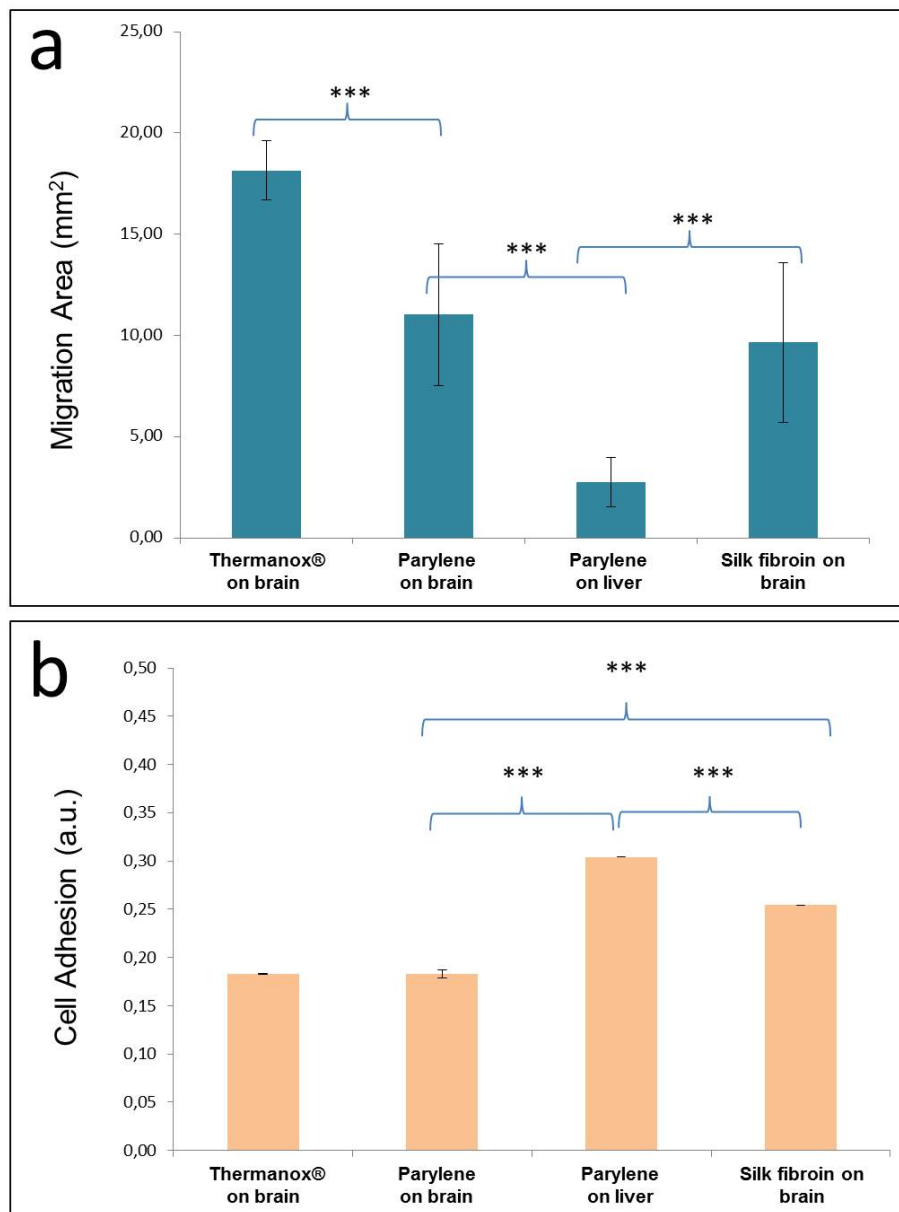


Figure 2.24: Biocompatibility assessment of parylene-C compared to the control Thermanox® and Silk fibroin: (a) Migration area (mm²) of the cell layers. (b) Cell adhesion of the cell layers. ***P < 0.001.

0.001). The brain explant, cultivated on silk fibroin for comparison purposes, while exhibiting cell migration comparable to the one on parylene-C, shows a stronger cell adhesion. This is primarily due to the aligned structure of the silk fibroin.

As explained before, it is important to confirm these results by the **SEM observation**, in order to state the health conditions of the cells by verifying their shape and aspect. Even cells that show a good growth (high values of migration) on certain materials can be subject to necrosis when observed by SEM.

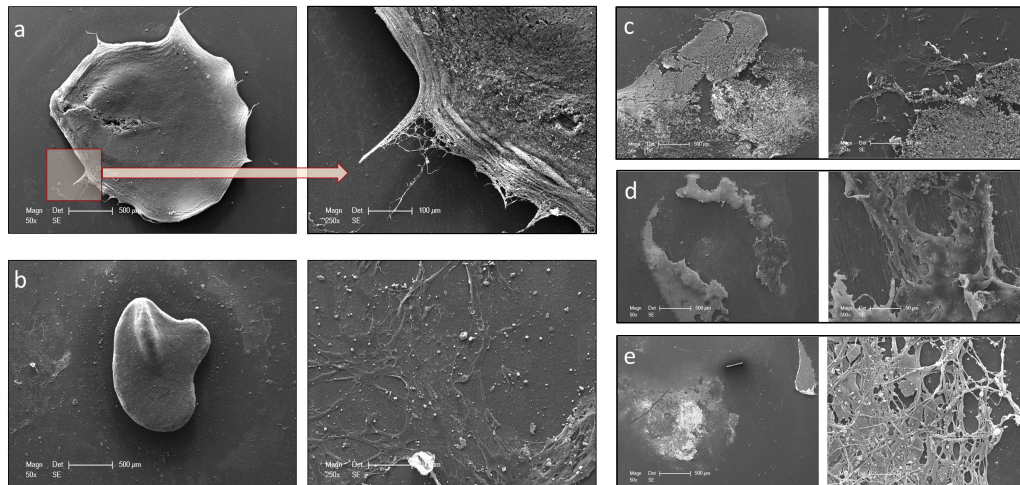


Figure 2.25: SEM pictures (magnification 50x and 250x) showing (a) the brain explant and (b) the liver explant grown on parylene-C and (magnification 50x and 250x or 500x) showing the brain explant grown on the different materials: (c) Thermanox® (d) silk fibroin (e) parylene-C.

The SEM images in Fig.2.25 confirm the good state of health of cells coming from various organs on the different substrates. In conclusion, parylene-C is a highly biocompatible material which induces a very low adhesion of neural cells.

2.7.3 Organotypic culture on PEDOT:PSS

The same kind of test has been carried out on PEDOT. To this end, *ad hoc* samples have been prepared by first evaporating gold on a Thermanox® coverslip to make it conductive. A layer of titanium have been used, as usual, to increase the gold adhesion on the substrate. Then, thanks to the electrochemical Teflon® cell shown in Fig.2.26, that has been made at the mechanical workshop in our laboratory, it was possible to deposit PEDOT:PSS (with a technique that will be described in Chapter 3) over a rounded area of 3 mm (which it will be called "small") and 8 mm ("big") of diameter to fit the organ dimensions.



Figure 2.26: Electrochemical Teflon® cell and resulting Thermanox® coverslip after the PEDOT:PSS polymerization over a 3 mm-diameter area.

Since the area is, in this case, 500 times bigger than usual (if we refer to the microelectrode active areas), the polymerization procedure was significantly longer, compared to the one described in the next chapter, in order to cover the entire area with PEDOT:PSS. Therefore, the morphology could exhibit some difference when compared to the polymerization

on microelectrodes.

Fig.2.27 depicts the migration and adhesion behaviour of the explanted brain on the PEDOT:PSS substrate compared to other Thermanox® and Titanium.

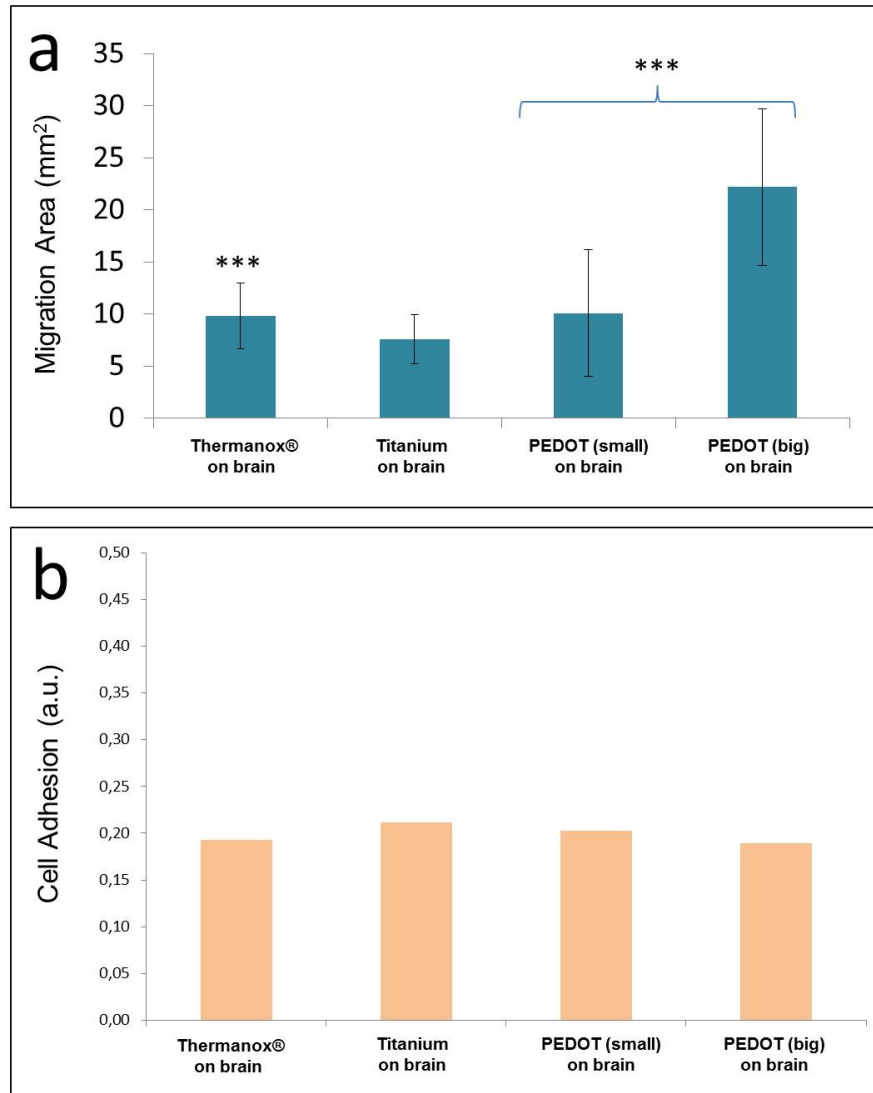


Figure 2.27: Biocompatibility assessment of PEDOT compared to the control Thermanox® and Titanium: (a) Migration area (mm²) of the cell layers. (b) Cell adhesion of the cell layers. ***P < 0.001.

PEDOT:PSS results as a very biocompatible material since, for the big-diameter deposition, the **cell migration is two times bigger when compared to the negative reference Thermanox®**. Statistical Tukey-Kramer analysis showed significant results between Thermanox® and big-diameter PEDOT:PSS and between PEDOT:PSS of big and small diameter.

The cell adhesion has been found particularly low, comparable to the one of Thermanox®. It was not possible to make statistics for the adhesion in this case because of the limiting number of samples.

In Fig.2.28, SEM images of the organs on PEDOT:PSS substrate are shown. Cells appear perfectly healthy and dendrites and axons populated neurons are clearly visible.

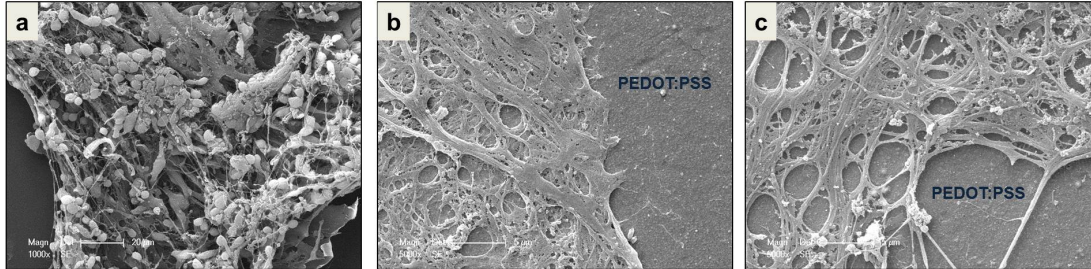


Figure 2.28: SEM pictures (magnification 1000x and 5000x) showing the brain explant (a) on Thermanox®, (b) on PEDOT:PSS big-diameter and (c) on PEDOT:PSS small-diameter. On the background of picture (c) and (d) the typical rough surface of PEDOT:PSS can be noticed.

These organotypic tests allow to go further in the biocompatibility statement of materials since they better reproduces the living complexity. To our knowledge, the organotypic culture on PEDOT:PSS has been performed for the first time, attesting the very high biocompatibility (with low cell adhesion) of PEDOT:PSS layer produced by electrochemical polymerization route in aqueous media (as it will be explained in details in the next chapter).

2.8 Conclusion

In this chapter, the fabrication process of microelectrodes on flexible substrate have been illustrated. The flexibility of the substrate is intended to provide a device which could better fit with the brain tissue and the brain movement once implanted, when compared to the classical Silicon-based implantable electrodes. As have been explained in the *General Introduction*, this should decrease the body immune response due to the mechanical mismatch between the probe and the living tissue. Another factor of remarkable importance to prevent the immune cell reaction and promote the long-term reliability of the device is the **biocompatibility of the materials and the processes**. To this end, in this work a special attention has been paid to the choice of the materials and cytotoxicity/biocompatibility test have been performed and illustrated in the latter part of the chapter.

Two materials have been chosen as a soft substrate for the fabrication: **polyimide and parylene-C**.

The first, thanks of its good mechanical properties, stability in wet microfabrication processes, ease of deposition and good indications on biocompatibility has been a convenient candidate for the production of prototype electrodes. The first devices produced on polyimide presented a rectangular shape, not suitable for the implantation. Each device was composed by 6 round-shaped sites of different diameters which constituted the active

electrode areas. These devices have been used for the optimization of the electrochemical parameters during the polymer (PEDOT) electrodeposition that will be treated in the following chapter.

The proposed technological process on polyimide is simple, suitable to achieve resolutions up to 6.5 μm in diameter and presents an originality: the low adhesion between the polyimide and the SiO_2 layer allow to bypass the use of a sacrificial layer. The adhesion between the spin coated polyimide and the silicon support is assured by an overcoating on the edge. In this way, the flexible substrate is hosted on a Si wafer along all the process and can be easily peel off at the end by simply scratching the edges of the wafer.

The fabrication process on parylene have exploited the same techniques. A silicon host support has been used for all the process. Particularly important, in this case, has been the optimization of the parylene etching parameters for both the active sites contacts opening and the structure cutting.

One of the main problems to face in the case of flexible implantable devices is how to achieve the necessary stiffness to accomplish the insertion into the brain tissue. Even though this issue is being studied in depth in the context of another PhD project, it was partially addresses along this work in order to perform the *in vivo* measures that will be illustrated in Chapter 4. Here, the temporary stiffening strategy based on the use of biodegradable silk fibroin has been briefly described.

Parylene-C, classified as a United States Pharmacopeia (USP) Class VI material, represents nowadays the one of the most promising candidate for implantable devices with long-life expectancy. Despite the very high biocompatibility of parylene-C, the produced devices are subjected to a series of chemical and physical processes that could modify the surface features. For this motivation, **cell viability tests** on cultured neuroblastoma cells have been performed after the fabrication process. The results showed a very good viability of the cells on the substrate, indicating a non-cytotoxicity. Moreover the chemical fixation of the cultured cells on the devices has allowed the **direct SEM observation of the cells state of health and of the cells attachment** on the electrodes.

To go further in the biocompatibility statement, in collaboration with the Université de Technologie de Compiègne, organotypic culture test have been carried out, one by one, on the materials in direct contact with the brain tissue (parylene-C, silk fibroin and PEDOT), showing the cells behaviour in terms of adhesion and migration. Again, the SEM observation confirmed the very good biocompatibility of the used materials.

Bibliography

- [1] Karen C Cheung. Implantable microscale neural interfaces. *Biomedical Microdevices*, 9(6):923–938, 2007.
- [2] John P Seymour and Daryl R Kipke. Fabrication of polymer neural probes with sub-cellular features for reduced tissue encapsulation. In *Engineering in Medicine and Biology Society (EMBS), 28th Annual International Conference of the IEEE*, pages 4606–4609, 2006.
- [3] S-H Cho, H M Lu, L Cauller, M I Romero-Ortega, J-B Lee, and G A Hughes. Biocompatible SU-8-based microprobes for recording neural spike signals from regenerated peripheral nerve fibers. *IEEE Sensors Journal*, 8(11):1830–1836, 2008.
- [4] M Marelli, G Divitini, C Collini, L Ravagnan, G Corbelli, C Ghisleri, A Gianfelice, C Lenardi, P Milani, and L Lorenzelli. Flexible and biocompatible microelectrode arrays fabricated by supersonic cluster beam deposition on SU-8. *Journal of Micromechanics and Microengineering*, 21(4):045013, 2011.
- [5] B J Kim, J T W Kuo, S A Hara, C D Lee, L Yu, C A Gutierrez, T Q Hoang, V Pikov, and E Meng. 3D Parylene sheath neural probe for chronic recordings. *Journal of Neural Engineering*, 10(4):045002, 2013.
- [6] Y Sun, SP Lacour, RA Brooks, N Rushton, J Fawcett, and RE Cameron. Assessment of the biocompatibility of photosensitive polyimide for implantable medical device use. *Journal of Biomedical Materials Research Part A*, 90(3):648–655, 2009.
- [7] Helena Gleskova and Sigurd Wagner. Amorphous silicon thin-film transistors on compliant polyimide foil substrates. *IEEE Electron Device Letters*, 20(9):473–475, 1999.
- [8] Sami Myllymaa, Katja Myllymaa, Hannu Korhonen, Juha Töyräs, Juha E Jääskeläinen, Kaj Djupsund, Heikki Tanila, and Reijo Lappalainen. Fabrication and testing of polyimide-based microelectrode arrays for cortical mapping of evoked potentials. *Biosensors and Bioelectronics*, 24(10):3067–3072, 2009.
- [9] Jaime R Ojeda and David C Martin. High-resolution microscopy of PMDA-ODA polyimide single crystals. *Macromolecules*, 26(24):6557–6565, 1993.
- [10] Karen C Cheung, Philippe Renaud, Heikki Tanila, and Kaj Djupsund. Flexible polyimide microelectrode array for in vivo recordings and current source density analysis. *Biosensors and Bioelectronics*, 22(8):1783–1790, 2007.
- [11] Stéphanie P Lacour, Raghied Atta, James J FitzGerald, Mark Blamire, Edward Tarte, and James Fawcett. Polyimide micro-channel arrays for peripheral nerve regenerative implants. *Sensors and Actuators A: Physical*, 147(2):456–463, 2008.

- [12] H Anderson, M Khojasteh, T McAndrew, and Krishna G Sachdev. Polyimide-substrate bonding studies using γ -aps coupling agent. *IEEE Transactions on Components, Hybrids, and Manufacturing Technology*, 9(4):364–369, 1986.
- [13] Steven P Kowalczyk and Jean L Jordan-Sweet. Formation of polyimide/substrate interfaces: investigation of interfacial chemistry of polyamic acid with surfaces of silicon, copper, and chromium. *Chemistry of Materials*, 1(6):592–596, 1989.
- [14] Dyi-Chung Hu and Hsi-Chieh Chen. Humidity effect on polyimide film adhesion. *Journal of Materials Science*, 27(19):5262–5268, 1992.
- [15] Damien C Rodger, Andy J Fong, Wen Li, Hossein Ameri, Ashish K Ahuja, Christian Gutierrez, Igor Lavrov, Hui Zhong, Parvathy R Menon, Ellis Meng, et al. Flexible parylene-based multielectrode array technology for high-density neural stimulation and recording. *Sensors and Actuators B: chemical*, 132(2):449–460, 2008.
- [16] William F Gorham. A new, general synthetic method for the preparation of linear poly-p-xylylenes. *Journal of Polymer Science Part A-1: Polymer Chemistry*, 4(12):3027–3039, 1966.
- [17] John P Seymour, Nick B Langhals, David J Anderson, and Daryl R Kipke. Novel multi-sided, microelectrode arrays for implantable neural applications. *Biomedical Microdevices*, 13(3):441–451, 2011.
- [18] Gerald E Loeb, MJ Bak, M Saleman, and EM Schmidt. Parylene as a chronically stable, reproducible microelectrode insulator. *IEEE Transactions on Biomedical Engineering*, (2):121–128, 1977.
- [19] Sohee Kim, R Bhandari, M Klein, S Negi, L Rieth, P Tathireddy, M Toepper, H Oppermann, and F Solzbacher. Integrated wireless neural interface based on the utah electrode array. *Biomedical Microdevices*, 11(2):453–466, 2009.
- [20] Shoji Takeuchi, Dominique Ziegler, Yumi Yoshida, Kunihiro Mabuchi, and Takafumi Suzuki. Parylene flexible neural probes integrated with microfluidic channels. *Lab on a Chip*, 5(5):519–523, 2005.
- [21] W Li, DC Rodger, JD Weiland, MS Humayun, and YC Tai. Integrated flexible ocular coil for power and data transfer in retinal prostheses. In *Engineering in Medicine and Biology Society (EMBS), 27th Annual International Conference of the IEEE*, pages 1028–1031, 2006.
- [22] Damien C Rodger and Yu-Chong Tai. Microelectronic packaging for retinal prostheses. *IEEE Engineering in Medicine and Biology Magazine*, 24(5):52–57, 2005.
- [23] Andrew J Spence, Keith B Neeves, Devon Murphy, Simon Sponberg, Bruce R Land, Ronald R Hoy, and Michael S Isaacson. Flexible multielectrodes can resolve multiple muscles in an insect appendage. *Journal of Neuroscience Methods*, 159(1):116–124, 2007.
- [24] J B Fortin and T Lu. A Model for the Chemical Vapor Deposition of Poly (para-xylylene) (Parylene) Thin Films. *Chemistry of materials*, 1:1945–1949, 2002.
- [25] Lianggong Wen, Kristof Wouters, Frederik Ceyskens, An Witvrouw, and R Puers. A Parylene temporary packaging technique for MEMS wafer handling. *Sensors and Actuators A: Physical*, 186:289–297, 2012.

-
- [26] Ellis Meng, Po-Ying Li, and Yu-Chong Tai. Plasma removal of Parylene-C. *Journal of Micromechanics and Microengineering*, 18(4):045004, 2008.
- [27] S Selvarasah, SH Chao, C-L Chen, S Sridhar, A Busnaina, A Khademhosseini, and MR Dokmeci. A reusable high aspect ratio Parylene-C shadow mask technology for diverse micropatterning applications. *Sensors and Actuators A: Physical*, 145:306–315, 2008.
- [28] Banani Kundu, Rangam Rajkhowa, Subhas C Kundu, and Xungai Wang. Silk fibroin biomaterials for tissue regenerations. *Advanced Drug Delivery Reviews*, 65(4):457–470, 2013.
- [29] Nianzhen Li, Anna Tourovskaia, and Albert Folch. Biology on a chip: microfabrication for studying the behavior of cultured cells. *Critical Reviews in Biomedical Engineering*, 31(5&6), 2003.
- [30] Kaili Chen, Yuji Umeda, and Kiyoshi Hirabayashi. Enzymatic hydrolysis of silk fibroin. *The Journal of Sericultural Science of Japan*, 65(2):131–133, 1996.
- [31] Danielle N Rockwood, Rucsanda C Preda, Tuna Yücel, Xiaoqin Wang, Michael L Lovett, and David L Kaplan. Materials fabrication from bombyx mori silk fibroin. *Nature Protocols*, 6(10):1612–1631, 2011.
- [32] Patrick Schiavone, Fabrice Chassat, Thomas Boudou, Emmanuel Promayon, F Valdivia, and Yohan Payan. *In vivo* measurement of human brain elasticity using a light aspiration device. *Medical Image Analysis*, 13(4):673–678, 2009.
- [33] Andrew A Sharp, Alicia M Ortega, Diego Restrepo, Douglas Curran-Everett, and Ken Gall. In vivo penetration mechanics and mechanical properties of mouse brain tissue at micrometer scales. *IEEE Transactions on Biomedical Engineering*, 56(1):45–53, 2009.
- [34] Zeike Taylor and Karol Miller. Reassessment of brain elasticity for analysis of biomechanisms of hydrocephalus. *Journal of Biomechanics*, 37(8):1263–1269, 2004.
- [35] Maria Asplund, Elin Thaning, J Lundberg, AC Sandberg-Nordqvist, B Kostyszyn, Olle Inganäs, and Hans von Holst. Toxicity evaluation of PEDOT/biomolecular composites intended for neural communication electrodes. *Biomedical Materials*, 4(4):045009, 2009.
- [36] Sarah M Richardson-Burns, Jeffrey L Hendricks, Brian Foster, Laura K Povlich, Dong-Hwan Kim, and David C Martin. Polymerization of the conducting polymer poly (3, 4-ethylenedioxythiophene)(PEDOT) around living neural cells. *Biomaterials*, 28(8):1539–1552, 2007.
- [37] H Zitter and H Plenck. The electrochemical behavior of metallic implant materials as an indicator of their biocompatibility. *Journal of Biomedical Materials Research*, 21(7):881–896, 1987.
- [38] Elazer R Edelman, Philip Seifert, Adam Groothuis, Alisa Morss, Danielle Bornstein, and Campbell Rogers. Gold-coated NIR stents in porcine coronary arteries. *Circulation*, 103(3):429–434, 2001.

- [39] June L. Biedler, Suzanne Roffler-Tarlov, Melitta Schachner, and Lewis S. Freedman. Multiple neurotransmitter synthesis by human neuroblastoma cell lines and clones. *Cancer Research*, 38(11 Part 1):3751–3757, 1978.
- [40] June L. Biedler, Lawrence Helson, and Barbara A. Spengler. Morphology and growth, tumorigenicity, and cytogenetics of human neuroblastoma cells in continuous culture. *Cancer Research*, 33(11):2643–2652, 1973.
- [41] Hong-Seok Noha, Yong Huangb, and Peter J Hesketha. Parylene micromolding, a rapid and low-cost fabrication method for parylene microchannel. *Sensors and Actuators B: Chemical*, 102(1):78–85, 2004.
- [42] Chantal E Holy, Chantelle Cheng, John E Davies, and Molly S Shoichet. Optimizing the sterilization of PLGA scaffolds for use in tissue engineering. *Biomaterials*, 22(1):25–31, 2000.
- [43] E Wolff and K Hafen. Organotypic culture to assess cell adhesion, growth and alignment of different organs on silk fibroin. *Journal of Experimental Zoology*, 119:381, 1952.
- [44] C Brunot-Gohin, J-L Duval, E-E Azogui, R Jannetta, I Pezron, D Laurent-Maquin, SC Gangloff, and C Egles. Soft tissue adhesion of polished *versus* glazed lithium disilicate ceramic for dental applications. *Dental Materials*, 29(9):e205–e212, 2013.
- [45] Clémence Demangel, Delphine Auzène, Muriel Vayssade, Jean-Luc Duval, Pascale Vigneron, Marie-Danièle Nagel, and Jean-Claude Puipe. Cytocompatibility of titanium metal injection molding with various anodic oxidation post-treatments. *Materials Science and Engineering: C*, 32(7):1919–1925, 2012.
- [46] JL Duval, M Letort, and MF Sigot-Luizard. Comparative assessment of cell/substratum static adhesion using an *in vitro* organ culture method and computerized analysis system. *Biomaterials*, 9(2):155–161, 1988.
- [47] Hervé Petite, Jean-Luc Duval, Valérie Frei, Nabil Abdul-Malak, Marie-Françoise Sigot-Luizard, and Daniel Herbage. Cytocompatibility of calf pericardium treated by glutaraldehyde and by the acyl azide methods in an organotypic culture model. *Biomaterials*, 16(13):1003–1008, 1995.
- [48] MF Sigot-Luizard, M Lanfranchi, JL Duval, S Benslimane, M Sigot, RG Guidoin, and MW King. The cytocompatibility of compound polyester-protein surfaces using an *in vitro* technique. *In vitro cellular & developmental biology*, 22(5):234–240, 1986.
- [49] J Duval, M Letort, and M Sigot-Luizard. Fundamental study of cell migration and adhesion toward different biomaterials with organotypic culture method. *Advances in Biomaterials*, 9:93–98, 1990.
- [50] J I Rosales-Leal, M A Rodríguez-Valverde, G Mazzaglia, P J Ramon-Torregrosa, L Diaz-Rodriguez, O Garcia-Martinez, M Vallecillo-Capilla, C Ruiz, and M A Cabrerizo-Vilchez. Effect of roughness, wettability and morphology of engineered titanium surfaces on osteoblast-like cell adhesion. *Colloids and surfaces A: Physicochemical and Engineering Aspects*, 365(1):222–229, 2010.
- [51] Håkan Nygren, Simon Alaeddin, Ingemar Lundström, and Karl-Erik Magnusson. Effect of surface wettability on protein adsorption and lateral diffusion. analysis of data and a statistical model. *Biophysical chemistry*, 49(3):263–272, 1994.

- [52] Christine Müller, Anne Lüders, Wiebke Hoth-Hannig, Matthias Hannig, and Christiane Ziegler. Initial bioadhesion on dental materials as a function of contact time, pH, surface wettability, and isoelectric point. *Langmuir*, 26(6):4136–4141, 2009.
- [53] Yusuke Arima and Hiroo Iwata. Effect of wettability and surface functional groups on protein adsorption and cell adhesion using well-defined mixed self-assembled monolayers. *Biomaterials*, 28(20):3074–3082, 2007.
- [54] Daisuke Yamashita, Miho Machigashira, Motoharu Miyamoto, Hironobu Takeuchi, Kazuyuki Noguchi, Yuichi Izumi, and Seiji Ban. Effect of surface roughness on initial responses of osteoblast-like cells on two types of zirconia. *Dental Materials journal*, 28(4):461–470, 2009.
- [55] Gombo Bolortuya, Arata Ebihara, Shizuko Ichinose, Satoshi Watanabe, Tomoo Anjo, Chizuko Kokuzawa, Hidetoshi Saegusa, Nobuyuki Kawashima, and Hideaki Suda. Effects of dentin surface modifications treated with Er: YAG and Nd: YAG laser irradiation on fibroblast cell adhesion. *Photomedicine and Laser Surgery*, 30(2):63–70, 2012.
- [56] Jean-Luc Duval, Tony Dinis, Guillaume Vidal, Pascale Vigneron, David L Kaplan, and Christophe Egles. Organotypic culture to assess cell adhesion, growth and alignment of different organs on silk fibroin. *Journal of Tissue Engineering and Regenerative Medicine*, 2014.

How can we enhance the signal-to-noise ratio of implantable microelectrodes?

Nanostructuring of microelectrode active sites

3

3.1 Introduction

In this chapter we will discuss the use of electroactive conductive polymers as bioelectronic materials for electrode-tissue interfaces. In particular, the microelectrode surface modification with PEDOT:PSS through electrochemical routes, will be illustrated. The obtained polymer morphologies and the electrical performances will be also shown, through a comparison of macro and micro properties.

3.1.1 Conductive polymers for biointerfaces

The use of polymers provides a lot of advantages over other materials because a wide range of chemical structures and tunable surface functionalities is exploitable. **Among synthetic polymers, electroactive conducting polymers (CPs) have received considerable attention since the initial discovery of polyacetylene in the late 1970s[1].**

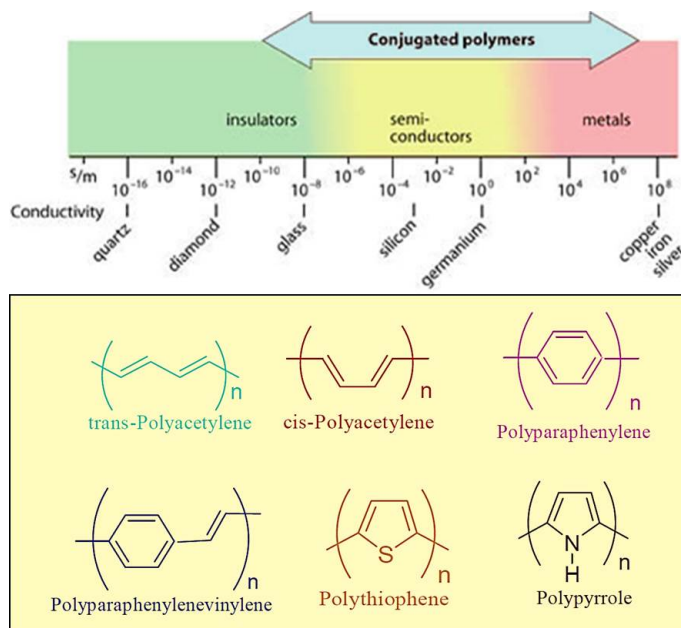


Figure 3.1: Conductivity of conductive conjugated polymers compared to metals, semiconductors and insulators (above) and some examples of conductive polymers chemical structures (below).

The conductivity of CPs, that lies between inorganic materials and metals, comes from their structure of alternate single and double bond conjugation (see Fig.3.1) and one of their most important properties is the possibility to modify the conductivity by the doping state. Usually, such doping states can be adjusted reversibly by chemical or electrochemical methods. In the doped state, electrons can move easily along the π -conjugated backbones of the CPs. When the CPs are immersed in solvents with electrolytes, ions diffuse in and

out of them during the doping/dedoping process to neutralize the net charge because of a change in oxidation status, as we can see Fig.3.2. This feature makes CPs conductive to both electrons and ions, in particular they can act as transducers, directly converting electrical signals, generally used in electronics, to ionic signals, mostly found in biology[2].

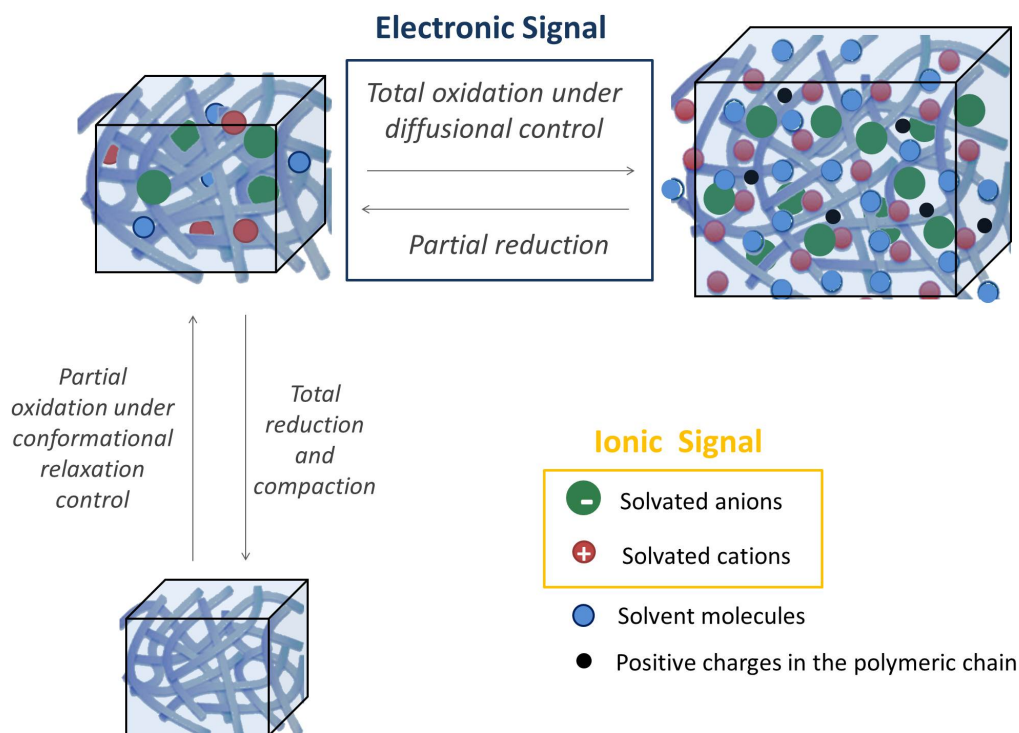


Figure 3.2: Schematic representation of the reversible variation of volume associated with the electrochemical-switching conducting polymers. Changes in free volume are mainly due to two effects: electrostatic repulsions between fixed positive charges and exchange of cations, anions, and solvent molecules between the polymer and the solution.

Moreover, reverse electrochemical reactions promote swelling and shrinking processes. Changes of volume are linked to the continuous shift of the polymeric composition. The packed molecular structure of a neutral polymer due to strong polymer-polymer Van der Waals interactions changes during oxidation. Electrons are extracted from the chains and as a consequence of the double bonds redistribution to locate the positive charges, conformational movements are induced generating the required free volume to balance counterions coming from the solution. Solvent molecules also penetrate from the solution. Conformational movements mean energetic changes on the polymeric chains. When a film of polymer is oxidized by an anodic polarization, electrons are extracted from the polymeric chains, giving rise to conformational movements. Free volume is generated, and counterions and solvent penetrate by diffusion control from the solution and the polymer swells. If the oxidized polymer is reduced by a potential sweep, opposite processes take place and the polymer shrinks. Meanwhile, counterions move toward the solution by diffusion control (Fig.3.2).

Thanks to the swelling and shrinking due to the doping/dedoping process (Fig.3.2),

CPs are also suitable to be used as substrate for controlled drug delivery platforms[3]. The drugs, physically trapped into CPs, can be released when a sequence of electrical potentials is applied. The control of CPs oxidation states allow the (counter)ions to diffuse in and out from CPs making CPs also good candidates for artificial muscles[4, 5].

3.1.2 Synthesis of conductive polymers

Conductive polymers can be manufactured using a variety of methods that are either chemical or electrochemical in nature[6]. Chemical polymerisation proceeds via many different routes, such as addition reactions stimulated by radicals, cations or anions, or condensation reactions[7]. Chemical polymerization, desirable for mass production, occurs in presence of oxidizing agents such as FeCl_3 or $\text{Fe}(\text{OTs})_3$ through condensation reactions carry out with the help of strongly reductors metal catalysts[8]. These polymers can be tailored to include a great variety of modifications, including covalent attachments to the backbone. Nevertheless the processing time is significantly longer than electrochemical polymerization and entails the use of non-biocompatible oxidants. Moreover, the electrical properties of the resulting film are very poor if compared to the polymer obtained from the electrochemical method and they often require post-fabrication doping to increase conductivity.

In electrodeposition the dopant is added to the monomer solution, the polymer is synthesised and no further processing is required. The simplicity and reproducibility of this technique make it the most commonly used fabrication process since the electrodeposition of the first conductive polymer in 1968.

3.1.2.1 Electrochemical polymerization

Electrochemical deposition is a superior technique for neuroprosthetic applications because CPs films can be formed in a simple one-step process with a high degree of control over the film thickness, surface properties, and electrical conductivity. It is useful particularly when well-defined thin films are deposited on a surface of metallic substrate and no further improvement process, such as doping, is required. Cui *et al.*[9] established that electrochemical polymerization can be used to deposit coatings of electroactive conducting polymers directly onto metal neural electrode sites for obtaining a lower impedance.

In this method, the monomer is electrochemically oxidized in the presence of an electrolyte solution. Polymerization occurs at the electrode surface with deposition of the polymer film onto the electrode.

In 1979 Diaz showed that polypyrrole films synthesized by electrochemistry presented a good homogeneity and a high conductivity and, thereafter, the technique was applied to a large number of aromatic compounds[10]. In a classical electrochemical cell, the synthesis of conductive polymers can be realized in three main ways, as we can see in Fig.3.3:

1) **potentiodynamic mode (PD)**: a scan of potentials is applied at a certain rate, reaching the oxidation potential of the monomer.

2) **potentiostatic mode (PS)**: the electrode potential is maintained at the oxidation potential of the monomer.

3) **galvanostatic mode (GS)**: the current is maintained constant.

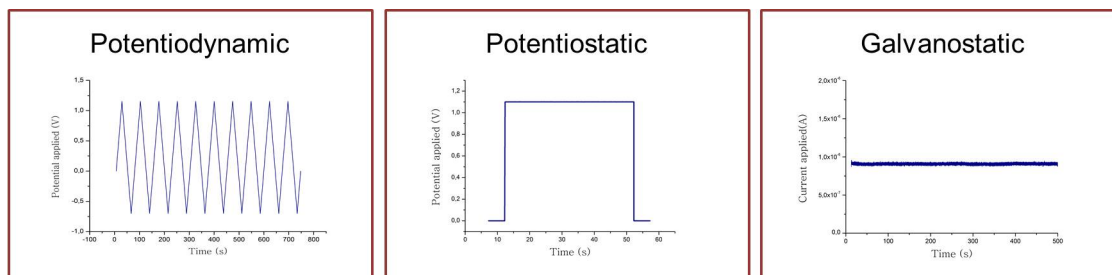


Figure 3.3: The three electropolymerization routes.

Henceforward in the manuscript the three polymerization routes will be treated by referring to the acronyms PD, PS and GS.

As can be seen in Fig 3.4, the electropolymerization mechanism started with a step of production of a radical cation, through the oxidation of the monomer, then two radicals react in order to form a dimer[10]. After deprotonation, the dimer will be oxidised as well, and the reaction propagates thanks to the coupling between the dimers cations and the radical cations; this is possible because the oxidation potential for a monomer is higher than the oxidation potential for an oligomer[11]. The resulting insoluble polymer adheres to the electrode surface by precipitation onto the electrode surface but this mechanism is still under investigation. The electrochemical synthesis can occur both in organic and aqueous environment, depending of the monomer solubility and potential window. Nevertheless, since radical cations present a very electrophilic behaviour, the reaction relies on the nucleophilic properties of the solvent.

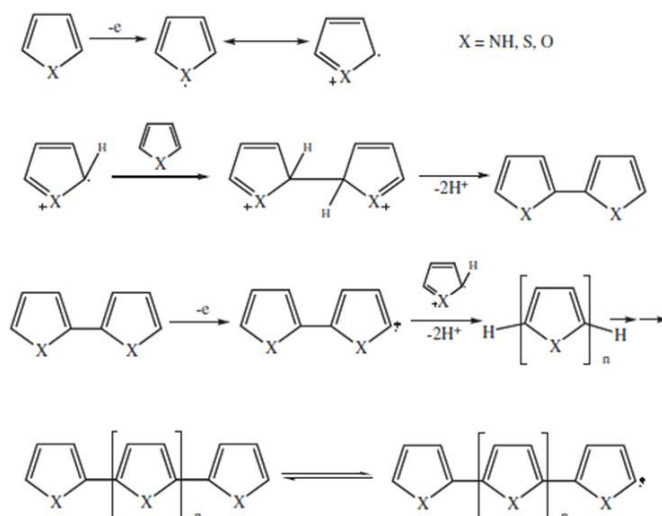


Figure 3.4: Mechanism for heterocycle polymerization via electrochemical synthesis[7].

3.2 Electrochemical polymerization of PEDOT

Poly(3,4-ethylenedioxythiophene), commonly called PEDOT (chemical structure in Fig.3.5), has been the subject of much interest among π -conjugated polymers because of its well-known properties such as high-conductivity, biocompatibility, excellent stability and transparency in its doped state.

The most commonly used counterion for PEDOT electropolymerization is Polystyrene sulfonate (PSS). Yamato *et al.*[12] reported that PEDOT:PSS was more chemically stable than PPy:PSS (Polypyrrole). Similarly, Cui and Martin[13] stated that PPy is easily reduced by biologically relevant reducing agents because of its higher reduction potential (0.1 V) compared to the one of PEDOT (-0.4 V).

PEDOT indeed exhibits improved conductivity and thermal stability because the dioxylethylene bridging groups across the 3 and 4 positions of the EDOT monomer block the possibility of coupling.

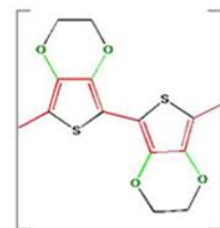


Figure 3.5: Chemical structure of PEDOT.

3.2.1 State-of-the-art

In 2003 Cui and Martin[13] proposed the electrochemical polymerization of EDOT for neural electrodes, directly onto the surface of the electrode sites, under either galvanostatic (0.5-2 mA/cm²) and potentiostatic (1.1 V) conditions (Fig.3.6).

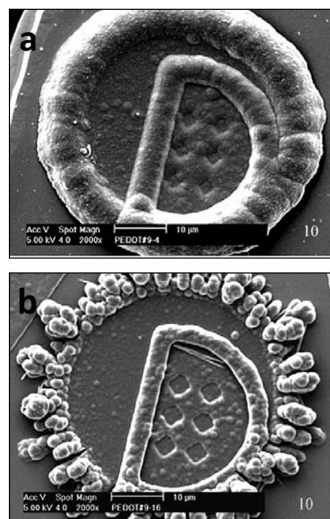


Figure 3.6: Electrochemical PEDOT deposition through a) galvanostatic and b) potentiostatic conditions[13].

PEDOT covered microelectrode were used by Ludwig *et al.*[14] for chronic local field potential (LFP) recording in rat brain, showing that the coating is suitable for obtaining high-quality neural recordings out to six weeks. The galvanostatic deposition, with a charge of 260 mC/cm² have been used in a surfactant-templated ordered synthesis (by adding 20 wt% surfactant poly(oxyethylene)10-oleyl ether to the initial monomer solution).

Again in 2007 Cui and Zhou[15] reported the electrodeposition of PEDOT on 100 μm diameter platinum electrodes. After two weeks of pulse current stimulation of the electrode in PBS, minor cracks and delaminations were observed on the PEDOT layer. With these results, the authors highlighted the need for optimizing the thickness of the deposition, as an essential parameter for the layer stability.

Wilks *et al.*[16] in 2009 reported again the galvanostatic deposition of PEDOT:PSS by applying 6 nA for 900 s. All these polymerizations were

performed on micromachined silicon Michigan arrays with Iridium active sites (discussed in Chapter 1).

PEDOT electropolymerizations are generally performed in organic media[17] because of the many difficulties experienced when the electrosynthesis of polythiophene and its derivatives is carried out in aqueous media. The main problems arise from the low solubility of the thiophene structures in water, from the oxidation potentials higher than that of water itself and from the water-catalyzed formation of thienyl cation radicals which can activate concomitant reactions and inhibit therefore the formation of the main polymer[18]. **Despite all these problems, water still remains the ideal solvent for economic, environmental and biocompatible reasons.**

In 2000 Bobacka *et al.*[19] studied the effect of various supporting electrolyte (NaPSS, KCl, NaCl) on the impedance properties of a PEDOT film deposited by galvanostatic electropolymerization on Pt disc electrodes from a deaerated aqueous solution, while Pigani *et al.*[20] in 2004 clarify the mechanism of potentiostatic deposition of PEDOT in water using Lithium perchlorate (LiClO_4) as supporting electrolyte. Again, in 2011 Venkatraman *et al.*[21] reported the galvanostatic deposition of PEDOT:PSS in aqueous environment (deposition charge $86.4 \mu\text{C}$) on neural microwire arrays in PtIr with a diameter varying from 25 to 75 μm , for *in vivo* recording.

In many cases an ordered surfactant-templated synthesis have been used in order to overcome the problem of the solubility in water[22, 23]. Xiao *et al.*[24] used EDOT-MeOH in order to increase the concentration of monomer in aqueous solution by increasing the solubility, exploiting the polarity given by the OH residues. The morphology of electrodeposited PEDOT produced by various electrochemical routes have been investigated in the literature through SEM images[25, 26, 27] but its morphology has not been clearly related to the electrical properties. Various morphologies have been observed for the potentiodynamic route: micro-rings, micro-arrows spongy-like and rod-like structures.

Moreover cracking and delamination have been again shown in the work of Tamburri *et al.*, mostly due to the overoxidation of PEDOT during the cyclic voltammetry with an upper potential reaching 2 V[27].

3.3 Electrochemical polymerization of PEDOT through different electrochemical routes

In this part, **three methods for the electrochemical polymerization of PEDOT will be discussed in terms of morphology and conductivity of the resulting layers.**

The choice of water solvent was dictated by the need of both a good solubility and biocompatibility for future implantable neural electrode. Since the limit of dissolution of EDOT in water was found to be $\sim 0.01 \text{ M}$ at room temperature [24], the polymerization occurs without the use of surfactants even in aqueous environment thanks to the low

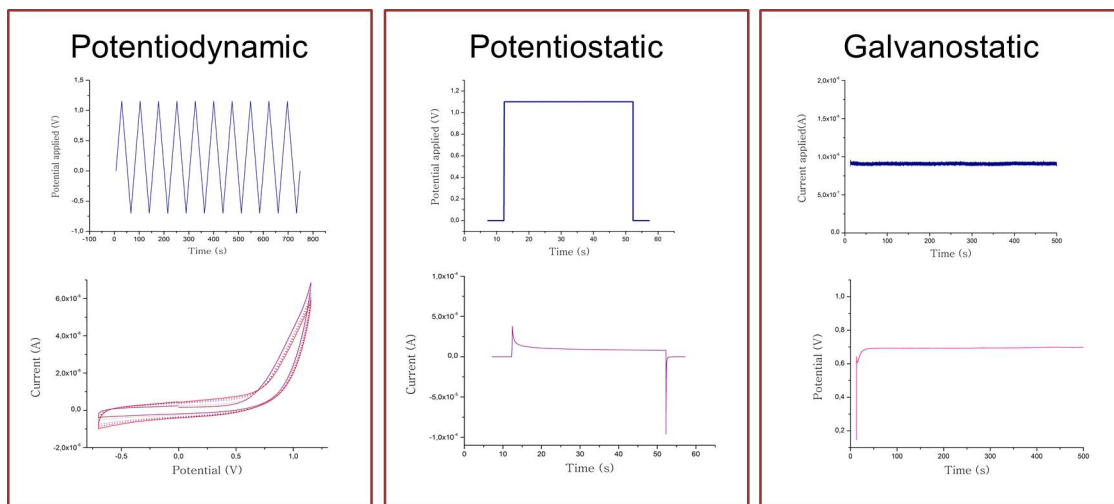


Figure 3.7: Representation of the three routes of polymerization with the corresponding current (or potential) curves.

concentration of EDOT used. The kinetic of dissolution was also found to be very slow and, for this reason, all the solutions have been prepared one day before the being used in order to guarantee the homogeneity. Moreover the use of NaPSS counterions allows to increase the EDOT solubility in water [28].

All the polymerizations were performed in a classical three-electrodes cell, by using a platinum wire as the counter electrode. The applied potentials are referred to the saturated calomel electrode (SCE) that has been chosen as reference electrode. Deaeration was obtained by purging the solution with nitrogen during 20 min previous to each experiment. The adopted parameters for the three routes of polymerization are presented in Table 3.1.

| | PD | PS | GS |
|-----------------|-----------------------|--------------------|------------------------|
| [EDOT] | 0.1% w/v → 0.025% w/v | | |
| [PSS] | 0.8% w/v → 0.2% w/v | | |
| upper potential | +1.2 V | +0.8 V - +1.2 V | — |
| lower potential | -0.9 V, -0.7 V | — | — |
| current density | — | — | 0.3-5 A/m ² |
| time | — | 10 s - 50 s | 10 s - 900 s |
| n° of cycles | 2 - 10 | — | — |
| scan rate | 5 mV/s - 25 mV/s | — | — |

Table 3.1: PEDOT electropolymerization parameters for the three routes.

The parameters for the three routes of polymerization were varied according to the electrode dimensions, in order to obtain a good trade-off between a homogeneous coating of the surface, a thin deposit (that should not extend out of the Au electrode surface) and a short polymerization time. For each polymerization route and active area, the deposition parameters were optimized in order to achieve, after deposition, the lower resulting impedance values over all the explored frequencies. In the case of the potentiodynamic route, the cyclic voltammogram for a 50 μm -diameter electrode is reported in Fig.3.8. It was performed by applying a potential scan from -0.7 V to 1.1 V at a scan rate of 0.01 V/s.

The oxidation of the monomer starts at 0.75 V and the anodic current reaches a peak value at 1.1 V. In the reverse scan the current decreases with a crossover at about 1 V and 0.7 V; this "nucleation loop" reveals the nucleation process of the polymer film. On the following cycles, the oxidation peak is shifted to more cathodic potential values because the produced oligomers are oxidized more easily than the monomer[29]. Moreover, the anodic current increase from cycle to cycle consequently to the growth of a conductive PEDOT film, thus increasing the apparent surface of the active electrode. Starting from the second cycle, at a potential close to -0.3 V the voltammogram shows a quasi-reversible signal corresponding to the redox activity of the polymer which increases with the number of potential cycles, depending on the amount of polymer synthesized on the electrode surface[30].

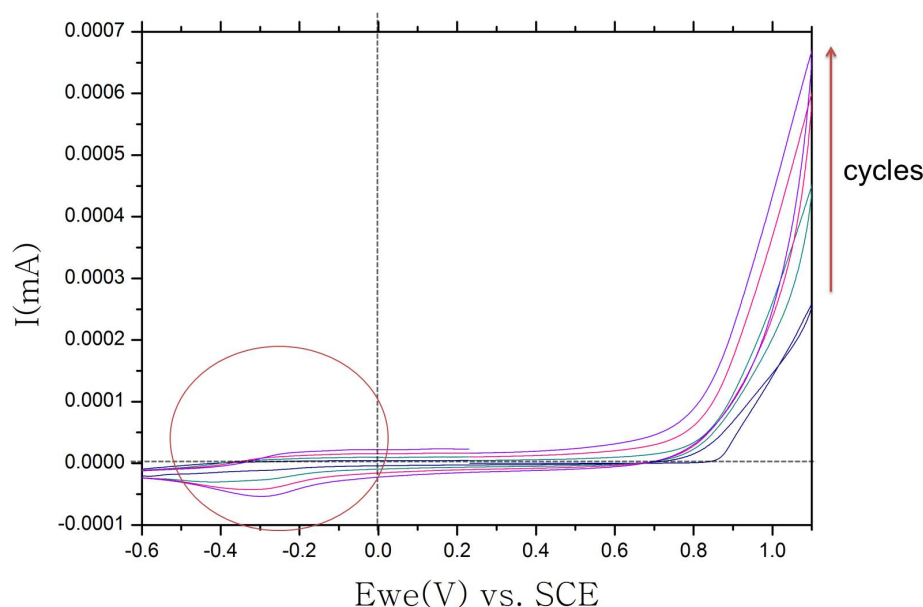


Figure 3.8: Cyclic voltammetry for polymerization for a 50 μm -diameter electrode: 4 cycles from -0.7 V to 1.1 V, scan rate = 10 mV/s.

Even if the electrochemical synthesis of polythiophenes and PEDOT in particular, have been investigated in literature[31, 32, 33, 34], the entire EDOT electropolymerization

mechanism is still under investigation. However, there are some overall mechanisms generally accepted by the scientific community [35, 20]. The primary nucleation process is divided into two periods in classical nucleation theory: one is called induction period and the other is the steady (or stationary) nucleation period.

On the basis of all these observations we can deduce that the following process occurs:

- during the induction time, EDOT monomers diffuse from the solution to the electrode surface (Fig.3.9);

- after the oxidation of the EDOT monomer unities, the coupling with radical cation and the oligomerization process take place (Fig.3.9);

- when an oligomeric saturated area is shaped in front of the electrode surface, oligomer clusters start to precipitate onto the electrode generating the polymer nuclei. During this step the process is controlled by diffusion of the monomers;

- the progressive nucleation is characterized by nuclei which do not grow only on the electrode surface sites formed at the beginning of the process, but also on new sites activated during the course of the electropolymerization. As a consequence nuclei with different dimensions are produced by this growth mechanism (Fig.3.10);

- later, different nuclei combine together forming polymer globules, as we can see from Fig.3.10. In the nucleation stage, the expansion of the polymer chains and the growth of globules on the electrode surface are the significant processes and, as shown in Fig.3.10, after a certain time, globules begin to overlap until a full coverage of the surface with polymer globules is reached.

- As a result of the continuous application of potential or current, PEDOT:PSS films follow instantaneous 2D and 3D growths induced by mass transport and charge transfer processes.

The polymerization morphology and conductivity (as we will see in the next sections) of electrodeposited polythiophenes are affected by a lot of different parameters such as the choice of the substrate[31, 34], the polymerization route[26, 36, 37, 38], the monomer concentration[39], the supporting electrolyte[40] and the solvent (aqueous or organic).

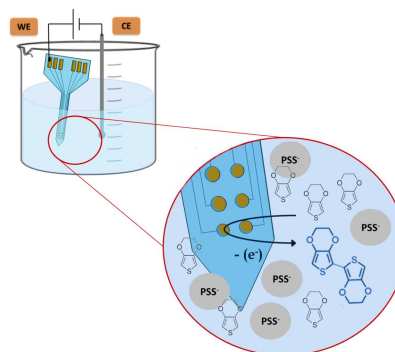


Figure 3.9: Schematic illustration of the first steps of the electrochemical polymerization process.

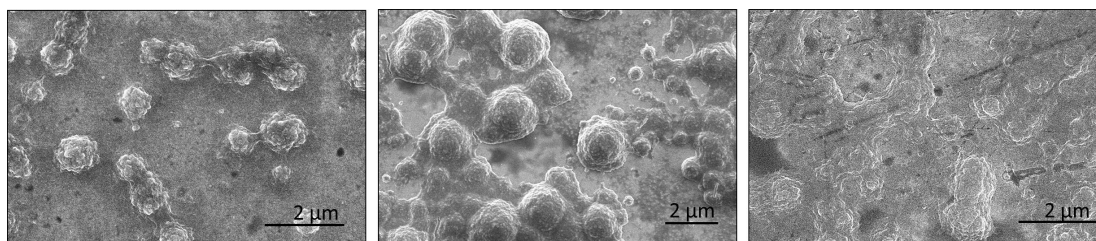


Figure 3.10: Formation of PEDOT nuclei, overlapping and full covering of the surface during the polymerization progress.

3.3.1 Microelectrode cleaning procedure

Before proceeding to the electropolymerization, the Au electrode areas were cleaned and activated by cycling them into a 0.5 M solution of H_2SO_4 with a potential scan from -0.25 V to 1.5 V at a scan rate of 0.5 V/s. As can be seen in Fig.3.11, after the cleaning procedure, the voltammogram shows the typical oxidation and reduction peaks for a clean Au electrode. The formation of gold oxides starts at around 1 V and they are subsequently reduced during the back scan starting from 1 V. This cleaning procedure after the microfabrication is very important for the PEDOT:PSS deposition as can be seen in Fig.3.17.a, especially when the electrode diameter is only a few μm , to eliminate possible traces and residues on the electrode surface. Moreover, recording the identical voltammogram for the same size of microelectrodes we can validate the quality of the passivation layer.

3.3.2 Electrochemical estimation of the active electrode area

The smallest electrochemically active area dimensions (10 μm in diameter) were also verified through linear sweep voltammetry (LSV) in a solution of $\text{K}_4\text{Fe}(\text{CN})_6$ [10 mM] and KCl [0.1 M] in phosphate buffer saline (PBS) solution, where KCl acts as a supporting electrolyte. When a linear scan of potential is applied, the oxidation of the hexacyanoferrate(II) is induced, as shown in the following equation: $[\text{Fe}(\text{CN})_6]^{4-} \rightarrow [\text{Fe}(\text{CN})_6]^{3-} + e^-$.

With ultramicroelectrode, a steady state is readily obtained, even without stirring. The same LSV was performed in the electrolyte in order to subtract this capacitive component (red line in Fig.3.12) to the measured curve and obtain the faradic component (black line in Fig.3.12). The radius of the electrode is determined using the current intensity limit, that corresponds to the diffusion plateau (see eq. 11 in Appendix B). Considering a value of $6.1 \cdot 10^{-6} \text{ cm}^2/\text{s}$ for the diffusion coefficient (D) of $[\text{Fe}(\text{CN})_6]^{4-}$ [41], and knowing the initial concentration (10 mM), the Faraday constant and the number of exchanged electrons (1 electron for this reaction), it was possible to estimate a value of the radius of $4.5 \pm 1 \mu\text{m}$.

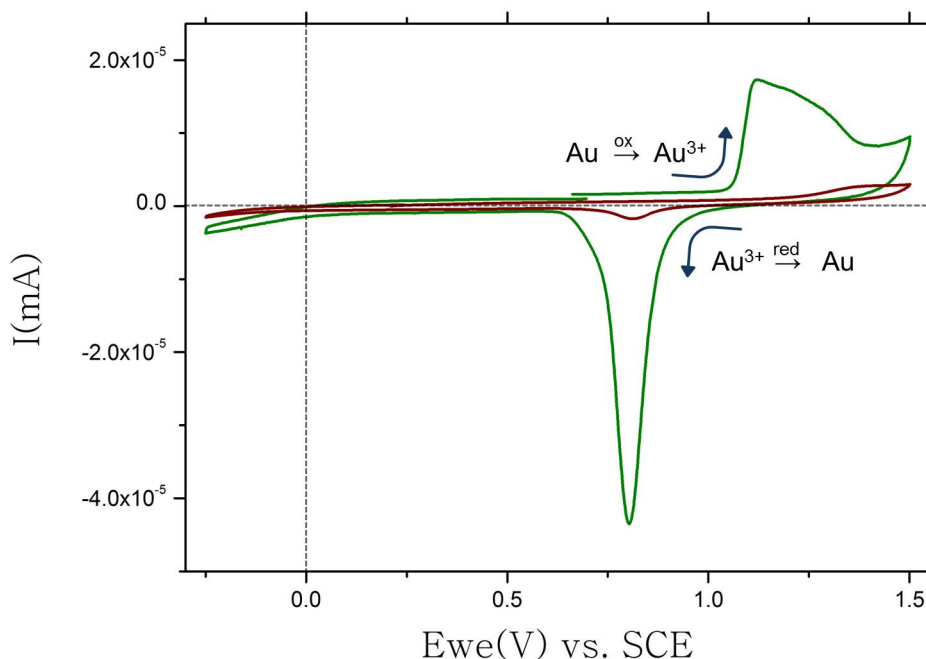


Figure 3.11: Au electrode voltammogram before (red) and after (green) electrode area cleaning by cyclic voltammetry with a potential scan from -0.25 V to 1.5 V, at the scan rate of 0.5 V/s, in H_2SO_4 [0.5 M] solution.

3.4 Morphological characterization of PEDOT:PSS deposition

3.4.1 Effect of the metal surface

The thickness of gold was 200 nm for both polyimide and parylene-based electrodes. **The quality of the gold electrode surface has a noticeable influence on the homogeneity of the PEDOT:PSS deposition**, as can be seen from Fig.3.13 and 3.15. The scratches on the gold surface favour the nucleation of PEDOT and, in general, all the inhomogeneities of the electrode surface, even those due to a high roughness, seem to be a starting point for the polymer nucleation process. This observation is likely to be explained by a local change in the wettability of the gold layer or by a local electrical field confinement.

For the polyimide substrate (PI 2525, HD Microsystem), with a thickness of 13 μm (4 layers of about 3 μm each), the roughness was found to be very low, around 1.3 nm. The scratches on the gold surface are mostly present on the polyimide substrate compared to the parylene substrate because of the deposition technique (spin coating vs CVD). For the parylene substrate of 23 μm -thick, the roughness is around 30 nm, identical to that of the Au layer. The roughness of parylene deposition considerably increases with the thickness

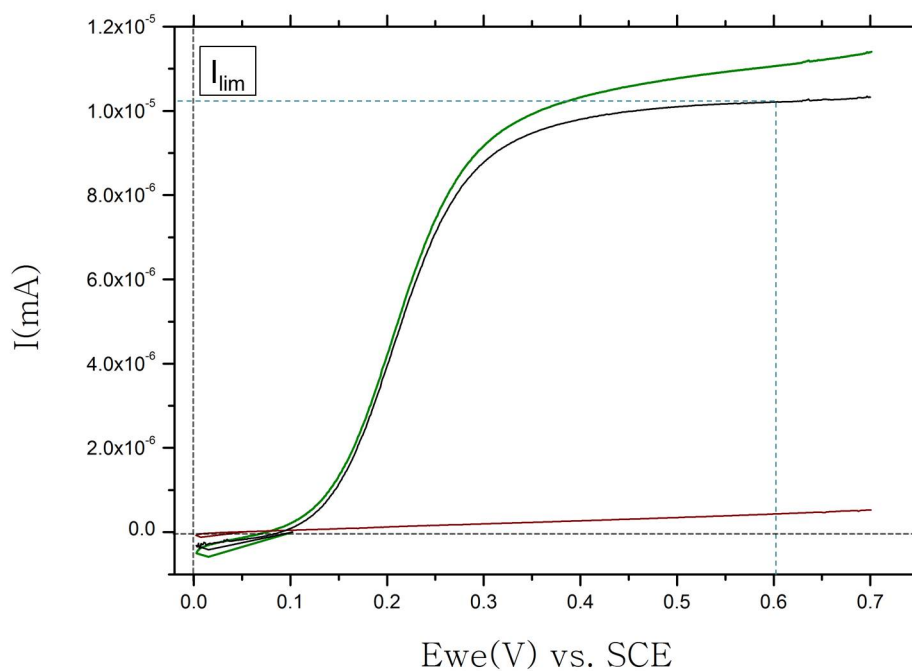


Figure 3.12: LSV from 0 V to 0.7 V, in $\text{K}_4\text{Fe}(\text{CN})_6$ [10 mM] and KCl [0.1 M] in PBS (green curve), in KCl [0.1 M] in PBS (red curve) and subtraction curve (black curve).

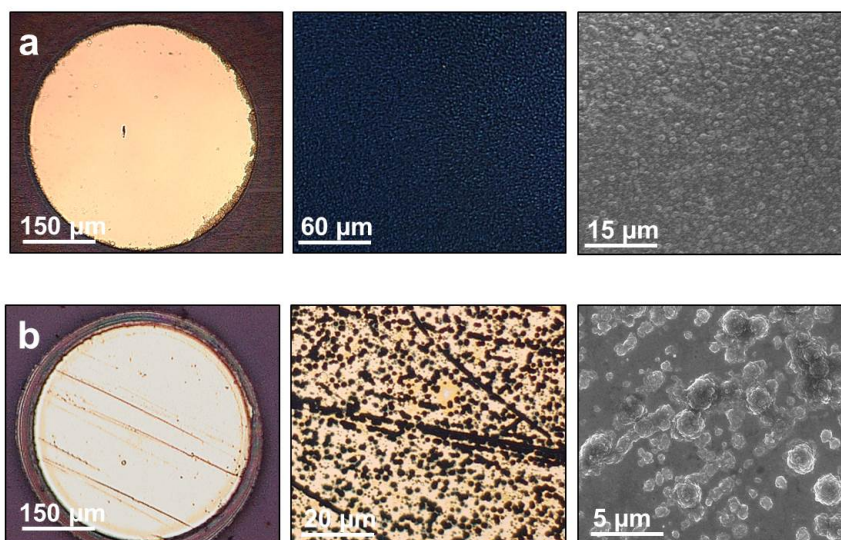


Figure 3.13: Optical Microscope and SEM images of the PEDOT:PSS films formed on a) very smooth and b) scratched gold surface.

or when it undergoes a plasma oxygen treatment.

3.4.2 Effect of the electropolymerization route

In Fig.3.14 the typical cauliflower-like morphology of electrodeposited PEDOT:PSS is shown through scanning electron microscopy (SEM) and atomic force microscopy (AFM) images. In PD conditions, the potential approaches the monomer oxidation region at a slower rate; as a consequence, the concentration of electrogenerated oligomers, thus the rate of their coupling, are lower, leading to a more uniform film deposition (Fig.3.14.a). On the contrary, PS and GS methods induce very similar films made of bigger aggregates islands and nude area. In SEM images we notice that these cauliflower-like structures are slightly brighter than the areas between grains: they correspond to the PEDOT-rich regions and they can be varied in size with the electrochemical synthesis mode. The tapping mode AFM images were obtained on at least 5 different areas of the electrodeposited layers. For the same experiments, all the morphologies obtained by the AFM are similar and only one for each polymerization route is presented in Fig.3.14. Furthermore, the determined RMS roughness of PEDOT:PSS is about 150 nm, 250 nm and 300 nm for a layer obtained by PD, PS and GS mode respectively. In conclusion, these data revealed an important influence of the electrochemical route on the deposition morphology: the PD mode leads to the most homogeneous and smooth deposition, which should promote charge hopping between grains and increase the conductivity (as it will be described in Section 3.5).

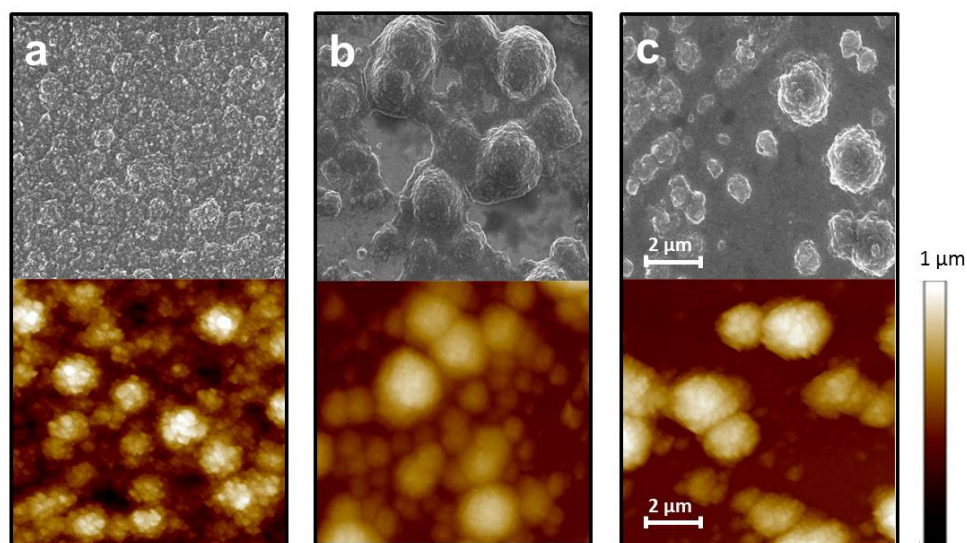


Figure 3.14: SEM and AFM images of the PEDOT:PSS films formed under (a) PD, (b) PS and (c) GS conditions.

3.4.3 Effect of the deposition time and oxidation potential in PS mode

Fig.3.15 shows optical microscope, SEM images and AFM topography of the PEDOT:PSS films formed under PS condition at different polymerization times.

The number of PEDOT:PSS nuclei on the gold surface as well as the grain size can be increased by tuning the polymerization time. With an increase in the polymerization time,

a second layer of much bigger polymer globules is formed as shown in the AFM image in Fig.3.15c.

A similar behaviour can be shown by tuning the oxidation potential from 0.9 V to 1.2 V. Higher oxidation potentials can lead to the overoxidation of the formed polymer[42]. The higher is the applied potential, the more serious is the overoxidation of PEDOT that leads to a decreased conductivity.

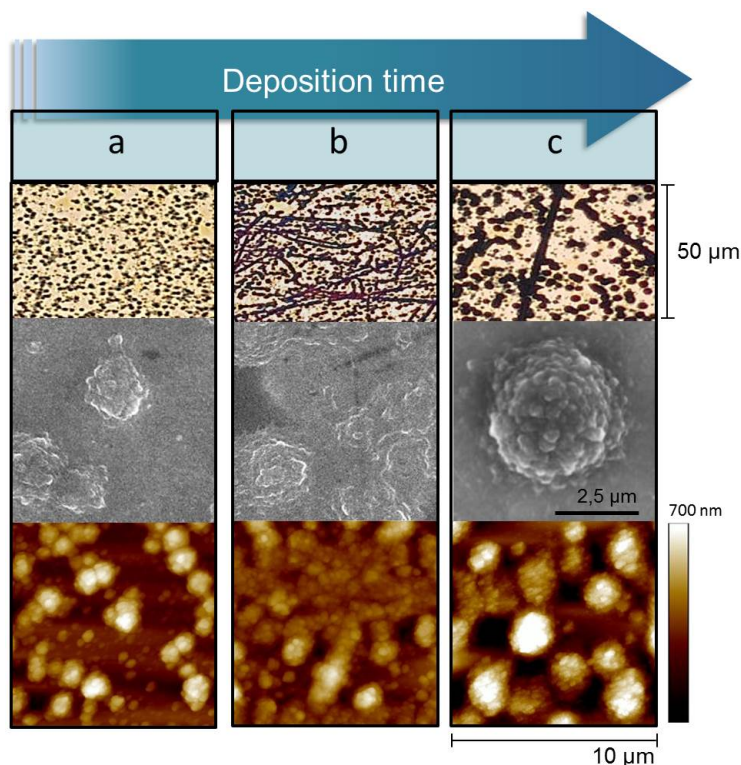


Figure 3.15: Optical Microscope, SEM and tapping mode AFM images of the PEDOT:PSS films formed under PS mode at 0.90 V for (a) 5 s, (b) 10 s, (c) 50 s (the scales are the same for the three images).

3.4.4 Effect of the surface area

In the case of an Ultramicroelectrode (UME) (left part in Fig. 3.16) it is clearly visible a huge edge effect during the polymerization, due to the particular charge distribution of the UME (explained in Annex 5.3).

To avoid or, at least, to reduce this effect, the polymerization parameters should be optimized as described in the next section to obtain an highly conductive homogeneous deposition.

3.4.5 Parameters impacting the deposition on the ultramicroelectrode

Fig.3.17 depicts different SEM morphology images for PEDOT:PSS deposition on 10 μm -diameter electrodes. In Fig.3.17.a, a 10 μm -diameter electrode uncleaned (left) and

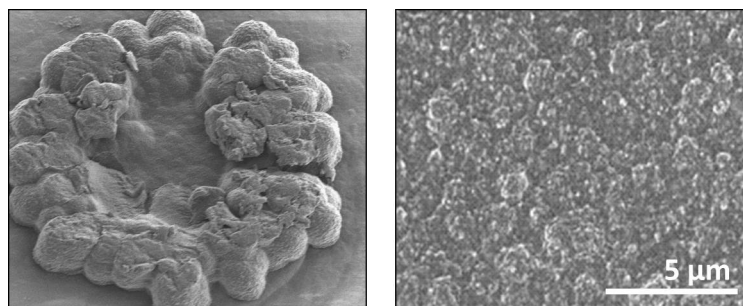


Figure 3.16: SEM images of a PEDOT:PSS layers on a 10 μm -diameter electrode (left) and 50 μm -diameter electrode (right).

cleaned in H_2SO_4 (right) are compared to show the importance of the cleaning procedure especially on the UME.

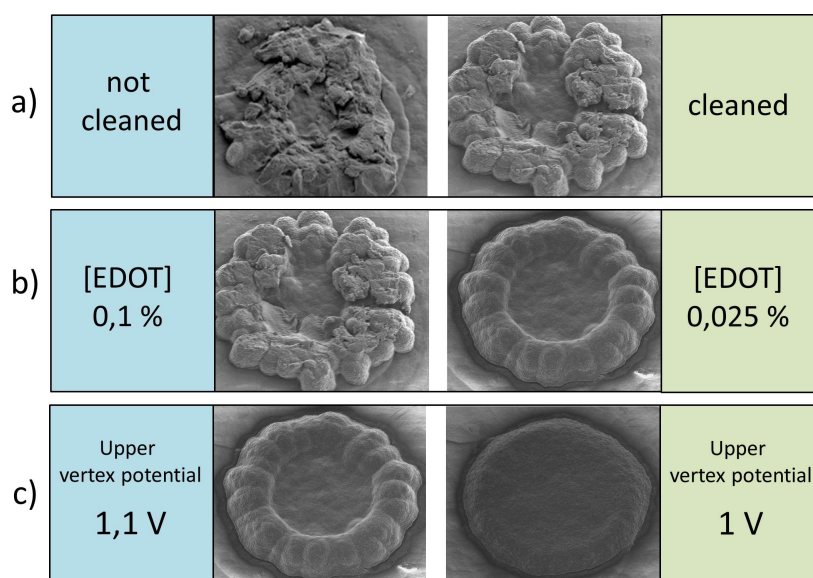


Figure 3.17: SEM images of different morphologies of PEDOT:PSS layers related to different electrochemical deposition parameters.

The effect of monomer concentration can be seen in Fig.3.17.b where EDOT concentrations of 0.1% (left) and 0.025% (right) are used in a potentiodynamic deposition from -0.7 V to 1.1 V at 10 mV/s for only 2 cycles. In Fig.3.17.c different upper maximum potentials (1.1 V, left and 1 V, right) were used.

For such electrode dimensions, the use of lower concentrations of monomer (0.025 % w/v), lower upper vertex potentials with low scan rates (10 mV/s) leads to a more homogeneous deposition and better performances in terms of impedance lowering as will be described in section 3.5.2.

3.5 Electrical characterization of PEDOT:PSS deposition

3.5.1 PEDOT conductivity: principles

In **saturated polymers**, such as polyethylene, all valence electrons are used in covalent σ -bonds. Hence, the gap between the valence band and the conduction band is very large and the material shows typical insulating properties.

In **conjugated polymers** a π -system is formed along the polymer backbone. The carbon atoms typically involved in the constitution of the polymer backbone form three σ -bonds with neighboring atoms and the remaining p orbitals, typically described as p_z orbitals, engage in the π -system.

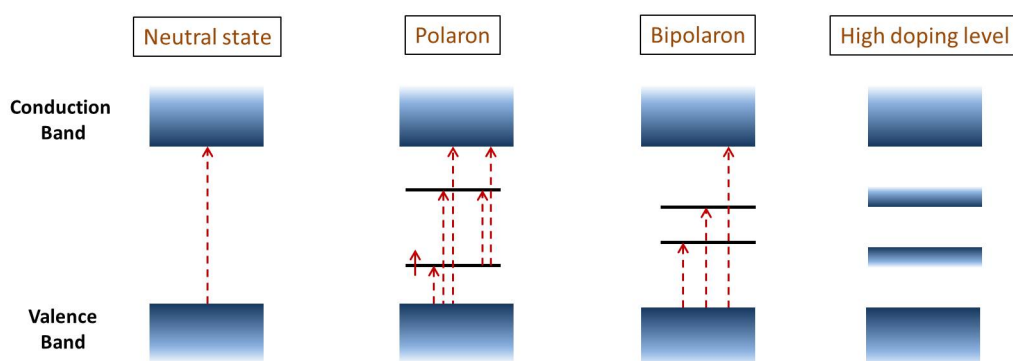


Figure 3.18: Energy level diagram of conductive polymers. Dashed red arrows indicate possible electronic transitions caused by light absorption.

To understand the conductivity of polymers, the way in which charges are stored along the polymer chain is important. When a CP is in its **neutral state**, electrons are delocalized along the conjugated backbones, forming an extended π -system with a filled **valence band**. The polymer usually stores charges in two ways. During the **oxidation process**, it could either lose an electron from one of the bands or it could localize the charge over a small section of the chain. A local distortion (an effective change in geometry) occurs when the charge is localized and this reduces the overall energy of the polymer. The generation of the local geometry decreases the ionization energy of the polymer chain and increases its electron affinity, hence increasing its ability to accommodate newly formed charges. A similar situation is experienced in the **reduction process**. This combination of a charge site and a free radical can be called **polaron** (Fig.3.19). The **polaron state** is formed by a localized hole gaining energy due to the coulombic relaxation of its vicinity.

When subjected to further oxidation, the free radical of the polaron is removed, creating a new spinless defect that is defined as **bipolaron** (Fig.3.19). For a very heavily doped polymer, the upper and the lower bipolaron bands will merge with the conduction and the valence bands respectively, to produce partially filled bands and metal-like conductivity[43]. The movement of bipolarons as a unit up and down the polymer chain is responsible for the conductivity of the polymer and charge transfer between the conducting domains takes place by thermally activated hopping or tunnelling[44].

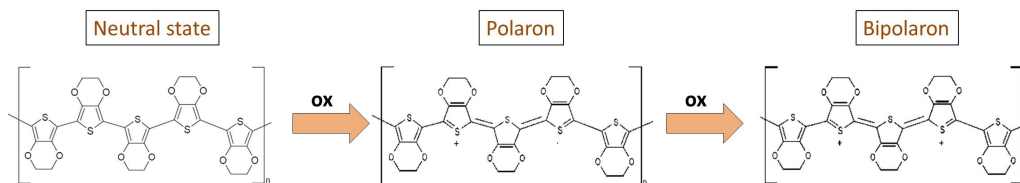


Figure 3.19: Neutral and oxidized (polaron and bipolaron) state for PEDOT and an example of counterion (PSS) in the oxidized state.

3.5.2 Impedance lowering on PEDOT-modified microelectrodes

The use of microelectrodes (in our case with a diameter ranging from 10 μm to 50 μm) minimizes the reactive cell response and provides high density of electrode sites but, as the electrode dimensions decrease, the impedance increases affecting the quality of signal recordings[15]. Signal transduction at the electrode/tissue interface is indeed a complex function of electrode properties and tissue characteristics. Transduction between the ionically conducting tissue and the electronically conducting electrode primarily takes place through capacitive and/or faradic currents from reversible reduction-oxidation reactions at the electrode surface. As we can see from Eq.3.1 and Eq.3.2, the electrode area (A) is directly proportional to the capacity of the electrical double layer (C_{dl}) and inversely proportional to the Charge Transfer Resistance (R_{ct})[45]:

$$C_{dl} = \epsilon_0 \epsilon_R \frac{A}{d} \quad (3.1)$$

$$R_{ct} = \frac{RT}{n^2 F^2 A K_h^0 c^0} \quad (3.2)$$

ϵ_0 and ϵ_R are the vacuum permittivity and the relative static permittivity respectively, d the thickness of the double layer, R the universal gas constant, T the absolute temperature, n the number of exchanged electrons, F the Faraday constant, K_h^0 is the standard rate constant, and c^0 the concentration of the oxidized (reduced) species. The impedance depends on both (C_{dl}) and (R_{ct}), according to Eq.3.3, 3.4, 3.5:

$$Z^2 = Z_{re}^2 + Z_{im}^2 \quad (3.3)$$

$$Z_{re} = R_s + \frac{R_{ct}}{1 + \omega^2 R_{ct}^2 C_{dl}^2} \quad (3.4)$$

$$Z_{re} = -\frac{\omega R_{ct}^2 C_{dl}}{1 + \omega^2 R_{ct}^2 C_{dl}^2} \quad (3.5)$$

Where Z_{re} and Z_{im} are the real and the imaginary part of the impedance respectively and ω is the frequency. Therefore, it is easy to understand the relation between the impedance and the active area, that is also shown in Fig.3.20 where the impedance values of over a frequency range of 10^1 - 10^4 Hz for different size of fabricated gold electrode are depicted. As the electrode dimensions decrease down to the microscale, the impedance signal becomes very noisy, especially at low frequencies, and is difficult to measure.

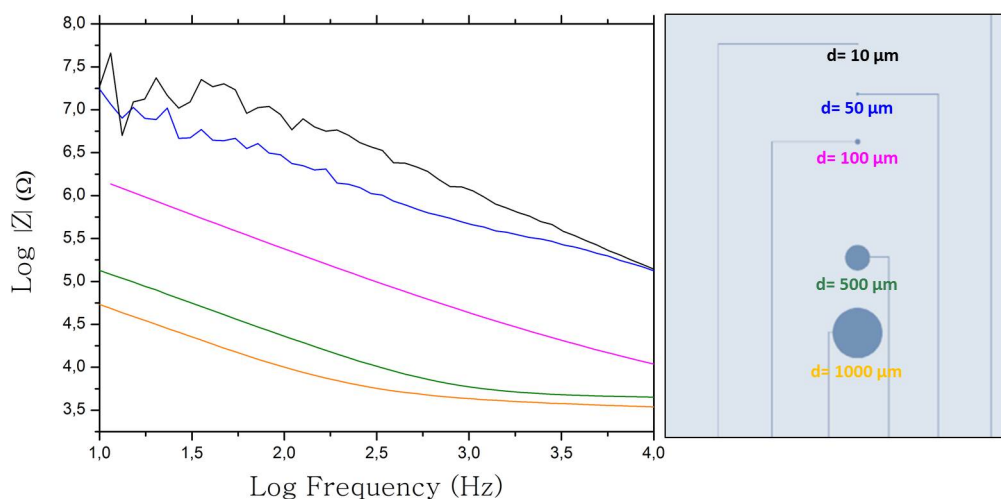


Figure 3.20: Mean impedance of gold electrode with related error bar for different electrodes diameters: 10 μm (black), 50 μm (blue), 100 μm (pink), 500 μm (green), 1000 μm (yellow).

To address this issue the use of PEDOT:PSS, with high roughness and porosity observed during the morphological characterization, represents a **simple and effective way to increase the surface/area ratio**.

Fig.3.21.a depicts Bode graphs of the impedance magnitude over a frequency range of 10^1 - 10^4 Hz, for a gold electrode of 10 μm in diameter, before and after polymerization of PEDOT:PSS. The impedances of the electrode at 1 kHz were used for comparison purposes as action potentials have a characteristic frequency band centred at that frequency. The mean impedance at 1 kHz for the unmodified 10 μm -diameter gold electrodes was around 700 k Ω , while after PEDOT electrochemical deposition, the mean impedance decreased down to 10 k Ω .

Another important parameters to assess is the charge capacity of the electrode and a cyclic voltammetry measurement was used to this purpose. The charge capacity, represented by the area under the voltammogram, shows the intrinsic redox reaction of the electrode material. The back and forth cycling of the potential of the electrode bias from negative to positive (between -0.6 V and 0.6 V at a scan rate of 0.05 V/s) propels ion exchange between the electrode and the electrolyte moving mobile charge carriers in and out of the PEDOT matrix. The charge storage capacity, that was compared with the one of uncoated gold electrodes, drastically increases after PEDOT:PSS deposition. High charge capacity, which is the measurement of charge transfer efficiency, should greatly

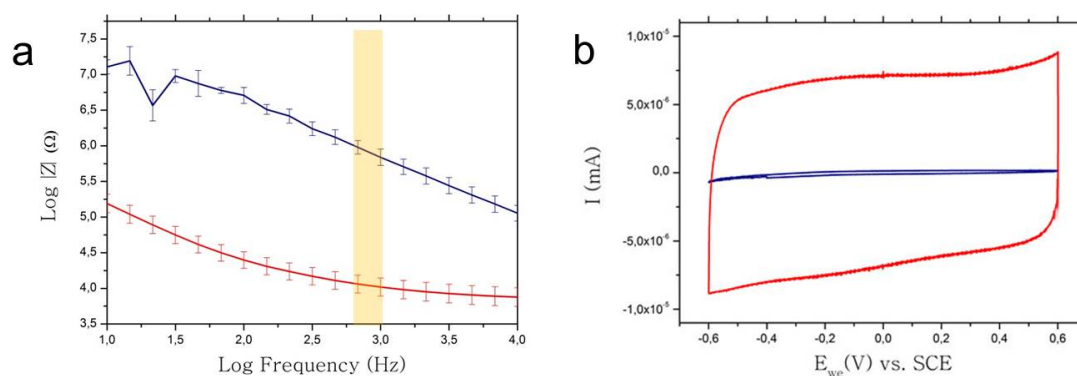


Figure 3.21: a) Electrochemical mean impedance spectroscopy over a range of 10^1 - 10^4 Hz and related error bar and b) charge capacity for the pristine gold electrode (blue) and for the PEDOT-modified electrode (red) for a $10 \mu\text{m}$ diameter electrode in a NaCl 0.9% solution.

improve recording of action potentials and stimulation of neuronal elements at a lower charge density at the device-tissue interface.

As mentioned in Section 3.3, for each polymerization route and active area the parameters of deposition were optimized in order to achieve, after deposition, the lower resulting impedance values over all the explored frequencies. In Fig.3.22 comparable decreases in impedance are shown for a PEDOT:PSS deposition on a $100 \mu\text{m}$ -diameter electrode. The parameters used for the three routes are reported in Table 3.2.

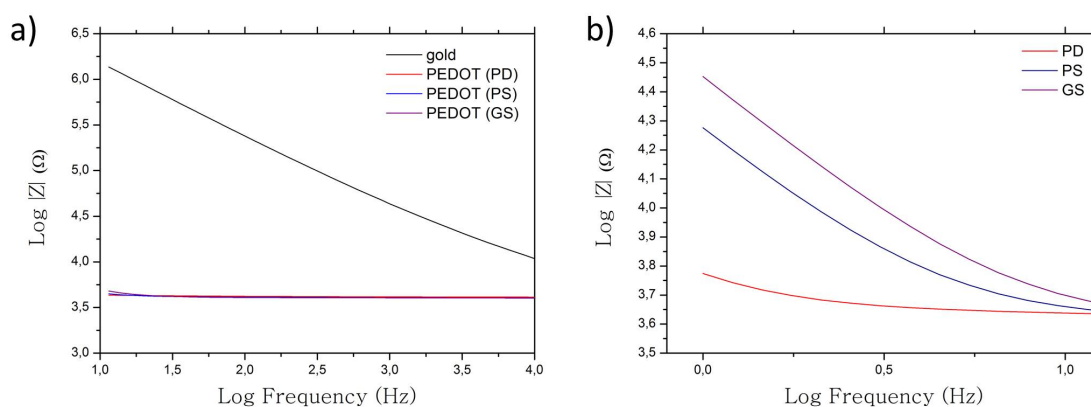
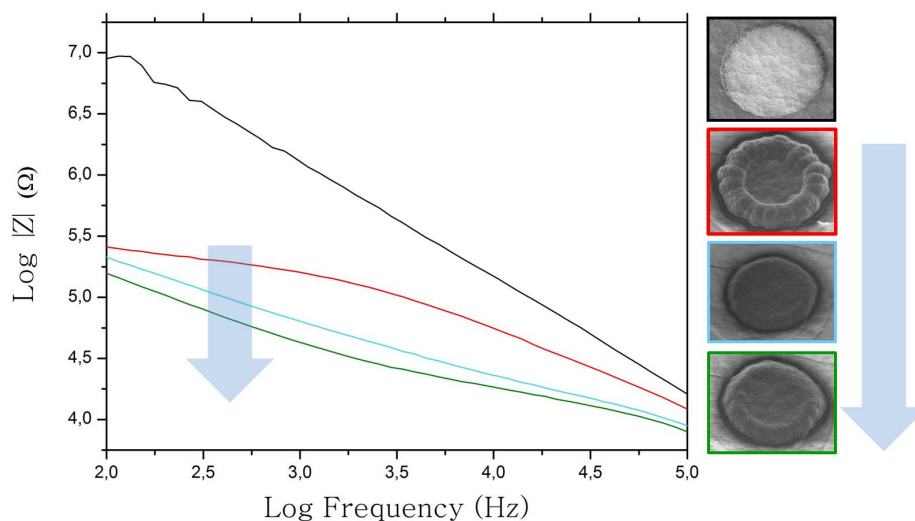
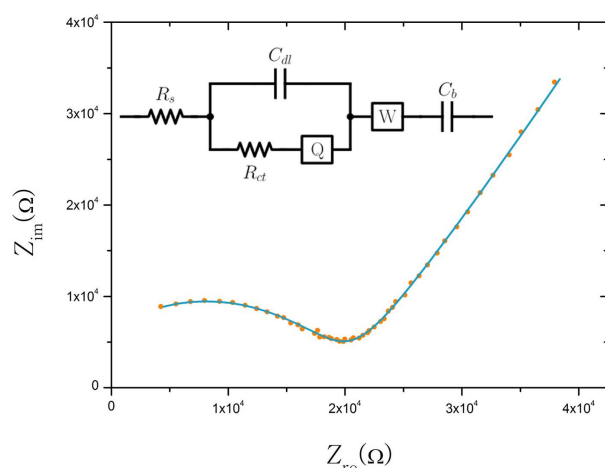


Figure 3.22: EIS over a range of a) 10^1 - 10^4 Hz and b) 1 - 10^1 Hz, for a $100 \mu\text{m}$ -diameter electrode in a NaCl 0.9% solution for different electropolymerization routes.

The same optimization of the deposition parameters have been done on the UMEs. As we stated in Section 3.4.5, using low monomer concentrations, low upper vertex potentials and scan rates (10 mV/s), an homogeneous deposition can be achieved, leading to lower impedance values over all the explored frequencies (see Fig.3.23).

| | |
|-----------|---|
| PD | from -0.9 V to 1.2 V at 25 mV/s for 10 cycles |
| PS | 0.9 V for 50 s |
| GS | 600 nA for 20 s |

Table 3.2: Electropolymerization parameters for the three routes.**Figure 3.23:** Impedance lowering (over a range of 10^2 - 10^5 Hz) and related morphology for different deposition conditions presented in Section 3.4.5 for $10\ \mu\text{m}$ -diameter electrodes.**Figure 3.24:** Nyquist diagram for a PEDOT-modified $10\ \mu\text{m}$ diameter electrode and related fitting curve using the equivalent circuit.

A fitting curve of the resulting impedance after PEDOT:PSS modification on the electrode can be performed on the Nyquist diagram, using the equivalent circuit shown in Fig.3.24. R_s represents the resistance of the solution NaCl 0.9%, C_{dl} and R_{ct} are the capacity of the double layer and the resistance to the charge transfer respectively, W the Warburg element (representing the diffusion within a thin layer of electrolyte) and C_b the electronic contribution to the bulk capacitance. Starting from

the model proposed by Danielsson *et al.*[46], we found that a better fit could be achieved by adding the Constant Phase Element (CPE), represented by Q in the image, which takes

into account the porosity of the modified electrode.

3.5.3 Local conductivity on PEDOT-modified microelectrodes

3.5.4 Coating thickness

To calculate the local electrical conductivity of the deposited PEDOT:PSS layer, it is necessary to know its thickness. Yang *et al.*[22] report an increase of coating thickness for surfactant template ordered PEDOT on electrodes as the deposition charge increases.

In our case, we faced some difficulties in measuring the thickness of the layer on our flexible substrate using common methods implemented for rigid substrate, such as Standard Profilometry and Confocal Laser Scanning Microscope.

Moreover the deposited layer has a high roughness and a polymeric passivation layer, thicker than PEDOT:PSS, around the electrodes surface that is subject to swelling with humidity. To overcome these problems the electrode polymerization was performed on rigid silicon substrates using the same PD, PS and GS conditions presented in Table 3.2 for a 100 μm diameter electrode. On these substrates we employed the same design for our gold electrodes but we used, as a passivation layer, a photoresist that can be easily removed in acetone after the electrodeposition, without damaging the coating, as can be seen in Fig.3.25.

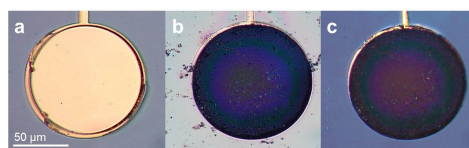


Figure 3.25: Optical microscope image of (a) the gold electrode passivated with a photoresist, (b) the electrode after PD electropolymerization of PEDOT:PSS (c) the electrode PEDOT covered after the dissolution of the photoresist in acetone.

| | PD | PS | GS |
|--------------------------------------|-------------|-------------|-------------|
| Mean Thickness (μm) | 1.568 | 0.556 | 0.301 |
| Standard Deviation (μm) | ± 0.011 | ± 0.031 | ± 0.037 |

Table 3.3: Mean thickness value and standard deviation for three different electropolymerization routes.

impedance values after deposition (see Table 3.2). From these data we observe that the PD deposition exhibits the thickest and, as observed from the tapping mode AFM images in section 3.4.2, also the flattest (because of its more homogeneous nature) morphology of the three deposition routes.

3.5.4.1 Conductive-AFM measures and calculation of local conductivity

The conductivity of PEDOT:PSS films can noticeably vary with respect to the used electropolymerization route: in the present study C-AFM has been performed, demonstrating

the changes in local current induced by different electrochemical synthesis. C-AFM experiments were performed on the electrodeposited layers in different zones for each sample. Fig.3.26 shows both the topography (a) and the corresponding current images (e, f, g, h) recorded concurrently into the same region of PEDOT:PSS films for a scanned area of $10\ \mu\text{m} \times 10\ \mu\text{m}$ for each sample.

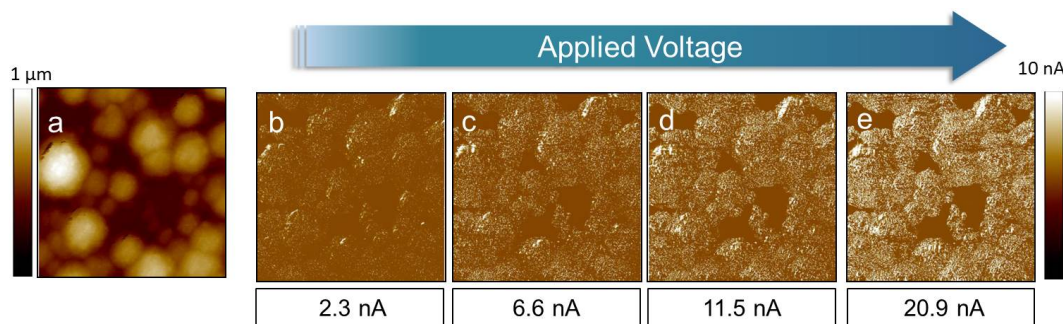


Figure 3.26: Contact mode AFM topography (a) of PEDOT:PSS layer formed under PS conditions (0.9 V for 50 s) and current corresponding images with C-AFM at (b) 10 mV, (c) 50 mV, (d) 100 mV, (e) 200 mV, recorded over a scanned area of $10\ \mu\text{m} \times 10\ \mu\text{m}$.

The current images were obtained by contacting a conductive tip with the film surface and by applying small bias voltages from 0 mV to 500 mV between the tip and the sample. In these images the bright regions are ascribed to the high current flowing domains and the dark regions represent low current carrying capabilities. The magnitude of maximum current can be seen from the colour scaling. For the first experiment, we progressively increased the bias applied between the tip and the sample to study the electrical behaviour of the layer.

The same tendency was found for samples obtained by different electrochemical methods and only the one obtained by PS mode is shown. When we applied 50 mV, we started to observe a **strong correlation between the current** (Fig.3.26.c) **and the topography images** (Fig.3.26.a). Vitoratos and co-workers[47] explain that, for commercial PEDOT:PSS, conductive PEDOT oligomers are electrostatically attached to twisted long insulating PSS chains. In our case, the higher cauliflower-like domains appear to have an increased density of conductive PEDOT domains. We interpret these conductive hotspots to be individual PEDOT domains, and deduce that the more insulating regions on the surface of the sample are likely PSS rich domains (as reported for spin coated PEDOT:PSS[48]). As a consequence, during electropolymerization, **the counter ion is probably embedded into the globular parts of the film, leading to highly conducting localized regions**. Fig.3.26.d and 3.26.e, corresponding to a bias of 100 mV and 200 mV respectively, show a significant increase of the measured current versus the applied bias.

As shown in Fig.3.26, PEDOT:PSS films obtained from PS deposition are composed of segregated localized conducting domains embedded in a largely non-conductive PSS matrix, while, as can be seen in Fig.3.28, PEDOT:PSS films produced by PD route are characterized

by interlinked conducting regions with very few insulating domains in between. Moreover the role of PSS as a doping agent is probably less pronounced in the PD film, due to the higher homogeneity of the different domains.

In a range of potential between 50 mV and 200 mV, the behaviour of PEDOT:PSS layer belongs to the ohmic region as shown in Fig.3.27.

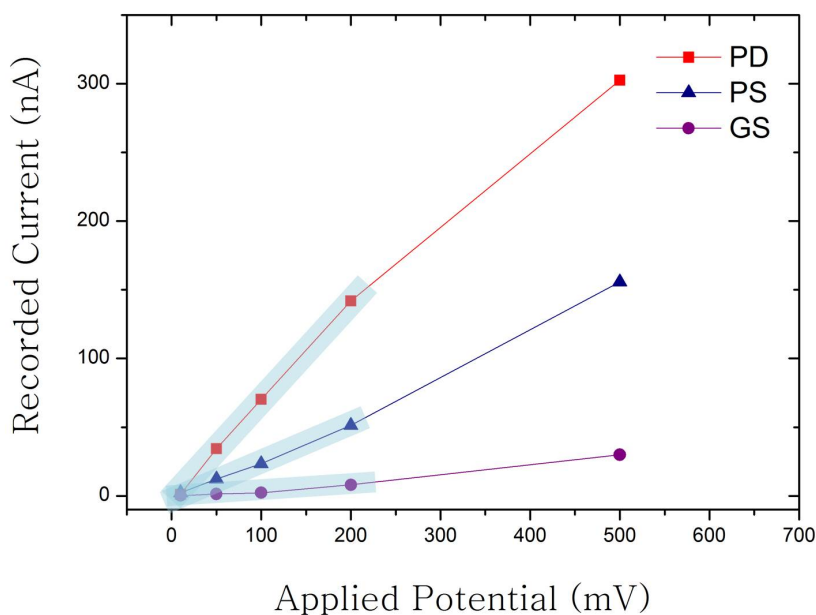


Figure 3.27: C-AFM I-V curve for the samples electropolymerized by three different ways, recorded over a scanned area of $10 \mu\text{m} \times 10 \mu\text{m}$. The ohmic zone is underlined in light blue.

The linear behaviour of the I-V curve undergoes a deviation at higher bias voltages. To understand this deviation, the charge carrier trapping must be considered. The electrochemically polymerized PEDOT is in an oxidized state that promotes the charge carriers at high doping levels: intra-gap states are formed by electrons, carrier transitions are free and, as a consequence, conductivity is high. Therefore at high bias, either the holes in the interstate bands are able to move freely (cf. Fig.3.18). The electronic conductivity at room temperature was determined from the ohmic region by using the following equation (3.6):

$$\sigma = \frac{1}{R} \frac{d}{A} \quad (3.6)$$

where R is the vertical resistance ($R=V/I$) obtained for an applied potential on the PEDOT:PSS film, A is the contact area between the conducting tip and the substrate and d is the thickness of the PEDOT:PSS film. To calculate the contact area we used the Hertz theory[49] with the following relation:

$$a^3 = \frac{3FR}{4E} \quad (3.7)$$

where a is the radius of the contact area between the tip and the sample ($A = \pi a^2$), F is the applied force (≈ 10 nN) and R is the actual curvature radius of the system tip-sample, and E the actual Young's modulus.

In Table 3.4 is shown the local conductivity corresponding to the different bias applied for a PD deposition over a $10 \mu\text{m} \times 10 \mu\text{m}$ scanned area. The conductivity values (σ) are mean values (with the related standard deviation) between measurements performed in three different areas of the same sample.

| Applied Potential (mV) | Mean σ (S/cm) | Standard Deviation (S/cm) |
|------------------------|----------------------|---------------------------|
| 10 | 67.3 | ± 12.3 |
| 50 | 101.0 | ± 9.1 |
| 100 | 94.7 | ± 9.0 |
| 200 | 107.3 | ± 11.3 |
| 500 | 121.7 | ± 12.8 |

Table 3.4: Conductivity related to the applied voltage for a PEDOT:PSS layer deposited under PD conditions.

To prove the reliability of this method we first calculated the conductivity of a commercially available PEDOT:PSS solution spin coated on the electrode sites. A mean conductivity value of 1.2 ± 0.2 S/cm was found for this solution, where the conductivity indicated by the supplier is 1 S/cm.

Optimized conditions for each polymerization route to obtain the best results in terms of conductivity have been used. The corresponding conductivity, calculated for at least 3 different samples, is reported in Table 3.5.

| | PD | PS | GS |
|-----------------------|--------|--------|------|
| σ range (S/cm) | 40-200 | 20-130 | 1-50 |

Table 3.5: Conductivity values for the three polymerization routes.

Despite the low intrinsic conductivity for the layer deposited by GS route, we have found a decrease in impedance very similar to the other two methods, especially at high frequencies. Therefore, the observed high roughness is responsible for a noticeable increase of the surface/area ratio, leading to low values of impedance.

3.5.5 Temperature dependence of the conductivity at the microscale

In PEDOT:PSS, with its granular structure of conductive PEDOT-rich grains enclosed in insulating PSS-rich shells, the electrical conductivity is not determined only from the hole

polareons transport into the PEDOT segments, but also by their hopping between segments and grains.

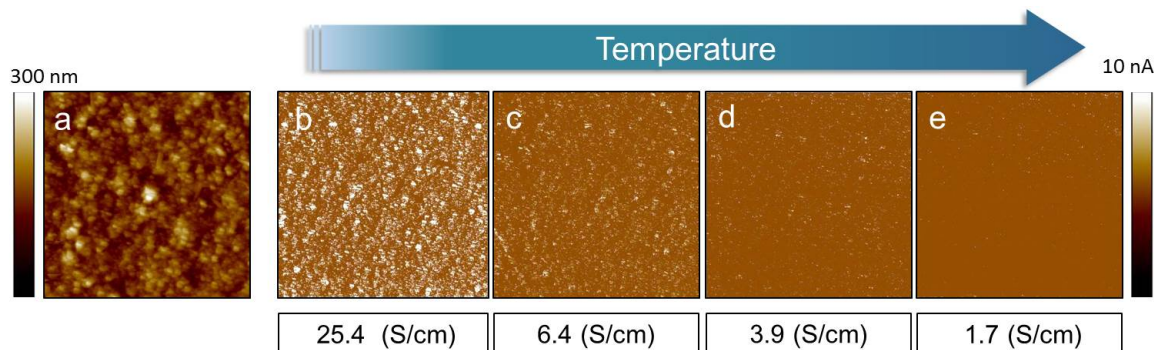


Figure 3.28: a) Contact mode AFM topography of PEDOT layer formed under PD mode (scan of potential from -0.9 V to 1.2 V, scan rate 0.025 V/s, 10 cycles) and current corresponding images with C-AFM under an applied potential of 50 mV at the temperature of b) 25, c) 50, d) 100, e) 150°C recorded after $\frac{1}{2}$ h, over a scanned area of 10 μm x 10 μm . Under every image the corresponding calculated conductivity is given.

The temperature-dependent current flow, and the related conductivity $\sigma(T)$ for potentiodynamically synthesized PEDOT:PSS thin films is presented in the C-AFM images in Fig.3.28. The temperature was varied back and forth from 25°C to 150°C. The C-AFM images were recorded after leaving the sample for $\frac{1}{2}$ h at 25°, 50°, 100°, 150°. The temperature dependence in electrodeposited PEDOT:PSS layer on Au exhibits a singular behaviour, opposed to that found for spin coated PEDOT:PSS layer [47]: **the conductivity extracted from I-V characteristics exhibited mild negative temperature dependence, decreasing as temperature increase from 25°C to 150°C**, as shown in Fig.3.29.

A similar behaviour has been reported for pentacene film deposited on Au electrodes[50], and various models have been suggested to explain it [51, 52, 53]. According to the model proposed by Orton and Powell [54], when the Debye length induced by traps at grain boundaries is comparable to the grain size, the grain is fully depleted of free carriers and the energy band will be essentially throughout each grain, and therefore throughout the whole film. There will be no barrier to current flow, and conductivity will not be thermally activated. A possible explanation to rationalize the negative temperature dependence of conductivity is that it can vary from band-like transport at low temperature, to hopping transport at high temperature. At low temperature, the π -orbital of molecules strongly overlaps to exhibit band-like transport with high conductivity. As the temperature increases, thermal vibration force becomes comparable to or larger than interaction force, so that the overlap of π -orbital gets too weak for charges to transport by hopping from molecule to molecule, leading to a low conductivity.

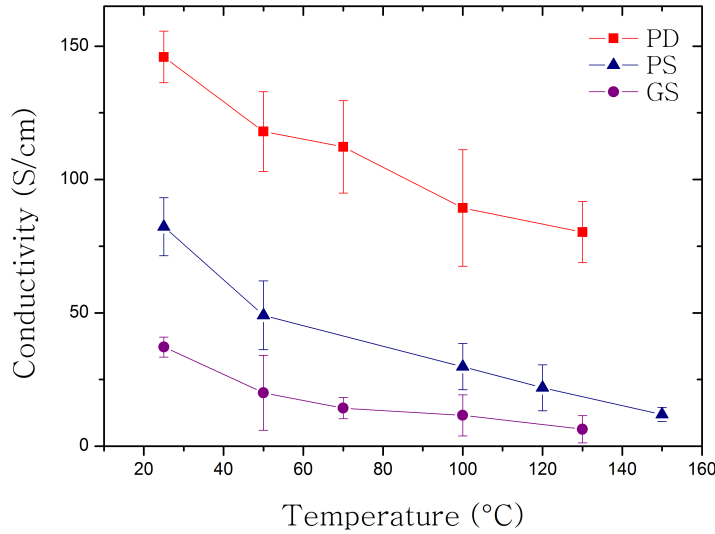


Figure 3.29: Variation of conductivity with temperature for three PEDOT:PSS layers electrodeposited under PD (red), PS (blue) and GS (violet) conditions.

3.5.6 Accelerated ageing test

3.5.6.1 Accelerated thermal ageing at a macroscale

It is commonly assumed that elevated temperature can be used as a way for accelerating the ageing. The so-called "**accelerated thermal ageing process**" has been used to investigate the effects of ageing on several polymers that are implanted into the body. The rate of ageing is increased by a factor:

$$f = 2^{\frac{\Delta T}{10}} \quad (3.8)$$

In Eq. 3.8 $\Delta T = T - T_{ref}$, where T_{ref} is a reference temperature, at which the effects of ageing are to be determined, and T is an elevated temperature used to accelerate these effects. It should be noted that Eq. 3.8 is an approximation to a more rigorous kinetic treatment. It has been stated that it is only valid for $\Delta T \leq 60^\circ C$ with a maximum value of T about $70^\circ C$ [55]. For a material that is to be implanted into the human body, T_{ref} will be the body temperature of $37^\circ C$. Here maintaining the material for 1 month at $70^\circ C$ is then considered to be equivalent to an ageing of $2^{\frac{70-37}{10}} = 2^{3.3} = 9.8$ months.

Fig.3.30 shows Bode graphs of the impedance before and after the ageing of the PEDOT:PSS layer electropolymerized by PD routes over a $100 \mu m$ electrode. A slight impedance increase after 1 week and 1 month can be observed. After 1 month of ageing at $70^\circ C$, the PEDOT-polymerized electrode impedance (dotted blue line in Fig.3.30) is quite similar to the PEDOT-polymerized electrode before ageing (blue line), this demonstrates a

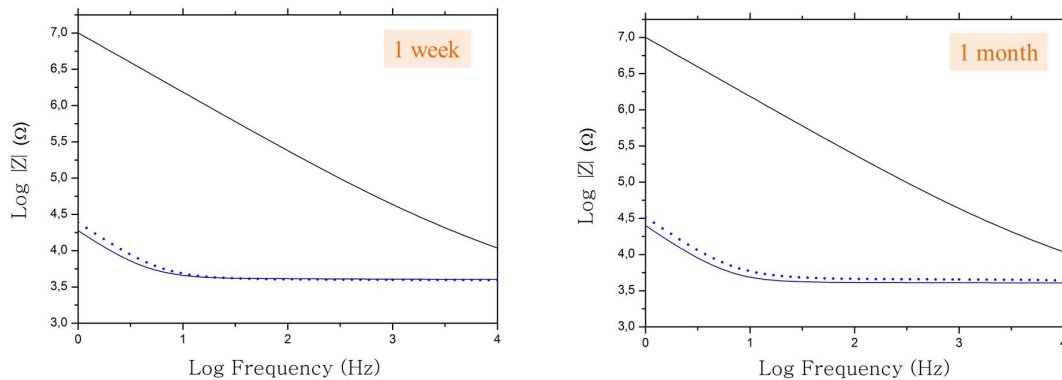


Figure 3.30: Impedance curve before (black) and after (blue) PEDOT:PSS polymerization and after ageing (dotted blue), over a frequency range of 10^0 - 10^4 Hz, after 1 week and 1 month of ageing process at 70°C ($f = 9,8$).

good stability of the PEDOT:PSS layer.

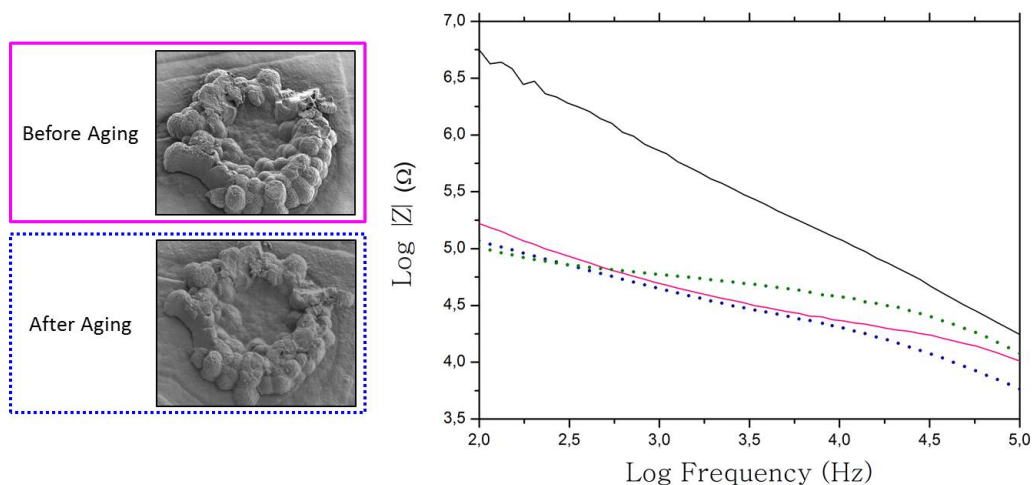


Figure 3.31: Impedance curve before (black) and after (pink) PEDOT:PSS deposition, suddenly after the ageing process (dotted blue), and left 1 day at room temperature after the ageing process (dotted green) over a frequency range of 10^2 - 10^5 Hz.

The same test have been performed on a $10\ \mu\text{m}$ electrode, polymerized by PD route. The electrode was left immersed in a physiological solution of NaCl 0.9% at 37°C for 1 month. If the impedance is directly measured after heating (dotted blue in Fig.3.31), the values show a slight decrease. This behaviour will be explained in the next section through an investigation of conductivity at the microscale. After leaving the electrode at room temperature for 1 day, the morphology and the impedance values have been measured. From the SEM images in Fig.3.31 we observe that thermal ageing process does not significantly impact the morphology of the PEDOT:PSS deposition. The measure of

impedance shows a slight increase at high frequencies, which allows us to conclude that a good stability of the nanostructuration has been obtained.

3.5.6.2 Accelerated thermal ageing at a microscale

After the thermal accelerated ageing process, the same samples were analysed by C-AFM in order to compare the local conductivity with the impedance values found before the ageing process. In Fig.5.2 the C-AFM images show the topography and the corresponding current flow for different applied potentials over the same $10\ \mu\text{m} \times 10\ \mu\text{m}$ scanned area.

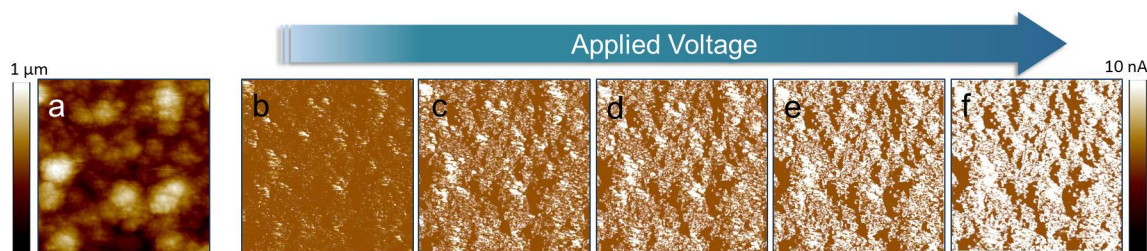


Figure 3.32: a) Contact mode AFM topography of PEDOT:PSS layer formed under PD conditions (scan of potential from $-0.7\ \text{V}$ to $1.15\ \text{V}$, scan rate: $0.05\ \text{V/s}$, 10 cycles) and current corresponding images with C-AFM at b) $10\ \text{mV}$, c) $50\ \text{mV}$, d) $100\ \text{mV}$, e) $200\ \text{mV}$, f) $500\ \text{mV}$, after 1 month at 70°C , recorded over a scanned area of $10\ \mu\text{m} \times 10\ \mu\text{m}$.

As explained before for a deposition with a granular structure **the electrical conductivity is not determined only from the hole polarons transport into the PEDOT segments, but also by their hopping between segments and grains.** The hopping transport occurrence is negligible as the distance between the grains is larger than the Debye length. We can state that, as a consequence, different morphologies of the layer and grain arrangements lead to different results on the local conductivity after ageing.

In Table 3.6 we report conductivity values for a PD and a PS deposition before and after 1 month of ageing process.

| Applied Potential (mV) | PD | | PS | |
|------------------------|-------------------------------|--|-------------------------------|--|
| | σ (S/cm) before ageing | \rightarrow σ (S/cm) after ageing | σ (S/cm) before ageing | \rightarrow σ (S/cm) after ageing |
| 50 | 104.2 | \rightarrow 127.3 | 102.8 | \rightarrow 34.4 |
| 100 | 98.7 | \rightarrow 133.9 | 104.9 | \rightarrow 30.2 |
| 200 | 108.4 | \rightarrow 135.7 | 106.1 | \rightarrow 31.6 |

Table 3.6: Conductivity values (related to different potentials applied within the ohmic zone) before and after the accelerated thermal ageing for two different coatings with different surface morphologies.

To understand these results we should remember that thermal degradation can be considered as a **corrosion process which reduces the size of the grains** and con-

sequently increases the gap, or equivalently increases the potential barrier for polaron transport, between them. Nevertheless, at the same time, charge transfer between the conducting domains takes place by **thermally activated hopping** or tunnelling. This thermally activated process has a more significant impact on a coating obtained by PD route, thanks to the homogeneity of the layer and the limited grain dimensions, than on a coating obtained by PS conditions, characterized by a large distance between grains. Therefore for the PD case the conductivity after one month of ageing varies from an average value of about 104 S/cm to an average value of about 132 S/cm. On the contrary, we record a significant decrease of conductivity for the PS case, in which, starting from a conductivity of about 104 S/cm we found an average value of about 32 S/cm after one month at 70°C, probably due to an increased distance between the grains that makes the hopping process less likely to occur.

3.6 Conclusion

The effect of three different electropolymerization routes (and of different preparation parameters) on a PEDOT:PSS electrodeposition, starting from an aqueous monomer solution, has been analysed. The nucleation mechanism of PEDOT electropolymerization has been explained, underling the influence of the substrate on the starting growth process. A strong correlation between the current-carrying ability and the topography of the PEDOT:PSS layer has been found. Moreover a significant decrease of the electrode impedance after PEDOT electropolymerization on gold electrode (up to 3 orders of magnitude), using three different electropolymerization routes, has been reported.

At a microscopic scale, analysing the electropolymerized coating by C-AFM, we showed that the intrinsic conductivity of PEDOT, obtained by measuring the current-voltage relationships in the ohmic zone, is higher compared to that of spin coated films. Moreover, contrary to the spin coated films, the electropolymerized PEDOT conductivity exhibits a negative temperature dependence. Finally, we investigated the PEDOT:PSS layers stabilities both at the macroscopic and microscopic level with an accelerated thermal ageing process. While the impedance has been shown to remain approximately the same after thermal ageing for the three polymerization routes, at the microscopic level we have found an increase of conductivity for the potentiodynamically deposited sample subjected to continuous heating at 70°C for 1 month (while a decrease of conductivity is showed in the case of a potentiostatically deposited layer after ageing).

From all these results we can extract important information that should be considered for designing nanostructured neural electrode for chronic implantation.

The intrinsic conductivity is strictly related to the thickness and the roughness of the deposited layer, the impedance of the neural electrode and the stability over time and they can be easily controlled by tuning the electropolymerization parameters. Using the PD route we obtain a very homogeneous PEDOT:PSS layer, with a high intrinsic conductivity and a high stability under thermal ageing process while the PS and GS routes are more

impacted by the quality of the electrode pristine surface. Nevertheless they can lead to a higher roughness of the deposition that is a critical aspect for reducing the impedance.

Bibliography

- [1] Pouria Fattahi, Guang Yang, Gloria Kim, and Mohammad R Abidian. A review of organic and inorganic biomaterials for neural interfaces. *Advanced Materials*, 26(12):1846–1885, 2014.
- [2] Shyh-Chyang Luo. Conducting polymers as biointerfaces and biomaterials: A perspective for a special issue of polymer reviews. *Polymer Reviews*, 53(3):303–310, 2013.
- [3] Mohammad R Abidian, D-H Kim, and David C Martin. Conducting-polymer nanotubes for controlled drug release. *Advanced Materials*, 18(4):405–409, 2006.
- [4] T F Otero and J M Sansinena. Artificial muscles based on conducting polymers. *Bioelectrochemistry and Bioenergetics*, 38(2):411–414, 1995.
- [5] T F Otero, J G Martinez, and J Arias-Pardilla. Biomimetic electrochemistry from conducting polymers. a review: Artificial muscles, smart membranes, smart drug delivery and computer/neuron interfaces. *Electrochimica Acta*, 84:112–128, 2012.
- [6] Rylie A Green, Nigel H Lovell, Gordon G Wallace, and Laura A Poole-Warren. Conducting polymers for neural interfaces: challenges in developing an effective long-term implant. *Biomaterials*, 29(24):3393–3399, 2008.
- [7] Nathalie K Guimard, Natalia Gomez, and Christine E Schmidt. Conducting polymers in biomedical engineering. *Progress in Polymer Science*, 32(8):876–921, 2007.
- [8] Takeo Ito, Hideki Shirakawa, and Sakuji Ikeda. Simultaneous polymerization and formation of polyacetylene film on the surface of concentrated soluble ziegler-type catalyst solution. *Journal of Polymer Science: Polymer Chemistry Edition*, 12(1):11–20, 1974.
- [9] Xinyan Cui, Valerie A Lee, Yehoash Raphael, James A Wiler, Jamille F Hetke, David J Anderson, and David C Martin. Surface modification of neural recording electrodes with conducting polymer/biomolecule blends. *Journal of Biomedical Materials Research*, 56(2):261–272, 2001.
- [10] K Keiji Kanazawa, AF Diaz, WD Gill, PM Grant, GB Street, Gian Piero Gardini, and JF Kwak. Polypyrrole: an electrochemically synthesized conducting organic polymer. *Synthetic Metals*, 1(3):329–336, 1980.
- [11] C P Andrieux, P Audebert, P Hapiot, and J M Saveant. Observation of some reactive pyrrolic radical-cations by use of fast voltammetry at ultramicroelectrodes. *Synthetic metals*, 43(1):2877–2880, 1991.
- [12] Hitoshi Yamato, Masaki Ohwa, and Wolfgang Wernet. Stability of polypyrrole and poly(3, 4-ethylenedioxythiophene) for biosensor application. *Journal of Electroanalytical Chemistry*, 397(1):163–170, 1995.

- [13] Xinyan Cui and David C Martin. Electrochemical deposition and characterization of poly (3, 4-ethylenedioxythiophene) on neural microelectrode arrays. *Sensors and Actuators B: Chemical*, 89(1):92–102, 2003.
- [14] Kip A Ludwig, Jeffrey D Uram, Junyan Yang, David C Martin, and Daryl R Kipke. Chronic neural recordings using silicon microelectrode arrays electrochemically deposited with a poly (3, 4-ethylenedioxythiophene)(PEDOT) film. *Journal of Neural Engineering*, 3(1):59, 2006.
- [15] Xinyan Tracy Cui and David Daomin Zhou. Poly (3, 4-ethylenedioxythiophene) for chronic neural stimulation. *IEEE Transactions on Neural Systems and Rehabilitation Engineering*, 15(4):502–508, 2007.
- [16] Seth J Wilks, Sarah M Richardson-Burns, Jeffrey L Hendricks, David C Martin, and Kevin J Otto. Poly (3, 4-ethylenedioxythiophene) as a micro-neural interface material for electrostimulation. *Frontiers in Neuroengineering*, 2, 2009.
- [17] H Randriamahazaka, V Noel, and C Chevrot. Nucleation and growth of poly (3, 4-ethylenedioxythiophene) in acetonitrile on platinum under potentiostatic conditions. *Journal of Electroanalytical Chemistry*, 472(2):103–111, 1999.
- [18] Nacer Sakmeche, Salah Aeiyaeh, Jean-Jacques Aaron, Mohamed Jouini, Jean Christophe Lacroix, and Pierre-Camille Lacaze. Improvement of the electrosynthesis and physicochemical properties of poly (3, 4-ethylenedioxythiophene) using a sodium dodecyl sulfate micellar aqueous medium. *Langmuir*, 15(7):2566–2574, 1999.
- [19] Johan Bobacka, Andrzej Lewenstam, and Ari Ivaska. Electrochemical impedance spectroscopy of oxidized poly (3, 4-ethylenedioxythiophene) film electrodes in aqueous solutions. *Journal of Electroanalytical Chemistry*, 489(1):17–27, 2000.
- [20] Laura Pigani, Aránzazu Heras, Álvaro Colina, Renato Seeber, and Jesús López-Palacios. Electropolymerisation of 3, 4-ethylenedioxythiophene in aqueous solutions. *Electrochemistry communications*, 6(11):1192–1198, 2004.
- [21] Subramaniam Venkatraman, Jeffrey Hendricks, Zachary A King, Andrew J Sereno, Sarah Richardson-Burns, David Martin, and Jose M Carmena. In vitro and in vivo evaluation of PEDOT microelectrodes for neural stimulation and recording. *IEEE Transactions on Neural Systems and Rehabilitation Engineering*, 19(3):307–316, 2011.
- [22] Junyan Yang, Dong Hwan Kim, Jeffrey L Hendricks, Michelle Leach, Rebecca Northey, and David C Martin. Ordered surfactant-templated poly (3, 4-ethylenedioxythiophene)(PEDOT) conducting polymer on microfabricated neural probes. *Acta Biomaterialia*, 1(1):125–136, 2005.
- [23] Yangping Wen, Jingkun Xu, Haohua He, Baoyang Lu, Yuzhen Li, and Bin Dong. Electrochemical polymerization of 3, 4-ethylenedioxythiophene in aqueous micellar solution containing biocompatible amino acid-based surfactant. *Journal of Electroanalytical Chemistry*, 634(1):49–58, 2009.
- [24] Yinghong Xiao, Xinyan Cui, Jessica M Hancock, Mohamed Bouguettaya, John R Reynolds, and David C Martin. Electrochemical polymerization of poly (hydroxymethylated-3, 4-ethylenedioxythiophene)(PEDOT-MeOH) on multichannel neural probes. *Sensors and Actuators B: Chemical*, 99(2):437–443, 2004.

-
- [25] Dongxue Han, Guifu Yang, Jixia Song, Li Niu, and Ari Ivaska. Morphology of electrodeposited poly (3, 4-ethylenedioxythiophene)/poly (4-styrene sulfonate) films. *Journal of Electroanalytical Chemistry*, 602(1):24–28, 2007.
- [26] S Patra, K Barai, and N Munichandraiah. Scanning electron microscopy studies of PEDOT prepared by various electrochemical routes. *Synthetic Metals*, 158(10):430–435, 2008.
- [27] Emanuela Tamburri, Silvia Orlanducci, Francesco Toschi, Maria Letizia Terranova, and Daniele Passeri. Growth mechanisms, morphology, and electroactivity of PEDOT layers produced by electrochemical routes in aqueous medium. *Synthetic Metals*, 159(5):406–414, 2009.
- [28] Ji Ho Youk, Jason Locklin, Chuanjun Xia, Mi-Kyoung Park, and Rigoberto Advincula. Preparation of gold nanoparticles from a polyelectrolyte complex solution of terthiophene amphiphiles. *Langmuir*, 17(15):4681–4683, 2001.
- [29] Claude P Andrieux, Pierre Audebert, Philippe Hapiot, and Jean Michel Saveant. Identification of the first steps of the electrochemical polymerization of pyrroles by means of fast potential step techniques. *The Journal of Physical Chemistry*, 95(24):10158–10164, 1991.
- [30] Fadhila Sekli-Belaidi, Pierre Temple-Boyer, and Pierre Gros. Voltammetric microsensor using PEDOT-modified gold electrode for the simultaneous assay of ascorbic and uric acids. *Journal of Electroanalytical Chemistry*, 647(2):159–168, 2010.
- [31] G Tourillon and F Garnier. New electrochemically generated organic conducting polymers. *Journal of Electroanalytical Chemistry and Interfacial Electrochemistry*, 135(1):173–178, 1982.
- [32] A F Diaz, Juan I Castillo, J A Logan, and Wen-Yaung Lee. Electrochemistry of conducting polypyrrole films. *Journal of Electroanalytical Chemistry and Interfacial Electrochemistry*, 129(1):115–132, 1981.
- [33] Said Sadki, Philippe Schottland, Nancy Brodie, and Guillaume Sabouraud. The mechanisms of pyrrole electropolymerization. *Chemical Society Reviews*, 29(5):283–293, 2000.
- [34] A Robert Hillman and Elizabeth F Mallen. Nucleation and growth of polythiophene films on gold electrodes. *Journal of Electroanalytical Chemistry and Interfacial Electrochemistry*, 220(2):351–367, 1987.
- [35] H Randriamahazaka, V Noël, and C Chevrot. Nucleation and growth of poly(3,4-ethylenedioxythiophene) in acetonitrile on platinum under potentiostatic conditions. *Journal of Electroanalytical Chemistry*, 472:103–111, 1999.
- [36] Mark C Morvant and John R Reynolds. In situ conductivity studies of poly (3, 4-ethylenedioxythiophene). *Synthetic metals*, 92(1):57–61, 1998.
- [37] Li Niu, Carita Kvarnström, K Fröberg, and Ari Ivaska. Electrochemically controlled surface morphology and crystallinity in poly (3, 4-ethylenedioxythiophene) films. *Synthetic metals*, 122(2):425–429, 2001.

- [38] A I Melato, M H Mendonça, and L M Abrantes. Effect of the electropolymerisation conditions on the electrochemical, morphological and structural properties of PEDOT films. *Journal of Solid State Electrochemistry*, 13(3):417–426, 2009.
- [39] J Roncali, M Lemaire, R Garreau, and F Garnier. Enhancement of the mean conjugation length in conducting polythiophenes. *Synthetic Metals*, 18(1):139–144, 1987.
- [40] John R Reynolds, Shing-guang Hsu, and Howard J Arnott. The effect of electrolyte-controlled growth morphology on the charge transport properties of poly (3-methylthiophene). *Journal of Polymer Science Part B: Polymer Physics*, 27(10):2081–2103, 1989.
- [41] A J Arvia, J C Bazan, and J S W Carrozza. The diffusion of ferro-and ferricyanide ions in aqueous potassium chloride solutions and in solutions containing carboxymethylcellulose sodium salt. *Electrochimica Acta*, 13(1):81–90, 1968.
- [42] Ming Liu, Yangping Wen, Dong Li, Haohua He, Jingkun Xu, Congcong Liu, Ruirui Yue, Baoyang Lu, and Guodong Liu. Electrochemical immobilization of ascorbate oxidase in poly (3, 4-ethylenedioxythiophene)/multiwalled carbon nanotubes composite films. *Journal of Applied Polymer Science*, 122(2):1142–1151, 2011.
- [43] L Lam, JW McBride, and J Swingler. The influence of thermal cycling and compressive force on the resistance of poly (3, 4-ethylenedioxythiophene)/poly (4-styrenesulfonic acid)-coated surfaces. *Journal of Applied Polymer Science*, 101(4):2445–2452, 2006.
- [44] Andreas Elschner, Stephan Kirchmeyer, Wilfried Lovenich, Udo Merker, and Knud Reuter. *PEDOT: principles and applications of an intrinsically conductive polymer*. CRC Press, 2010.
- [45] Riaz Ahmed and Kenneth Reifsnider. Study of influence of electrode geometry on impedance spectroscopy. In *ASME 2010 8th International Conference on Fuel Cell Science, Engineering and Technology*, pages 167–175. American Society of Mechanical Engineers, 2010.
- [46] Petter Danielsson, Johan Bobacka, and Ari Ivaska. Electrochemical synthesis and characterization of poly (3, 4-ethylenedioxythiophene) in ionic liquids with bulky organic anions. *Journal of Solid State Electrochemistry*, 8(10):809–817, 2004.
- [47] E Vitoratos, S Sakkopoulos, E Dalas, N Paliatsas, D Karageorgopoulos, F Petraki, S Kennou, and SA Choulis. Thermal degradation mechanisms of PEDOT:PSS. *Organic Electronics*, 10(1):61–66, 2009.
- [48] Alexandre Mantovani Nardes, Martijn Kemerink, René A J Janssen, Jolanda A M Bastiaansen, Nicole M M Kiggen, Bea M W Langeveld, Albert J J M van Breemen, and Margreet M de Kok. Microscopic understanding of the anisotropic conductivity of PEDOT:PSS thin films. *Advanced Materials*, 19(9):1196–1200, 2007.
- [49] Jacob N Israelachvili. *Intermolecular and surface forces: revised third edition*. Academic press, 2011.
- [50] Geon-Joo Kim and Chung-Kun Song. Negative temperature dependence of conductivity in pentacene thin film deposited on au electrode. *Journal of the Korean Physical Society*, 45:S564–S567, 2004.

- [51] S F Nelson, Y-Y Lin, D J Gundlach, and T N Jackson. Temperature-independent transport in high-mobility pentacene transistors. *Applied Physics Letters*, 72(15):1854–1856, 1998.
- [52] David Emin. Lattice relaxation and small-polaron hopping motion. *Physical Review B*, 4(10):3639, 1971.
- [53] T H Holstein. Studies of polaron motion. *Annals of Physics*, 8(3):325–342, 1959.
- [54] J W Orton, B J Goldsmith, M J Powell, and J A Chapman. Temperature dependence of intergrain barriers in polycrystalline semiconductor films. *Applied Physics Letters*, 37(6):557–559, 1980.
- [55] D W L Hukins, A Mahomed, and S N Kukureka. Accelerated aging for testing polymeric biomaterials and medical devices. *Medical Engineering & Physics*, 30(10):1270–1274, 2008.

Preliminary results on brain signal recording

4

4.1 Introduction

The results presented in this chapter have been obtained from *in vitro* and *in vivo* experiments on mice's brain. The experiments have been carried out in close collaboration with L. G. Nowak, at the Centre de Recherche Cerveau et Cognition (CerCo) and L. Dahan at the Centre de Recherches sur la Cognition Animale (CRCA). The *in vitro* recording section will show preliminary test carried out in order to validate the PEDOT:PSS coating, presented in the previous chapter, and to investigate noise phenomena related to the modified electrode-tissue interface. The *in vivo* recordings have been done by implanting, into a mouse brain, the parylene based nanostructured devices produced along this thesis, with a special focus on the improvement provided by the PEDOT:PSS coating.

The microelectrodes fabricated along the course of this thesis will be employed in L. Dahan's group, to investigate the synaptic transmission between two regions of the hippocampus (namely CA3 and CA1) before and after a behavioral task during which mice have to learn a new context. For this purpose, multiple independent small (less than 100 microns) recording sites with low impedance are required.

4.1.1 Consideration about noise during brain recording

It is important to point out that recorded neural signals are affected by several noise sources, both of biological and non-biological origins[1].

The **non-biological sources** include:

- the electronic noise due to the amplifier (shot noise, 1/f noise).
- the thermal noise and a number of noise sources associated with the double layer interface between the solution and the microelectrode surface.

This noise can result in current fluctuations which can produce, for an electrode with non-zero impedance, voltage fluctuations. It is then necessary to estimate the amplitude of such voltage fluctuations.

The **biological sources** include:

- the additional thermal noise component due to the presence of brain tissue.
- small neural signals, emitted by distant neurons/neuronal processes too far to be detected as single units and therefore considered as noise for most neural signal analyses.

Shot noise: Shot noise results from quantization of the charge: the number of charge carriers passing a given point is a random variable. If the charge carriers move independently of each other, the statistics are relatively simple and result in current noise given by[2]:

$$\psi_I = 2qI \quad (4.1)$$

where q = charge on charge carrier, I = mean current. Note that ψ_I does not vary with measurement frequency; hence, shot noise is white.

Thermal noise: Thermal noise is considered the dominant noise source encountered when performing cortical microelectrode recordings and it is largely due to the high impedance of the microelectrodes. Thermal noise results from the thermally-activated motion of charge carriers. The motion causes a random separation of charge across resistors and thereby generates a voltage noise given by[2]:

$$\psi_E = 4kTR \quad (4.2)$$

where k = Boltzmann constant, T = absolute temperature, and R = resistance. Note that ψ_E is frequency-independent; hence, thermal noise is white. Because of the relationship between noise power and power spectral density (PSD), this relationship may also be written as:

$$\psi_{E_{rms}}^{th} = \sqrt{4kTRb} \quad (4.3)$$

or

$$\psi_{E_{rms}}^{th} = \sqrt{4kTZ_{real}b} \quad (4.4)$$

where b = bandwidth of measurement. It can be seen that thermal noise will be most significant when large value resistances are involved and where the measurement bandwidth is large.

Since the thermal noise is directly related to the electrode impedance, it is also related to the surface area of the electrode contact (as explained in Chapter 3, small contact means high impedance then high noise). In addition, the surface area of the contact impacts the signal amplitude recorded from the neuron (large contact means low amplitude)[3].

Flicker noise: This form of noise results from a large variety of effects and is widely observed in a range of physical systems. In biological systems, $1/f$ fluctuation observed in many biological time series may result from the fact that biological process have many inputs with differing time scales[4].

Electrochemical systems: The PSD from electrochemical systems, comprising of electronic conductors (electrodes) and ionic conductors (electrolytes), originates from two main sources: shot noise (if a charge transfer occurs at the interface, a current-dependent fluctuation becomes apparent) and thermal noise (originating from all dissipative components). Shot noise is inherently frequency dependent, and its exact spectrum is denoted by the charge transfer and mass transfer processes of the electro-active species, in proximity of the interface. If the mass transfer process is dominated by electric field effects, the noise spectra possess a $1/f^2$ dependency, while in diffusion-dominant regime (see Appendix B), ionic relocation can potentially bring about excess noise obeying an inverse frequency power law (i.e., $1/f$ noise)[5].

In general, from the user's point of view, during an electrophysiological recording, the thermal noise can be lowered by using low impedance electrodes. The electric hum (at 50 or 60 Hz) remains the main source of noise which makes necessary the use of an HumBug filter. Sometimes, even with the use of this filter the electric hum cannot be removed, than it is not possible to achieve any recording.

4.2 *In vitro* recording in brain slice

Through these preliminary measurements it was intended to evaluate the PEDOT:PSS layer in terms of electrical performances. The quality of the recorded signal and the noise in the measured signals have been evaluated during these tests. Mice brain slices dimensions are very limiting in terms of thickness (400-500 μm thick) and it is preferable to record neural signals with unitary wire electrodes or tetrodes. Moreover this kind of measurements is not suitable for the evaluation of the probe biocompatibility and signal stability over time, since the slice can stay alive only for a few hours. For these reasons, commercially available wire unit electrodes have been used, after nanostructuration with PEDOT:PSS through potentiodynamic electrochemical route (as described in Chapter 3).

4.2.1 Experimental set-up

In Fig.4.1 the experimental set-up for the recording in brain slices is reported. For measuring, the slice is placed in a two compartment chamber. In the external compartment deionized water is warmed with a thermostat system. The slice is placed in the inner chamber onto a tissue spun support. An *in vivo*-like artificial cerebrospinal fluid (ACSF) is injected in the chamber (after a preventive warming), and, thanks to the tissue support, it can flow through both sides of the slice. It is very important to assure a good oxygenation of the slice in order to keep it alive.

From the picture in Fig.4.1 three micromanipulators can be recognized. The micromanipulators can be both manual or electronic and the electrodes are fixed on them, allowing a high precision positioning in the brain slice. In this particular case only one recording electrode has been used. Spontaneous activity, which consists in isolating action potentials from independent neural sources, has been recorded.

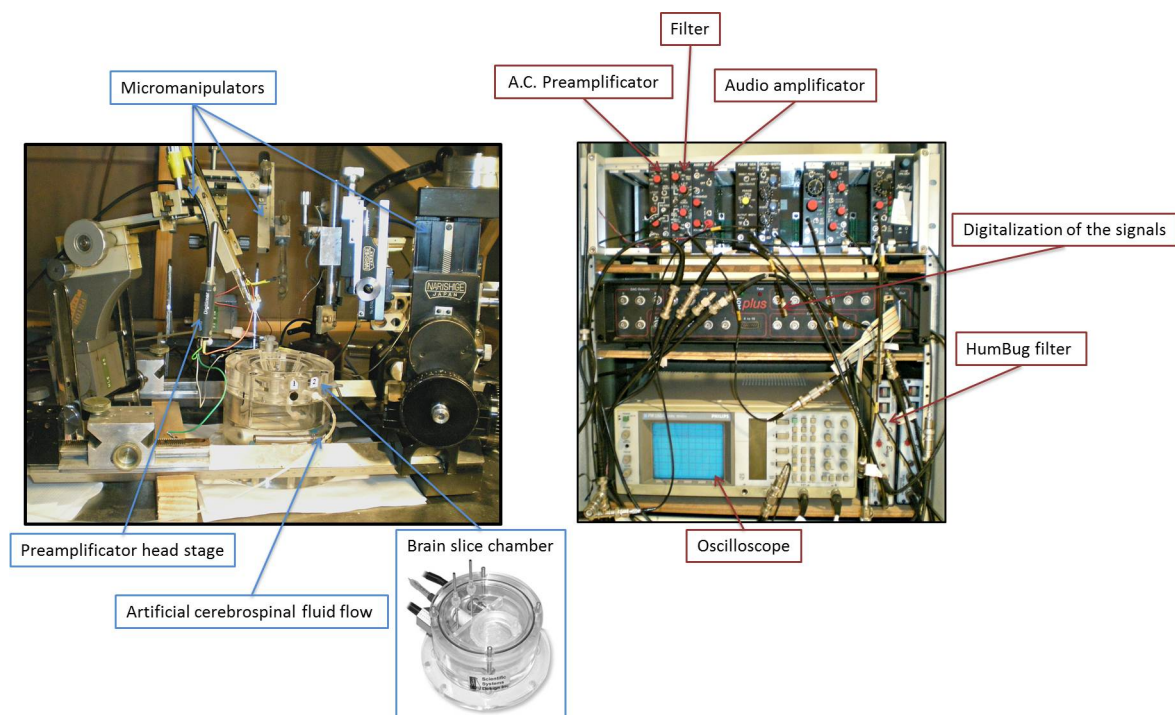


Figure 4.1: Picture of the experimental set-up for recording signals in brain slices, depicting the slice chamber and all the components for the signal digitalization.

The picture on the right in Fig.4.1 displays the set-up for recording and transcription of electrophysiological signals into digital information: an amplifier with different gain possibilities (normally set to 1000-10000), a filter for different frequencies, an HumBug filter specific for the 50 Hz electric hum, an amplifier audio that allows to "hear" the activity and possibly adjust the positioning of the electrode, and an oscilloscope.

The protocol for *in vitro* brain slice preparation was adapted from Nowak and Bullier[6] and is briefly summarized in Annex D.

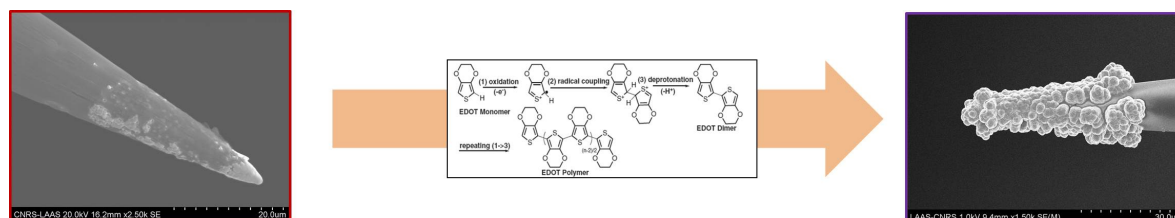


Figure 4.2: PEDOT:PSS deposited on an FHC PtIr unitary electrode through potentiodynamic electrochemical route (cyclic voltammetry from -0.7 V to 1.1 V, scan rate 50 mV/s, 2 cycles).

4.2.2 Pristine and PEDOT-modified commercial unitary electrodes: noise comparison

Commercially available microelectrodes (alphaOmega, FHC from the same batch, with identical characteristics) were modified through electrochemical polymerization of PEDOT:PSS (Fig.4.2). Different electrode materials were tested: the best results in terms of homogeneity of the deposition and impedance lowering were achieved with PtIr electrodes, while it was impossible to obtain a good polymer layer on Tungsten (W) electrodes.

As we mentioned in previous paragraphs, during an electrophysiological measurement, several noise sources, both biological and non-biological, can affect the recording. Thermal noise is thought to be the dominant noise source encountered, which is directly related to the electrode impedance and as a consequence, to the surface area of the electrode contact. This contribution to the noise can therefore be easily reduced by increasing the surface/area ratio, thanks to the PEDOT:PSS nanostructuration.

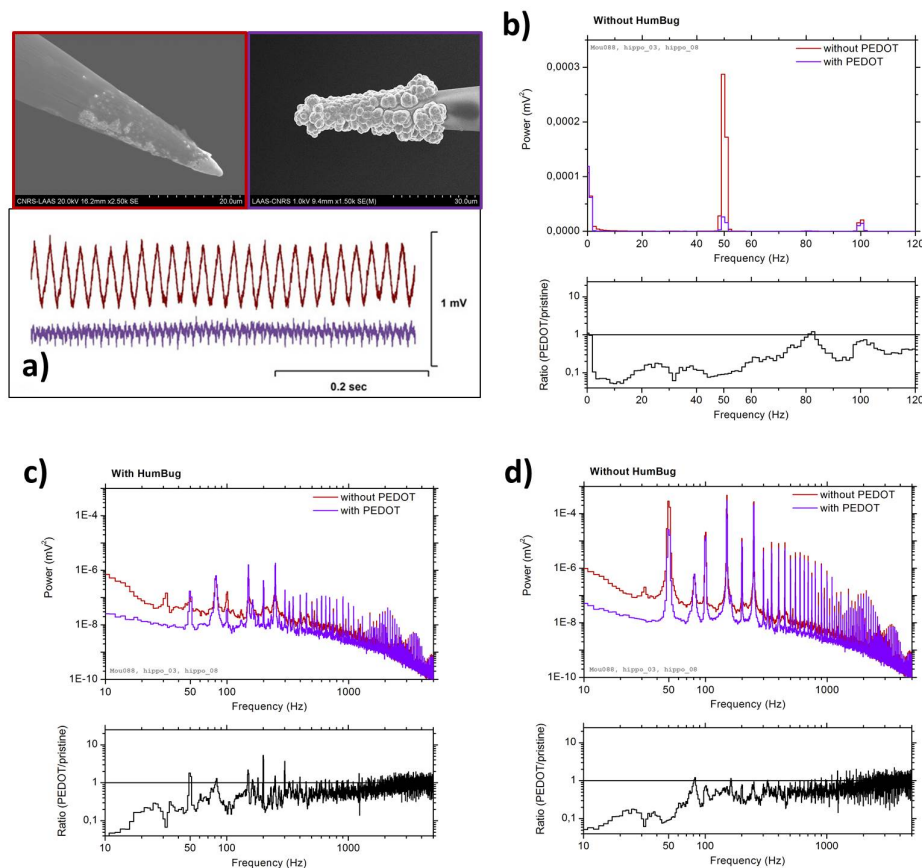


Figure 4.3: a) Comparison of electric hum recorded in a mouse brain slice maintained *in vitro*, using identical commercial microelectrodes: pristine (red) and nanostructured (violet). The signal was obtained by bypassing the HumBug, the device normally used to remove it. The 50 Hz hum is nearly negligible after nanostructuration. b) The power spectra computed from a few seconds of the same recordings shows a prominent peak at 50 Hz when the recording was obtained with the non-nanostructured electrode. Noise power spectrum between 10 Hz and 5000 Hz c) with and d) without the HumBug, and related ratio of the power without/with PEDOT coating.

Another effect can be observed, resulting from the PEDOT modification: the **removal of the electric hum at 50 Hz** (Fig.4.3.a-b)

The noise in measured signals obtained through commercially available microelectrodes (alphaOmega, FHC from the same batch, with identical characteristics) was evaluated. Some of the electrodes were used as received and the others were coated with PEDOT:PSS. Fig.4.3.a shows unfiltered records obtained the same day and in the same experimental conditions (the same brain slice). Electric hum was considerable when recordings were performed through non-nanostructured electrodes, as shown on the red trace in Fig.4.3.a. In comparison, the hum was largely reduced with the nanostructured microelectrodes (violet curve in Fig.4.3.a). This is further quantitatively evidenced when examining the power spectra (Fig.4.3.b) computed from a few seconds of the same recordings. The prominent peak at 50 Hz observed for the non-modified microelectrode is hardly visible for the PEDOT-modified one.

The same recording in presence and absence of the HumBug line noise eliminator is shown in Fig.4.3.c and 4.3.d. This comparison allows us to evaluate the noise component related to the double layer interface in the presence of PEDOT[7]. As we can see, also from the ratio of the power with and without PEDOT coating (lower part of the figure), the noise is reduced by PEDOT coating in both cases, especially at low frequencies, and, without the HumBug filter, the 50 Hz hum is reduced by a factor 10 through the PEDOT coating.

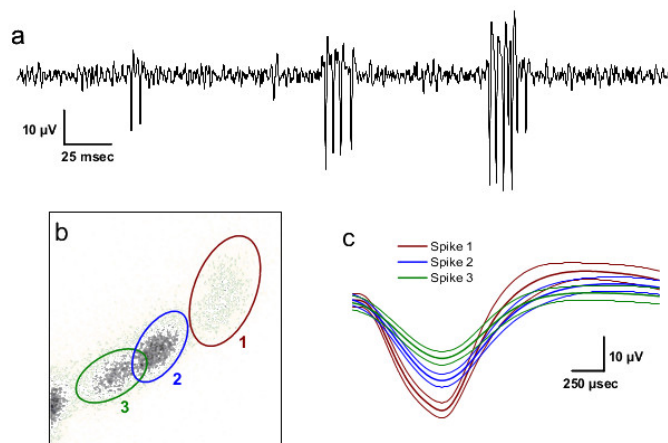


Figure 4.4: Action potentials recorded in area CA3 of the mouse hippocampus maintained *in vitro*. a) Raw trace corresponding to a portion (350 ms) of the recording. Spontaneous activity consisted in bursts of 2-5 spikes, as is typical of CA3 neurons. Action potentials displayed different groups of amplitude, suggesting that several neurons were recorded from the same electrode. b) Clustering based on spike amplitude and spike duration reveals 3 distinct group of spikes labelled 1-3. Each group correspond to the action potentials of a single neuron (refractory period >3 ms, not illustrated). The fourth cluster on the bottom left corresponds to unresolved multiunit activity. c) Average of the spikes from the three single units. Thick line: mean; thin line: mean \pm 1 SD. The isolation of 3 single units is further supported by the lack of overlap of the mean \pm SD on the downstroke of the spikes.

4.2.3 PEDOT-modified commercial electrodes: signal recording

An additional validation of the PEDOT coating consisted in determining whether PEDOT coated microelectrodes allowed the recording of spontaneous neuronal activity *in vitro*, with a signal quality comparable to, or better than that achieved with non-coated electrodes.

Figure 4.4 shows action potentials recorded in area CA3 of the mouse hippocampus. The **excellent signal-to-noise ratio of the PEDOT-modified microelectrode** allowed us to obtain well segregated signals from three neighbouring neurons. This establishes that neuronal activity can be recorded with PEDOT coated microelectrodes with a quality at least comparable to that of non-coated microelectrodes.

4.3 *In vivo* recording in mice brain

4.3.1 Implantation in the hippocampus

For the *in vivo* implantation in mice's brain, electrodes were implanted in the hippocampus, which is located in the medial part of the temporal lobe of the cortex (Fig.4.5) and plays a crucial role in memory process.

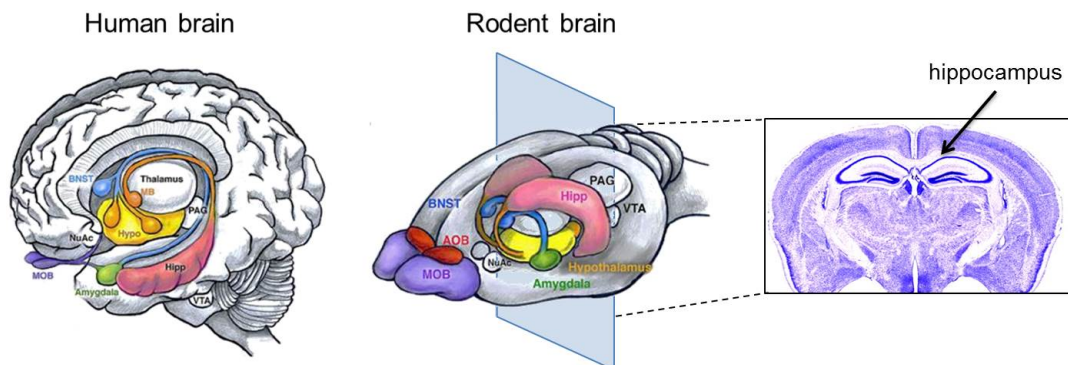


Figure 4.5: Structure of human and rodent brain. The pink zone represents the hippocampus, which is also shown in cross section (adapted from [8]).

The three main histological divisions of the hippocampus are the dentate gyrus, CA1 and CA3. A cross section of the hippocampus with its main parts is shown in Fig.4.6. The areas CA1 and CA3 are composed by pyramidal neurons which cell bodies form a compact layer, well defined and clearly visible with a microscope. Their dendrites are perpendicular to this layer. This 3D architecture makes it easier to record electrophysiologically the global activity of this population of neurons. **Schaffer collaterals** are axon collaterals given off by CA3 pyramidal cells and projecting to area CA1, where they make synapses on the dendrites of CA1 pyramidal neurons. In this way, the signals of information from the CA3 region leave via the Schaffer collateral pathways for the CA1 pyramidal neurons and stimulating artificially these axons allow to trigger simultaneously a large set of synapses. Schaffer collaterals are subject to experience dependant plasticity and play a critical role in the aspects of learning and memory[9, 10].

For all these reasons, Schaffer collaterals are one of the most studied synapses in the world. Many scientists use the Schaffer collateral synapse as a sample synapse in order to try to identify the rules synaptic functioning and synaptic plasticity.

These studies could find applications in developing medication and treatment to cure the chronic diseases, such as dementia and Alzheimer's disease[11].

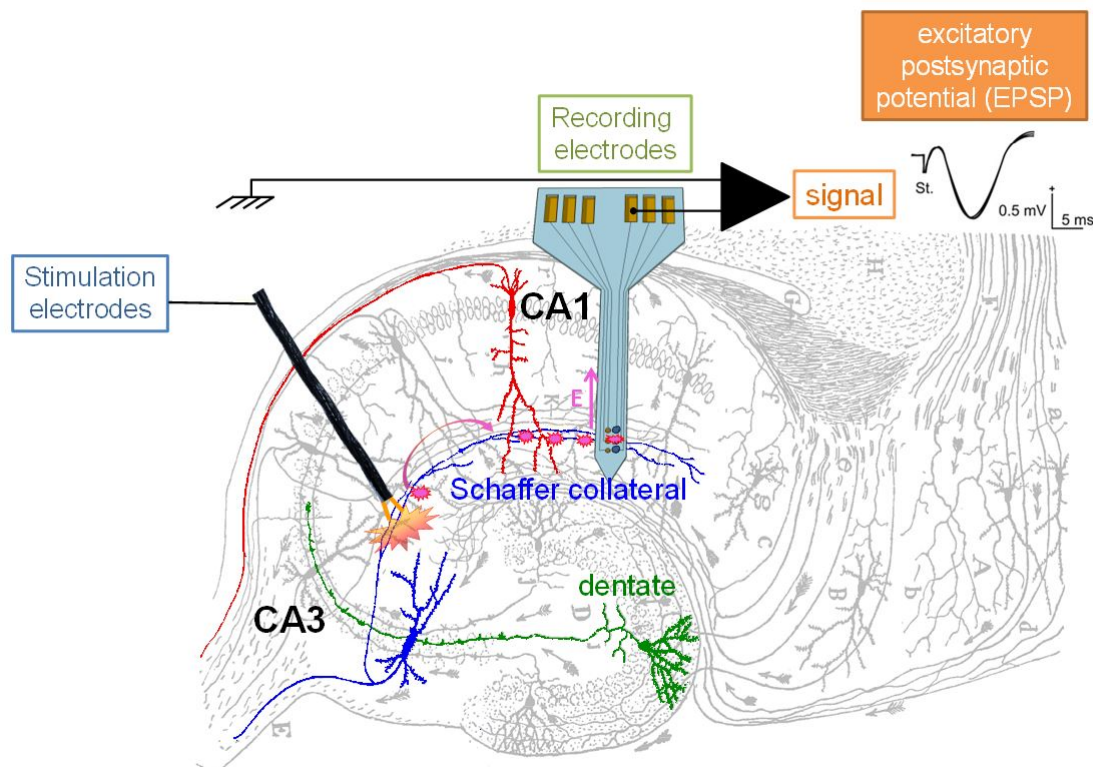


Figure 4.6: Cross section of the hippocampus (with its main regions of interest) and the placement of the stimulation and recording electrodes with the configuration used in the reported experiments (adapted from [12]).

The aim of L. Dahan's group studies is to identify the synaptic changes induced by learning at hippocampal synapses. Using the electrodes manufactured in their laboratory, they can only record from one site into the mouse hippocampus, while only some synapses are supposed to be modified. Ideally, a simultaneous recording from several spatially defined sites (less than $100 \mu\text{m}$) would be needed into the area CA1 of the hippocampus which, in mice, represents a tiny volume (less than 1 mm^3). Since recording field potentials in CA1 requires small impedance (less than $300 \text{ k}\Omega$), this is not compatible with most of small electrodes commercially available.

4.3.2 Experimental set-up

After the skin incision, a craniotomy was performed to allow unilateral access to the hippocampus, and the positioning of three electrodes (Fig.4.8 and 4.7). The insertion

into the cortex has been made possible thanks to the stiff silk layer (about 250 μm -thick) deposited on the electrode backside (as showed in Chapter 2).

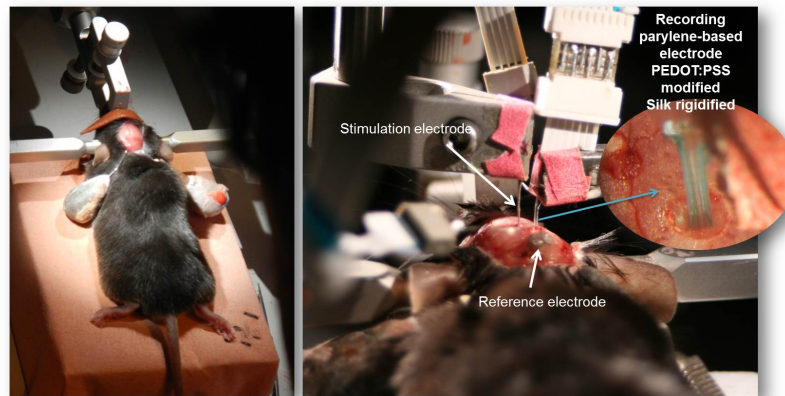


Figure 4.7: Picture of the positioning of the mouse head into the stereotaxic headholder, skin incision and electrodes positioning.

The **stimulation electrode** was constituted by two NiCr 50 μm -diameter wires, passivated by a Teflon® layer and disrobed for 250 μm -high. The **reference electrode** configured as a screw inserted into the skull. The **parylene-based microfabricated recording electrode** featured by pairs of pristine Au and PEDOT-modified microelectrodes, placed at three different depths (Fig.4.8).

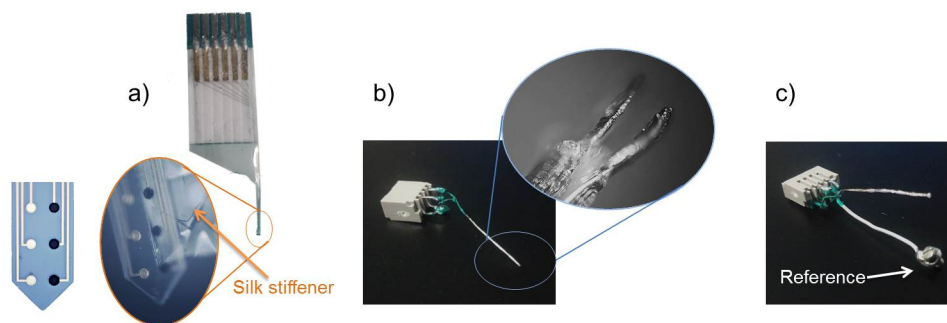


Figure 4.8: Images of the electrodes employed during the *in vivo* measurements: a) recording parylene-based electrode, constituted by 6 40 μm -diameter active areas, half PEDOT:PSS modified (dark circles) and half pristine (for details see Chapter 2), silk covered on one side. b) stimulation electrode constituted by two NiCr 50 μm -diameter wires, passivated by a Teflon® layer and disrobed for 250 μm -high. c) recording electrode (similar to the stimulating one) used for comparison purposes and reference electrode (the stainless steel screw is anchored on the skull and linked to the connector by a silver wire).

In this way it is possible to record from the electrode placed at the same depth and obtain a direct comparison between the modified and non-modified microelectrode, being sure that the recordings come from the same population of neurons. The set-up for the electrodes placement (micromanipulators) and for the transcription into digital information are similar to one shown in Fig.4.1.

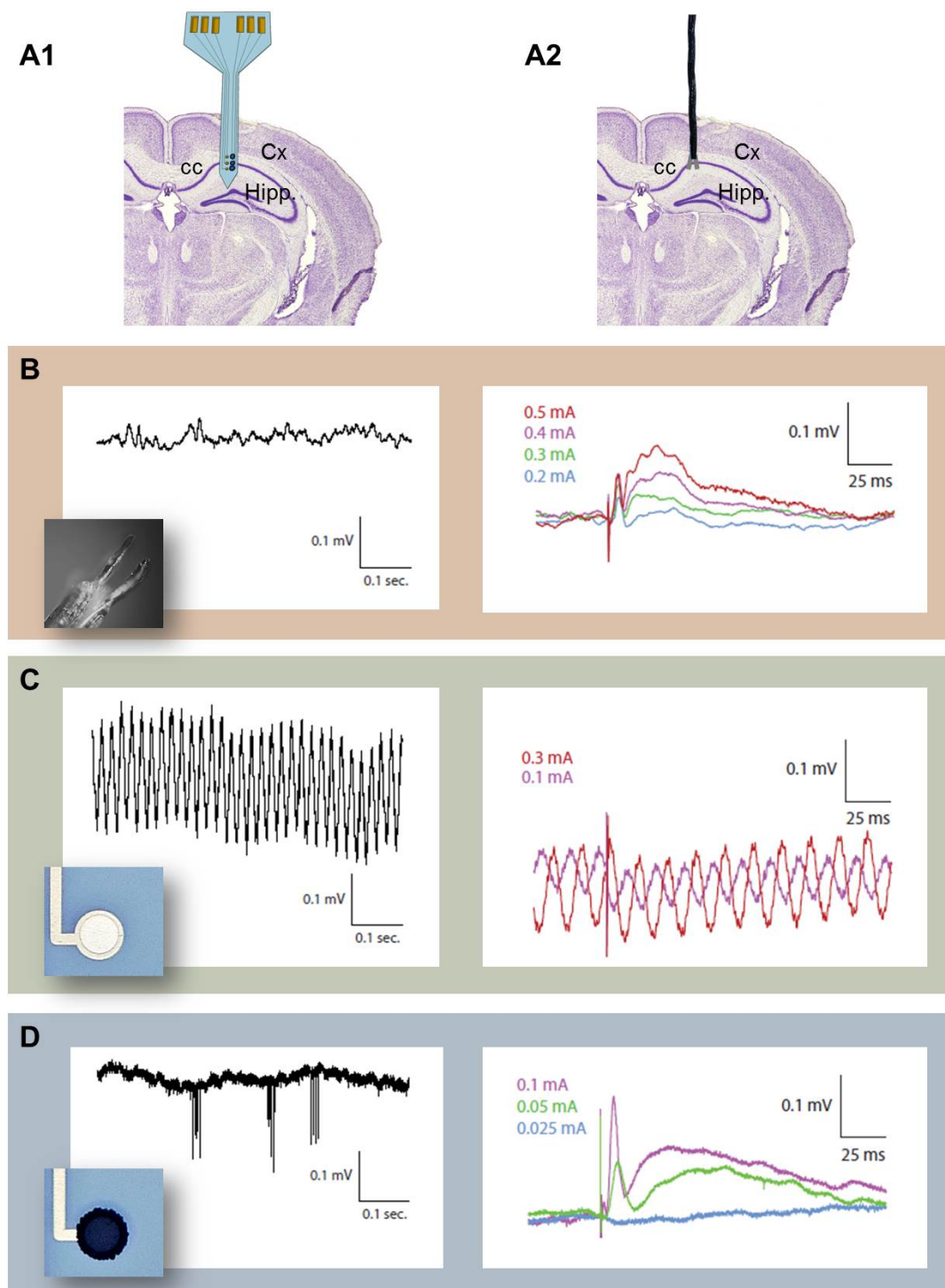


Figure 4.9: Scheme of the placement of A1) parylene-based hexatrode with 3 pristine microelectrodes and 3 PEDOT-modified microelectrodes and A2) twisted NiCr electrode, across the pyramidal layer of area CA1. Signal recording and magnification of LFPs at different stimulation intensities using B) the NiCr twisted electrode, C) pristine Au parylene-based microelectrode, D) PEDOT:PSS modified parylene-based microelectrode. Cx: Cortex, cc: corpus callosum, Hipp.: hippocampus.

4.3.3 Signal recording

The implantation of parylene based electrodes in the brain of anaesthetized mice confirmed the improvement of the recording quality produced by PEDOT:PSS nanostructuration on the microfabricated electrodes.

Figure 4.9.B presents the signal recorded by a homemade high surface electrode (NiCr twisted wires). The recordings (evoked responses) are proper, and the signal shows few high frequency noise, which is characteristic from a high surface electrode.

Note that after a stimulation artefact, the signal shows an upward deflection, called **evoked post-synaptic field potential**, reflecting the glutamatergic transmission between CA3 and CA1. This is followed by a second component, which most likely involves GABAergic transmission or network effect. Nonetheless this second component is very hard to interpret.

The signal obtained with the pristine gold parylene-based microelectrode (Fig.4.9.C) is mainly affected by the 50 Hz electromagnetic noise, with an amplitude comparable to that usually obtained before inserting the electrode in the brain or when the electrode is faulty. This is most likely a consequence of the small diameter of the electrode active area (50 μm), which resulted in a high impedance.

In Fig.4.9.D is shown that, lowering the impedance of the very same electrodes with PEDOT nanostructuration, enabled the recording of very good electrophysiological signals with very high S.N.R. The raw trace of the signal exhibits some high frequency noise but, nevertheless, since signal on noise ratio is very high, action potentials can be clearly distinguished. **The initial peak of evoked responses presents high amplitude, with field potentials even higher than the ones recorded by the NiCr electrode.**

4.4 Conclusion

In this chapter, preliminary results on *in vitro* and *in vivo* validation of the PEDOT:PSS coating have been shown. Particularly interesting is the capability (confirmed both *in vitro* and *in vivo*) of the PEDOT:PSS layer to eliminate the 50 Hz electric hum, thanks to a significant decrease of the impedance, making it possible to measure signals with an excellent S.N.R. even on micrometer-sized electrodes. We are aware of the fact that a lot still remains to be optimized, not only in terms of experiment to be carried out for *in vitro* and *in vivo* recordings, but also in terms of long term reliability of the recordings, provided by the high biocompatibility and flexibility features of the probes. The stability of the PEDOT:PSS coating also need to be evaluated in the near future.

The collaboration with L. Dahan's group allowed first to evaluate the performances of the produced devices which showed a significant improvement of neurophysiological recordings quality compared to the homemade electrodes currently used in their laboratory. The employment of our PEDOT:PSS modified electrodes will represent the possibility to progress in the fundamental studies on the learning mechanisms.

Bibliography

- [1] Gytis Baranauskas, Emma Maggiolini, Elisa Castagnola, Alberto Ansaldo, Alberto Mazzoni, Gian Nicola Angotzi, Alessandro Vato, Davide Ricci, Stefano Panzeri, and Luciano Fadiga. Carbon nanotube composite coating of neural microelectrodes preferentially improves the multiunit signal-to-noise ratio. *Journal of Neural Engineering*, 8(6):066013, 2011.
- [2] R A Cottis. Interpretation of electrochemical noise data. *Corrosion*, 57(3):265–285, 2001.
- [3] Scott F Lempka, Matthew D Johnson, David W Barnett, Michael A Moffitt, Kevin J Otto, Daryl R Kipke, and CC McIntyre. Optimization of microelectrode design for cortical recording based on thermal noise considerations. In *Engineering in Medicine and Biology Society (EMBS), 28th Annual International Conference of the IEEE*, pages 3361–3364, 2006.
- [4] Jeffrey M Hausdorff and C-K Peng. Multiscaled randomness: A possible source of 1/f noise in biology. *Physical review E*, 54(2):2154, 1996.
- [5] Arjang Hassibi, Reza Navid, Robert W Dutton, and Thomas H Lee. Comprehensive study of noise processes in electrode electrolyte interfaces. *Journal of Applied Physics*, 96(2):1074–1082, 2004.
- [6] Lionel G Nowak and Jean Bullier. Spread of stimulating current in the cortical grey matter of rat visual cortex studied on a new in vitro slice preparation. *Journal of Neuroscience Methods*, 67(2):237–248, 1996.
- [7] Takashi D Yoshida Kozai, Nicholas B Langhals, Paras R Patel, Xiaopei Deng, Huanan Zhang, Karen L Smith, Joerg Lahann, Nicholas A Kotov, and Daryl R Kipke. Ultrasmall implantable composite microelectrodes with bioactive surfaces for chronic neural interfaces. *Nature materials*, 11(12):1065–1073, 2012.
- [8] Katie Sokolowski and Joshua G Corbin. Wired for behaviors: from development to function of innate limbic system circuitry. *Frontiers in Molecular Neuroscience*, 5(55):1–15, 2012.
- [9] Roger D Traub and Richard Miles. *Neuronal networks of the hippocampus*, volume 777. Cambridge University Press, 1991.

- [10] George Paxinos and Keith BJ Franklin. *The mouse brain in stereotaxic coordinates*. Gulf Professional Publishing, 2004.
- [11] Marcello D’Amelio, Virve Cavallucci, Silvia Middei, Cristina Marchetti, Simone Pacioni, Alberto Ferri, Adamo Diamantini, Daniela De Zio, Paolo Carrara, Luca Battistini, et al. Caspase-3 triggers early synaptic dysfunction in a mouse model of alzheimer’s disease. *Nature neuroscience*, 14(1):69–76, 2011.
- [12] John O’keefe and Lynn Nadel. *The hippocampus as a cognitive map*, volume 3. Clarendon Press Oxford, 1978.

5.1 Main outcomes emerged from this work

The PhD project here presented is born with the aim to propose a strategy for the long term reliability of implanted devices for deep brain recording and stimulation. This is a key point to make this technology available for clinical purposes. Until now, most of the implanted devices undergo a quick deterioration and they need, after a certain time, to be completely removed or replaced (in part or in whole). This prevents a widespread use of this technology since they bring into play the patient's safety. In order to address this issue, the main causes of this lack of reliability have been taken into account:

- 1) **the acute body reaction** triggered by the electrode penetration injury, which leads to the encapsulation the device in an insulating glial scar, consequently affecting the recording quality;
- 2) the **poor electrical performances of micrometric-sized electrodes**, which suffer of very high impedance. Strategies to address these issues have been proposed in the literature: the use of a flexible, highly conformable devices to reduce the tissue inflammation by reducing the mechanical mismatch between the probe and the target tissue; the modification of the active microelectrode surface with polymeric nanostructures with high intrinsic conductivity and roughness, to increase the surface/area ratio and decrease the impedance.

Since the two causes of failure are strictly related, strongly influencing each other, here a coupling of these two features (a flexible device with nanostructured microelectrodes) has been proposed. Importantly, the high biocompatibility of the chosen materials and procedures has been the guideline of the work.

Flexible parylene-based implantable devices have been fabricated, implementing a straightforward process which exploits the poor adhesion properties of parylene on silicon. Indeed, all the classical clean room technological steps could be performed, with a good stability of the parylene substrate. At the end, the device was simply released by peeling off from the silicon wafer. Among the technological steps, the physical etching of thin and thick layer of parylene has been particularly optimized, solving a problem commonly found in the literature: the etching residues.

The fabrication procedure here implemented can be exploitable, in future works, for the production of more dense implantable microelectrode arrays, ECoG devices or retinal implants, in order to meet the needs expressed in neuroscience for implants with high density of active sites, recording from a large populations of cells with high time stability.

Parylene-C, classified as a United States Pharmacopeia (USP) Class VI material, represents nowadays one of the most promising candidate for implantable devices with long-life expectancy. Nevertheless, a tricky drawback is related to its flexible feature: the lack of stiffness to perform the implantation. During this work, the problem has started to be addressed, founding an optimized solution along the progression of another PhD project devoted to this topic. A highly biocompatible and biodegradable polymer, the silk fibroin, has been deposited on the back side of the devices, allowing *in vivo* implantation in mice brain as described in Chapter 4.

As mentioned before, special attention has been paid to the choice of the materials and *in vitro* cytotoxicity/biocompatibility test have been performed. Since the produced devices undergo both chemical and physical treatments, the good viability of cultured neuroblastoma cells has been stated. A more-in-depth biocompatibility investigation have been performed on the used materials through organotypic culture methods. SEM observations, both on fixed cell and organs, confirmed the very good biocompatibility of the used substrate that will interface with the living brain tissue.

Once the fabrication step accomplished, the electrical performances of the microelectrodes have been considered. The electrochemical polymerization of 3,4-ethylenedioxythiophene (EDOT) in a polyanion, sodium poly(styrene-4-sulfonate)(NaPSS), has been performed through three different oxidative electropolymerizations on the electrodes active area. This part of the work focused on the study of the polymerization mechanism of PEDOT:PSS and of the conductivity of the polymer layers both from the macro and the microscopic point of view. The main outcomes related to this part of the work are:

- the **elucidation of the electropolymerization mechanism**, through SEM and AFM images.
- the achievement of an **impedance lowering over all the explored frequencies** after the polymer deposition, strongly dependent by the electropolymerization parameters and then optimized to achieve, for certain frequencies of interest in neurophysiology, up to 3 order of magnitude of lowering.
- a **good stability statement** of the produced layers after accelerated ageing process.
- a strong **correlation between the current-carrying ability and the topography of the PEDOT:PSS**, clearly showed for the first time through C-AFM measurement.
- a measured **intrinsic conductivity of PEDOT:PSS layers up to 200 S/cm** which confirms the power of the electrochemical deposition in terms of conductivity increase.
- a **negative temperature dependence of the conductivity** but an increase of the conductivity for a layer subjected to continuous heating in the case of highly homogeneous polymer grains on the surface; this is likely to be explained considering the **thermally activated hopping transport in the conductivity mechanism**.

The obtained devices, optimized in terms of mechanical and electrical properties,

have been implanted in mice's brain, allowing the recording and the comparison between nanostructured and pristine electrodes on the same implanted device. **The capability of PEDOT:PSS layer to eliminate the electric hum at 50 Hz** has been demonstrated both *in vitro* and *in vivo* recordings. Moreover the noise component related to double layer interface electrode-tissue, in the presence and in the absence of PEDOT:PSS have been considered by recording with and without the HumBug filter. Here, this aspect, has been investigate, and a significant **lowering of the overall noise in the case of PEDOT:PSS coating has been observed**. From the *in vivo* measurements, **very clean signals with high signal-to-noise ration have been recorded**, proving the capability of our device to detect no only post synaptic induced field potentials but also single spikes.

5.2 Short-term perspectives

Few mice are currently implanted, allowing us to produce in the next months, proper statistics on the recorded signals. Moreover, recordings over several months will permit to study the electrode stability over time, and will give us also an idea of the progress of the glial reaction. It will also be possible through postmortem histological exams, to verify the state of the tissues around the implant. These experiments, which are really time-consuming, are currently on progress and they could be the object of a future publication.

5.3 Future research guidelines for this project

The two research guidelines that have been contemplated for future works, lie in: 1) the nanostructuration aspects; 2) the coupling with optogenetics.

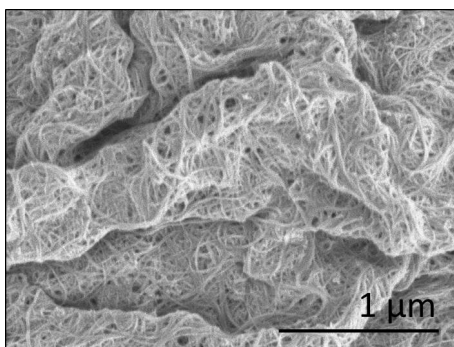


Figure 5.1: SEM image of CNTs-PEDOT:PSS embedded electrochemical deposited on a gold electrode.

1) It has been stated that the conductivity of PEDOT can be increased by the use of solvent or dopant molecules that can function as plasticizer, decreasing inter-chain interaction and helping reorientate the polymer chains in a more favourable conformation[1]. Another interesting aspect, that has emerged in recent works, is the integration of nanomaterials onto the electrode surface, both for *in vitro* MEA and *in vivo* recording[2, 3, 4, 5]. In particular carbon nanotubes (CNTs) have aroused interest because of their well-known mechanical and electrical properties. Moreover, many recent *in*

vitro studies have displayed a relation between the CNTs and the neural cell behaviour, such as a stimulation and orientation of the neurite outgrowth[6, 7, 8, 9]. Nevertheless, the

debate over the toxicity of these materials, when implanted in the human body, is still open, especially in cases where delamination of the nano-objects can occur. A strategy to follow could be, therefore, the encapsulation of the nanostructure into a very stable polymer matrix, that could be obtained by electropolymerization of PEDOT in a CNTs containing solution[10, 11, 12, 13, 14]. These kinds of nanostructuration could provide electrical and mechanical enhancement and could increase the stability of the layer overtime.

Moreover, as mentioned in Chapter 1, a new generation of implantable devices, incorporating bioactive components, such as anti-inflammatory drugs or nerve growth factor (NGF), has been reported. Since the produced electrodes need a biodegradable layer of polymer (silk) to enhance the mechanical properties for the cortical insertion, a new strategy for the integration of bioactive components into this layer is currently on progress.

2) **Optogenetics** means the use of light and genetically encoded light-sensitive proteins (called opsins) to modulate the activity of specific cells. This technique, which combines optics and genetics, is an emerging field in neuroscience and it is employed to control and monitor the activities of individual neurons in living tissue, for example rapidly activating or inhibiting a specific population of neurons in the brain[15, 16, 17, 18]. To perform optogenetics, a photosensitive molecule targeted to specific cells (viral vectors are commonly used to deliver opsin genes to neurons) is required. Transgenic mice will then allow the viral-mediated expression of these opsins in a specific neuronal population. At this point it is necessary to deliver light into the brain, and then perform electrophysiological or behavioral readouts for optogenetic manipulation of a system.

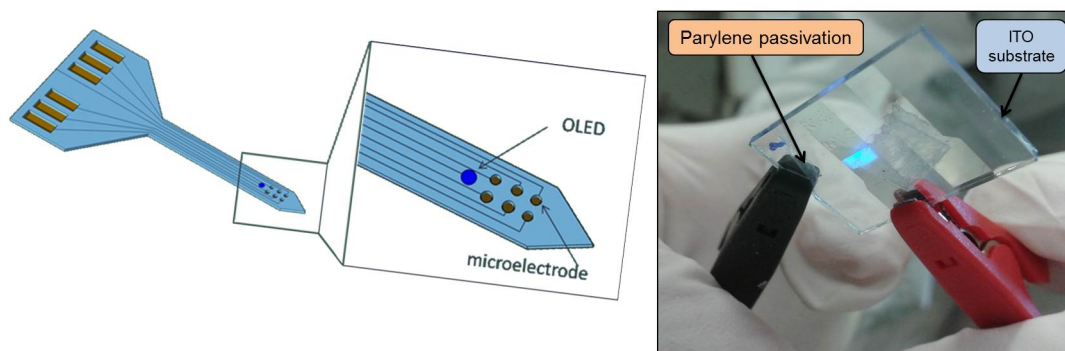


Figure 5.2: Schematic representation of the OLED integrated electrode and first test of blue (470 nm) OLED encapsulation into parylene-C.

Optogenetics is potentially an ideal technology to be combined with microelectrode arrays to create a bidirectional neuroprosthetic. The possibility to use a flat and homogeneous light source, as an organic light-emitting diode (OLED) has a clear advantage for implantable integrated device. Blue (470 nm) OLEDs based on small organic molecules in bottom configuration can be used as a bright and power efficient solid-state light to excite the neurons. This paved the way to the integration of OLED organic multilayer heterojunction on a flexible substrate, which constitutes the neural probe. By encapsulating

the device with parylene, the biocompatibility of the entire device is ensured. Coupling optogenetic stimulation to recording electrodes with improved long term reliability holds great promise to become an invaluable clinical and diagnostic tool in the near future, that, in particular, could find application for the comprehension of mechanisms behind common disease such as Alzheimer's disease.

Bibliography

- [1] SKM Jönsson, Jonas Birgeron, Xavier Crispin, Grzegorz Greczynski, Wojciech Osikowicz, AW Denier Van Der Gon, William R Salaneck, and Mats Fahlman. The effects of solvents on the morphology and sheet resistance in poly (3, 4-ethylenedioxythiophene)–polystyrenesulfonic acid (PEDOT–PSS) films. *Synthetic Metals*, 139(1):1–10, 2003.
- [2] Nicholas A Kotov, Jessica O Winter, Isaac P Clements, Edward Jan, Brian P Timko, Stéphane Campidelli, Smita Pathak, Andrea Mazzatenta, Charles M Lieber, Maurizio Prato, et al. Nanomaterials for neural interfaces. *Advanced Materials*, 21(40):3970–4004, 2009.
- [3] E Ben-Jacob and Y Hanein. Carbon nanotube micro-electrodes for neuronal interfacing. *Journal of Material Chemistry*, 18(43):5181–5186, 2008.
- [4] Asaf Shoval, Christopher Adams, Moshe David-Pur, Mark Shein, Yael Hanein, and Evelyne Sernagor. Carbon nanotube electrodes for effective interfacing with retinal tissue. *Frontiers in Neuroengineering*, 2(4):1–8, 2009.
- [5] Lilach Bareket-Keren and Yael Hanein. Carbon nanotube-based multi electrode arrays for neuronal interfacing: progress and prospects. *Frontiers in Neural Circuits*, 6(122):1–16, 2012.
- [6] Hui Hu, Yingchun Ni, Vedrana Montana, Robert C Haddon, and Vladimir Parpura. Chemically functionalized carbon nanotubes as substrates for neuronal growth. *Nano Letters*, 4(3):507–511, 2004.
- [7] Muhammed K Gheith, Vladimir A Sinani, James P Wicksted, Robert L Matts, and Nicholas A Kotov. Single-walled carbon nanotube polyelectrolyte multilayers and freestanding films as a biocompatible platform for neuroprosthetic implants. *Advanced Materials*, 17(22):2663–2670, 2005.
- [8] Tamir Gabay, Eyal Jakobs, Eshel Ben-Jacob, and Yael Hanein. Engineered self-organization of neural networks using carbon nanotube clusters. *Physica A: Statistical Mechanics and its Applications*, 350(2):611–621, 2005.
- [9] Xuan Zhang, Shalini Prasad, Sandip Niyogi, Andre Morgan, Mihri Ozkan, and Cengiz S Ozkan. Guided neurite growth on patterned carbon nanotubes. *Sensors and Actuators B: Chemical*, 106(2):843–850, 2005.

- [10] Chuang Peng, Jun Jin, and George Z Chen. A comparative study on electrochemical co-deposition and capacitance of composite films of conducting polymers and carbon nanotubes. *Electrochimica Acta*, 53(2):525–537, 2007.
- [11] Xiliang Luo, Cassandra L Weaver, David D Zhou, Robert Greenberg, and Xinyan T Cui. Highly stable carbon nanotube doped poly (3, 4-ethylenedioxythiophene) for chronic neural stimulation. *Biomaterials*, 32(24):5551–5557, 2011.
- [12] Ramona Gerwig, Kai Fuchsberger, Birgit Schroepfel, Gordon Steve Link, Gerhard Heusel, Udo Kraushaar, Wolfgang Schuhmann, Alfred Stett, and Martin Stelzle. PEDOT–CNT composite microelectrodes for recording and electrostimulation applications: fabrication, morphology, and electrical properties. *Frontiers in Neuroengineering*, 5, 2012.
- [13] Sanyuan Chen, Weihua Pei, Qiang Gui, Rongyu Tang, Yuanfang Chen, Shanshan Zhao, Huan Wang, and Hongda Chen. PEDOT/MWCNT composite film coated microelectrode arrays for neural interface improvement. *Sensors and Actuators A: Physical*, 193:141–148, 2013.
- [14] Haihan Zhou, Xuan Cheng, Li Rao, Tao Li, and Yanwen Y Duan. Poly (3, 4-ethylenedioxythiophene)/multiwall carbon nanotube composite coatings for improving the stability of microelectrodes in neural prostheses applications. *Acta Biomaterialia*, 9(5):6439–6449, 2013.
- [15] Jiayi Zhang, Farah Laiwalla, Jennifer A Kim, Hayato Urabe, Rick Van Wagenen, Yoon-Kyu Song, Barry W Connors, Feng Zhang, Karl Deisseroth, and Arto V Nurmikko. Integrated device for optical stimulation and spatiotemporal electrical recording of neural activity in light-sensitized brain tissue. *Journal of Neural Engineering*, 6(5):055007, 2009.
- [16] Karl Deisseroth. Optogenetics. *Nature methods*, 8(1):26–29, 2011.
- [17] Ramin Pashaie, Polina Anikeeva, J Lee, Rohit Prakash, and Ofer Yizhar. Optogenetic brain interfaces. *IEEE Reviews in Biomedical Engineering*, 7:3–30, 2013.
- [18] Thomas J Richner, Sanitta Thongpang, Sarah K Brodnick, Amelia A Schendel, Ryan W Falk, Lisa A Krugner-Higby, Ramin Pashaie, and Justin C Williams. Optogenetic micro-electrocorticography for modulating and localizing cerebral cortex activity. *Journal of Neural Engineering*, 11(1):016010, 2014.

APPENDIX

A. Microfabrication Techniques

In this appendix, some common techniques used in typical microfabrication processes are explained. However, only the techniques employed to accomplish the fabrication part in this project are presented.

Spin coating

Spin coating is a widespread practice in modern science and engineering, where it is used to deposit uniform coatings of organic materials and/or to uniformly distribute particulate matter on a flat surface. In particular, spin coating is used in the microelectronics industry, to coat silicon wafers with a photoresist at the start of the lithographic patterning process. In order to achieve high-fidelity lithography, a smooth, uniform photoresist film of predictable and reproducible thickness is required. A great deal of effort has been invested in cataloguing the dependence of film thickness and uniformity on the experimental parameters. In this process, a compound is dissolved in a volatile liquid solvent, poured on a wafer and the rotated at high speed. The liquid spreads, the volatile solvent evaporates on a hotplate and it leaves a uniform solid thin layer of the material on the sample (or wafer). Fig.3.a illustrates the scheme of a spin-coating process and Fig.3.b-c illustrate the machines available in our laboratory and used in our process.



Figure 3: a) spin coating scheme, b) and c) spin coaters available in our laboratory.

Photolithography

Photolithography, literally meaning light-stone-writing in Greek, is the process by which patterns are transferred onto a substrate using light and UV lithography (perhaps the most commonly used photolithography technique in operation today). It is the means by which the small-scale features of integrated circuits are created.

A typical photolithographic process consists of producing a photomask having the desired pattern and subsequently transferring in parallel manner those patterns onto a wafer substrate using an UV-light sensitive resists (photoresist). Usually the mask is constituted by a glass substrate with clear and opaque regions. Materials used to fabricate it are either soda-lime glass (transmittance from 360 nm to 2750 nm) or quartz (fused silica: transmittance from 200 nm); the choice depends on the photosensitive material used and the wavelength sensitivity.

Photoresists have two basic forms: Negative and Positive. Negative photoresist reticulates during radiation exposure so that the unexposed resist is removed in the development process leaving an inverse image of the mask in the resist. Positive resist is broken down during radiation, so exposed areas can be easily removed in the development process step. Then positive image of the mask is obtained in the photoresist. Fig.4 illustrates the photolithographic process and the two resist types.

The overall process of UV lithography can be summarized in eight steps:

1. Surface Preparation: before the resist is applied to the substrate, the surface is cleaned to remove any traces of contamination from the surface of the wafer such as dust, organic, ionic and metallic compounds and a layer of Silicon dioxide is formed by a wet or dry oxidation process. Sometimes adhesion promoters are used to assist resist coating.
2. Resist Coating: after the surface is cleaned and primed, the photoresist is applied by spin coating (see subsection 5.3). The photoresist bonds uniformly to the surface, with the excess flying off during spinning. A coating solvent is then used to dissolve the buildup along the edge of the surface.
3. Pre-Bake: it is a simple process of heating the surface in a convection oven or through a heated plate placed below the surface. The purpose of the pre-bake is to evaporate the excess coating solvent and to compact and harden the photoresist.
4. Mask Alignment: the mask creates a sort of shadow between the light and the surface: less light passes through sections blocked by the mask. Mask must be aligned correctly in reference to the surface. This procedure is accomplished by hand using certain marks on the mask and the surface, or by using an automatic pattern recognition device. There are several different ways the mask can be placed in reference to the surface, including:
 - *Contact*: The mask is in contact with the surface during exposure.
 - *Proximity*: The mask is close but not touching the surface during exposure.
 - *Projection*: The mask is not close to the surface, and the light passing between them is subject to imaging optics.
5. Exposure: during the exposure the photoresist, surface, and mask are subjected to UV light via a UV lamp for a certain time optimized for each photoresist type and thickness.
6. Development: during the exposure process, the resist undergoes a chemical reaction and depending on its chemical composition (negative or positive), it can react in two ways when the light strikes the surface, as we described before.
7. Post-Bake: although not necessary for all processing, the post-bake is used to stabilize and harden the photoresist. It also removes any trace of development chemicals.

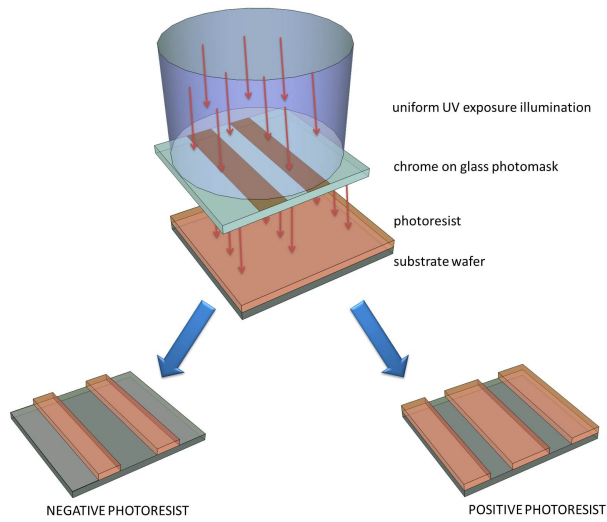
8. Photoresist removal/processing.

Figure 4: Scheme of the main processes in the photolithography.

The theoretical resolution capability (minimum size of the individual photopatterned elements of shadow photolithography) consists of equal lines and spaces of width b , is given by:

$$b_{min} = \frac{3}{2} \sqrt{\lambda \left(s + \frac{d}{2} \right)} \quad (1)$$

Where, b_{min} is the minimum feature size transferable, s is the gap between the mask and the photoresist surface, λ is the wavelength of the exposing radiation and d is the photoresist thickness. From this equation we notice that to improve resolution, it is necessary to get shorter wavelength, smaller gaps and thinner resist layers.

Lift-off process

Lift-off is a technique to pattern a metal layer starting from a negative image of the pattern on a photoresist layer before the metal deposition step. After depositing the metal (e.g. by evaporation), the resist is removed taking the unwanted metal with it. Fig. 5 schematizes the basic steps of the lift-off process.

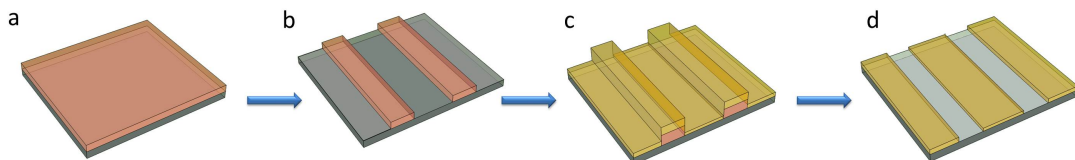


Figure 5: Scheme of the lift off process: a) resist deposition, b) resist patterning, c) metal evaporation, d) resist dissolution.

The resist wall profile (shown in Fig.6) are a critical parameter in this technique, and

they can be controlled during the photolithography by adjusting resist tone, exposure dose, developer strength, and development time.

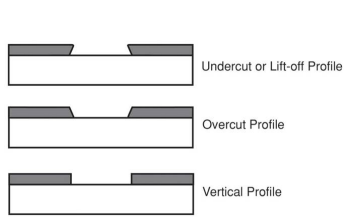


Figure 6: The three different photoresist profiles.

The undercut profile is the most used in the lift-off, and it is normally obtained with a negative resist. The overcut profile is the profile that is normally obtained from a positive-tone photoresist. The vertical profile achieves the best pattern fidelity, but is relatively difficult to obtain.

The major problems in lift-off process are retention of unwanted parts of the metal layer on the wafer, metal "ears" along the sidewall (especially in case of overcut or vertical profile) and redeposition of metal particle onto the wafer surface.

Metal deposition: evaporation

The process of thin film coating by means of Physical Vapour Deposition (PVD) is to apply electric current and voltage or bombardment of inert gas to ionize the desired material. Once the material is ionized into vapour form it is deposited on the desired substrate. Thermal evaporation is one of the most commonly used metal deposition techniques. It consists of vaporising a solid material (pure metal, eutectic or compound) by heating it to sufficiently high temperatures and recondensing it onto a cooler substrate to form a thin film. In resistive thermal evaporation the heating is carried out by passing a large current through a filament container (usually in the shape of a basket, boat or crucible) which has a finite electrical resistance. A bombardment with a high energy electron beam, usually several KeV, from an electron beam gun can also be used to achieve the heating. The choice of this filament material is dictated by the evaporation temperature and its inertness to alloying/chemical reaction with the evaporant. This technique is also known as "indirect" thermal evaporation since a supporting material is used to hold the evaporant. Normal vacuum levels are in the medium to high vacuum range of 10^{-5} to 10^{-9} Torr.

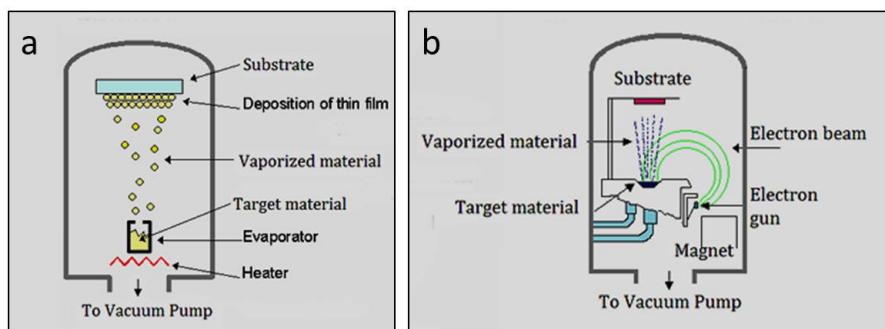


Figure 7: Scheme of the PVD machine in the case of a) resistance heating evaporation and b) electron beam evaporation.

The film thickness is then determined by using a crystal quartz microbalance. For our processes the electron beam physical vapour deposition was performed at room temperature ($20 \pm 1^\circ \text{C}$) at the working pressure of 2×10^{-7} mbar, with a deposition rate of 1 nm/s both

for Au and Ti and 0.2 nm/s for Ni. Fig.7 depicts the schematic image of a PVD machine.

Plasma etching

Plasma etching is a technique introduced in the seventies, mainly for stripping resists. In the eighties, plasma etching became a mature technique to etch layers and was introduced in the production of integrated circuits. A plasma contains positive ions, electrons, neutral gas atoms or molecules, UV light and also excited gas atoms and molecules, which can carry a large amount of internal energy. In the plasmas, free electrons collide with neutral atoms/molecules and, through a dissociative process, they can remove one electron from the atom/molecule, which gives a net result of two electrons and one ion. Depending on the energy of the incoming electron, this collision can result also in other species, such as negative ions, because of electron association, excited molecules, neutral atoms and ions. The light emitted by the plasma is due to the return of excited electrons to their ground state. If the ions from a plasma are accelerated towards a substrate via an electrical field, then these ions can react with substrate atoms and cause etching or deposition of layers. This process is called plasma etching or dry etching (in comparison with wet etching, using chemicals in an etching bath). Capacitively coupled RF plasmas are still the most common plasmas used in dry etching. By choosing the gas mixture, power, pressure etc. we can quite precisely tune, or specify, the effects of the plasma upon the surface and the etching rate. In reactive ion etching (RIE), the technique used in this work, ions have a higher probability to have a movement in the direction given by the electric field. This makes a tendency to anisotropic etching.

In general, plasma etching is a chemical etching, not a physical etching. This means that a chemical reaction takes place between the solid atom (from the film to be etched) and gas atoms to form a molecule, which is removed from the substrate. Because of the existing DC bias, there is always some sputtering. For the large majority of etching processes, this physical etching component is so small that can be neglected. The main steps in the etching process are: 1. formation of the reactive particle, 2. arrival of the reactive particle at the surface to be etched, 3. adsorption of the reactive particle at the surface, 4. chemisorption of the reactive particle at the surface, i.e. a chemical bond is formed, 5. formation of the product molecule, 6. desorption of the product molecule and 7. removal of the product molecule from the reactor.

Many parameters, first of all, the DC voltage, can influence the etching process and the etching rate. In general, the dimensions of the reactor are fixed. In this case, the DC voltage can be influenced by the process parameters. The DC voltage is created to repel electrons, therefore, the higher the electron density and the higher the electron energy, the higher the modulus of the DC voltage will be: a more negative voltage is necessary to repel a larger number of electrons, with higher energies. Using this reasoning, we are able to predict the tendencies of the DC bias voltage. The electronegativity of used gas(es) is another determining factor. When all other process parameters remain constant, the electronegativity of the gas will determine the DC voltage. Gases with low electronegativity,

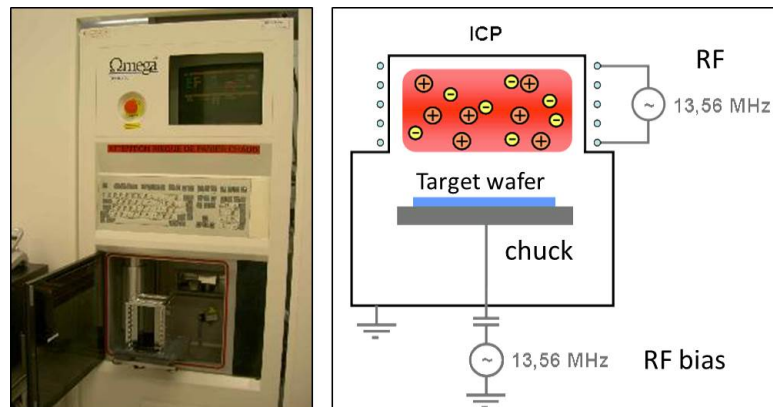


Figure 8: The machine Aviza Technology Omega 201 used in our process (on the left) and a scheme of the machine functioning (on the right).

such as O_2 (used for our process), N_2 etc. have very negative DC bias voltages. The pressure of the plasma and the temperature also influence the DC bias voltage. The influence of power is straightforward: an increase of power increases both the density and the energy of the free electrons. Therefore, the DC voltage becomes more negative with increasing power.

A schematic draw of the RIE machine and the equipment used for this work are shown in Fig.8.

B. Electrochemical Processes

Electrochemistry is the discipline that deals with chemical reactions which take place at the interface between a solid metal or a semiconductor electrode and an ionic conductor usually called the electrolyte.

These sections, far from being exhaustive about electrochemistry, set the objective to clarify the results of Chapter 3 by giving some relevant fundamental notions.

When an electronic conductor is immersed in an electrolyte a separation of charges at the interface takes place: this phenomenon is called formation of an electrochemical **double layer** and it could be modeled as a plane capacitor. Between the two phases a difference of potential has therefore been created. It is not possible to measure the absolute value of this potential but we can know the **relative potential (E)** of the electrode by comparing it to that of another electrochemical interface that has been chosen as **reference**. For these reasons, a classical electrochemical experiments normally occur in a three-electrodes cell controlled by a potentiostat (Fig.9): a difference of potential is applied between the **working electrode (WE)** and the so called **counter electrode (CE)** and, thanks to a **reference electrode (RE)**, we are able to measure the current passing between the two.

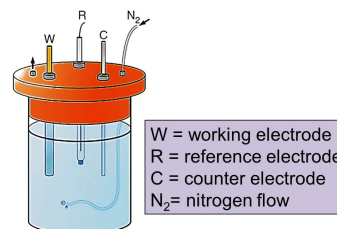


Figure 9: Scheme of a classical three-electrode cell.

An electrochemical reaction is a heterogeneous chemical process involving the transfer of electrons between a metal or a semiconductor, the electrode, and an ionic conductor, the electrolyte. The electrode reaction may be an anodic (or cathodic) process when a species is oxidized (or reduced) by the loss (or gain) of electrons to (or from) the electrode.

Kinetic regimes

At the electrode surface, oxidation/reduction reactions can occur. Let us consider, for example, a general reaction as $Ox + ne^- \rightarrow Red$.

The reaction can be decomposed in different consecutive steps: mass transport from the solution to the electrode, electron transfer at the electrode surface and mass transport of products toward the solution (Fig.10).

Because electrochemical reactions are localized at the contact between the electrolyte and the electrode, an electrochemical reaction can evolve only if the electroactive species involved are present on the surface. This means that the dissolved species arrive at the electrode surface by some transport process through the electrolyte in which they are initially homogeneously distributed. Various transport modes can occur:

- For ionic species, an electric field in the solution produces transport by **ionic electromigration**.
- The consumption or the production of a species at the electrode surface leads to

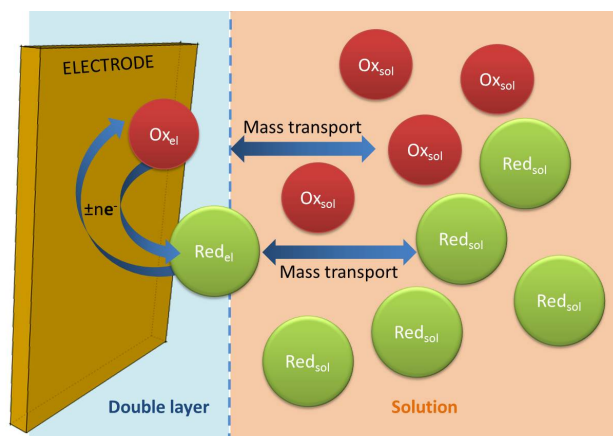


Figure 10: Schematic image of the mass transport and charge transfer at the electrode/solution interface.

a decrease or an increase of the concentration of this species in the vicinity of the electrode. This concentration gradient produces transport by **diffusion**.

- In liquid electrolytes, a movement of the ensemble of the electrolyte produces transport by **convection** (i.e., stirring or flowing of the electrolyte or electrode movement).

In the **permanent regime**, equilibrium is established between the fluxes imposed by the various transport processes on the one hand, and the flux of the electric charges transferred across the interface to produce the electrode reaction on the other hand. This equilibrium is traduced by a relationship between the mass flux and the current density corresponding to the electrochemical reaction. This relationship implies that the global rate of the electrochemical process depends not only on the kinetics of the reaction occurring at the electrode but also on the mass transport kinetics. Therefore, the rate-determining step of the global process can be controlled by either the reaction kinetics or the mass transport, or both. If the governing step is the charge transfer at the metal-solution interface the process is called **Faradic**, since the oxidation/reduction reaction induced by the electron transfer follows the Faraday law:

$$Q = It = nFN \quad (2)$$

where Q is the charge quantity in Coulomb, and N the number of moles of formed product or consumed reactive.

If the governing step is the mass transport to the electrode surface the process is called **non-Faradic**. Other non-faradic phenomena can occur during an electrochemical reaction, such as reorientation of solvent dipoles and adsorption or desorption (corrosion) of species at the interface that modify the interface structure.

When the heterogeneous charge transfer reaction is very fast, the mass transport rate should be fast enough to balance the consumption velocity of the species at the electrode and

allow the reaction progress. In this case the supporting electrolyte, a species in which the ions are not involved in the charge transfer reaction, allow to increase the conductivity of the solution, minimizing the migration. Moreover, the convection phenomena are negligible close to the electrode surface, and this zone, only subjected to the diffusion mass transport, is called the diffusion layer. The mass transport is described by the Fick's laws of diffusion:

$$J_i(x, t) = -D_i \frac{\partial C_i(x, t)}{\partial x} \quad (3)$$

where the diffusion flux per unit area per unit time (the amount of substance that will flow through a small area during a small time interval) is proportional to the concentration gradient of the species i at the interface and to the diffusion coefficient D_i , considering a distance x from the electrode.

In a permanent regime the thickness of the diffusion layer has a fixed value of δ and, considering a linear diffusion profile at the interface, it is possible to express the current corresponding to the electrochemical reaction as follow:

$$I = nFSD \frac{C^{sol} - C^{el}}{\delta} \quad (4)$$

where the concentration of the species in the solution and at the interface of the electrode are expressed by C^{sol} and C^{el} respectively. If the applied voltage is high enough to consider the concentration at the interface negligible, the current reaches a limit value:

$$I_{lim} = nFSD \frac{C^{sol}}{\delta} \quad (5)$$

The permanent regime can be obtained by hydrodynamic constant stirring (rotating disk electrode) of the solution or by changing the electrode geometry (ultramicroelectrodes).

Ultramicroelectrodes

Ultramicroelectrodes (UME) appeared for the first time independently in the work of Wightman and Fleischmann around 1980 and they are often used for *in vivo* voltammetry[1, 2]. Even though many definition have been created for the UME we can consider it as an electrode that has at least one dimension (the critical dimension) smaller than 25 μm . The main characteristic of the UME is to get steady-state conditions without stirring of the electrochemical system. This phenomenon is due to the spherical or hemispherical diffusion profile (Fig.11) that lead to noticeable edge effect in addition to the linear diffusion.

In a non permanent regime the thickness of the diffusion layer δ is not constant but it increases with time. This dependence is expressed in the second Fick's law:

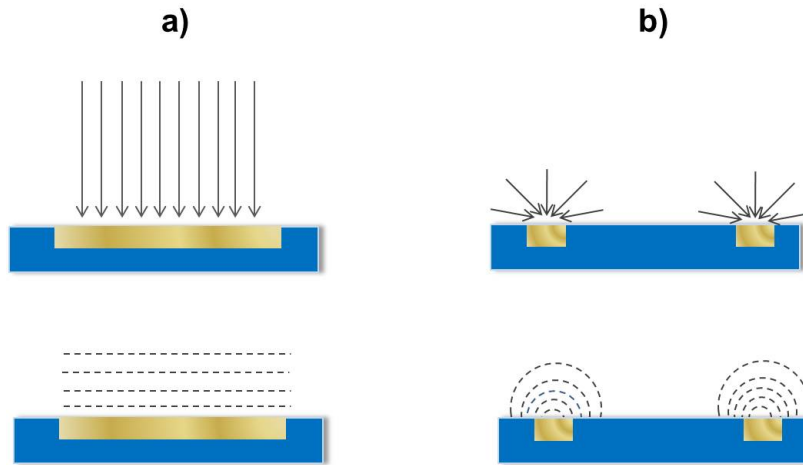


Figure 11: Diffusion flux and diffusion profile for a) plane conventional electrode (linear diffusion) and b) disk microelectrode (hemispherical diffusion).

$$\frac{\partial C_i(x, t)}{\partial t} = -D_i \frac{\partial^2 C_i(x, t)}{\partial x^2} \quad (6)$$

This equation can be solved for both a linear or a spherical diffusion, considering the boundary conditions and by using the Laplace transform, resulting in the following equations, for the linear profile:

$$I(t) = nFSDC^{sol} \frac{1}{\sqrt{\pi Dt}} \quad (7)$$

also known as **Cottrell equation** and, for the spherical diffusion:

$$I(t) = nFSDC^{sol} \left(\frac{1}{\sqrt{\pi Dt}} + \frac{1}{r_0} \right) \quad (8)$$

where r_0 is the radius of the microelectrode. As could be seen this equation is the sum of two terms: the Cottrell equation and a constant. For very short time, the thickness of the diffusion layer is smaller than the microelectrode radius and the mass transport can be considered to have a linear diffusion and the current decrease as function of time (according to the Cottrell equation). For longer times, the first term become negligible and the mass transport follow a radial diffusion. The current is in a steady-state and it does not depend to the time.

$$I_{lim} = \frac{nFSDC^{sol}}{r_0} \quad (9)$$

The time at which the steady state is reached depend from both r_0 and D . The more r_0 is small, the shorter is the time to reach the steady-state. **For the microelectrode the current density at the electrode surface is not an homogeneous and it is higher on the edges.** Therefore, the second Fick's law can be rewritten as:

$$\frac{\partial C_i}{\partial t} = D_i \frac{\partial^2 C_i}{\partial r^2} + \frac{D_i}{R} \frac{\partial C_i}{\partial r} + D_i \frac{\partial^2 C_i}{\partial z^2} \quad (10)$$

where r is the electrode radius ($z=0$) and z the distance from the electrode perpendicular to the center ($r=0$). The current for a plane disk microelectrode is then given by the **Saito equation**:

$$I_{lim} = 4\pi nFDC^{sol}r_0 \quad (11)$$

Electrochemical impedance spectroscopy

Potentiodynamic electrochemical impedance spectroscopy (PEIS) is a powerful tool for the study of structure and electrical features of the electrochemical interface. The technique consists in measuring the current flowing in the electrochemical cell after the application of a sinusoidal modulated potential. It is called "spectroscopy" because the modulation of potential is done over a certain range of frequencies and it constitute, at the end, a frequency spectra.

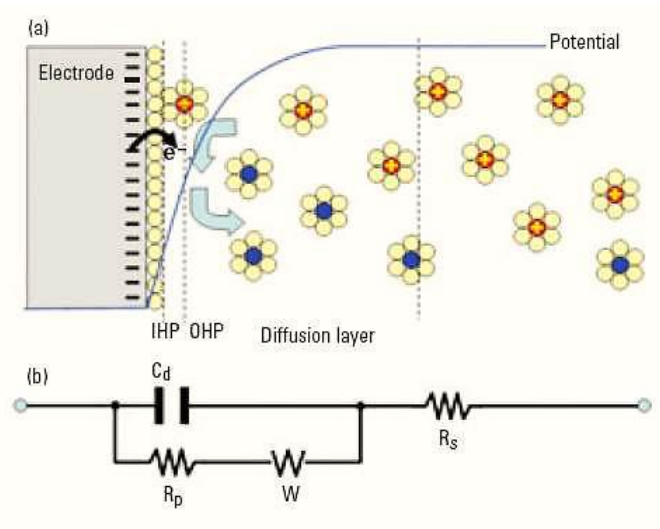


Figure 12: Schematic image of the a) interface electrode/solution and b) associated Randless circuit.

Normally the electrode/solution interface is represented through an equivalent circuit called "**Randless circuit**" (Fig.12), which is basically constituted by a capacitor, C_d (representing the capacity of the double layer) with a resistance, R_p , in parallel (which

represent the resistance to the polarization or to the charge transfer). In series with R_p , it can be found a constant phase element (CPE) called **Warburg diffusion element (W)**. All the circuit is connected in series with the resistance of the electrolytic solution, R_s . EIS provides a lot of information about the interface and it make possible to distinguish the Faradic component from the non-Faradic one.

From the mathematical point of view the applied potential has a profile described by:

$$\Delta E = \Delta E_0 \sin(\omega t) \quad (12)$$

where ω represent the frequency dependence. The answer in terms of current can be written as:

$$\Delta I = \Delta I_0 \sin(\omega t + \varphi) \quad (13)$$

the current indeed has two components: one in phase and one out of phase ($+\varphi$) to the applied potential. The measure of impedance can be considered as $\Delta E/\Delta I$ and it is described by a complex number:

$$Z(\omega) = Z'(\omega) + iZ''(\omega) \quad (14)$$

Z' is the real part in phase with the potential and represent the resistive component of the current; Z'' , which represent the imaginary part out of phase, is related to the capacitive component of the current. The diagram which depict Z'/Z'' is called **Nyquist diagram** and a typical example is shown in Fig.13.

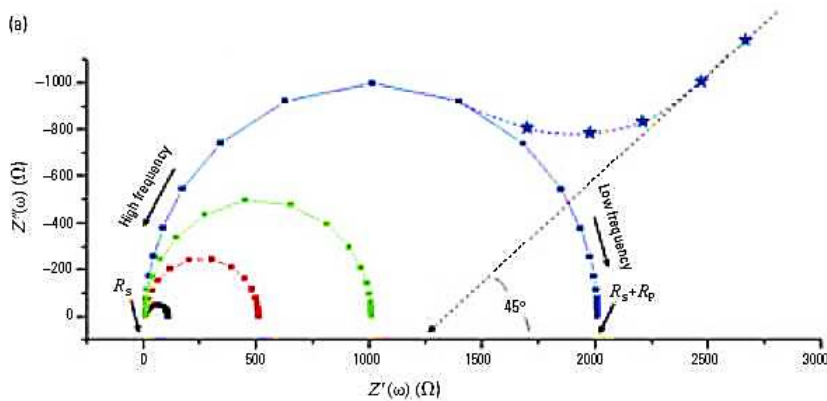


Figure 13: Nyquist-type diagram.

From the Nyquist diagram it could be possible to extract the values of the different components of the equivalent circuit. It is interesting to note that at high frequencies,

$Z(\omega) = Z'(\omega) = R_s$, represented by the intercept on the abscissa for ($\phi = 0$ e $Z''(\omega) = 0$). For $\omega \rightarrow 0$, $Z(\omega) = R_s + R_p$, the intercept on the abscissa at low frequencies.

Other kind of representations can also be employed. For example, since Z is a complex number, it can be represented in polar coordinates, by considering the impedance vector which has as a module the relation $\Delta E/\Delta I$ and as direction the phase angle φ .

$$Z = |Z|e^{i\varphi} \quad (15)$$

$$|Z| = |\Delta E/\Delta I| \quad (16)$$

This representation, $|Z|(\Omega)$ (and φ)/Frequency (ω) is known as **Bode diagram** and it has been mostly reported in this manuscript.

Bibliography

- [1] R. Mark Wightman. Microvoltammetric electrodes. *Analytical Chemistry*, 53:1125A–1134A, 1981.
- [2] A.M. Bond, M. Fleischmann, and J. Robinson. Electrochemistry in organic solvents without supporting electrolyte using platinum microelectrodes. *Journal of Electroanalytical Chemistry and Interfacial Electrochemistry*, 168:299 – 312, 1984.

C. Conductive Atomic Force Microscopy

Atomic Force Microscopy

The Atomic Force Microscopy (AFM), first implemented by G. Binnig et al. in 1986, is a well-known technique based on the interaction between the final atoms of a sharp probe tip and the atoms which constitute a sample surface[1]. It is a very high-resolution type of scanning probe microscopy, very different from an imaging microscope, which measures a two-dimensional projection of a sample surface.

An AFM physically "feels" the sample surface with the probe, building up a map of the surface height (topography). The nature of the interactions between the tip and the sample can be varied: Coulombic forces, Van der Waals forces, dipole-dipole interactions, electrostatic forces, magnetic forces etc.

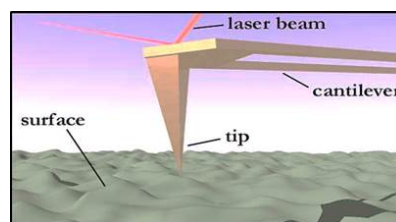


Figure 14: Interaction between the tip and the surface in the AFM (from [2]).

The tip is assembled on a flexible microcantilever and they are integral. The cantilever is displaced by means of piezoelectric materials that expand or contract in the presence of a voltage gradient. This allows a three-dimensional positioning of the device with a very high accuracy. During the probe scanning of the surface, the cantilever undergoes to deflections related to the interaction between the tip and the sample. A laser beam is focused on the cantilever extremity, over the tip (Fig.14) and the laser spot is reflected over a photodiode (Fig.15). Since the laser beam follows the deflection of the cantilever, it is possible to translate this deflection into an electrical signal (through the photodiode detector) and then correlate the deflection to the interaction force between the tip and the surface.

The three concepts at the basis of the operation mode of an AFM are the **piezoelectric transducers** (which the tip over the sample surface), **force transducers** (which senses the force between the tip and the surface), and **feedback control** (which feeds the signal from the force transducer back in to the piezoelectric, to maintain a fixed force between the tip and the sample). The presence of a feedback loop is very important because it allows to adapt the force on the sample and corrects the cantilever deviations very rapidly[3].

The AFM is a powerful tool to study different kind of materials, for example conductive or insulating, giving information about the topography but also about the local properties of the surface. Two of the principal operating mode in which the AFM can be used are:

Contact mode AFM In contact mode, the tip is in permanent contact with the surface of the sample then the surface topography can be measured either using the deflection of the cantilever directly or, more commonly, using the feedback signal required to keep the

cantilever at a constant position. The first mode is suitable for high roughness surfaces, it allows to scan on a large-scale but at the expense of the scan rate. The second mode is mostly used for flat surfaces or small-scale scan and it allow a high scan rate.

Tapping mode AFM In this mode, normally used for topography images, the cantilever vibrate at its resonance frequency on the sample surface without entering in intermittent contact with it. The interaction with the surface modifies the mechanical properties of the oscillating system, modulating the oscillation amplitude and the phase. A servo loop keeps the cantilever excitation to a defined amplitude: The servo adjusts the height to maintain a set cantilever oscillation amplitude as the cantilever is scanned over the sample. In this way, a tapping AFM image is produced by recording the force of the intermittent contacts of the tip with the sample surface.

The tapping mode presents the advantage to minimize the damage done to the surface and the tip compared to the contact mode.

Conductive-AFM

Conductive-atomic force microscopy (C-AFM) is a specific technique to probe electronic properties of a materials at the nanoscale. It is a powerful current-sensing technique in which the sensor signal is the electric current between tip and sample for an applied DC bias (Fig.15).

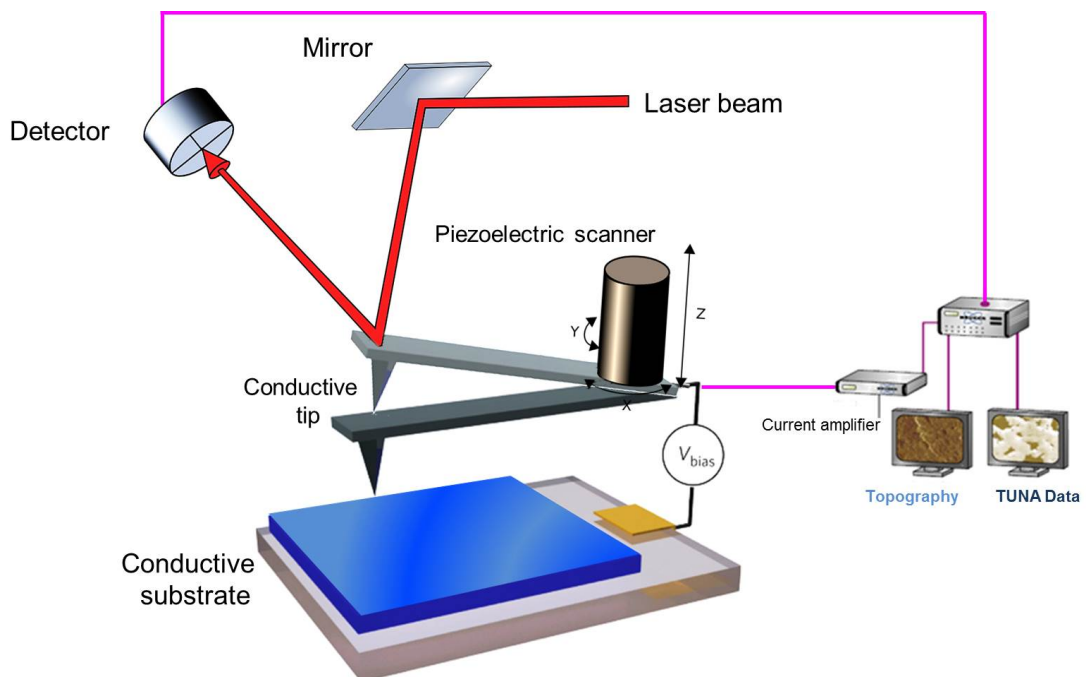


Figure 15: Schematic drawing of a conductive AFM (adapted from [4, 5, 6]).

The functioning of this AFM conductive mode (extended TUNA mode) is the following:

a certain bias voltage is applied between the substrate and a conductive cantilever (which is grounded). The current flow vertically through the sample surface and it is recorded then topographic and current images can be obtained simultaneously.

The conductive AFM works in contact mode, the tip has to be conductive and the sample has to be electrically connected to the AFM stage, by mean, for example, of a conductive tape. The extended TUNA mode has two amplifier stages : C-AFM (1 nA/V-100 nA/V) allowing to measure current from 100 pA to 1 μ A and TUNA (1 pA/V-10 pA/V) allowing to measure current from 50 fA to 120 pA. Moreover, current-voltage characteristics can be achieved on selected spots.

C-AFM is a unique tool for studying the conductivity of organic thin films at the nanoscale[7, 8] and the mechanisms underlying the electrical conduction[9]. In Fig.16 the equipment used in this work is depicted.

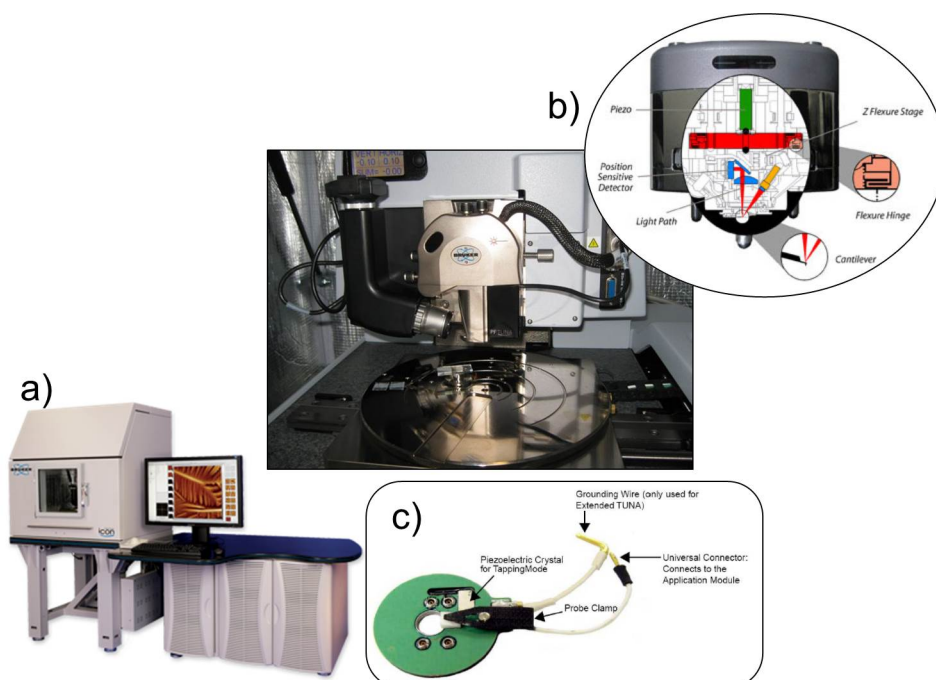


Figure 16: The used equipment: a) the cage, vibration isolation platform and the electronic control with computer; b) the AFM "head" and a scheme of its composition; c) the tip holder for the conductive module.

Local conductivity calculation

For the calculation of the electronic conductivity at room temperature in Chapter 3 the following equation has been used:

$$\sigma = \frac{l}{R A} \quad (17)$$

where R is the vertical resistance ($R=V/I$) obtained for an applied potential on the PEDOT:PSS film, A is the contact area between the conducting tip and the substrate and d is the thickness of the PEDOT:PSS film. To calculate the contact area between the conducting tip and the substrate, the Hertz theory has been employed with the following relation[10]:

$$a^3 = \frac{3FR}{4E^*} \quad (18)$$

where a is the radius of the contact area between the tip and the sample ($A = \pi a^2$), F is the applied force (≈ 10 nN) and R is the actual curvature radius of the system tip-sample ($1/R = 1/R_{tip} + 1/R_{sample}$), and E^* the actual Young's modulus that is defined as:

$$1/E^* = \frac{1 - \nu^2}{E} \quad (19)$$

where E is Young's modulus and ν the Poisson ratio. In the case treated in Chapter 3:

$$1/E^* = \frac{1 - \nu_{PEDOT}^2}{E_{PEDOT}} + \frac{1 - \nu_{tip}^2}{E_{tip}} \quad (20)$$

from the literature E_{PEDOT} is 3.2 GPa. E_{tip} is calculated as follow:

$$k = \frac{3E_{tip}I}{L^3} \quad (21)$$

where k is the spring constant of the tip (0.2 N/m), L^3 the length of the cantilever and I the moment of inertia of the tip defined as:

$$I = \frac{wt^3}{12} \quad (22)$$

where w and t are the width and the thickness of the cantilever respectively.

$$E_{tip} = \frac{4L^2k}{wt^3} \quad (23)$$

from the equation E_{tip} resulted 182.25 GPa. Giving from literature $\nu_{PEDOT} = 0.38$ and $\nu_{tip} = 0.42$, it was possible to calculate the contact area $A = 37.2 \text{ nm}^2$. **This value**

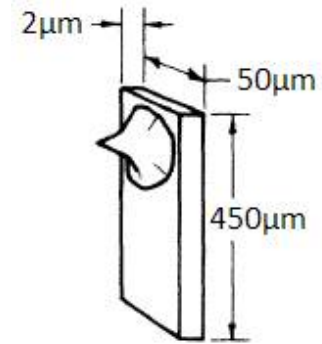


Figure 17: Cantilever dimensions.

is in good agreement with other ones found in the literature[9, 11, 12, 13].

Bibliography

- [1] G. Binnig, C. F. Quate, and Ch. Gerber. Atomic force microscope. *Physical Review Letters*, 56:930–933, 1986.
- [2] Ucla Art-Scicenter. BLUE MORPH, @online:<http://artsci.ucla.edu/bluemorph/concept.html>.
- [3] Peter Jonathan Eaton and Paul West. *Atomic force microscopy*, volume 10. Oxford University Press Oxford, 2010.
- [4] Tal Dvir, Brian P Timko, Mark D Brigham, Shreesh R Naik, Sandeep S Karajanagi, Oren Levy, Hongwei Jin, Kevin K Parker, Robert Langer, and Daniel S Kohane. Nanowired three-dimensional cardiac patches. *Nature Nanotechnology*, 6(11):720–725, 2011.
- [5] Charles Roduit. Free software in biology, @online:<http://www.freesbi.ch/en>.
- [6] Bruker. Conductive AFM, @online:<http://www.bruker.com/products/surface-analysis/atomic-force-microscopy/modes/modes/nanoelectrical-modes/c-afm.html>.
- [7] Hyo Joong Lee, Joowook Lee, and Su-Moon Park. Electrochemistry of conductive polymers. 45. Nanoscale conductivity of PEDOT and PEDOT:PSS composite films studied by current-sensing AFM. *The Journal of Physical Chemistry B*, 114(8):2660–2666, 2010.
- [8] Liam SC Pingree, Bradley A MacLeod, and David S Ginger. The Changing Face of PEDOT:PSS Films: Substrate, Bias, and Processing Effects on Vertical Charge Transport. *The Journal of Physical Chemistry C*, 112(21):7922–7927, 2008.
- [9] Cristian Ionescu-Zanetti, Adam Mechler, Sue A Carter, and Ratnesh Lal. Semiconductive polymer blends: correlating structure with transport properties at the nanoscale. *Advanced Materials*, 16(5):385–389, 2004.
- [10] Jacob N Israelachvili. *Intermolecular and surface forces: revised third edition*. Academic press, 2011.
- [11] Dong-Hun Han, Jae-Woo Kim, and Su-Moon Park. Electrochemistry of conductive polymers 38. electrodeposited poly (3, 4-ethylenedioxy-thiophene) studied by current

- sensing atomic force microscopy. *The Journal of Physical Chemistry B*, 110(30):14874–14880, 2006.
- [12] Shin Hyo Cho and Su-Moon Park. Electrochemistry of conductive polymers 39. contacts between conducting polymers and noble metal nanoparticles studied by current-sensing atomic force microscopy. *The Journal of Physical Chemistry B*, 110(51):25656–25664, 2006.
- [13] Heh-Nan Lin, Hui-Lien Lin, Shen-Shen Wang, Liang-Sheng Yu, Gung-Yeong Perng, Show-An Chen, and Sy-Hann Chen. Nanoscale charge transport in an electroluminescent polymer investigated by conducting atomic force microscopy. *Applied Physics Letters*, 81(14):2572–2574, 2002.

D. Materials and Equipments

Chapter 2

Fabrication: The polyimide resins used (PI-2525, PI2771, PI-2611) have been all purchased from HD Microsystem GmbH, Germany.

All the photoresists (AZ-nLOF 2035, AZ-ECI 3027, ecc) and the developer MFCD26 have been purchased from MicroChemicals. The photoresist Dow BPn-65A, and the adapted developer and photo stripper have been purchased by MMT (microfabrication materials technologies) company.

The developer cyclopentanone comes from Sigma-Aldrich chemicals.

The parylene-C (PXC) dimer was provided by Comelec SA and the deposition has been performed through a machine C30S, provided by Comelec SA.

For the realization of the photolithographic mask the software Clewin4.0 for drawing and a laser lithography machine Heidelberg DLW 200 have been used.

The used aligner is the MA6 or MA150 type (Karlsuss).

The metallization has been performed by magnetron sputtering in a cluster (Oerlikon Univex 450C) and by electron beam physical vapour deposition using the equipment EVA 600 (Alliance Concept).

For the plasma etching a machine Reactive-ion etching (RIE) Aviza Technology Omega 201 has been used.

All the thickness were measured by mechanical profilometer KLA tencor P10.

Cell culture Dulbecco's Modified Eagle Media (D-MEM), Horse Serum (Heat Inactivated), Fetal Bovine Serum, Antibiotic-Antimycotic (containing penicillin-streptomycin), and Trypsin were purchased from Thermo Scientific (HyClone). SH-SY5Y cell line was kindly provided by the Institut de Pharmacologie et de Biologie Structurale (IPBS) of Toulouse. The LIVE/DEAD® Viability/Cytotoxicity Kit for mammalian cells was purchased from Invitrogen.

Organotypic culture: Culture dishes were pretreated with nutrient medium consisting of Dulbecco's modified Eagle's medium (DMEM; Gibco®, Invitrogen, Cergy Pontoise, France), 20% fetal calf serum (FCS; Gibco®, Invitrogen, Cergy Pontoise, France), 2% L-glutamine (Gibco®) and 0.15% penicillin-streptomycin solution (Gibco®).

Organs were isolated from 14 day-old White Leghorn chicken eggs and placed in sterile PBS.

The cultures were incubated at 37°C with 5% CO₂ for 7 days, after which the materials were removed and stained with neutral red. Next, the total surface area covered by tissue was measured using a stereomicroscope equipped with camera and ImageJ software. This area corresponded to the total surface of the cell layer minus the initial explant surface. Additionally, the cells were detached from the materials using 0.025% trypsin-EDTA

(Gibco®) in Isoton® II electrolyte solution (Beckman Coulter, Villepinte, France). The rate of cell detachment was determined by counting the detached cells with a Multisizer® (Beckman Coulter, Villepinte, France) after 5, 10, 20, 30, 60 and 75 min. The rate of detachment as a function of time was used as a measure of adhesion strength, and we defined an arbitrary index.

All data are represented as mean \pm standard error. The data were compared using a one-way ANOVA, followed by a Tukey-Kramer multiple comparisons test (GraphPad InStat 3.01), thereby comparing samples and control (Thermanox®); $P < 0.001$ was considered to be statistically significant.

For the cell migration assessment on parylene-C : Thermanox® on brain $n = 20$; parylene-C on brain $n = 48$; parylene-C on liver $n = 12$; Silk fibroin on brain $n = 12$.

For the cell adhesion assessment on parylene-C : Thermanox® on brain $n = 2$ (these results are the mean of 40 samples); parylene-C on brain $n = 5$ (these results are the mean of 48 samples); parylene-C on liver $n = 1$ (the result is the mean of 12 samples); Silk fibroin on brain $n = 2$ (these results are the mean of 12 samples).

For the cell migration assessment on PEDOT:PSS : PEDOT "small" $n = 8$; PEDOT "big" $n = 8$.

Statistics Tukey-Kramer of cell migration on PEDOT:

Thermanox® versus PEDOT "small" -0.2600 0.1499 ns $P > 0.05$;

Thermanox® versus PEDOT "big" -12.360 7.556 *** $P < 0.001$;

PEDOT "small" versus PEDOT "big" -12.100 6.974 *** $P < 0.001$.

For the cell adhesion assessment on PEDOT:PSS: data are not available.

Chapter 3

The monomer 3,4-ethylenedioxythiophene (EDOT), the poly (sodium 4-styrenesulfonate) (NaPSS, average $M_w = 70,000$) and the Potassium hexacyanoferrate(II) ($K_4Fe(CN)_6$) were all provided by Sigma Aldrich and used as received. Poly(3,4-ethylene dioxythiophene)-poly(styrenesulfonate) 1.3 wt % dispersion in deionized water, conductive grade, for spin coating, was also purchased from Sigma Aldrich. Deionized water was used to prepare all solutions.

To perform electrochemical studies, 200 nm-thick gold round shaped electrodes have been used as working electrode. A platinum wire was used as the counter electrode and a standard calomel electrode (SCE) as the reference. The cell solutions were de-aerated by bubbling N_2 for 20 minute prior to all electrochemical experiments, which were successively carried out under N_2 atmosphere.

Electrochemical polymerizations and measurements were carried out using both an Autolab potentiostat PGSTAT30 (Metrohm Autolab) coupled with NOVA 1.8 software and a VMP3 (Biologic) potentiostat coupled with ECLab software, at room temperature ($23 \pm 1^\circ C$).

The morphology of the PEDOT:PSS coatings was analysed by Scanning Electron Microscopy (SEM Hitachi S-4800). The optical microscope images were performed with a Hirox

Microscope (HI-SCOPE Advanced KH-3000). PEDOT films were also characterized by Atomic Force Microscopy (AFM Dimension Icon) controlled by a Nanoscope III and a Tuna extension module (Veeco) for the conductivity analysis. The morphology is characterized in open air by tapping mode AFM, using a probe RTESP (spring constant 20-80 N/m, resonant frequency of 293-328 kHz). Topography and current images were moreover recorded simultaneously in open air by contact mode using a conducting probe (SCM-PIC, Pt/Ir coated, spring constant 0.2 N/m, resonant frequency of 10-16 kHz) with a probe tip radius of curvature of about 20 nm. For current acquisition, the current sensitivity was 100 nA/V.

Electrochemical Impedance spectroscopy (EIS) measurements were made through both an Autolab potentiostat PGSTAT30 (Metrohm Autolab) coupled with NOVA 1.8 Software and a VMP3 (Biologic) potentiostat coupled with ECLab software, by applying a 5 mV RMS sine wave with frequencies varied logarithmically from 1 Hz to 10 kHz. Measurements were made by immersing the electrode active sites in 0.1 M NaCl.

The thickness of the PEDOT:PSS deposit has been measured by standard Profilometer (KLA Tencor).

Chapter 4

***In vitro* electrophysiological recordings:** Adult (> 2 month old) female mice were deeply anesthetized with isoflurane and killed by decapitation. The scalp, skull and dura mater were taken off and the brain was removed. These operations were made in the presence of ice-cold, modified artificial cerebrospinal fluid (ACSF composition in mM: NaCl 124, NaHCO₃ 26, KCl 3.5, MgSO₄ 1, MgCl₂ 9, NaH₂PO₄ 1.25, and glucose 10). Brain slices (400 μ m thick) were cut on a vibratome (752M vibroslice, Campden Instrument, UK). Once obtained, the slices were kept at room temperature for at least one hour in a storage chamber filled with an *in vivo*-like artificial cerebrospinal fluid (ACSF, composition in mM: NaCl 124, NaHCO₃ 26, KCl 3.5, MgSO₄ 1, NaH₂PO₄ 1.25, CaCl₂ 1.2, and glucose 10). The ACSF was aerated with a 95% O₂-5% CO₂ mixture (pH 7.4). For recording, one slice was placed on the net of a submersion recording chamber (Scientific System Design, Mississauga, Ontario, Canada). The temperature was maintained at 33-34°C. The ACSF was gravity fed at a flow rate of 2.5-3.5 ml/min. Extracellular recordings of spontaneously active neurons were performed in the hippocampus (CA1, CA3). Signals were amplified and filtered with a Neurolog recording system (gain $\times 10^3$ or $\times 10^4$), and digitized with a 1401plus interface (CED Systems, Cambridge, UK) with a digitization rate of 20-40 kHz. On-line visualization and Off-line analysis were achieved using Spike2 (CED Systems) software.

***In vivo* electrophysiological recordings:** Two male C57BL/6J mice (10 to 16 weeks old, obtained from Charles River) were deeply anaesthetized with vetoflurane (2%) and secured to a stereotaxic apparatus placed in a faraday cage. Lidocaine was applied before

(subcutaneous) and after skin incision. A craniotomy was performed to allow unilateral access to the hippocampus. The parylene hex-trode was then lowered in the hippocampus (1.8 mm posterior, 1.3 lateral and 1.1 ventral to the Bregma) and a stainless steel screw was placed through the occipital bone to serve as a reference and ground electrode. Electrophysiological recordings were made using each electrode of the hex-trode. The signal was filtered and amplified (0.3 Hz-3 kHz; P511, Grass Instruments, West Warwick, USA) fed to a 50 Hz noise eliminator (Hum-Bug, Quest Scientific, Vancouver, Canada) before being digitalized at 10 kHz (1401Plus, CED Systems, Cambridge, UK) and visualized and analyzed using Spike2 software (CED Systems).

E. Ethical issues related to the BCI

It is very difficult to imagine how mental entities such as thoughts and emotions could be implemented by physical entities such as neurons and synapses, or by any other type of mechanism. The German mathematician and philosopher Gottfried Wilhelm von Leibniz, wrote in his famous contribution *Monadology* (1714)[1]:

„One is obliged to admit that perception and what depends upon it is inexplicable on mechanical principles, that is, by figures and motions. In imagining that there is a machine whose construction would enable it to think, to sense, and to have perception, one could conceive it enlarged while retaining the same proportions, so that one could enter into it, just like into a windmill. Supposing this, one should, when visiting within it, find only parts pushing one another, and never anything by which to explain a perception. Thus it is in the simple substance, and not in the composite or in the machine, that one must look for perception”.

Leibniz’s argument seems to be this: if we imagine the brain as a complex machine, the visitor of the machine, upon entering it, would observe nothing but the properties of the parts, and the relations they bear to one another. But no explanation of perception, or consciousness, can possibly be deduced from this conglomerate. No matter how complex the inner workings of this machine, nothing about them reveals that what is being observed are the inner workings of a conscious being.

Neuroscience studies the brain and mind, and thereby some of the most profound aspects of human existence.

In the last decade, advances in imaging and manipulating the brain have raised ethical challenges, particularly about the moral limits of the use of such technology, leading to the new discipline of **neuroethics, that concerns the ethical, legal and social impact of neuroscience, including the ways in which neurotechnology can be used to predict or alter human behavior.**

Some neuroethics problems are not fundamentally different from those encountered in bioethics. Others are unique to neuroethics because the brain, as the organ of the mind, has implications for broader philosophical problems, such as the nature of free will, moral responsibility, self-deception, and personal identity: these relatively newer issues force us to think about the relation between mind and brain and its ethical implications.

Neuroethics is a young field and any attempt to define its scope and limits now will undoubtedly be proved wrong in the future, as neuroscience develops and its implications continue to be revealed.

Important activity in Neuroethics

In 2002 several meetings were organized to the scope of discuss about neuroethics: the American Association for the Advancement of Science with the journal *Neuron*, the University of Pennsylvania, the Royal Society of London, Stanford University, and the Dana Foundation. This last meeting was the largest, and resulted in the book "Neuroethics: Mapping the Field"[2].

That same year, articles on neuroethics began to appear in journals including *Nature Neuroscience*, *Neuron*, and *Brain and Cognition*[3, 4, 5]. Thereafter, the number of neuroethics meetings, symposia and publications continued to grow and several relevant books were published[6].

In 2009 was established the Oxford Centre for Neuroethics that aims to address concerns about the effects neuroscience and neurotechnologies will have on various aspects of human life. Its research focuses on five key areas: 1) cognitive enhancement, 2) borderline consciousness and severe neurological impairment, 3) free will, responsibility and addiction, 4) the neuroscience of morality and decision making, and 5) applied neuroethics.

2006 marked the founding of the International Neuroethics Society. The mission of the International Neuroethics Society is *"to promote the development and responsible application of neuroscience through interdisciplinary and international research, education, outreach and public engagement for the benefit of people of all nations, ethnicities, and cultures"*.

Several journals are now soliciting neuroethics submissions for publication, including the *American Journal of Bioethics-Neuroscience*, *Biosocieties*, the *Journal of Cognitive Neuroscience*, and *Neuroethics*. The web now has many sites, blogs and portals offering information about neuroethics.

Ethical considerations

At present, we can discern two general categories around which precipitate the current public debate about the neuroethical issue:

1. In the first category (emerging from what we can do) are the ethical problems raised by advances in functional neuroimaging, psychopharmacology, brain implants and brain-machine interfaces. It concern problems of actuality summarized in questions as: *"does the benefit of the prosthetic implant justify the risk of adverse effects to the individual and to society?"*
2. In the second category (what we know and what we could do) are the ethical problems raised by our growing understanding of the neural bases of behaviour, personality, consciousness, and states of spiritual transcendence and issues related to the future use of the knowledge. A typical question in this case could be: *"is it desirable to enhance human capabilities by neuroelectronic devices?"*[7]

We can enumerate a series of considerations/questions that belongs to the first category: **how can we obtain informed consent from people who have difficulty communicating? how to ensure that responsible group decisions in the BCI team can be made? what are the consequences of BCI technology for the quality of life of patients and their families? what about the side-effects? who is responsible for erroneous actions with a neuroprosthesis? what about issues concerning personality and person-hood and its possible alteration?**[8]. One of the first technical problems regard the obtaining of an informed consent from potential patients. Informed consent is a patient's agreement to receive certain medical treatment after being fully advised of the related facts and possible risks associated with the surgery or procedure. For some patients with locked-in syndrome, doctors must establish some kind of communications code, for example point the eyes on the left to indicate "yes" and on the right to indicate "no". Nevertheless, patient with total locked-in syndrome have no way to communicate with the world and for them the technical issue of informed consent transforms into an ethical issue. Most of these patients have family acting as legal guardians, which are, therefore responsible for the patients. But if the patients does not have any legal guardian, should doctors refuse to treat a person who is unable to legally agree to surgery or should they treat the person with the aim of simply trying to improve their life? According to the **Principle of Utility, that states that actions or behaviours are right so far as they promote happiness or pleasure, wrong as they tend to produce unhappiness or pain**, treatment with BCIs is moral because it aims to improve the lives of people who have been disabled. So the final question is: is it ethical to intentionally violate a person's body, even for therapeutic reasons?

Other issues, that could arise from the commercialization of neuroprosthetics, are the warranties of durability of the probe and the availability to people in need. All the problems related to the product durability, and then the patient safety should be legally addressed, to ensure the quality of the produced device. Moreover, since this technology is still new, if only a limited number of BCI are available in a region or interval of time, would one kind of patient get preference over the others?

Finally, communication to the media should be considered; overly positive media articles or exaggerated product claims could raise false expectations in stakeholders and subsequent disappointment can certainly be considered as one harmful consequence of this research[9].

In the second category different kind of considerations have to be faced, **starting from risks of excessive use of the therapeutic applications or questions of research ethics that arise when progressing from animal experimentation to application in human subjects, until arrive to questions about mind-reading and privacy, mindcontrol, selective enhancement and social stratification, human dignity, mental integrity and regulating safety**. If even an artificial system, such as a cultured neural network could be used to control heavy robotics[10, 11], what about relation between mind and brain? This question entitles a wide possibilities of discussion about the definition of "person" or "entity".

Moreover, it is easy to imagine how this technology could be used in order to enhance the performances of humans, even the one not affected by neural impairments. If we take these considerations to the extreme, is possible to imagine the creation of super-human powers by replacing a healthy human features with bionic enhanced ones or the possibility to manipulate object directly connected to the thoughts, potentially interesting application for national governments and military forces. We can think for example to soldiers who communicates via recognizable brainwave patters that are instantaneously transmitted to the other troops to make the communication easier in hostile environments, or BCI-controlled exoskeletons to provide human augmentation suits. All these possibilities not only involve the ethics of the applications of his research but also lead to a further important question: what happens if the BCI stop working when it is implanted inside someone?

In the conclusion the question remains the same, any time a groundbreaking research field arises: to what extent (and with which intent) the research on this field want to push on?

Bibliography

- [1] Gottfried Wilhelm Leibniz. *The monadology*. Springer, 1989.
- [2] Steven J Marcus. Neuroethics: Mapping the field. In *Proceedings of the Dana Foundation Conference, University of Chicago Press*, 2002.
- [3] Judy Illes and Thomas A Raffin. Neuroethics: An emerging new discipline in the study of brain and cognition. *Brain and Cognition*, 50(3):341–344, 2002.
- [4] Judy Illes, Matthew P Kirschen, and John DE Gabrieli. From neuroimaging to neuroethics. *Nature neuroscience*, 6(3):205–205, 2003.
- [5] Martha J Farah. Emerging ethical issues in neuroscience. *Neuroethics Publications*, page 13, 2002.
- [6] Judy Illes. *Neuroethics: Defining the issues in theory, practice, and policy*. Oxford University Press, 2006.
- [7] Kevin Warwick, Mark Gasson, Benjamin Hutt, and Iain Goodhew. An attempt to extend human sensory capabilities by means of implant technology. In *Systems, Man*

and *Cybernetics*, 2005 *IEEE International Conference on*, volume 2, pages 1663–1668, 2005.

- [8] Veronica Johansson. Do brain-machine interfaces on nano scale pose new ethical challenges. *Size matters: Ethical, legal and social aspects of nanobiotechnology and nano-medicine*, pages 75–99, 2009.
- [9] Femke Nijboer, Jens Clausen, Brendan Z Allison, and Pim Haselager. Researchers' opinions about ethically sound dissemination of bci research to the public media. *International Journal of Bioelectromagnetism*, 13(3):108–109, 2011.
- [10] Kevin Warwick, Dimitris Xydias, Slawomir J Nasuto, Victor M Becerra, Mark W Hammond, Julia Downes, Simon Marshall, Benjamin J Whalley, et al. Controlling a mobile robot with a biological brain. *Defence Science Journal*, 60(1):5–14, 2010.
- [11] Kevin Warwick, Slawomir J Nasuto, Victor M Becerra, and Benjamin J Whalley. Experiments with an in-vitro robot brain. In *Computing with instinct*, pages 1–15. 2011.

Valorization

National Conferences

27ème congrès de Médecine Physique et Réadaptation SOFMER, October 17th-19th 2012, Toulouse (Oral presentation)

V. Castagnola, C. Bayon, S. Charlot, C. Bergaud, E. Descamps

"Microélectrodes implantables pour la stimulation et l'enregistrement de l'activité cérébrale"

Bionicamp, December 6th 2012, Paris (Oral presentation)

V. Castagnola, C. Bayon, S. Charlot, C. Bergaud, E. Descamps

"Microélectrodes implantables pour la stimulation et l'enregistrement de l'activité cérébrale"

Journées électroniques "Electronique et Santé", November 7th-8th 2013, Limoges (Oral presentation)

V. Castagnola, C. Bayon, A. Lecomte, E. Descamps, C. Bergaud

"Microélectrodes implantables flexibles pour la stimulation et l'enregistrement de l'activité cérébrale"

Atelier "Nano-matériau, nano-objets pour la détection et les capteurs, December 2nd-4th 2013, Nailloux (Poster presentation)

V. Castagnola, E. Descamps, C. Blatchè, L.G. Nowak and C. Bergaud

"Perylene-based flexible neural probes with PEDOT-coated surface for brain stimulation and recording"

International Conferences

International Winterschool on Bioelectronics, February 22nd - March 1st 2014, Kirchberg in Tirol, Austria (Oral presentation)

V. Castagnola, E. Descamps, C. Blatchè, L.G. Nowak and C. Bergaud

"Flexible technology for PEDOT-modified neural probes"

Smart Systems Integration (SSI), March 26th - 27th 2014, Wien, Austria (Poster presentation)

S. Charlot, V. Castagnola, E. Descamps

"Low stress polyimide multilayers integration for flexible substrate"

Biosensors, May 27th - 30th 2014, Melbourne, Australia (Poster presentation)

V. Castagnola, E. Descamps, L.G.Nowak, L.Dahan, C.Bergaud

"Parylene-based flexible neural probes with PEDOT coated surface for brain stimulation and recording"

NanoBioEurope, June 2nd - 4th 2014, Münster, Germany (Oral presentation)

V. Castagnola, E. Descamps, L.G.Nowak, L.Dahan, C.Bergaud

"Parylene-based flexible neural probes with PEDOT- coated surface for recording of the brain activity"

Publications in Peer Reviewed Journals

V. Castagnola, C. Bayon, E. Descamps, C. Bergaud, *Morphology and conductivity of PEDOT layers produced by different electrochemical routes*

2014, published on **Synthetic Metals**

V. Castagnola, E. Descamps, A. Lecestre, L. Dahan, J. Remaud, L.G. Nowak, C. Bergaud, *Parylene-based flexible neural probes with PEDOT coated surface for brain stimulation and recording*

2014, published on **Biosensors and Bioelectronics**

A. Lecomte, V. Castagnola, E. Descamps, L. Dahan, C. Blatchè, E. Leclerc, C. Bergaud, *Silk and PEG as means to stiffen a parylene probe for insertion in the brain: a double time-scale solution for local drug delivery*

2014, *in preparation*

Reviewer for

Nanotechnology (July 2013)

Biosensors and Bioelectronics (July 2014)